



TECHNISCHE UNIVERSITÄT MÜNCHEN
Physik Department E21 (Lehrstuhl für Experimentalphysik III)

Superconductivity and non-Fermi liquid behavior on the border of itinerant ferromagnetism

Dipl.-Phys. Univ. Robert Ritz

Vollständiger Abdruck der von der Fakultät für Physik der Technischen Universität München zur Erlangung des akademischen Grades eines

Doktors der Naturwissenschaften (Dr. rer. nat.)

genehmigten Dissertation.

Vorsitzender: Univ.-Prof. Dr. Martin Zacharias

Prüfer der Dissertation: 1. Univ.-Prof. Dr. Christian Pfleiderer
2. Prof. Andrew Huxley Ph.D.,
Univ. Edinburgh/UK

Die Dissertation wurde am 24.09.2013 an der Technischen Universität München eingereicht und durch die Fakultät für Physik am 04.10.2013 angenommen.

Abstract

The border of magnetism, where a phase transition into a magnetically ordered state is suppressed to zero temperature, is an interesting playground to study exotic electronic ordering phenomena that are driven by quantum fluctuations like unconventional forms of magnetic or superconducting order. Numerous important discoveries in contemporary condensed matter physics like, e.g., high temperature superconductivity, are attributed to such zero temperature phase transitions, so-called quantum phase transitions [1]. A deeper understanding of these phenomena promises the development of new technologically relevant materials.

The conventional scenario for a quantum phase transition is a continuous, i.e., second order, phase transition that is suppressed to zero temperature. As in classical continuous phase transitions at finite temperature, these phase transition are governed by fluctuations whose length and timescale diverges on approaching the phase transition point. However, at zero temperature the fluctuations are not thermal but quantum fluctuations. Furthermore, the control parameter is non-thermal like pressure, magnetic field, or doping. The point where a second order phase transition is suppressed to zero Kelvin is called quantum critical point (QCP). There, the free energy landscape is rather flat so that even exotic forms of order with tiny energy scales can become the groundstate. The presence of a QCP can be felt at finite temperatures leading to a characteristic V-shaped region in the phase diagram where anomalous temperature dependences of physical properties like, e.g., the specific heat or resistivity are observed. The QCP is often masked by a dome of an exotic ordered phase.

The probably best known scenario for studying the effects of QCPs is the border of antiferromagnetic order. Numerous studies exist where the second order phase transition at the Néel temperature is suppressed to low temperatures. E.g., in CePd₂Si₂ [2], CeRh₂Si₂ [3], CeCu₂ [4], and CeIn₃ [5] a superconducting dome emerges in the vicinity of the QCP. In YbRh₂Si₂ [6] and CeCu_{1-x}Au_x [7] the physical properties substantially deviate from the fundamental theory of metals at low temperatures, the Fermi liquid theory.

In contrast to antiferromagnetic order, it was found in all systems studied so far that at the border of itinerant ferromagnetism the transitions at the Curie temperature turn from second to first order before they are suppressed, precluding a QCP together with the emerging quantum critical behavior. In a classical picture, first order phase transitions are driven by local minima in the free energy where fluctuations do not play an important role. However, due to the special nature of quantum phase transitions, quantum fluctuations can also drive a first order quantum phase transition giving rise to interesting phenomena like the coexistence of superconductivity and ferromagnetism [8] or non-Fermi liquid behavior (NFL) extending over a wide range in the phase diagram [9, 10]. Furthermore, it was proposed that at ferromagnetic quantum phase transitions magnetic textures generically emerge above the critical pressure p_c [11, 12]. In this thesis we study the properties of two prominent itinerant ferromagnets around the critical pressures: The superconducting ferromagnet UGe₂ and the helimagnet MnSi.

In UGe_2 a superconducting dome emerges inside the ferromagnetically ordered phase just below the critical pressure p_c . It has a maximum of the superconducting transition temperature T_{SC} at a pressure p_X where a second transition T_X between two ferromagnetic states is suppressed. Both ferromagnetic transitions turn first order before they are suppressed to zero Kelvin. The superconductivity is attributed to magnetic fluctuations associated with the first order quantum phase transitions at p_X and p_C . For further insights we chose to study the evolution of the T_X transition under pressure in the thermal expansion along all crystal axes of the orthorhombic UGe_2 . The thermal expansion promises vital informations as the unit cell volume, and hence the thermal expansion, is the conjugate physical property to these pressure induced phase transitions. The neutron spin-echo technique of Larmor diffraction allowed us to track the thermal expansion concomitant with the magnetization. This way we are able to separate contributions from the crystal lattice from magnetostriction and other contributions to the thermal expansion. In total we measured six pressure points between ambient pressure and 12.4 kbar.

On approaching p_X , we find signatures of an additional transition T_L several Kelvin above the T_X transition along the c -axis thermal expansion that can not be attributed to contributions from the crystal lattice or magnetostriction. Hence, the T_L transition has to originate from a different mechanism. Possibly, the T_L transition is the signature of a topological change of the Fermi surface a so-called electronic topological transition also known as Lifshitz transition. This finding provides new information that might help to identify the mechanisms behind the unconventional superconductivity found in UGe_2 .

In MnSi a non-Fermi liquid phase is observed above the critical pressure p_c that extends over a large pressure range up to at least $3 \times p_c$ rather than to a V-shaped region around the quantum phase transition [10, 13]. As in UGe_2 , the transition temperature T_c turns first order before it is suppressed to zero Kelvin. MnSi is probably the best studied weak ferromagnetic system. It played a big role for the creation of a theory of band-magnetism in the presence of strong fluctuations [14]. However, MnSi is a ferromagnet only in a first approximation. Due to a missing inversion symmetry in the crystal structure a Dzyaloshinskii-Moriya interaction arises that causes a helical modulation of the magnetization with a long wavelength of $\approx 180 \text{ \AA}$. In a specific field and temperature interval of the phase diagram these helices form a periodic structure of magnetic whirls, so-called skyrmions. One signature of a skyrmion lattice is a special contribution to the Hall effect called topological Hall effect (THE) that is sensitive to the topology of the magnetic structure [15]. In MnSi the THE contribution appears as top-hat shaped signal that rides on top of the anomalous Hall effect contribution. We chose to study the Hall effect in MnSi to track the evolution of the skyrmion lattice with pressure. Our specific interest was whether we can find signatures of topologically non-trivial magnetic textures above the critical pressure p_c where magnetic order is suppressed. And if yes how these signatures can be linked to the extended non-Fermi liquid phase. Our experiments represent a comprehensive study where we carefully checked the influence of various parameters as sample quality, sample orientation, different pressure media, and different cooling procedures. In total we measured 38 pressure points between ambient pressure and 18.1 kbar.

We find that the top-hat shaped signature in the Hall effect evolves continuously with increasing pressure. This clearly links the signature under pressure to the skyrmion lattice phase at ambient pressure. In addition, we can clearly identify the top-hat signature as THE through comparison of Hall effect with magnetization measurements. With increasing pressure at which the transition T_c shifts to lower temperature, the THE signal increases tenfold from its ambient pressure value of $\Delta\rho_{xy}^{\text{top}} \approx 4.5 \text{ n}\Omega\text{cm}$ to $\approx 40 \text{ n}\Omega\text{cm}$ at $p \approx 12 \text{ kbar}$.

Furthermore, we find that the skyrmion lattice phase, and hence the THE signal, can be conserved down to the lowest temperatures measured (typically $\approx 2 \text{ K}$) when cooling in a magnetic field in the range of the skyrmion lattice phase. As finite temperature effects like spin-flip scattering are essentially switched off at low temperatures, this reveals the generic size of the THE in MnSi $\Delta\rho_{xy}^{\text{top}} \approx 50 \text{ n}\Omega\text{cm}$. A theoretical analysis by Rosch and collaborators [16] can quantitatively account for the tenfold increase of the THE under pressure and shows that the large size of the THE under pressure represents the generic THE size in MnSi. The decreased THE size at ambient pressure and high temperatures can be attributed to the change of the local polarization close to T_c for the most important part. The remaining part is most likely due to one or a combination of several mechanisms including changes of the Fermi surface, a change of the scattering processes, competition between exchange splitting and spin-orbit coupling, and spin-flip scattering.

Moreover, we find a topological contribution to the Hall effect in the non-Fermi liquid region above the critical pressure p_c where magnetic order is already suppressed. The THE signal clearly evolves from the THE signal seen in the skyrmion lattice phase of MnSi at ambient pressure. Sign and size of the THE remain unchanged below and above p_c pointing at skyrmion structures. The field boundaries of the THE coincide with the metamagnetic transition where the NFL behavior abruptly switches back to Fermi liquid behavior under applied magnetic field. Also the temperature and pressure boundaries of the NFL state and the THE coincide. Thus, the magnetic textures and the NFL are clearly linked to each other. This could be a first example of a more general phenomenon where magnetic textures form on the border of ferromagnetism [11, 12]. Those complex spin structures could be the long-sought intrinsic mechanism driving the breakdown of Fermi liquid behavior in MnSi.

Abbreviations

AHE	anomalous Hall effect
CF	crystal field interactions
Chap(s).	chapter(s)
dHvA	de Haas-van Alphen effect
DMFT	dynamical mean-field theory
DOS	density of states
ETT	electronic topological transition
Eq(s).	equation(s)
fc/fh	field heating after cooling in the same magnetic field
FI	Fluorinert mixture FC72:FC84 with volume ratio 1:1
Fig(s)	figure(s)
FLT	Fermi liquid theory
FL	Fermi liquid
FM	ferromagnetic
FWHM	full width at half maximum
ILT	itinerant-localized transition
LD	Larmor diffraction
ME	Methanol:Ethanol mixture with volume ratio 4:1
NFL	non-Fermi liquid
NHE	normal Hall effect
PM	paramagnetic
QCP	quantum-critical point
Ref(s).	reference(s)
RRR	residual resistivity ratio
SANS	small angle neutron scattering
SC	superconductor
Sec(s).	section(s)
SLP	skyrmion lattice phase, a.k.a. A-phase
SOC	spin-orbit coupling
TCP	tri-critical point
THE	topological Hall effect
zfc/fh	field heating after cooling in zero magnetic field

Contents

1	Motivation and theoretical background	1
1.1	The border of itinerant magnetism	1
1.2	Quantum phase transitions in ferromagnets	3
1.3	Lifshitz transitions	8
1.4	Fermi liquids and non-Fermi liquids	9
I	Thermal expansion of UGe₂ under pressure	13
2	The superconducting ferromagnet UGe₂	17
2.1	Thermal expansion of UGe ₂	21
2.2	Scenarios for the T_X transition	23
3	Experimental methods	27
3.1	Thermal expansion at low temperatures	27
3.1.1	Contributions to the thermal expansion	27
3.1.2	Thermal expansion at phase transitions	28
3.1.3	Experimental methods	29
3.2	Introduction to Larmor diffraction	30
3.2.1	Principle of neutron spin-echo technique	31
3.2.2	Measurement of lattice constants	32
3.2.3	Measurement of the distribution of lattice constants	33
3.2.4	Spin-echo mode	37
3.3	Experimental setup	37
3.3.1	Spectrometer TRISP at FRM II	37
3.3.2	Samples	38
3.3.3	Cryostats and pressure cells	39
3.4	Data analysis	40
3.4.1	Determination of pressures	40
3.4.2	Thermal expansion	42
3.4.3	Distribution of lattice constants	42
3.5	Larmor diffraction on UGe ₂ : Specific challenges	43
3.5.1	Depolarization	43
3.5.2	Non-vanishing spin-echo phase	47

4	Results and Discussion	51
4.1	Comparison with literature	51
4.1.1	Ambient pressure	51
4.1.2	Under pressure	52
4.2	Additional transition T_L	57
4.3	Discussion of the T_L transition	62
II	Skyrmions and the non-Fermi liquid puzzle of MnSi	65
5	The helimagnet MnSi	69
5.1	MnSi at ambient pressure	69
5.1.1	More about skyrmions	70
5.2	MnSi under hydrostatic pressure	74
6	Experimental methods	79
6.1	Resistivity of metals at low temperatures	79
6.1.1	Non-magnetic metals	79
6.1.2	Ferromagnetic metals	80
6.1.3	Magnetoresistance	82
6.1.4	Resistivity and magnetoresistance of MnSi	82
6.2	Hall effect	84
6.2.1	General remarks	84
6.2.2	Normal Hall effect	87
6.2.3	Intrinsic anomalous and topological Hall effect	88
6.2.4	Extrinsic anomalous Hall effect	96
6.2.5	Hall Effect in MnSi	98
6.3	Experimental setup	104
6.3.1	Crystals	104
6.3.2	Magnetocryostat	104
6.3.3	Measurement electronics	105
6.3.4	Pressure cells	106
6.4	Data analysis	111
6.4.1	Symmetrization & antisymmetrization	111
6.4.2	Geometry factors	111
6.4.3	Demagnetization factors	113
6.4.4	Determination of pressures	115
6.4.5	Influence of pressure media and cooling procedures	116
7	Results $p < p^*$	119
7.1	Magnetic field dependence	119
7.2	Temperature dependence	128
7.3	Magnetic phase diagram	131

8 Discussion $p < p^*$	135
8.1 $\Delta\rho_{xy}^{\text{top}}$ under pressure	135
8.2 Generic size of $\Delta\rho_{xy}^{\text{top}}$	136
8.2.1 Normal Hall constant R_0 under pressure	138
8.2.2 Emergent magnetic field B^e under pressure	139
8.3 Temperature dependence of $\Delta\rho_{xy}^{\text{top}}$	139
8.4 Conclusions	140
9 Results $p > p^*$	143
9.1 Temperature dependence	143
9.2 Magnetic field dependence at high fields	144
9.3 Magnetic field dependence at small fields	146
9.4 Magnetic phase diagram under pressure	153
9.4.1 Definition of transition fields and temperatures	153
9.4.2 Phase diagrams	154
10 Discussion $p > p^*$	157
III Summary and outlook	159
Publications	165
Acknowledgements	167
A Overview LD and SE scans	169
Bibliography	169

Chapter 1

Motivation and theoretical background

1.1 The border of itinerant magnetism

The border of magnetism, i.e., a phase transition into a magnetically ordered state that is suppressed to 0 K, is an especially interesting and active field in solid state physics where new, exotic electronic ordering phenomena can be observed. Such ordering phenomena include unconventional forms of superconductivity, magnetic textures like spin density waves, and deviations from the fundamental theory for metals at low temperatures, the Fermi liquid theory. The physics close to the suppression of magnetic order is special in that quantum fluctuations are the driving mechanism for a phase transition into an exotic ordered state rather than thermal fluctuations that drive classical phase transitions. In a more general context, this kind of phase transitions, called quantum phase transitions, are also observed when other types of order like superfluidity or ferroelectricity are suppressed. The research on quantum phase transitions has been very active over the past two decades and numerous reviews can be found in the literature. For further reading we refer, e.g., to Refs. [1, 17–26]. This section gives a general introduction into the field of quantum phase transitions. This is followed by Sec. 1.2 which focuses on first order quantum phase transitions observed at the border of itinerant ferromagnetism as in the systems studied in this thesis, UGe_2 and MnSi . Both systems are introduced and the goals of this thesis are presented. At the end of this chapter, Lifshitz transitions and non-Fermi liquids are briefly introduced in Secs. 1.3 and 1.4 as both phenomena are relevant for the discussion of our experimental results.

In general two types of phase transitions are classically observed that are classified as first and second order phase transitions according to Ehrenfest. Their basic properties may be summarized as follows (see e.g. Refs. [1, 27, 28]): A first order phase transition is governed by local minima in the free energy landscape F as illustrated in the upper row of Fig. 1.1. The system occupies one minimum of F and “jumps” over the potential barrier into another minimum when the free energy landscape changes with increasing control parameter x . The change from one into another groundstate happens at a critical value x_c of the control parameter where two local minima are energetically equal. Examples for the control parameter x are temperature, magnetic field, pressure, and doping. To describe the ordered phase a unique thermodynamic quantity called the order parameter U is used.

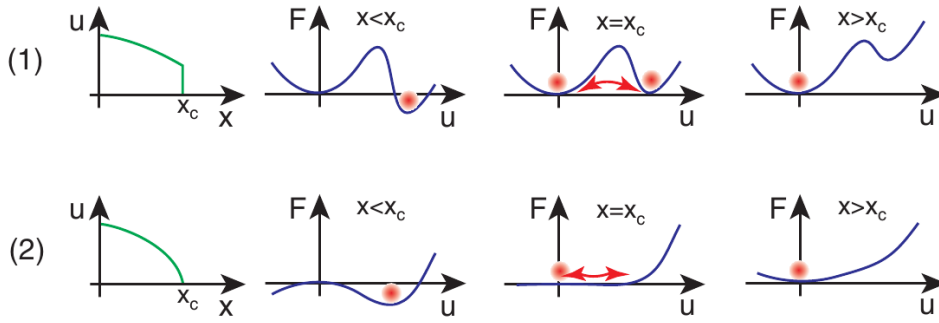


Figure 1.1: Order parameter and free energy at first and second order phase transitions. *Upper row:* Discontinuous change of order parameter U with changing control parameter x and free energy landscape F at a first order phase transition. *Bottom row:* Continuous change of order parameter U with changing control parameter x and free energy landscape F at a second order phase transition. Figure from [29].

U is non-zero in the ordered phase and zero in the disordered phase. An example for U is the magnetization of a ferromagnet. Characteristic for a first order phase transition are a discontinuously vanishing order parameter U , a phase coexistence, and the release of a certain amount of energy, the so-called latent heat, at the phase transition. Fluctuations of the order parameter typically do not play an important role.

A second order phase transition, also referred to as continuous phase transition, is governed by order parameter fluctuations that drive the system towards a global minimum in the flat free energy landscape F as illustrated in the bottom row of Fig. 1.1. With increasing control parameter x the global minimum in the free energy landscape evolves continuously and with it the groundstate of the observed system. Characteristic for a second order phase transition is a continuously vanishing order parameter U . Close to the transition point at x_c the length and timescale of the fluctuations diverge rendering details of the free energy landscape unimportant. Consequently, entire classes of phase transitions show the same behavior close to the transition point even if they appear in very different physical systems. This phenomenon is called universality. The divergence of the order parameter fluctuations lead to singularities of physical observables, the so-called critical behavior. The divergence of the physical observables can be described by the distance from the critical point $t = |T - T_c|/T_c$ to the power of critical exponents. According to the scaling relation, the critical exponents of the four thermodynamic observables specific heat, order parameter, susceptibility, and critical isotherm are connected to each other. A particular class of phase transitions is completely characterized by its critical exponents and called universality class.

Particularly interesting are second order phase transitions at zero temperature. Due to the zero temperature these transitions are accessible by a non-thermal control parameter like magnetic field, pressure, or doping. In contrast to classical phase transitions that are driven by thermal fluctuations, at zero temperature a phase transition is governed by quantum fluctuations as $\hbar\omega_c > k_B T$. This circumstance was first realized by Hertz [30]

who introduced the term “quantum phase transitions”. In particular, the point in the phase diagram where a second order phase transition is suppressed to zero Kelvin is called quantum critical point (QCP). The presence of a QCP leads to effects that are not only detected at zero temperature but also at finite temperatures. This raises quantum phase transitions from a purely academic to a real world problem that can be studied experimentally. Fig. 1.2a shows schematically a typical phase diagram that is observed when a magnetically ordered phase (green shading) is suppressed through an increasing control parameter. The QCP is usually masked by a dome of an emerging order like unconventional superconductivity or a spin-density-wave (blue shading). In a characteristic V-shaped region at temperatures above the QCP, called the quantum critical region, anomalous temperature dependences of physical properties like the resistivity or the specific heat are observed (yellow shading). On the far side of the QCP a Fermi liquid phase can emerge that may possess heavy fermion character in certain f -electron compounds (red shading) (see Ref. [23] for details).

The probably best known examples for QCPs are observed at the border of antiferromagnetic order. Two examples of antiferromagnetic QCPs are illustrated in Fig. 1.2b and c where the second order phase transition at the Néel temperature T_N is suppressed with pressure and magnetic field, respectively. In CePd_2Si_2 weak antiferromagnetic order with T_N below 10 K is suppressed with pressure. The QCP at a critical pressure $p_c \approx 28$ kbar is masked by a superconducting dome. In YbRh_2Si_2 weak antiferromagnetic order with $T_N < 70$ mK is suppressed through the application of a magnetic field along the crystallographic c -axis. In a V-shaped region around the critical field $B_c = 0.66$ T the resistivity, $\rho(T) = AT^\alpha + \rho_0$, deviates from Fermi liquid behavior with exponent $\alpha = 2$ (blue shading) and shows a linear behavior with $\alpha = 1$ (orange shading).

Besides in magnetic systems, quantum criticality can also be found related to other kinds of order. For example, the paraelectric materials SrTiO_3 and KTaO_3 are very close to a ferroelectric quantum critical point, i.e., they become ferroelectric through small perturbations of the material or chemical environment like strain and element substitution [31]. As a consequence they exhibit quantum critical behavior without further tuning through, e.g., pressure or doping as observed in an electric susceptibility that deviates substantially from the Curie-Weiss dependence. Another example for quantum criticality are insulating Ising ferromagnets like CoNb_2O_6 [32] and LiHoF_4 [33]. When applying a transverse field to these magnetically uniaxial Ising ferromagnets, the ordered phase undergoes a quantum phase transition into a disordered state at a critical field value.

1.2 Quantum phase transitions in ferromagnets

In ferromagnetic systems the “standard” QCP scenario where a second order phase transition is continuously suppressed to zero temperature (Fig. 1.3a and b) is not observed experimentally. Instead, ferromagnets follow certain “escape routes” to avoid the degeneracies of quantum fluctuations at QCPs. In itinerant ferromagnets studied so far as

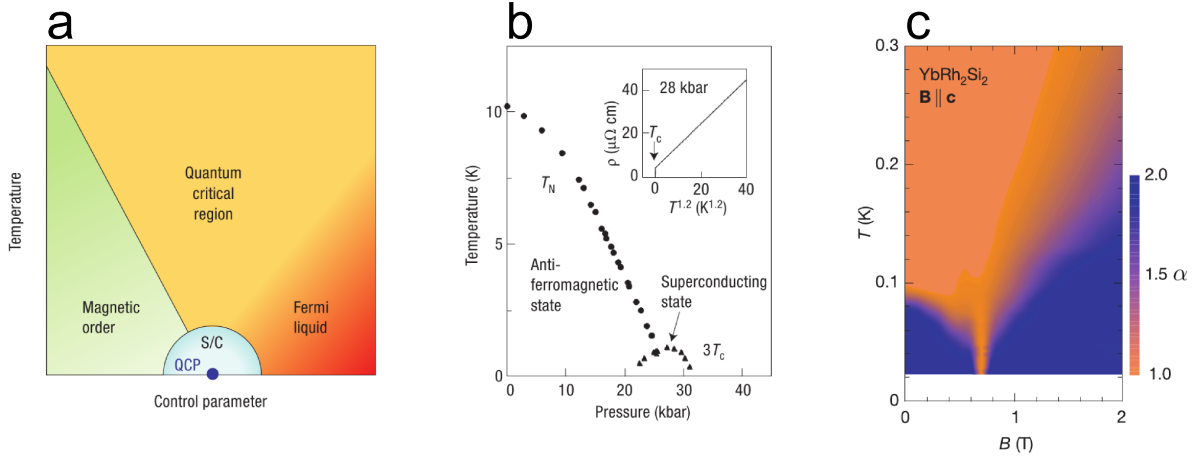


Figure 1.2: Quantum critical points. (a) Schematic phase diagram with a quantum critical point on the border of magnetic order. Figure from [23]. (b) In CePd_2Si_2 a superconducting phase emerges where antiferromagnetic order is suppressed with pressure. The inset shows the drop of the resistivity at the superconducting transition. Figure from [2]. (c) In YbRh_2Si_2 antiferromagnetic order is suppressed by a magnetic field along the crystallographic c -axis. Non-Fermi liquid behavior is observed in a V-shaped region around the quantum critical point (orange shading). Figure from [6].

ZrZn_2 [34], UGe_2 [35], MnSi [9, 36], and CoS_2 [37] the second order transition from para- to ferromagnetism at the Curie temperature T_C turns first order at a tri-critical point (TCP) when suppressed to low temperatures (Fig. 1.3c and d). At control parameter values above the TCP, tri-critical wings emerge under an applied magnetic field. In the majority of cases the control parameter is pressure. The tri-critical wings consist of sheets of first order transitions that are bounded by second order phase transition lines. The second order phase transition lines can be tuned to $T = 0$ and form a pair of QCPs. When crossing the first-order sheets, the magnetization shows a metamagnetic jump. The change from a second to a first order character of the para- to ferromagnetic phase transition can be explained through particle-hole excitations at the Fermi surface that couple to the magnetic order parameter fluctuations [38, 39]. Another scenario how a second order transition can be driven to first order is the Brazovskii scenario observed in MnSi at ambient pressure where isotropic chiral fluctuations drive the paramagnetic to helimagnetic transition to first order [40, 41]. An open issue concerns a quantum version of the Brazovskii scenario that might persist up to the critical pressure in MnSi with a potential connection to the partial order and the extended non-Fermi liquid phase (see Part II). In addition to the behavior described above, a superconducting phase can emerge near the suppression of T_C as, e.g., observed in UGe_2 [8] and UCoGe [42].

It was proposed that ferromagnets can also avoid a QCP through the emergence of a modulated magnetic order [11, 12, 43–45]. Fig. 1.3e and f illustrate this for $\text{Nb}_{1-x}\text{Fe}_{2+x}$ where a spin-density wave order is discussed that masks a putative QCP [46].

The fact that the para- to ferromagnetic transition turns first order before it is suppressed

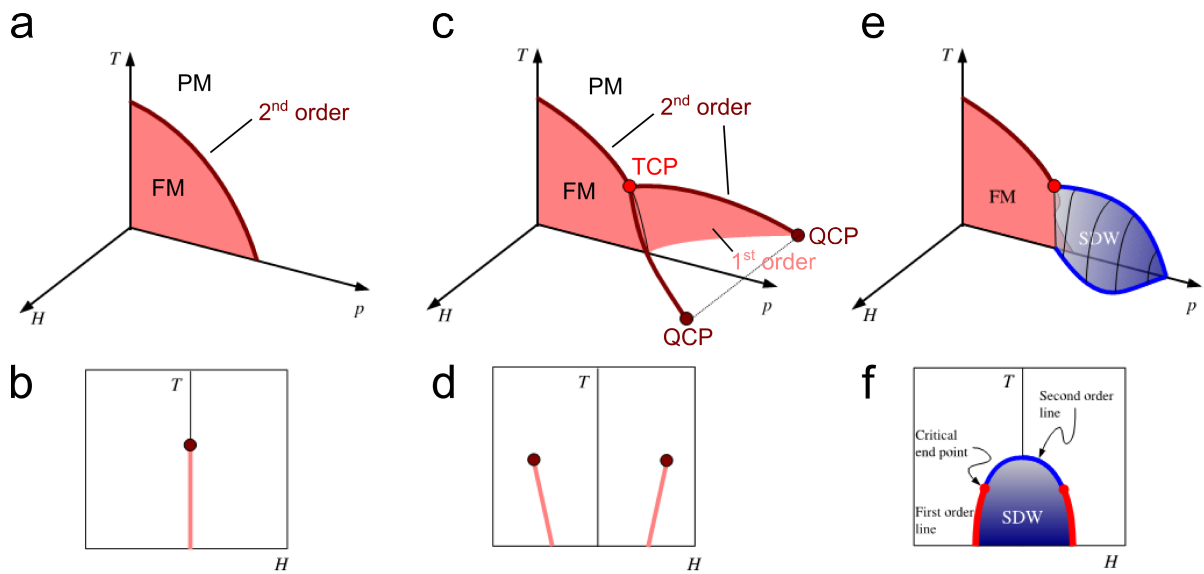


Figure 1.3: Quantum phase transitions in ferromagnets. (a) Schematic T - p - H phase diagram where a second order phase transition is suppressed to zero temperature with pressure. This classical quantum critical scenario is not observed in ferromagnets. (b) Schematic T - H phase diagram just below the critical pressure corresponding to panel a. (c,d) In ferromagnets the transition turns first order at a tri-critical point (TCP) before it is suppressed. At pressures above the TCP, tri-critical wings emerge. (e,f) A scenario where a magnetic ordering masks a QCP has been proposed. This scenario is in discussion for NbFe_2 where a spin-density-wave order is proposed. Figure from [47].

precludes the presence of a quantum critical point (at zero field). Nonetheless, unusual behavior is observed. From a classical point of view, first order phase transitions are driven by local minima in the free energy where fluctuations do not contribute significantly. However, due to the special nature of quantum phase transitions, quantum fluctuations can play an important role at so-called first order quantum phase transitions. The quantum critical behavior found at first order quantum phase transitions yields similar phenomena as the “conventional” second order quantum phase transitions, e.g., deviations from the Fermi liquid theory [9, 37, 48] and unconventional forms of superconductivity [8]. In this thesis we study the properties of two prominent itinerant ferromagnets around their critical pressures: The superconducting ferromagnet UGe_2 and the itinerant helimagnet MnSi .

UGe₂ In UGe_2 a superconducting dome emerges just below the critical pressure p_c deep inside the ferromagnetic phase (Fig. 1.4a). As the magnetism in UGe_2 is of itinerant character, magnetism and superconductivity are carried by the same electrons. The superconducting dome has a maximum transition temperature T_{SC} at a pressure p_X where a second transition T_X between two ferromagnetic states with different magnetic moments is suppressed. Both ferromagnetic transitions turn first order before they are suppressed to zero Kelvin. According to the experimental evidence, the first order quantum phase transition at p_X appears to be closely connected to the emerging superconductivity that is consequently thought to be driven by critical magnetic fluctuations. A deeper understanding of the T_X transition thus seems to be the key to understand the unconventional superconductivity in UGe_2 .

To gain new information about the T_X transition we used a new neutron spin-echo technique called Larmor diffraction which allows to measure thermal expansion, magnetization, and the distribution of lattice constants under pressure in the same experimental setup. The thermal expansion yields crucial informations about the excitations of a system, since the unit cell volume and hence the thermal expansion is the conjugate physical property to this pressure induced phase transition. Moreover, studies on MnSi [49] recently showed that the thermal expansion is a good probe for the investigation of quantum phase transitions. Together with magnetization data it is possible to separate contributions from the crystal lattice and magnetic contributions from other contributions to the thermal expansion. The distribution of lattice constants allows to check for uniaxial strain within the crystal lattice. We find a yet unknown transition T_L in the c -axis thermal expansion that lies several Kelvin above the T_X transition. The T_L transition may be the signature of a so-called Lifshitz transition where the Fermi surface changes its topology. Our experiments on UGe_2 are presented and discussed in part I of this thesis. A brief introduction to Lifshitz transitions is given in Sec. 1.3.

MnSi In MnSi a non-Fermi liquid (NFL) regime is observed above the critical pressure p_c that extends over a large pressure range up to at least $3 \times p_c$ rather than to a V-shaped region around the quantum phase transition. As in UGe_2 , the transition temperature T_c turns first order before it is suppressed to zero Kelvin. In a small part of the phase

diagram just above the critical pressure p_c , a fluctuating long-range magnetic order on timescales between 10^{-10} s and 10^{-11} s, so-called partial order, was reported in elastic neutron scattering and NMR experiments [36, 50] (Fig. 1.4b). This partial order points at magnetic textures as possible origin of the extended NFL regime. However, this peculiar magnetic order is found only in a small part of the NFL regime so that its origin still remains unclear. MnSi is probably the best studied weak ferromagnetic system. It played an important role for the development of a theory of band-magnetism in the presence of strong fluctuations [14]. However, MnSi can be considered as a ferromagnet only in a first approximation. Due to a missing inversion symmetry of the crystal structure a Dzyaloshinskii-Moriya interaction arises that causes a helical modulation of the magnetization with a long wavelength of ≈ 180 Å. In a specific field and temperature interval of the phase diagram a periodic structure of magnetic whirls, so-called skyrmions, is observed. One signature of a skyrmion lattice is that it causes a special contribution to the Hall effect called topological Hall effect due to its non-zero winding number.

We report a study of the Hall effect in MnSi to track the evolution of the skyrmion lattice with pressure. The basic idea behind our study is that the partial magnetic order above p_c could be connected to the skyrmion lattice phase observed at ambient pressure. The partial order would then consist of fluctuating skyrmionic textures that possess a winding number and show a topological Hall effect signal. Furthermore, since the Hall effect probes different timescales than elastic neutron scattering and NMR experiments, magnetic textures could be detected in regions where they are too fast for the latter two techniques. Specifically interesting is thereby how the magnetic textures are connected to the extended NFL regime.

Moreover, the evolution of the topological Hall effect signal below p_c represents an interesting project by itself since the topological Hall effect directly relates to the Berry phase which is the coupling mechanism between current and magnetic structure in spin transfer torque experiments. The critical current density j_c above which the skyrmion lattice begins to drift was reported to be exceptionally small compared to conventional spin transfer torque experiments on ferromagnetic domain walls [51, 52]. Hence, understanding how the topological Hall effect changes under pressure may yield important information for possible spintronics applications.

We find that the topological Hall effect signal increases tenfold under pressure up to 12 kbar [16]. Above the critical pressure p_c we find signatures of topologically non-trivial magnetic textures [53]. The phase boundaries of the topological Hall signal coincides with the boundaries found for the non-Fermi liquid phase in the resistivity. This implies that the NFL regime is closely connected to (fluctuating) skyrmionic textures. Our experiments on MnSi are presented and discussed in part II of this thesis. A brief introduction to Fermi liquid theory and non-Fermi liquids is given in Sec. 1.4.

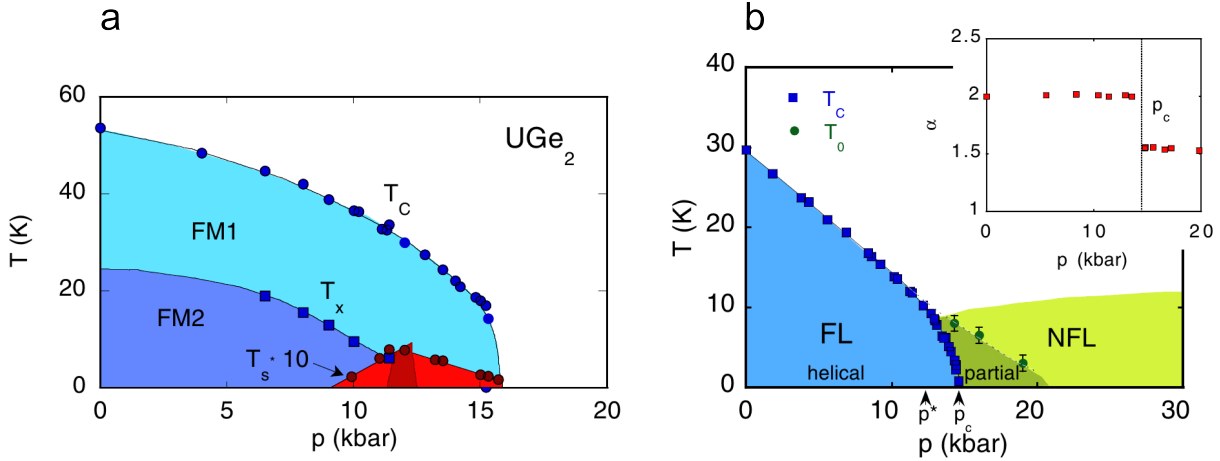


Figure 1.4: Temperature-pressure phase diagrams of UGe_2 and MnSi . The inset in panel b shows the resistivity exponent α . Figures from [29].

1.3 Lifshitz transitions

A Lifshitz transition, also known as electronic topological transition (ETT), describes a topological change of the Fermi surface of a metal that leads to anomalies in the electron dynamics [54]. The basic properties can be summarized as follows [55]: The Fermi surface of a metal changes when the position of the Fermi energy changes relative to the band structure and/or the band structure changes itself. This can be induced by external parameters as pressure or doping. When during such a change a van-Hove singularity of the density of states (DOS), i.e., an extremum or a saddle-point of the band structure with $\frac{\partial \epsilon_n(\vec{k})}{\partial k} = 0$, crosses the Fermi energy, the Fermi surface can change its topology. Here, $\epsilon_n(\vec{k})$ represents an energy band. In three dimensions four possibilities for topological transitions in the Fermi surface exist (see Fig. 1.5): (1) Disruption or (2) creation of a neck in the Fermi surface which is the case when a saddle-point of the band structure crosses the Fermi energy. (3) Appearance or (4) disappearance of a new pocket of the Fermi surface when a maximum (minimum) of the band structure crosses the Fermi energy. A maximum leads to a hole like pocket while a minimum leads to an electron like pocket. A Lifshitz transition is not associated with a symmetry breaking and it is assumed to be a continuous transition defined only at $T = 0$ that becomes a crossover at finite temperatures. A detailed theory of Lifshitz transition can be found in Ref. [56].

When the corresponding van-Hove singularity is large enough, a Lifshitz transition can be observed experimentally as anomaly of thermodynamic properties such as the specific heat, the compressibility, and the thermal expansion. However, the effects of a changing Fermi surface are often small and obscured by thermal effects. Therefore, a Lifshitz transition only becomes observable when other degrees of freedom such as lattice or spin couple strongly with electronic states. For example, the strong ferromagnet YCo_5 exhibits a first order Lifshitz transition under pressure (≈ 210 kbar) as a large peak in the spin-up DOS is shifted through the Fermi surface which leads to a drop of magnetic moment of about 35% accompanied by a volume collapse of 1.4% [55, 57]. The volume decrease of this hexagonal

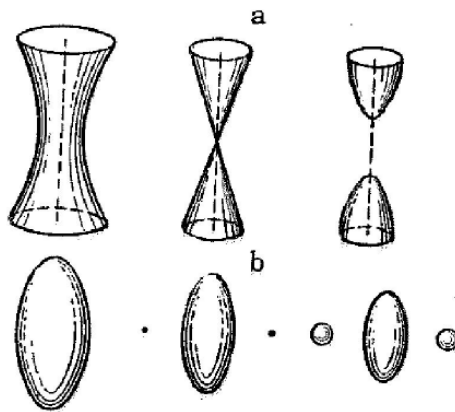


Figure 1.5: Lifshitz transitions. Possible transitions of the Fermi surface in three dimensions. (a) Disruption (left to right) or creation (right to left) of a neck in the Fermi surface. (b) Creation (left to right) or disappearance (right to left) of a new pocket of the Fermi surface. Figure from [54,55].

structure is anisotropic with a collapse of the c -axis at the transition pressure while the other axes contract smoothly with increasing pressure. A field tuned Lifshitz transition was reported in the ferromagnetic superconductor URhGe creating conditions favorable for high-field superconductivity [58]. Other recent examples and proposals for Lifshitz transitions include [59] electron-doped iron arsenic superconductors [60], the strongly correlated electron system Na_xCoO_2 [61], and the heavy-fermion metal YbRh_2Si_2 [62].

1.4 Fermi liquids and non-Fermi liquids

The Fermi liquid theory (FLT), developed by Landau in 1957 [63–65], is the fundamental theory for metals at low temperatures. Since at low temperatures the interactions between electrons cannot be neglected anymore, like it is the case with the Fermi gas description valid at high temperatures, electron-electron interactions need to be considered. The FLT preserves the non-interacting picture of the Fermi gas theory through the principle of adiabatic continuity, i.e., when the interactions are turned on slowly the eigenstates of the non-interacting system evolve continuously into the eigenstates of the interacting system. The energy levels change but the quantum numbers remain valid so that the interacting system can be described as a non-interacting system of quasiparticles with a renormalized mass that accounts for the interactions. The quasiparticles carry the same spin, charge, and momentum as the electrons in the non-interacting system [66].

The FLT predicts specific temperature dependences for various physical quantities. For example, a linear temperature dependence of the electronic contribution to the specific heat, $C(T)/T \approx \gamma_0$, is predicted. For the low temperature resistivity a quadratic temperature dependence $\rho \propto T^2$ is predicted. When other temperature dependences are experimentally observed, the FLT is obviously violated and one talks about a non-Fermi

liquid (NFL). Today, a large number of systems is known in which the thermodynamic and transport properties deviate from the FLT. These systems consist of strongly correlated d - and f -electron systems based on intermetallic compounds containing transition metal, lanthanide, or actinide ions [67].

There are numerous mechanisms how deviations from the FLT can be caused and only for some cases models exist. Most commonly, NFL behavior is found in the vicinity of QCPs. In a widely accepted picture the order parameter fluctuations at a QCP can couple to the electron density and lead to a NFL behavior [67, 68]. Also in the vicinity of first order quantum phase transitions, as observed in ferromagnets, NFL behavior is found. Fig. 1.6 illustrates schematic phase diagrams for different NFL scenarios in the vicinity of QCPs. As discussed above, the NFL behavior observed in MnSi, a central topic of this thesis, is a special case where NFL behavior is not only observed close to the suppression of magnetic order but within a large region of the phase diagram (Fig. 1.6b). Furthermore, the NFL behavior in MnSi occurs without the presence of a QCP. As will be discussed in Chap. 9, the NFL regime in MnSi may be related to topologically non-trivial spin textures. Another example where NFL behavior is observed are one-dimensional systems where the Fermi liquid model breaks down and has to be replaced by the concept of a Luttinger liquid. Taken together, up to now the only known mechanism for producing NFL behavior are soft modes coupling to the relevant degrees of freedom [68]. Further information about NFL can be found in the literature as, e.g., in Refs. [18, 66, 67, 69, 70].

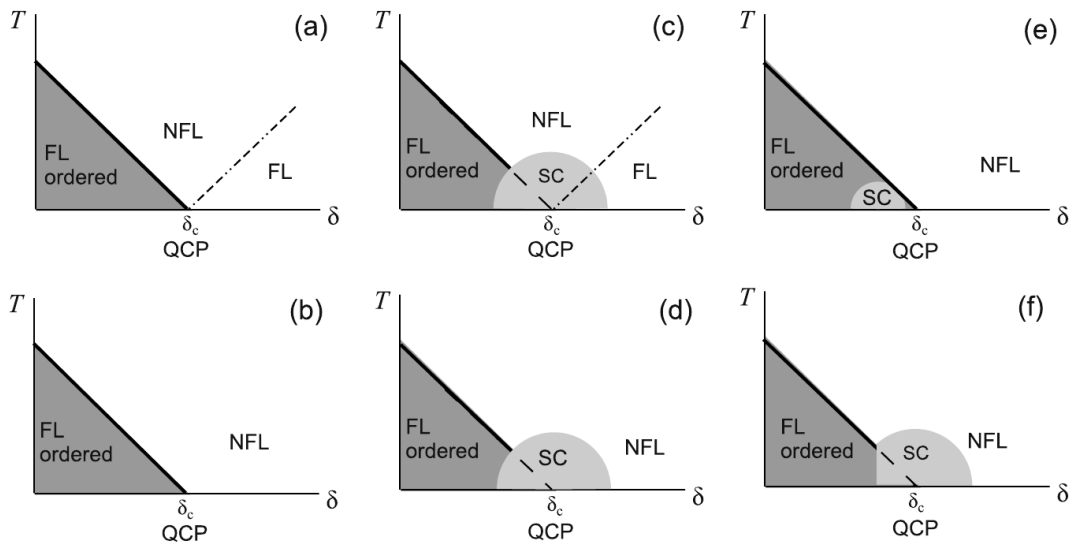


Figure 1.6: NFL behavior in the vicinity of QCPs. Schematic temperature vs. control parameter δ phase diagrams for different NFL scenarios in the vicinity of QCPs. In some situations a QCP is masked by a SC dome. (a) NFL behavior appears in a V-shaped region around the QCP. This example is observed in YRh_2Si_2 with magnetic field as control parameter. [6, 71, 72]. (b) An extended NFL regime appears for $\delta > \delta_c$ in $\text{Ce}_{1-x}\text{Y}_x\text{RhIn}_5$ as function of Y concentration [73] and in MnSi as function of pressure [74]. However, no QCP is present in MnSi [49] (c) A superconducting dome masks the QCP in CeIn_3 under applied pressure [5]. In a V-shaped region around the QCP NFL behavior is found. (d) This phase diagram similar to panel c but with an extended NFL regime was not observed so far. (e) Superconductivity only exists in a phase pocket inside the ordered phase. An extended NFL regime is observed for $\delta > \delta_c$. UGe_2 shows a similar phase diagram under pressure, however, without NFL behavior [8, 75]. (f) Superconductivity only exists outside the ordered phase as seen in CeRhIn_5 as a function of pressure [76]. Figure from [67].

Part I

Thermal expansion of UGe_2 under pressure

UGe₂ is one of only four systems presently known in which superconductivity and ferromagnetism coexist and are carried by the same electrons [77]. The superconductivity appears in a dome under pressures between 9 kbar and 16 kbar close to where ferromagnetism is suppressed. However, in contrast to superconductivity observed in the standard quantum-critical point (QCP) scenario, e.g., on the border of antiferromagnetism, the whole superconducting (SC) dome lies within the ordered (ferromagnetic) phase. The SC dome has a maximum of the SC transition temperature T_{SC} at $p_X \approx 12$ kbar where a transition T_X between a low (FM1) and a high moment (FM2) ferromagnetic phase is suppressed. Hence, the SC seems to be closely connected to the FM1 \rightarrow FM2 transition at T_X and therefore, a detailed understanding of the T_X transition appears to be an essential step to understand the superconductivity in UGe₂.

To gain further insights into the nature of the T_X transition we performed thermal expansion measurements under pressure of all crystalline axes and systematically tracked the T_X transition. The technique of Larmor diffraction allows us to directly compare the temperature dependence of the thermal expansion to the temperature dependence of the magnetization. Hence, contributions to the thermal expansion due to magnetostriction can be distinguished from other contributions. We find that while the thermal expansion along the a - and b -axes can be explained by standard magnetostriction, the thermal expansion along the c -axis shows an additional feature at a temperature T_L that evolves with pressure approaching p_X . The presence of an additional, non-magnetic transition close to p_X shows that the phase diagram of UGe₂ is more complex than assumed so far. Furthermore, this implies that the superconducting pairing mechanism could be non-magnetic contrary to what is discussed in the literature.

In the following, the basics about the superconducting ferromagnet UGe₂ are covered in Chap. 2. Chap. 3 gives an introduction to Larmor diffraction and a description of the experimental methods. Finally, our results are presented and discussed in Chap. 4.

Chapter 2

The superconducting ferromagnet UGe₂

The properties of the superconducting ferromagnet UGe₂ can be summarized as follows [78, 79]: UGe₂ crystallizes in the orthorhombic $Cmmm$ structure (space group 65) with the lattice constants $a = 3.997(3) \text{ \AA}$, $b = 15.039(7) \text{ \AA}$, $c = 4.087(2) \text{ \AA}$ [80, 81]. As can be seen in Fig. 2.1, the Uranium atoms form zig-zag chains along the a -axis with a distance $d_{U-U} = 3.85 \text{ \AA}$ which is above the Hill limit indicating no direct overlap of the $5f$ wavefunctions. Due to the Uranium zig-zag lines the crystal structure has a certain two dimensionality with respect to the b -axis, where the Uranium zig-zag chains form corrugated sheets that are separated by Germanium atoms. The two dimensional character also manifests itself in the electronic structure (see below).

Below the Curie temperature $T_C = 52 \text{ K}$, UGe₂ becomes ferromagnetic (Fig. 2.2) with a strong uniaxial character with large anisotropy fields of the magnetically hard b - and c - axes with respect to the magnetically easy a -axis (e.g. $\approx 100 \text{ T}$ for the c -axis) [82]. A particular feature are two ferromagnetic phases FM1 and FM2 with different ordered moments $\mu_{s,FM1} \approx 1.2 \mu_B/U$ and $\mu_{s,FM2} \approx 1.5 \mu_B/U$ that are separated through a crossover at a temperature $T_X \approx 25 \text{ K}$. Experimentally, the crossover at T_X occurs, e.g., in the resistivity as broad maximum in $d\rho/dT$ [83] and as minimum in the a -axis thermal expansion [84]. The T_X transition also appears in other observables as in the thermal conductivity [85], in the Hall effect [86], and in the specific heat [87].

The magnetism is of itinerant character as can be seen, e.g., in the susceptibility where the zero-temperature ordered moment, $\mu_{s,FM2} \approx 1.5 \mu_B/U$, is found to be considerably smaller than the Curie-Weiss-Moment, $\mu_{CW} \approx 2.7 \mu_B$. The itineracy can also be seen in the good electrical conductance of UGe₂ that manifests itself in residual resistivities well below $1 \mu\Omega cm$. De Haas-van Alphen (dHvA) experiments [88] show charge carriers with high cyclotron masses of (15-20) m_0 indicating that the $5f$ -states are itinerant but strongly correlated. The electronic specific heat coefficient of UGe₂, $C(T)/T = \gamma \approx 35 \text{ mJ/K}^2$ [82], is, however, one order of magnitude smaller than in conventional heavy-fermion Uranium compounds implying that UGe₂ is not as strongly correlated [89].

As illustrated in the temperature-pressure phase diagram in Fig. 2.2, both the T_C and the T_X transition can be suppressed at pressures $p_c \approx 16 \text{ kbar}$ and $p_X \approx 12 \text{ kbar}$. Under

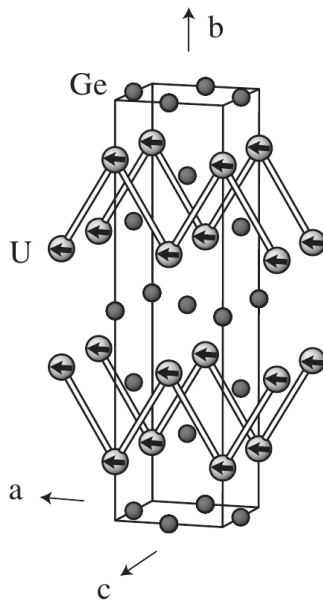


Figure 2.1: Orthorhombic $Cmmm$ crystal structure of UGe_2 . The arrows on the Uranium sites indicate magnetic moments aligned along the magnetically easy a -axis. Figure from [79].

pressure, the transition at T_C turns from second order to first order at a tricritical point $H = 0$, $T_{\text{TCP}} = 24 \text{ K}$, $p_{\text{TCP}} = 14.2 \text{ kbar}$ [90–92]. The crossover at T_X that separates the low moment FM1 phase from the high moment FM2 phase at low pressures turns into a first order phase transition at pressures close to p_X . The crossover and the first order phase transition lines are separated through a critical end-point at $H = 0$, $T_{\text{CEP}}^X \approx 7 \text{ K}$ and $p_{\text{CEP}}^X \approx 11.6 \text{ kbar}$ [92]. The evolution of the T_X transition with pressure can be nicely seen in the temperature dependence of the magnetization under pressure (Fig. 2.3) [93]. There, T_X appears as an increase of magnetic moment (when coming from high temperatures) and becomes more pronounced with increasing pressure. At low temperatures, the ordered moment changes discontinuously at p_X and p_c resulting in two jumps (Fig. 2.4b) [93].

DHvA experiments [94,95] with field along the b -axis show that the Fermi surface changes when crossing both p_X and p_c . On crossing p_X , the Fermi surface changes smoothly which is indicated by a change in the dHvA spectrum: Out of the three fundamental dHvA frequencies (α, β, γ) observed in the FM1 state two vanish (α, γ) and one decreases substantially (β). On top a new frequency emerges (δ) which can be interpreted as a change in the Fermi surface, however, without a complete reconstruction. On crossing p_c , the Fermi surface changes drastically: Four new frequencies emerge that are not connected to the frequencies found in the FM1 and FM2 state indicating a complete reconstruction of the Fermi surface.

At pressures above p_X and p_c , UGe_2 shows metamagnetic behavior and one can reenter the FM1 and FM2 phase when applying a magnetic field along the magnetically easy a -axis. The reentrant behavior is observed as jumps in the magnetization at the metam-

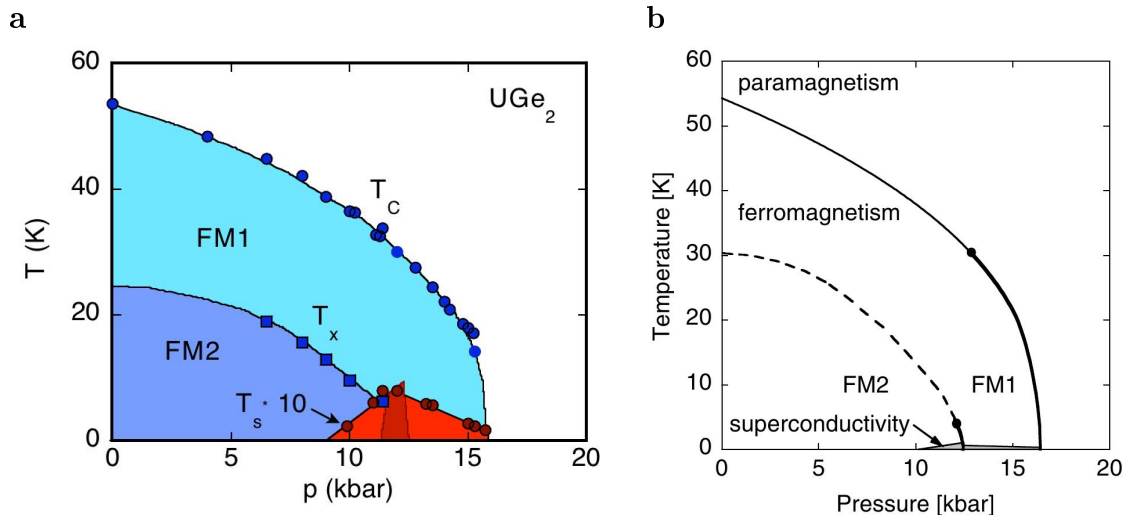


Figure 2.2: Temperature-pressure phase diagram of UGe_2 . (a) Experimental phase diagram [8]. (b) Schematic phase diagram [97]. Thin lines represent 2nd order phase transitions, thick lines represent 1st order phase transitions, broken lines represent crossovers.

agnetic transition fields H_X and H_m (Fig. 2.4c) [93]. The metamagnetic transition at H_m terminates at a quantum critical endpoint at $p_{\text{QCEP}} \approx 35$ kbar and $H_{\text{QCEP}} \approx 18$ T [90, 96]. Both the jumps in the low temperature magnetization and the metamagnetism indicate the first order character of the phase transitions at p_X (FM2 \rightarrow FM1) and at p_c (FM1 \rightarrow PM). Taken together, the T - p - B phase diagram of UGe_2 exhibits tri-critical wings as also observed in other ferromagnets (see Fig. 1.3b).

In the pressure range between $9 \text{ kbar} \leq p \leq p_c = 16 \text{ kbar}$ a superconducting phase emerges at low temperatures that lies entirely in the FM phase (Figs. 2.2 and 2.5) [8]. The transition temperature T_{SC} is pressure dependent and has a maximum of $T_{\text{SC}} \approx 0.7$ K at the pressure p_X . Neutron diffraction experiments [98] prove the coexistence of SC and FM. Together with the itinerant character of the magnetism this implies that FM and SC are carried by the same set of electrons.

The SC appears to be of unconventional nature as: (i) It is very sensitive to impurities [99]. (ii) The critical current density is very low, i.e., of order $j_c \approx 0.1 \text{ A/cm}^2$ which is between one and two orders of magnitude smaller than for typical heavy-fermion superconductors and three orders of magnitude smaller than for conventional superconductors [87]. (iii) The entire SC dome lies within the FM phase, in contrast to the standard QCP scenario, implying that FM is a precondition for SC in UGe_2 . (iv) The large upper critical fields exceed paramagnetic and orbital limits for weak coupled s -wave SC implying an unconventional pairing mechanism [100]. Currently, there is no concluding picture about the mechanisms behind the SC phase in UGe_2 . The experimental evidence points at an unconventional spin-triplet SC. As the SC is strongest around p_X , the T_X transition seems to be closely connected to the SC. Hence, a natural candidate for mediation of SC are fluctuations associated with the critical endpoint of the T_X transition. To set the stage

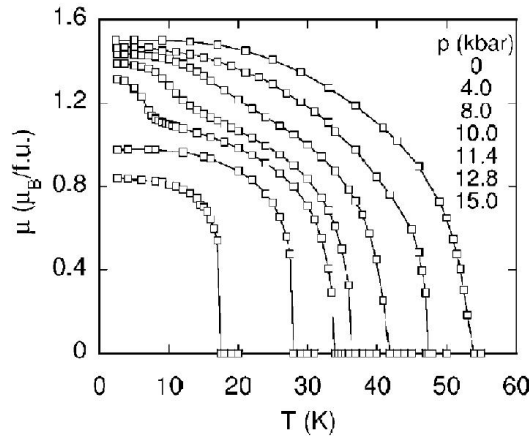


Figure 2.3: Temperature dependent magnetization of UGe_2 under pressure [93]. Under pressure the T_X transition appears as additional increase of the magnetic moment. T_X becomes more pronounced on approaching p_X and vanishes above p_X . The transition at T_C changes from second order at low pressure to first order at pressures close to p_c .

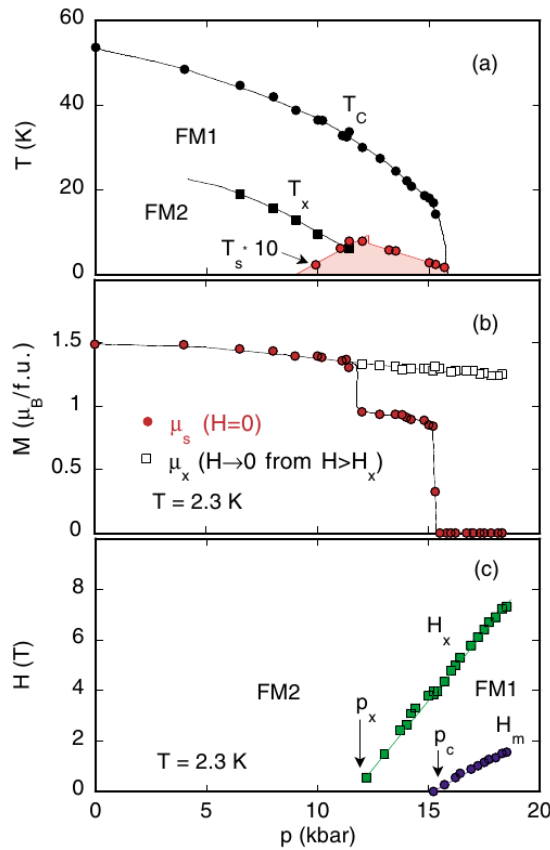


Figure 2.4: Ferromagnetism in UGe_2 under pressure. (a) Temperature-pressure phase diagram with T_X and T_C inferred from the magnetization [93] and T_s inferred from the resistivity [87]. (b) Low temperature magnetic moment μ_s at zero field (red datapoints) and the magnetic moment μ_X extrapolated from fields above H_X . (c) Pressure dependence of the metamagnetic transitions at H_X and H_m at 2.3 K. Figure from [93].

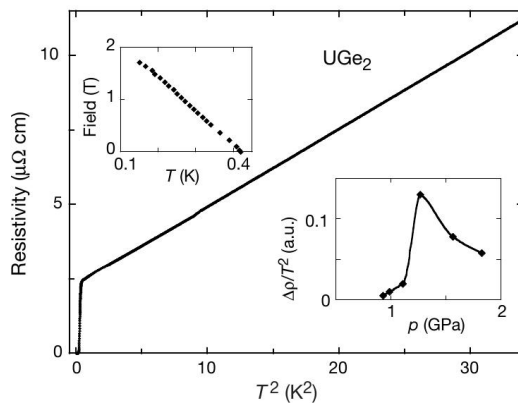


Figure 2.5: Initial observation of superconductivity in the resistivity of UGe₂ from Ref. [8]. The graph shows the resistivity ρ versus the temperature squared, T^2 , at ≈ 14 kbar. ρ is roughly consistent with the Fermi liquid relation $\rho = \rho_0 + AT^2$. The upper inset shows the magnetic field dependence of the SC transition temperature T_{SC} . The lower inset shows the pressure dependence of the parameter A .

for our thermal expansion studies, Sec. 2.1 summarizes the thermal expansion of UGe₂ reported so far, and Sec. 2.2 focuses on scenarios proposed to drive the T_X transition.

2.1 Thermal expansion of UGe₂

Thermal expansion data of UGe₂ at ambient pressure by means of strain gauges [84, 101] and capacitive dilatometry [102] has been reported for all crystallographic axes. Under pressure, the a - and b -axis thermal expansion [91, 92, 101–104] and the volumetric thermal expansion [105, 106] all by means of strain gauges has been reported. No c -axis thermal expansion data under pressure was reported so far. The basic properties of the thermal expansion of UGe₂ can be summarized as follows:

At ambient pressure all axes contract down to the Curie temperature $T_C \approx 52$ K (Fig. 2.6a)¹. Below T_C the a -axis contracts further with a slightly steeper slope until it reaches a minimum around 37 K below which the a -axis expands again. The b -axis expands below T_C up to a flat maximum between 37 K and 26 K below which the b -axis contracts again. The c -axis expands below T_C down to the lowest temperatures measured. Summarized, at ambient pressure, on cooling, all axes contract down to T_C . Below T_C the thermal expansion is connected to the ferromagnetic state through standard magnetostriction. This is indicated through a $\Delta d/d$ which behaves as a smooth function of the magnetic moment squared, m^2 , as will be discussed later (see Fig. 4.6). The magnetostriction effects are most pronounced along the b - and the c -axes. A spontaneous volume magnetostriction effect of $\Delta V_{\text{mag}}/V (T \rightarrow 0 \text{ K}) = 1.23 \cdot 10^{-3}$ is observed at ambient pressure [101]. The min-

¹Note that in Ref. [101] the a - and c -axis are interchanged as a $Cmcm$ crystal structure instead of a $Cmmm$ crystal structure was assumed in studies before 1996 [95]. Labels in the figure caption of Fig. 2.6 are corrected.

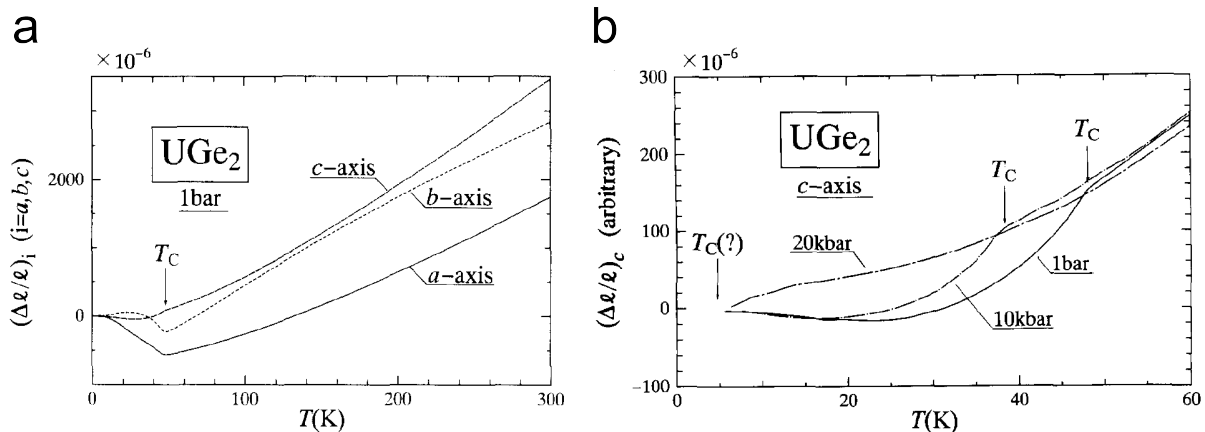


Figure 2.6: Thermal expansion of UGe_2 from Nishimura *et. al* [101]. (a) a -, b -, and c -axes thermal expansion of UGe_2 at ambient pressure. The low temperature part of this figure is shown magnified in Fig. 4.1 on p. 53. (b) a -axis thermal expansion under pressure. In Ref. [101] the a - and c -axis labels are interchanged. See text for details.

ima and maxima in the a - and b -axis below T_C already point at the crossover T_X which develops under pressure, respectively. Comparison with specific heat and magnetization data shows that the magnetic and thermodynamic properties of UGe_2 can be understood in the context of a molecular field theory [102]. At ambient pressure T_X can be clearly identified as a crossover rather than a phase transition as the T_X transitions appear at different temperatures along the different crystallographic axes. As it is known from magnetization measurements [93] that T_X is a first order phase transition at pressures close to p_X this corroborates that the T_X phase transition is separated from the crossover at lower pressures by a critical end point. The ferromagnetic contribution can be described by two parts with distinct Grüneisen parameters.

With increasing pressure the T_X transition evolves from a broad crossover to a clear shoulder that can be seen in the volume and in the b -axis thermal expansion (Fig. 2.7). The shape is analog to the magnetization data. The T_X feature seen as peak in thermal expansion coefficient α_b becomes larger under pressure. Above $p_X \approx 12$ kbar the T_X transition vanishes as known from magnetization data. In contrast, the a -axis thermal expansion under pressure is relatively featureless except a change of slope at T_C (Fig. 2.6b). The spontaneous volume magnetostriction $\Delta V_{\text{mag}}/V$ decreases under pressure and vanishes above p_c [101].

In Chap. 4 we report thermal expansion measurements on UGe_2 under pressure by means of the neutron spin-echo method Larmor diffraction (LD). Our measurements distinguishes itself from prior studies in that the LD technique allowed us to measure the thermal expansion along all crystallographic axes and the magnetization in the same experimental setup. Therefore, we can directly compare the transition temperatures T_C and T_X of the individual axes and the magnetization. We find an additional transition T_L along the c -axis thermal expansion that lies several Kelvin above the T_X transition in the magnetization and the other axes. Furthermore, with LD we could measure the distribution

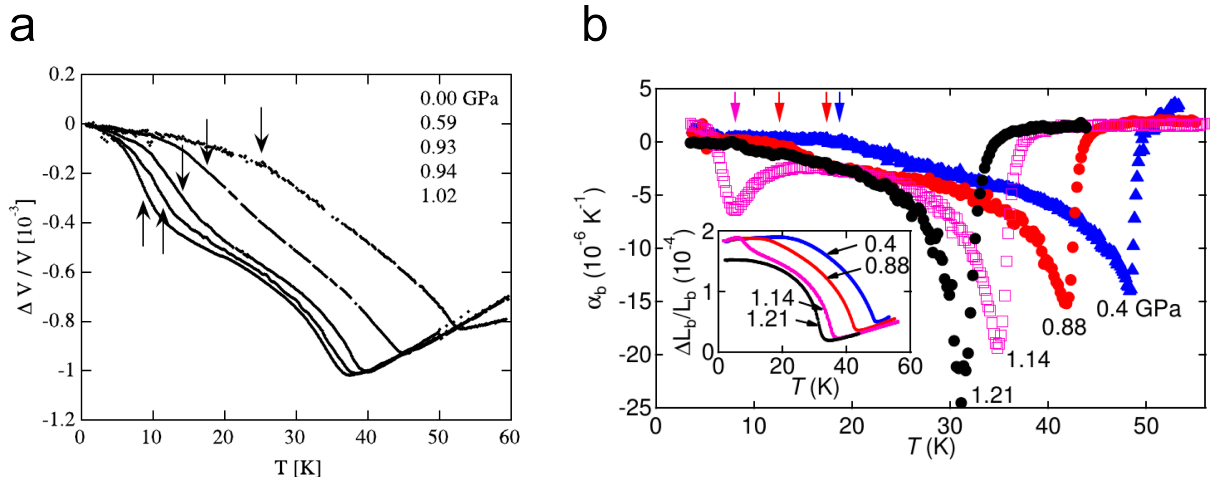


Figure 2.7: Thermal expansion of UGe_2 under pressure. (a) Volumetric thermal expansion under pressure. Figure from [106]. (b) b -axis thermal expansion coefficient α_b and thermal expansion $\Delta L_b/L_b$ (inset) under pressure. Figure from [92].

of lattice constants to check for uniaxial strains of the crystal lattice when UGe_2 enters the Ising-ferromagnetic state (see Sec. 3.4.3). To corroborate our thermal expansion data which represents the first Larmor diffraction measurements on a ferromagnet, we compare our data to data reported in the literature in Sec. 4.1. Overall, we find a good agreement.

2.2 Scenarios for the T_X transition

The experimental evidence suggests that as the the SC is strongest around p_X where the T_X transition is suppressed, the T_X transition is the key to understanding the superconductivity in UGe_2 . Up to now there is no concluding picture about the T_X transition, but several scenarios have been proposed including (i) the formation of a coupled spin and charge density wave [107], (ii) nearly degenerate FM1 and FM2 ground states that differ in their orbital moment [108], (iii) special features of the density of states (DOS) [109], (iv) a coexistence of Kondo effect and magnetism [110, 111], and (v) a transition between a localized and an itinerant ferromagnetic phase [112]. These scenarios will be discussed in this section.

(i) Watanabe *et al.* [107] propose a scenario where the T_X transition may be related to the formation of a coupled charge and spin density wave. This is in accordance with the charge density wave forming in α -Uranium [113] which has a similar structure as UGe_2 with the Uranium atoms aligned along zig-zag chains. In favor with this scenario are electronic structure calculations [89] showing that the Fermi surface is dominated by a cylindrical sheet with strong nesting. However, so far no direct experimental evidence for a charge density was found and several experimental observations render this scenario unlikely. First, in UGe_2 the distance between the Uranium atoms is larger than in α -Uranium making nesting less important. Second, dHvA experiments [94] show fre-

quencies belonging to extremal orbits on the Fermi surface that could not exist together with a CDW. A CDW due to nesting of two parallel sheets of the Fermi surface would imply a gap opening in the Fermi surface which would destroy the extremal orbit. Third, neutron scattering experiments under pressure show that the U-U distance is reduced to $d_{\text{U-U}} = 3.5 \text{ \AA}$ and that the zig-zag lines straighten [87]. Such large structural changes would probably destroy the preconditions for nesting.

(ii) Shick *et al.* [108] propose a scenario based on LDA+ U calculations in which they consider not only the spin moment μ_S but also the orbital moment μ_L , since in actinide systems spin-orbit coupling (SOC) becomes of the same order of magnitude as crystal-field interactions (CF) [114]. In systems with a less than half filled f -shell, μ_S opposes the dominating μ_L so that the total moment is given by $\mu = \mu_L - \mu_S$. Taking this into account, Ref. [108] finds solutions for the FM1 and FM2 ground states that are nearly degenerate and differ in the orbital moment. The FM1 \rightarrow FM2 transition is driven by the competition of SOC and CF, where SOC $>$ CF in the FM2 state and CF $>$ SOC in the FM1 state. This scenario implies that fluctuations of the orbital moment at the T_X transition might drive the SC in UGe_2 . Such fluctuations have longitudinal character in agreement with the proposal by Fay and Appel [115] that longitudinal magnetic fluctuations can mediate unconventional spin-triplet superconductivity. Two experimental findings are in favor of the scenario proposed by Shick *et al.*: First, longitudinal magnetic fluctuations were reported in the magnetic excitation spectrum of UGe_2 measured by neutron scattering [97]. And second, the ratio of orbital to spin moment $R = \mu_L/\mu_S$ was reported to increase when crossing p_X with $R_{\text{FM1}}/R_{\text{FM2}} = 1.10 \pm 0.05$ [97, 116].

(iii) Sandeman *et al.* [109] assume a zero-temperature Stoner model where the T_X transition is associated with a double peak in the density of states (DOS). Tuning the peaks in the DOS through the Fermi level produces the jumps in the magnetization observed at p_X and p_c . Furthermore, they show that a large DOS at the majority spin Fermi surface associated with the T_X transition can lead to superconductivity that favors the FM state. Such a double peaked DOS can arise naturally from a quasi one dimensional part of the band structure. However, the model of Sandeman *et al.* is limited in that it only considers the effects of spin but not spin-orbit coupling and crystal electric fields that are known to be important in UGe_2 .

(iv) The underscreened Kondo lattice model can explain the coexistence of ferromagnetism and Kondo effect [110]. There, the conduction electrons are not sufficient to screen all local moments so that unscreened local moments remain. In an extension to this model by Thomas *et al.* [111] in which a weak delocalization of $5f$ -electrons is taken into account a jump in the magnetization resembling the T_X transition in UGe_2 can be observed at low temperatures in a specific scenario : If the Kondo temperature T_K lies a bit higher than the Curie temperature T_C , apart from the Kondo phase and the ferromagnetic phase a coexistence region is observed. The coexistence region originates in unscreened f -electrons that can order ferromagnetically in the Kondo phase if the exchange interaction is large enough. At lower temperature the magnetic moments, which act as an internal magnetic field, increase and destroy the Kondo effect at some point. The transition from the Kondo

phase to the coexistence region then refers to the T_C transition and the transition from the coexistence region to the purely ferromagnetic region refers to T_X . However, so far no experimental evidence confirming or disproving this model was observed.

(v) In a theoretical study using dynamical mean-field theory (DMFT), Hoshino *et al.* [112] discuss a generalized scenario in which the magnetism in heavy-fermion systems changes from localized to itinerant heavy-electron magnetism. There, an itinerant-localized transition (ILT) of the f -electrons results from the competition of Heisenberg exchange interaction and the Kondo effect. The Heisenberg interaction J_H promotes ordering of localized f -electron states while the Kondo effect leads to itinerant f -electrons. This ILT takes place inside the magnetically ordered phase. In the case of UGe_2 T_X then refers to a ILT between a localized and an itinerant ferromagnetic phase, as the Kondo effect J_K increases with increasing pressure. The nice thing about this scenario is that it is very general and could explain the phase diagrams of a number of systems including $\text{CeRh}_{1-x}\text{Co}_x\text{In}_5$, $\text{CeRu}_2(\text{Si}_x\text{Ge}_{1-x})_2$, UGe_2 , and $\text{CeT}_2\text{Al}_{10}$ ($T=\text{Fe,Ru,Os}$). However, in the case of UGe_2 the scenario of a ILT from localized to itinerant f -electrons inside the FM phase stands in contrast to two experimental observations which yield evidence against a delocalization of the $5f$ electrons: First, the ratio of orbital to spin moment $R = \mu_L/\mu_S$ was reported to increase when crossing p_X (see scenario (ii)) [97, 116]. This implies that the $5f$ electrons do not delocalize on crossing p_X as the orbital contribution is then expected to decrease. Second, measurements of the magnetic form factor of the Uranium atom show that both at ambient pressure and under pressure it is account equally well for by a U^{3+} or a U^{4+} configuration.

As will be discussed in Chap. 4, we find evidence of an additional phase transition T_L at pressures close to p_X that lies several Kelvin above the T_X transition. Such a second transition in the ferromagnetic phase is hard to combine with scenario (i), (ii), and (iii) from above. However, the T_L transition is compatible with the scenarios (iv) and (v) that explain T_X through a competition of Heisenberg and Kondo exchange interactions (see Sec. 4.3).

Chapter 3

Experimental methods

3.1 Thermal expansion at low temperatures

Along with the specific heat, the thermal expansion is an important property of a solid. Its temperature dependence allows conclusions about the excitations of a system. In the context of pressure driven phase transitions the thermal expansion yields crucial information since the unit cell volume is the conjugate physical property to the control parameter pressure. This section gives an overview of the basic properties and conventional measurement methods of the thermal expansion. For a broad introduction see, e.g., Ref. [117].

The thermal expansion can be expressed through the coefficient of volumetric expansion $\beta = \left(\frac{\partial V}{\partial T}\right)_p$, the coefficient of linear expansion $\alpha = \left(\frac{\partial d}{\partial T}\right)_p$, or directly through the relative change of lattice constants $\Delta d/d$. Here, V refers to the crystal volume and d refers to a lattice constant.

3.1.1 Contributions to the thermal expansion

The temperature dependence of the thermal expansion as well as the specific heat C_V reflects the excitations of a system. Since thermal expansion and specific heat are closely related to each other, it is useful to discuss these two properties together. The two main contributions to the specific heat and the thermal expansion are the phononic contribution and the electronic contribution. In the case of a dominant phonon contribution C_V and β scale with $\propto T^3$ to first order. It is important to note that while all phonons contribute similarly, i.e. positive, to C_V , which therefore is always positive, they can have a quite different effect on the thermal expansion, which can therefore also become negative (Fig. 3.1a). Especially in non-cubic systems the thermal expansion can have a complex behavior. The electronic contribution is usually much smaller than the phonon contribution and becomes typically visible not until $T \leq 1$ K. In the case of simple metals like Copper the electronic contribution to specific heat and thermal expansion scales linearly with temperature.

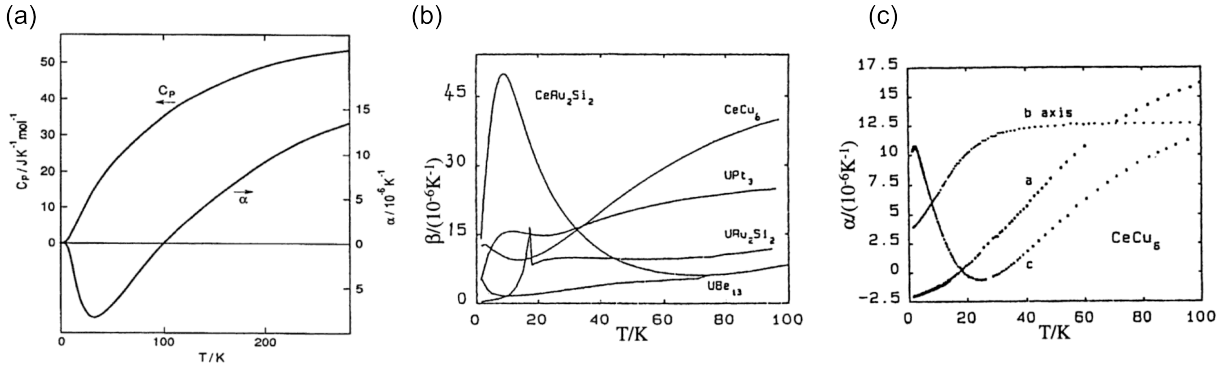


Figure 3.1: Examples of thermal expansion data. (a) Heat capacity C_p and thermal expansion coefficient α of the cubic material CuCl. C_p is dominated by the phonon contribution and decreases as T^3 . α is also dominated by the phonon contribution and also decreases with T^3 at higher temperatures. At low temperatures, however, α becomes negative as some vibrational modes contribute positively and some negatively to the thermal expansion. (b) Volumetric thermal expansion coefficient β for various heavy fermion materials. The correlation effects between electrons lead to strong signatures in the thermal expansion. (c) Anisotropic thermal expansion of the orthorhombic heavy fermion material CeCu_6 . Figures from Ref. [118].

In the presence of ordering phenomena like superconductivity or magnetism the behavior of specific heat and thermal expansion can be quite different from the simple cases described above. It is especially difficult to distinguish the different contributions from each other since new excitations like magnons in magnetic systems arise. Furthermore, d electrons from transition metals or f electrons from rare earth or Actinide elements can lead to correlation effects that greatly enhance the electronic contributions.

The basic contributions arising from the most prominent ordering phenomena can be summarized as follows: In a simple model for ferromagnets, the magnetic contributions to C_V and β , C_m and β_m , scale with $\propto T^{3/2}$ due to magnons. In turn, in antiferromagnets C_m and β_m scale with $\propto T^3$ in a simple model. Also, magnetism can couple to the lattice, so called magnetoelastic coupling, and lead to large volume changes up to a few percent. In superconductors the basic feature is a “jump” is observed in the electronic contribution to C_V and α at the superconducting transition. The temperature dependence of the thermal expansion in the superconducting phase depends on material specific details. In general, specific heat and thermal expansion are complex in the presence of ordering phenomena and/or correlation effects and the thermal expansion is often very anisotropic (see Fig. 3.1b and c).

3.1.2 Thermal expansion at phase transitions

When studying phase transitions that are driven by the control parameter pressure as it is the case for many quantum phase transitions, the thermal expansion $\beta = \left(\frac{\partial V}{\partial T}\right)_p$ yields important informations since the unit cell volume, or equivalently the lattice constants, is the conjugate physical property to the control parameter pressure [49]. This is in anal-

ogy to temperature driven phase transitions where the conjugate variable to the control parameter temperature is the entropy S which can be probed via the observable specific heat $C_p = T (\partial S / \partial T)_p$. The behavior of the thermal expansion at phase transitions can be summarized as follows [118]: At first order phase transitions discontinuities in volume are observed. I.e., $\Delta V/V$ and $\Delta d/d$ show characteristic “jumps” at the transition temperature. At second order phase transitions discontinuities in the thermal expansion coefficients α and β are observed.

An interesting side note is that with the knowledge of the discontinuities of α and C at an superconducting transition one can predict the pressure dependence of T_c via the Ehrenfest relation from ambient pressure data (see e.g. Refs. [117, 118]):

$$\beta^n - \beta^s = \left(\frac{C^n - C^s}{V} \right) \frac{d \ln T_c}{dp} \quad (3.1)$$

The superscripts n and s denote the normal and the superconducting state.

The thermal expansion is a useful observable in the field of quantum criticality. For a pressure induced quantum-critical point a sign change and divergence are predicted to occur in the thermal expansion [119, 120]. Therefore, thermal expansion data allows to identify and classify quantum-critical points. Observations on several systems like CeRu₂Si₂, CeCu_{6-x}Au_x, TlCuCl₃, and URu₂Si₂ support this prediction (see Ref. [120] and references therein). Furthermore, a missing divergences in the thermal expansion was used to rule out the presence of quantum-critical points in MnSi [49].

3.1.3 Experimental methods

Standard experimental methods for measuring the thermal expansion of solids are (i) capacitive dilatometers (see e.g. Ref. [121]), (ii) strain gauges (see e.g. Ref. [122]), and (iii) scattering methods with X-rays or neutrons. The operation principle and typical resolutions are briefly introduced below. This is followed by a discussion why we chose a different measurement method, namely the sophisticated and rather new neutron spin-echo technique called Larmor diffraction, to perform our experiments on UGe₂.

(i) In a capacitive dilatometer the sample is put between two plates of a capacitor. A changing lattice constant then changes the distance between the capacitor plates and hence can be detected by measuring the capacitance. The resolution of a capacitive dilatometer can be as high as $\Delta d/d \approx 10^{-10}$ [121]. (ii) A strain gauge is a conductive path on a flexible, insulating backing that is glued onto the surface of a sample. Due to the thermal expansion of the sample, the conductive path is compressed or stretched and changes its resistance. The typical resolution of strain gauges is $\Delta d/d \approx 10^{-6} - 10^{-7}$ (see e.g. [122]). (iii) In conventional X-ray or neutron diffraction the lattice constants are measured via the scattering angle of a nuclear Bragg peak. Compared to the techniques mentioned above, the typical resolution of $\Delta d/d \approx 10^{-4}$ is relatively low due to limitations caused by the monochromaticity and the beam divergence of the used x-ray or

neutron beam. Efforts to increase the resolution through, e.g., tighter beam collimation considerably decrease the intensity yielding long experiment times.

For our experiments we used a sophisticated neutron spin-echo technique called Larmor diffraction. There, the change of lattice constant is measured through the phase of a polarized neutron beam. Therefore, Larmor diffraction has certain advantages compared to the conventional methods presented above. The most important being the combination of a high resolution with a high intensity. This will be covered in detail in Sec. 3.2. We chose Larmor diffraction mainly for two reasons: (1) As Larmor diffraction is a scattering method, it is easy and reliable to use for high pressure experiments since no measurement apparatus has to be mounted inside a pressure cell. Larmor diffraction distinguishes itself in comparison to other scattering methods through its relatively high resolution of $\Delta d/d \approx 10^{-6}$, a high intensity and low heating effects compared to X-ray scattering. (2) Larmor diffraction allows to measure the magnetization concomitantly with the thermal expansion. Accordingly, transition temperatures can be compared directly. This is essential when trying to separate the different contributions to the thermal expansion.

3.2 Introduction to Larmor diffraction

Larmor diffraction (LD) is a neutron scattering technique for measuring the change of lattice constants that distinguishes itself from conventional scattering techniques through the combination of a high resolution and a high intensity. The resolution of LD of $\Delta d/d \approx 10^{-6}$ is much higher than the resolution of conventional scattering techniques with $\Delta d/d \approx 10^{-4} - 10^{-5}$. This is achieved by encoding the information of the change of lattice constant in the spin precession of a polarized neutron beam rather than in its scattering angle. Therefore, LD is insensitive to beam divergence and wavelength spread yielding a high intensity. As a unique feature of LD, the distribution of lattice constants over the whole sample volume can be determined. First proposed in 2000 by Rekveldt [123] and implemented by Rekveldt, Keller, and Golub [124], LD was used to tackle its first major scientific problem in 2007 by Pfleiderer *et al.* [49]. There, the absence of quantum critical points in the temperature-pressure phase diagram of MnSi could be shown, underscoring the unusual nature of the extended non-Fermi liquid regime reported under pressure (cf Sec. 5.2, p.74).

For the experiments presented in this thesis, LD provided two crucial features: (i) When measuring magnetic systems, LD opens up the possibility of directly comparing magnetic transition temperatures through measuring the magnetization (via the intensity of a magnetic Bragg peak) in the same setup as the change of lattice constants. (ii) Being a scattering technique, LD it is well suited for high-pressure experiments since no measurement apparatus has to be mounted inside a pressure cell. Thus, difficulties concerning the interplay of pressure transmitting medium, measurement apparatus, and sample are avoided. This distinguishes LD from conventional techniques for measuring changes of

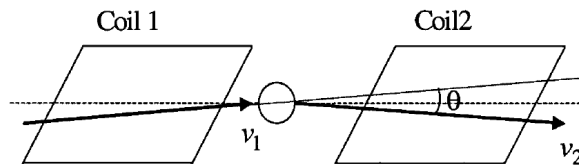


Figure 3.2: Trajectory of a neutron moving through two magnetic field regions produced by two coils. When the field boundaries are tilted with respect to the neutron trajectory, the path length through the magnetic field depends on the scattering angle Θ . Picture from [124].

lattice constants, like strain gauges and capacitive dilatometers.

Experimentally, LD is realized on neutron spin-echo instruments. Thus, the following text briefly introduces the principle of neutron spin-echo and subsequently the basic principle of LD along Ref. [124].

3.2.1 Principle of neutron spin-echo technique

Neutron scattering techniques using the spin-echo method are designed to measure excitations, like magnons, with a high accuracy in the μeV range. The high accuracy is achieved though using the precession of neutron spins to detect energy transfers between neutron beam and sample. A detailed introduction to the neutron spin-echo technique can be found in Ref. [125].

In a spin-echo experiment, the neutrons move through two magnetic field regions of same magnitude and size before and after they scatter at the sample. In each field the neutron precesses with a Larmor frequency ω_L and picks up a Larmor phase

$$\phi = \omega_L L_i / v_i \quad (3.2)$$

with the length L_i of and the velocity v_i in each field region (Fig. 3.2). In a conventional spin-echo setup the field directions are reversed, so that the total Larmor phase $\Phi = \phi_1 - \phi_2$ cancels out in cases where the neutron velocity before and after the scattering event is the same. However, if the neutron velocity is changed due to an inelastic scattering event, from v_1 to v_2 , a non-vanishing Larmor phase remains and can be used to measure energy transfers δE with a high resolution:

$$\Phi = \phi_1 - \phi_2 = \omega_L L \left(\frac{1}{v_1} - \frac{1}{v_2} \right) = \frac{\omega_L L}{v^2} \delta v = \frac{\omega_L L}{2vE} \delta E. \quad (3.3)$$

When the boundaries of the magnetic field regions are tilted like in Fig. 3.2 the path length through the fields depends on the angle of the trajectory. Hence, a change in the angle of the neutron trajectory results in a phase shift. This can be used to measure q -dependent excitations at a high resolution.

3.2.2 Measurement of lattice constants

In the so-called “parallel” mode the fields in both spectrometer arms are set to point in the same direction at which the precession of the neutron spins adds up. The advantage of this field configuration is that lattice constants can be measured with a high accuracy via the total neutron precession independent of beam divergence and wavelength spread provided that the instrument is arranged in a certain geometry (see below).

With the instrument set up in the parallel mode, the total precession of the scattered neutrons is sensitive to the lattice constant of the analyzed sample when the precession field boundaries are oriented parallel to the lattice planes of the analyzed sample. This geometry is schematically illustrated in Fig. 3.3a (where the effective magnetic field regions are shown as one extended region for didactic reasons). The neutron spins of a polarized neutron beam (black) rotate in a magnetic field (gray shading) before and after they scatter at the lattice planes of a sample. The total rotation only depends on the velocity component v_{\perp} which is the same for all neutrons fulfilling the Bragg condition $\vec{Q} = 2k_B \sin(\Theta_B) = \vec{G}$, with the reciprocal lattice vector \vec{G} ($|\vec{G}| = 2\pi/d$). It can be shown that the total precession phase Φ is linearly proportional to the lattice spacing d (see Ref. [124] for details):

$$\Phi = \frac{2\omega_L L m}{\pi \hbar} d. \quad (3.4)$$

Thus, a change Δd in the lattice spacing can be measured through a change in the Larmor phase $\Delta\Phi$, which can be determined with a high precision, via the relation:

$$\frac{\Delta d}{d} = \frac{\Delta\Phi}{\Phi}. \quad (3.5)$$

Typical values for the total Larmor precession are $\Phi \approx 10^4$ rad corresponding to $\approx 10^3$ precessions of the neutron spins. The resolution is presently $\Delta\Phi/\Phi = \Delta d/d \approx 10^{-6}$ (see below).

Since in this measurement geometry the total precession phase depends only on the velocity component v_{\perp} and hence on the time the neutrons spend in the precession fields, the total phase is independent of the angle of incidence Θ and the neutron wavelength. I.e., the neutrons along the red, blue, and black trajectory in Fig. 3.3a acquire the same Larmor phase. Therefore, a LD experiment can be performed with open collimation yielding a combination of a high resolution with a high intensity. Furthermore, the Larmor phase remains unchanged to first order, when the lattice plains are tilted with respect to the field boundaries (Fig. 3.3b).

In the actual experimental setup the effect of the magnetic fields is produced by four radio-frequency coils that use short alternating fields (Fig. 3.3c). On the neutron spin the radio-frequency coils have the same effect as the extended magnetic field region indicated by the dashed line. This type of setup is called neutron resonance spin-echo (NRSE). For a detailed description of the NRSE technique see Refs. [126, 127]. The advantages are that the radio-frequency coils can be tilted by large angles, that outside the

radio-frequency coils the magnetic field is $B = 0$ avoiding stray fields at the sample position, and that the neutron phase is governed by the frequency with which the coils are operated which is easier to determine than a field integral of an extended magnetic field. To measure the Larmor phase Φ , the intensity of a fixed polarization direction is detected at the detector while the length of the effective magnetic field region is varied through translating one coil (C4 in Fig. 3.3c). The result is a sinusoidally varying intensity as a function of the coil translation x_{TC4} . Fig. 3.4 shows as example UGe₂ at 9 kbar. The change in the Larmor phase between the 225 K (black) and the 5 K (red) curve can be clearly seen as horizontal shift between the two curves.

As proof of principle, Fig. 3.5 shows the comparison of the thermal expansion of single crystal Cu measured by LD [49] and with a capacitive dilatometer [128]. The data shows an excellent parameter-free agreement and illustrates the high accuracy of LD. At the instrument TRISP at FRM II, where we performed our experiments, the present relative resolution is $\Delta d/d \approx 10^{-6}$ [49, 129]. Experimentally, the resolution is presently limited in leading order by the size of the precession distances L_1 and L_2 (see Fig. 3.3) [49]. Theoretically, the resolution of LD is limited by the Darwin width of the Bragg peaks which is typically around 10^{-7} [129].

It is also possible to determine the absolute value of a lattice constant with a high accuracy of $7 \cdot 10^{-5} \text{ \AA}$ [130] through comparing the total Larmor phase of the sample of interest $\Phi_{\text{tot, sample}}$ with the total Larmor phase of a reference sample $\Phi_{\text{tot, reference}}$ and applying the relation:

$$d_{\text{sample}} = \frac{\Phi_{\text{tot, sample}}}{\Phi_{\text{tot, reference}}} d_{\text{reference}}. \quad (3.6)$$

3.2.3 Measurement of the distribution of lattice constants

A unique feature of Larmor diffraction is the possibility to determine the distribution of lattice constants through the dependence of the polarization P on the total Larmor phase Φ [124, 131]. This allows to study sample qualities and check for parasitic phases¹ across the entire sample volume. With this method it was, e.g., found that in URu₂Si₂ the small antiferromagnetic moment reported in the hidden order phase is purely parasitic [132].

If a crystal has a distribution of lattice constants around an average value, the polarization detected at the analyzer is reduced compared to a perfect crystal, where the polarization at the analyzer is given as the average of the spin projection of the neutron beam. This is,

¹A parasitic phase in the sense presented here means that a part of the sample volume has such distorted lattice constants, that it effectively is at a different position in the pressure dependent phase diagram as the rest of the sample volume.

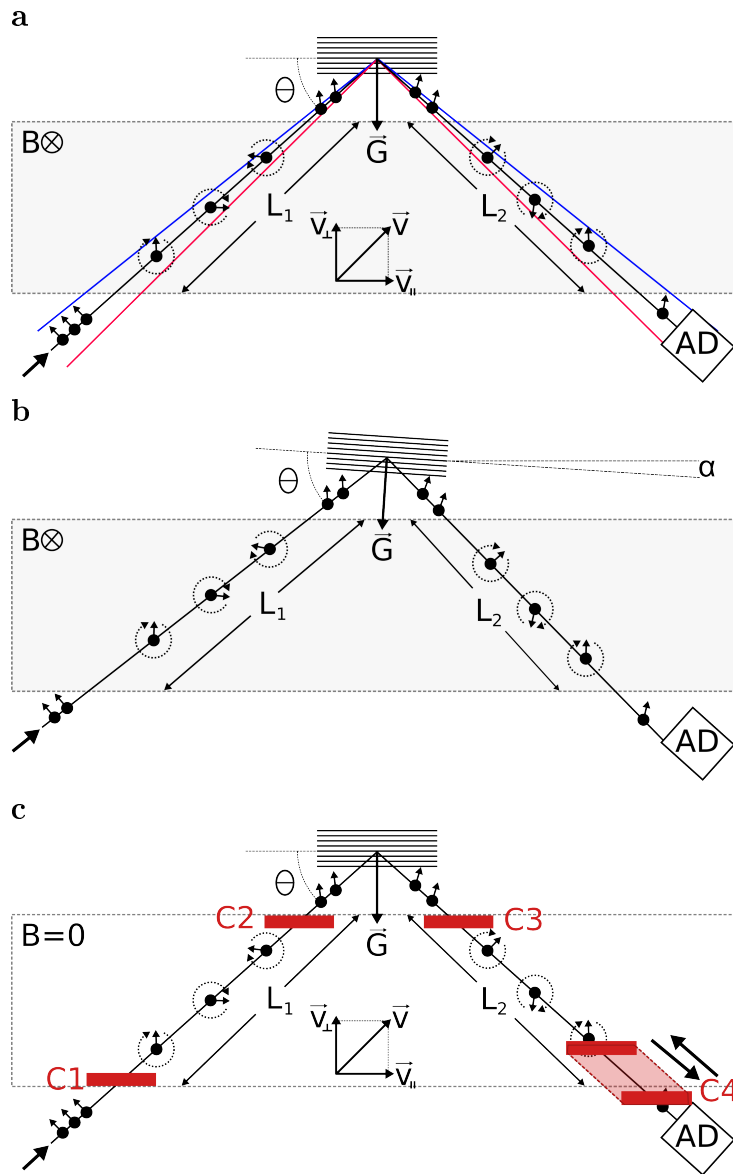


Figure 3.3: Geometry of a Larmor diffraction (LD) experiment. (a) The neutron spins of a polarized neutron beam (black) rotate in a magnetic field (gray shading) before and after they scatter at the lattice planes of a sample. See text for details. AD: Analyzer and detector. (b) When the lattice planes are tilted with respect to the magnetic field boundaries, the Larmor phase remains unchanged to first order. I.e., when the lattice planes are tilted like illustrated, the additional phase the neutrons acquire along an elongated path L_1 is compensated by a shortened L_2 . (c) Illustration of the experimental setup with four radio-frequency coils (C1,C2,C3,and C4) producing the effective magnetic field region indicated by the dashed line (see text for details).

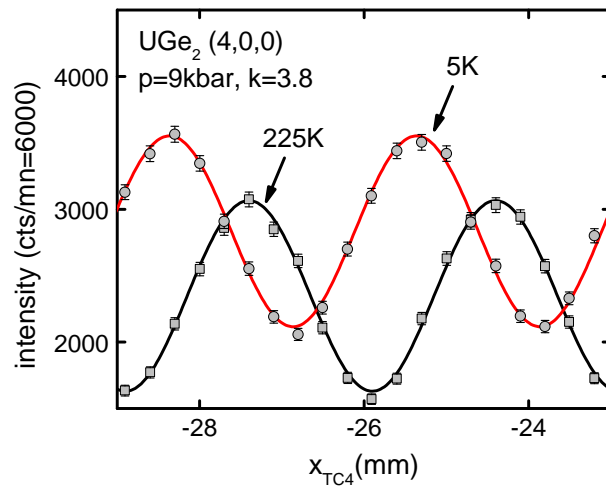


Figure 3.4: Larmor diffractions scans on UGe_2 under 9 kbar at 225 K and 5 K. Shown is the intensity, I , versus translation of coil C4, x_{TC4} . The Larmor phase changes with temperature which results in a horizontal shift of the I -vs- x_{TC4} curves.

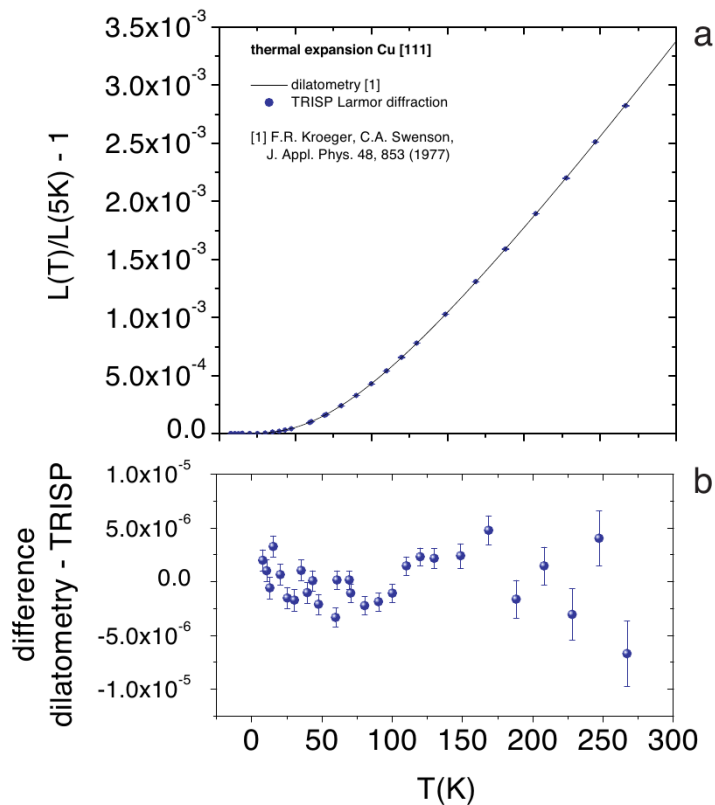


Figure 3.5: Comparison of Larmor diffraction and capacitive dilatometry. (a) Thermal expansion of single crystalline Cu measured by LD [49] and with a capacitive dilatometer [128] at ambient pressure. The parameter-free comparison yields excellent agreement. (b) Difference of LD and dilatometry data. Figure from [49].

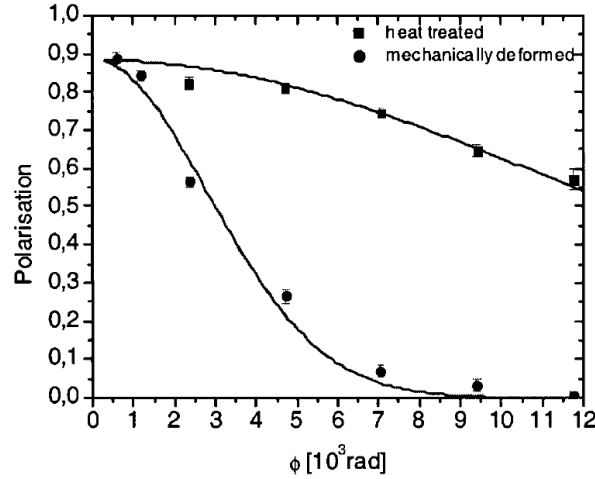


Figure 3.6: Polarization versus total Larmor phase Φ of mechanically deformed and annealed polycrystalline aluminum. The lines represent fits corresponding to Gaussian distributions of $\Delta d/d_{\text{HWHM}} = 6.9 \cdot 10^{-5}$ for the annealed sample and $2.9 \cdot 10^{-4}$ for the mechanically deformed sample. Figure from [124].

because each d value produces a different Larmor phase according to Eq. 3.4. Assuming a Gaussian distribution of lattice constants

$$f(\epsilon) = \sqrt{\frac{4 \ln 2}{\pi}} \frac{1}{\epsilon_{\text{FW}}} \exp\left(-4 \ln 2 \frac{\epsilon^2}{\epsilon_{\text{FW}}^2}\right) \quad (3.7)$$

with $\epsilon = \frac{\Delta d}{d} = \frac{\Delta \Phi}{\Phi_0}$ and FWHM ϵ_{FW} , the polarization as a function of the total Larmor phase $\Phi_0 = \omega_L \frac{2L}{v}$ becomes

$$P(\Phi_0) = P_0 \langle \cos \Delta \Phi(\Phi_0) \rangle \quad (3.8)$$

$$= P_0 \int_{-\infty}^{\infty} f(\epsilon) \cos \Delta \Phi(\epsilon) d\epsilon \quad (3.9)$$

$$= P_0 \exp\left(-\frac{\Phi_0^2}{16 \ln 2} \epsilon_{\text{FW}}^2\right) \quad (3.10)$$

Fig. 3.6 shows an example of $P(\Phi_0)$ for a mechanically deformed and an annealed sample of polycrystalline aluminum [124]. A crystal of good quality has a $\epsilon_{\text{FW}} = \frac{\Delta d}{d}_{\text{FW}} \approx 10^{-5}$.

In case of multiple Gaussian distributions Eq.3.10 changes to

$$P(\Phi_0) = P_0 \sum w_i \exp\left(-\frac{\Phi_0^2}{16 \ln 2} \epsilon_{i\text{FW}}^2\right) \quad (3.11)$$

with $\sum w_i = 1$.

3.2.4 Spin-echo mode

When the fields in both spectrometer arms are set to point in opposite directions, like in the usual spin-echo configuration, we have to distinguish two cases depending on the orientation of the precession field boundaries:

(i) When the boundaries of the effective magnetic fields are parallel to the lattice planes, the neutron phase is sensitive to the mosaic spread of the sample (see [124] for details).

(ii) When the field boundaries are orthogonal to the neutron beam, the rotation of the neutron spins is both sensitive to changes of the neutron velocity due to inelastic scattering events, as described above (see p.31), and sensitive to rotations of the neutron spins due to magnetic fields besides the fields produced by the radio-frequency coils like, e.g., stray fields. Accordingly, when performing a LD experiment, this spin-echo mode configuration allows to check for contributions to the neutron phase that are not related to the change of lattice constant². We refer to such contributions to the neutron phase in this spin-echo configuration as “spin-echo phase” in the following.

When a non-vanishing spin-echo phase is observed, the phase detected in the corresponding LD experiment not only consists of a component related to the change of lattice constant, but also has a component related to either inelastic scattering events or stray fields. The latter component of the neutron phase can be determined in spin-echo mode and directly subtracted from the LD data to obtain the actual change of lattice constants. In our LD experiments on UGe₂ under pressure we observed non-vanishing spin-echo phases. This will be covered in Sec. 3.5.

3.3 Experimental setup

3.3.1 Spectrometer TRISP at FRM II

The spectrometer TRISP (Triple Axis Spin Echo) at the research reactor FRM II in Munich combines neutron resonant spin-echo spectroscopy with triple-axis spectroscopy [133, 134]. It is designed to measure lifetimes of dispersive excitations, like phonons and magnons, over the entire Brillouin zone with a μeV energy resolution. The use of small radio frequency spin flipper coils (RF coils) instead of large DC coils, used in conventional neutron spin-echo instruments, to define the effective precession regions of the neutrons, allows to use the tilted coil focusing technique [135]. There the RF coils are rotated to achieve tilted boundaries of the precession fields relative to the neutron beam, allowing to tune the spin-echo resolution function to the slope of the dispersive curve. The tiltable precession field boundaries can also be used to measure lattice constants with a high resolution of $\Delta d/d \leq 10^{-6}$ as we did with our experiment (see Sec. 3.2) [133].

²Conveniently, only the direction of the precession field in one spectrometer arms has to be reversed to switch from LD to spin-echo mode configuration.

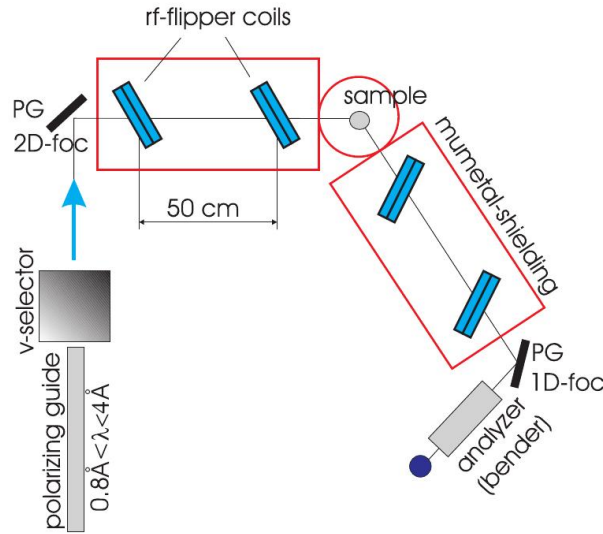


Figure 3.7: Schematic drawing of the TRISP spectrometer. Picture from [133].

Fig. 3.7 shows a schematic drawing of the TRISP spectrometer. As TRISP is designed for measuring excitations with high energies (1 – 100 meV, resolution 1 – 100 μeV), it is placed at a thermal neutron beam. Coming from the moderator the thermal neutrons enter a neutron guide where the neutrons are polarized through FeCoV/TiN supermirrors ($m = 2.5$ [136], critical wavelength 0.8 \AA) in the polarizing section of the guide, yielding typically 90% polarization and 60% transmission in a $0.8 \text{ \AA} \leq \lambda \leq 4 \text{ \AA}$ wavelength band with a collimation of $30' \lambda [\text{\AA}]$. The guide is curved to block the direct view on the moderator to achieve lower background. In combination with a pyrolytic graphite monochromator the polarizing neutron guide outperforms Heusler monochromators (factor 3 at 2 \AA) and ^3He spin filters. Between monochromator and neutron guide a velocity selector is mounted as higher order filter [133].

Two tiltable RF coils are mounted in each spectrometer arm providing an effective field of 1.2 kG. Tiltangles $> 50^\circ$ can be reached. The spectrometer arms as well as the sample space region is shielded by μ -metal to eliminate crosstalk of the spectrometer arms and to be insensitive to external fields. After the second spectrometer arm the neutrons are analyzed through a pyrolytic graphite analyzer together with a bender [133].

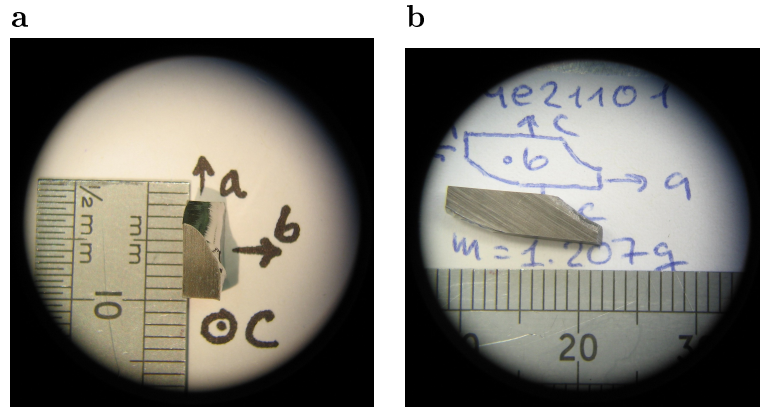
For our experiments on UGe_2 we operated at effective frequencies ω_{reff} of typically 2513 kHz (LD-scans) and between 628 kHz and 6786 kHz (distribution-of-lattice-constants-scans). We used wavelength of 1.55 \AA^{-1} (b -axis), 1.9 \AA^{-1} (a - and c -axis), and 2.51 \AA^{-1} (magnetic peak and alignment).

3.3.2 Samples

The single crystalline UGe_2 samples used for the Larmor diffraction experiment were grown by the Czochralski technique under a purified Argon atmosphere by D. Sokolov.

Table 3.1: UGe₂ samples used for Larmor diffraction experiments.

sample	pressure cell	weight (g)	mosaicity	pressures (kbar)	axes
s1	-	0.82	$\approx 1.0^\circ$	ambient	a,b,c
s2	pc1	0.42	$\approx 1.5^\circ$	9.3, 10.2, 11.8, 12.3	c
s3	pc1	0.39	$\approx 1.5^\circ$	9.3, 10.2, 11.8, 12.3	a,b
s4	pc2	1.20	$\approx 2.4^\circ$	12.4	b,c

**Figure 3.8: UGe₂ single crystals.** (a) Sample s1. (b) Sample s4. Pictures from [138].

Crystal mosaics were $\approx 1^\circ$ (FWHM), RRR $\approx 70 - 120$ and $T_C = 52.6$ K [137]. All samples, together with measured pressures and axes, are summarized in Table 3.1. Figs. 3.8a and b show pictures of typical samples.

In preparation for our Larmor diffraction experiments, we checked for possible transitions of the crystal structure under pressure via neutron single crystal diffraction on the diffractometer RESI at the research reactor FRM II in Munich at which we determined the crystal structure of our highest quality sample, s1 ($\approx 1.0^\circ$ mosaicity), at ≈ 1 kbar and ≈ 10 kbar. We found that at both pressures UGe₂ has a $Cmmm$ structure and that no structural transition can be observed. The determined structure is in good agreement with published structure data [80].

3.3.3 Cryostats and pressure cells

The samples were placed in a standard closed cycle CCR cryostat (temperature range ≈ 3 K-300 K) mounted on the spectrometer. For some experiments the CCR cryostat was combined with a ³He insert to access temperatures down to ≈ 300 mK (cf Ref. [139]). The temperature was measured with Cernox thermometers attached on the outside of the pressure cells close to the sample position.

In order to obtain sufficient polarization for Larmor diffraction scans ($> 10\%$) at temperatures below T_C , it was necessary to cool the sample down in an AC magnetic field

ensuring that the domains of the Ising FM UGe_2 were populated equally. Therefore, a coil was mounted around the sample region of the cryostat and an AC magnetic field of order 0.1 T ($f = 50$ Hz) applied during cooldowns. This way the drop of polarization could be reduced. This will be discussed in detail in Sec. 3.5.1.

A scaled version of the Cu:Be piston-cylinder cell described in Sec. 6.3.4 (see p.106 ff and Ref. [140] for details) with a bore diameter of 6 mm was used for Larmor diffraction experiments (see Fig. 6.11 (p.108)). As in contrast to the Hall effect experiments no wiring was needed for the Larmor diffraction experiments, the obturator was replaced by a second cutting ring and the lower end of the Teflon capsule was sealed with a Teflon cap. A Fluorinert mixture FC72:FC84 with 1:1 volume ratio was used as pressure transmitting medium providing approximately hydrostatic pressure conditions up to ≈ 20 kbar [141].

3.4 Data analysis

3.4.1 Determination of pressures

To determine the pressure values, the Curie temperature T_C at each pressure was inferred from the temperature dependence of the intensity of the magnetic Bragg peak (0,4,0) as illustrated in Fig. 3.9a. With the phase diagram of Pfeleiderer *et al.* [93], deduced from magnetization measurements (Fig. 3.9b), a pressure value could be assigned to each T_C . All values are listed in table 3.2.

As two samples were mounted in pressure cell pc1, s2 and s3, we could determine the pressure inhomogeneity and anisotropy through a comparison of the Curie temperatures T_C of the two samples. A similar quality and hence comparable T_C were assumed since s2 and s3 were cut from adjacent pieces of one UGe_2 ingot. We find a pressure inhomogeneity of ± 0.2 kbar.

Table 3.2: Pressure values. The pressure values were determined from the Curie temperature via the magnetization phase diagram of Ref. [93].

T_C (K)	p (kbar)
38.2	9.3
34.8	10.2
31.8	11.8
30.3	12.3
30.0	12.4

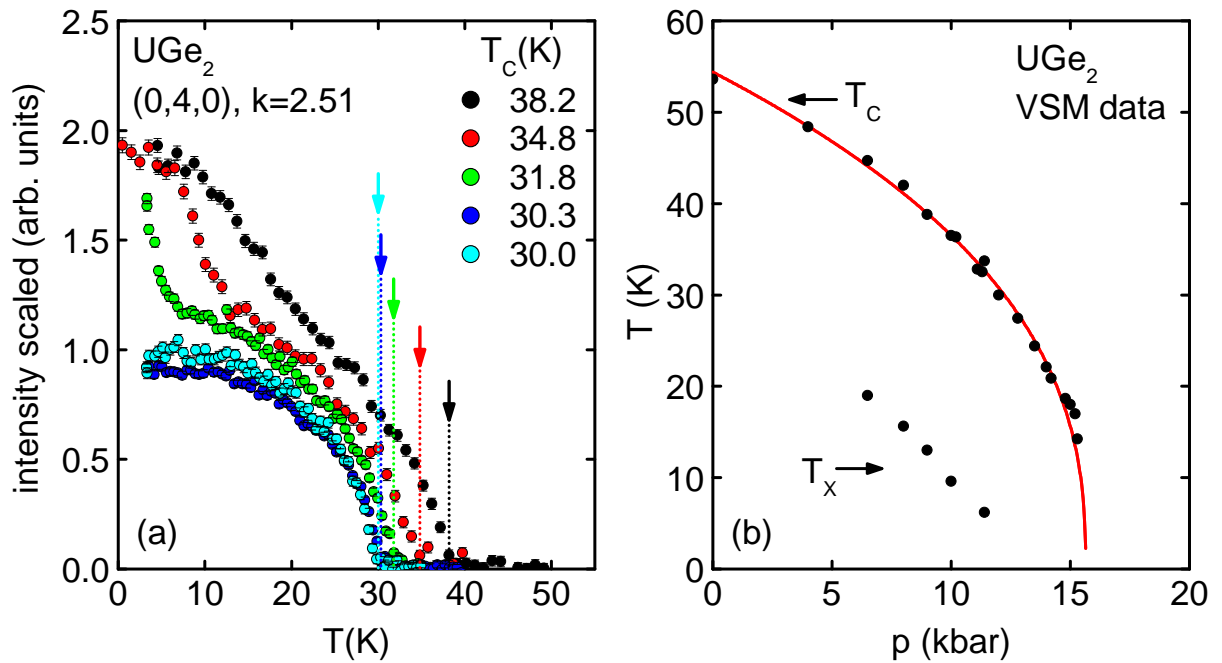


Figure 3.9: Determination of pressures via the magnetic peak intensity. (a) Intensity of the magnetic Bragg peak $(0,4,0)$ versus temperature under pressure. The intensity is scaled so that the low temperature value agrees with magnetization data in units $\mu_B/\text{f.u.}$ (see Fig. 2.4b). The Curie temperature was deduced from the onset of intensity increase coming from high temperatures as illustrates by arrows. With the known Curie temperature the pressure was then inferred from the phase diagram of Pfeleiderer *et al.* [93] shown in panel (b).

3.4.2 Thermal expansion

For the analysis, the intensity I versus coil translation x_{TC4} curve at each temperature is fitted with the formula

$$I = I_0 \left(1 + P \cos \left(2\pi \frac{x_{\text{TC4}} - x_{\text{TC4},0}}{\Delta L} \right) \right) \quad (3.12)$$

where the fit parameters are the average intensity I_0 , the polarization P , and the distance the neutrons travel during one full rotation of its spin ΔL (see Fig. 3.4). The change of lattice constant is then

$$\frac{\Delta d}{d} = \frac{\Delta \Phi}{\Phi} = \frac{x_{\text{TC4}} - x_{\text{TC4},0}}{L_{\text{sp}}} \quad (3.13)$$

with the length of the spectrometer arms L_{sp} .

Data taken in spin-echo geometry was analyzed analog to the LD scans with Eq. 3.12. However, in this case only the second equal sign of Eq. 3.13, i.e., $\Delta \Phi / \Phi = (x_{\text{TC4}} - x_{\text{TC4},0}) / L_{\text{sp}}$ is true as the data refers to the spin-echo phase rather than to the change of lattice constant $\Delta d/d$.

An overview of all LD and SE datasets acquired during this thesis with the corresponding parameters $\Delta d/d$ (or spin-echo phase), I_0 , and P is given in the appendix in Figs. A.1, A.2, A.3, A.4, A.5, and A.6.

All data was corrected for contributions related to the thermal expansion of the spectrometer due to changes in the room temperature. These contributions were determined with the temperature of the spectrometer that was tracked along all measurements and with the thermal expansion coefficient of Aluminum, the material from which the spectrometer is mainly built, $\alpha_{\text{Al}} = 2.3 \cdot 10^{-5} \text{ K}^{-1}$. All x_{TC4} determined with Eq. 3.12 were then corrected with the relation

$$\tilde{x}_{\text{TC4}} = x_{\text{TC4}} (1 + \alpha_{\text{Al}} \Delta T). \quad (3.14)$$

Here, ΔT represents the temperature difference between the spectrometer at the initial scan, relative to which the data is normalized, and the momentarily considered scan.

3.4.3 Distribution of lattice constants

To determine the distribution of lattice constants, the polarization was measured as a function of total precession phase Φ_0 . As Φ_0 is governed by the operation frequencies of the RF-coils described in Sec. 3.3.1, a change in Φ_0 was experimentally realized though changing bespoke frequencies. The data was then fitted with Eq. 3.10, assuming a Gaussian distribution of lattice constants. Subsequently, the resulting $P(\Phi_0)$ data was corrected for depolarization effects caused by the spectrometer itself.

Fig. 3.10a shows typical depolarization scans taken along the b -axis at temperatures above and below the Curie temperature at a pressure of 9.3 kbar. Fits of the data with Eq. 3.10 yield a FWHM of $\epsilon_{\text{FW}}(T = 60 \text{ K}) = 7.6 \cdot 10^{-4}$ and $\epsilon_{\text{FW}}(T = 0.5 \text{ K}) = 8.7 \cdot 10^{-4}$ indicating a medium crystal quality along the b -axis under pressure.

To consider the frequency dependent depolarization of the spectrometer itself, the polarization values of our data at each frequency, i.e., Φ_0 , were normalized to the dataset of a high quality germanium crystal taken at a temperature of 7.6 K (see Fig. 3.10b) which was taken as a measure for the depolarization caused by the spectrometer. It was assumed that the depolarization caused by the high quality germanium crystal is considerably smaller than the depolarization caused by the spectrometer itself.

Fig. 3.11 illustrates the distribution widths ϵ_{FW} according to Eq. 3.10 for UGe_2 at various pressures at temperatures below and above the Curie temperature. The general trends are: (i) The distribution of lattice constants is broader in the ferromagnetic phase ($T < T_C$) than in the paramagnetic phase ($T > T_C$). This implies that the crystal lattice becomes slightly distorted when the sample becomes ferromagnetic with all moments aligning along the a -axis. (ii) The distribution becomes broader with increasing pressure. Increasing pressure gradients in the pressure cell probably contribute to this trend. However, as a caveat, the data scatters by a fair amount and the depolarization curves at some pressures are better fitted with Eq. 3.11 with $n = 2$, i.e., the presence of two Gaussian distributions.

3.5 Larmor diffraction on UGe_2 : Specific challenges

Our experiments on UGe_2 represent the first Larmor diffraction measurements on a ferromagnetic system. Consequently, we encountered two major challenges that we had to overcome: (i) A large depolarization of the neutron beam when the sample is in the ferromagnetic state leading to a loss of information encoded in the neutron phase. (ii) A non-vanishing spin-echo phase, i.e., a phase rotation not related to a change of lattice constant, that occurred in Larmor diffraction scans under pressure. The characteristics and solutions of these two challenges are discussed below.

It is important to emphasize that our Larmor diffraction experiments on UGe_2 represent a comprehensive study covering 68 days of beamtime at TRISP. The large amount of beamtime is mainly due to the orthorhombic crystal structure which makes it necessary to measure all three crystalline axes, a relatively low intensity due to the large absorption of the Cu:Be pressure cells, and the necessity to measure the spin-echo phase in addition to the Larmor diffraction scans.

3.5.1 Depolarization

As illustrated in Fig. 3.12, a beam of polarized neutrons loses its polarization when it traverses a ferromagnetic sample. In each ferromagnetic domain the neutrons are subject

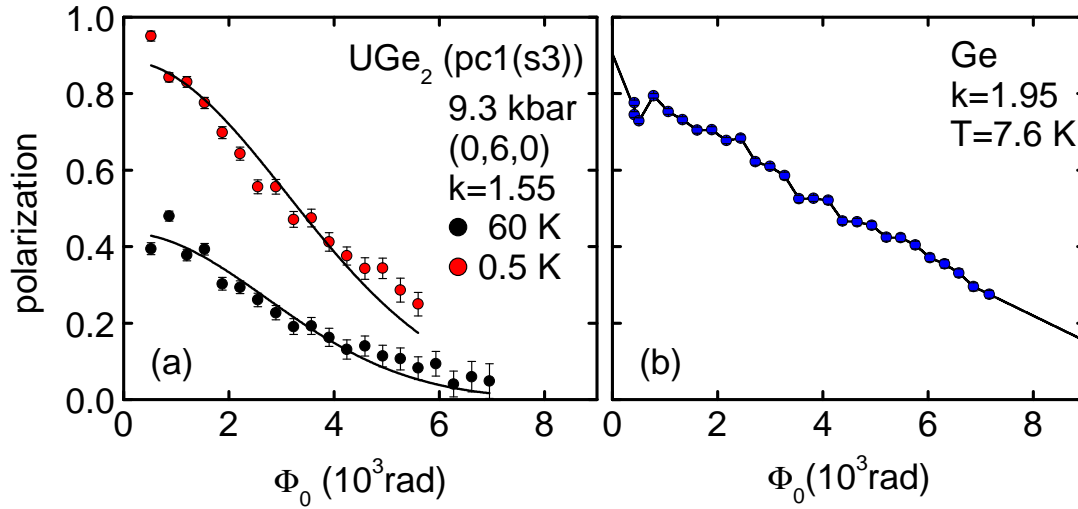


Figure 3.10: Depolarization scans to determine the distribution of lattice constants. (a) Typical depolarization scans of UGe_2 at 9.3 kbar on the (0,6,0) Bragg reflexion at temperatures below and above the Curie temperature. Fits of the data with Eq. 3.10 yield a FWHM of $\epsilon_{\text{FW}}(T = 60 \text{ K}) = 7.6 \cdot 10^{-4}$ and $\epsilon_{\text{FW}}(T = 0.5 \text{ K}) = 8.7 \cdot 10^{-4}$ indicating a medium crystal quality along the b -axis under pressure. (b) Depolarization scan of a high quality germanium crystal. The black line are interpolated and extrapolated values. This dataset was used as reference to correct for depolarization effects of the spectrometer itself. All data was normalized to this dataset.

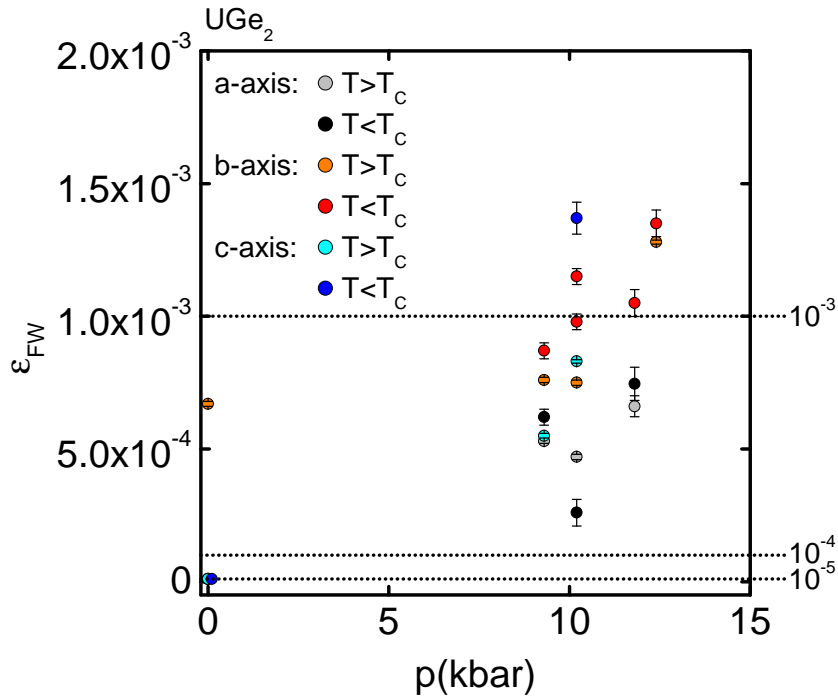


Figure 3.11: Distribution width of lattice constants. Width ϵ_{FW} according to Eq. 3.10 for various pressures at temperatures below and above the Curie temperature.

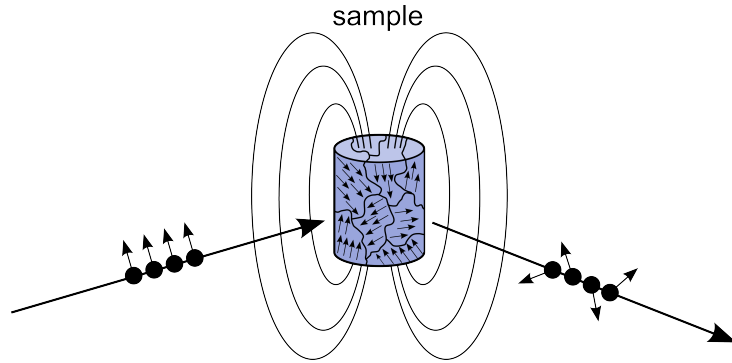


Figure 3.12: Depolarization due to a magnetic sample. Schematic illustration of a magnetic sample depolarizing a polarized neutron beam.

to a rotation of its spins according to the magnetization direction of the individual domain. Accordingly, the detailed trajectory of a neutron through the sample determines its spin direction on leaving the sample. Thus, neutrons with slightly different trajectories leave the sample with different spin directions so that the neutron beam depolarizes and information encoded in the neutron phase is lost. In our case, this means that the amplitude of the sinusoidal signal shown in Fig. 3.4 decreases with decreasing polarization. The phase Φ itself does not change with decreasing polarization, but the signal to noise ratio becomes smaller. A polarization $>10\%$ is needed to perform useful LD scans, i.e., to be able to determine the phase through fitting the raw data with the sinusoidal function given in Eq. 3.12. Neutron depolarization measurements of Sakarya *et al.* [142] in 2005 yielded a polarization loss between $T > T_C = 52\text{ K}$ and 4 K of $\approx 30\%$. Hence, LD measurements in UGe_2 appeared feasible provided that the initial polarization at high temperature is sufficiently large.

In our experiments we observed a polarization loss about the same magnitude as Ref. [142]. However, as our initial polarization was only around 50% when using pressure cells, we had to demagnetize our samples in an AC magnetic field while cooling to prepare the sample in the (Ising) ferromagnetic state with an equal domain population to have minimal depolarization effects. As all moments are aligned along the magnetically easy a -axis in the Ising ferromagnetic state of UGe_2 (see Fig. 2.1), rotations of the neutron phase caused by domains with magnetic moment in $+a$ direction can be compensated by domains with magnetic moment in $-a$ direction and vice versa, provided that the domains are equally populated along the path of the neutrons through the sample. In order to achieve such an equal domain population, we applied an AC magnetic field to our UGe_2 samples while cooling through the Curie temperature. This way we were able to retain sufficient polarization at low temperatures. The AC magnetic field of order 0.1 T ($f = 50\text{ Hz}$) was produced by a coil wound around the sample region of the cryostat. Fig. 3.13 shows the typical temperature dependence of the polarization during LD scans taken on heating from base temperature after an initial cooldown in the bespoke AC magnetic field. In turn, cooling the sample without AC magnetic field resulted in polarization values below 10% rendering LD scans impossible.

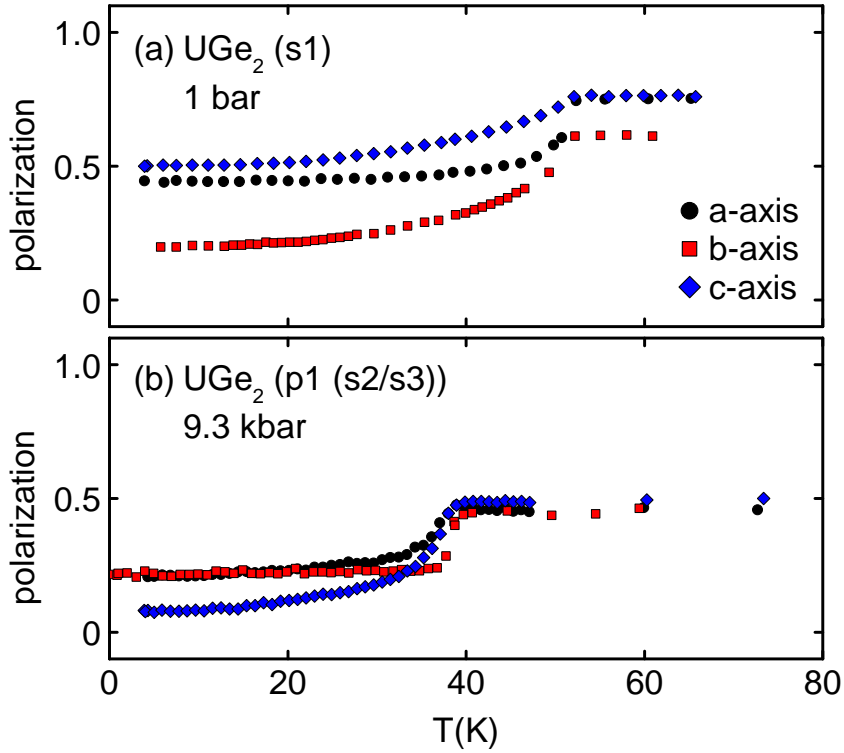


Figure 3.13: Typical temperature dependence of the polarization during Larmor diffraction scans in UGe_2 . Coming from high temperatures, the polarization begins to drop at T_C . (a) At ambient pressure the polarization between $T_C \approx 52$ K and base temperature (typically ≈ 3 K) drops between 25% to 40%. (b) At 9.3 kbar the samples are mounted in a pressure cell. Hence, all polarization curves are shifted by roughly 20% to lower polarization. The polarization also shows a drop between 25% to 40% between $T_C = 38.2$ K and base temperature, as observed at ambient pressure.

3.5.2 Non-vanishing spin-echo phase

As already mentioned in Sec. 3.2.4, when performing a LD experiment it is important to check for a spin-echo (SE) phase to detect possible contributions to the neutron phase that are not related to a change of lattice constant. Such additional contributions can either relate to a change in the neutron velocity in the scattering process (inelastic scattering) or to a magnetic field integral besides the precession fields. Consequently, we performed scans in SE geometry along the LD measurements and found a non-vanishing SE phase at the high pressure experiments. Accordingly, the LD data was corrected through subtraction of the SE phase signal. As will be discussed below, we so far cannot explain the origin of the spin-echo phase. However, as all our results are inferred from data around the T_X transition, i.e. data at $T < 20$ K, where the temperature dependence of the SE phase is much smaller than the LD signal, our conclusions are independent of the SE phase subtraction.

To determine the spin-echo phase we used a geometry with the effective magnetic fields in the spectrometer arms pointing in opposite directions (see Fig. 3.14b). The field boundaries were oriented orthogonal to the propagation direction of the neutron beam so that they are not sensitive to the mosaic spread of the sample. A non-vanishing signal in this geometry is then either related to a change in the neutron velocity in the scattering process (inelastic scattering) or due to a magnetic field integral.

In the experiments under pressure (pressure cell pc1) we find a non-vanishing, temperature dependent spin-echo phase. Fig. 3.15a-c illustrate the SE phase (dark cyan datapoints) together with LD data (cyan datapoints) for the c -axis at 9.3 kbar, 10.2 kbar, and 11.8 kbar. Coming from low temperatures, the SE phase increases and has a peak around T_C . Above T_C the SE phase drops over a range of several Kelvin down to a constant value. Through this additional contribution to the neutron phase, the raw data of the LD scans does not directly relate to the change of lattice constant and shows, e.g., a sharp dip around T_C as artifact. However, the LD data can be easily corrected for this contributions when subtracting the SE phase yielding a dataset that purely represents the change of lattice constants (red datapoints).

The temperature dependence of the SE phase with a peak around T_C implies that it is connected to the sample. This leads to several possible origins that are most likely: (i) Inelastic scattering; (ii) a magnetic field integral in the sample volume due to, e.g., an incomplete demagnetization or stray fields. As LD is performed on a strong Bragg peak, inelastic contributions are insignificant and hence can be dismissed as possible origin which leaves a magnetic field integral in the sample volume. As a quantitative estimate, if the phase rotation is due to a vertical magnetic field in the sample volume, the field value would have to be on the order of 1 mT. Considering this large value and the fact that the SE phase extends to several Kelvin above T_C makes an incomplete demagnetization unrealistic.

Another possibility are stray fields produced by the tungsten carbide (WC) anvil used in

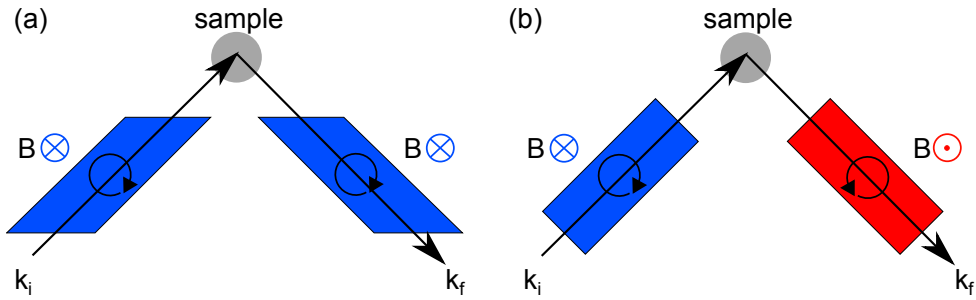


Figure 3.14: Measurement geometries. Schematic illustration of the TRISP spectrometer in the (a) Larmor diffraction (LD) and (b) spin-echo (SE) geometry. The colored regions represent effective magnetic fields pointing up (red) and down (blue). The rotation of the neutron spins is indicated by arrows.

the pressure cell. Those fields could be magnified by the differential susceptibility of the sample which would explain the temperature dependence with a peak around T_C . Furthermore, this would be consistent with the observation that the SE phase only appeared when using a pressure cell. The WC anvils are made with a sintering process in which either Nickel or Cobalt, both ferromagnets, are used as binder. Hence, impurities of the binder in the anvils can provide a source of stray fields. However, an estimate shows that the magnetization of the WC anvil would need to be around $M_{\text{anvil,est.}} \approx 60 \text{ mA/m}^2$ which is unrealistically high. Separate magnetization measurements of several WC anvils yield a saturation magnetization of the most magnetic anvil that is about two orders of magnitude smaller than $M_{\text{anvil,est.}}$, and a residual magnetization on the order of $100 \mu\text{A/m}^2$ [143].

In conclusion, the origin of the SE phase is an open question but does not affect the interpretations given in this thesis. Further experiments are required to unravel the mechanisms behind the SE phase. An overview of all LD and SE datasets acquired during this thesis together with $\Delta d/d$ calculated from the SE-phase corrected LD data is given in the appendix in Figs. A.1-A.6.

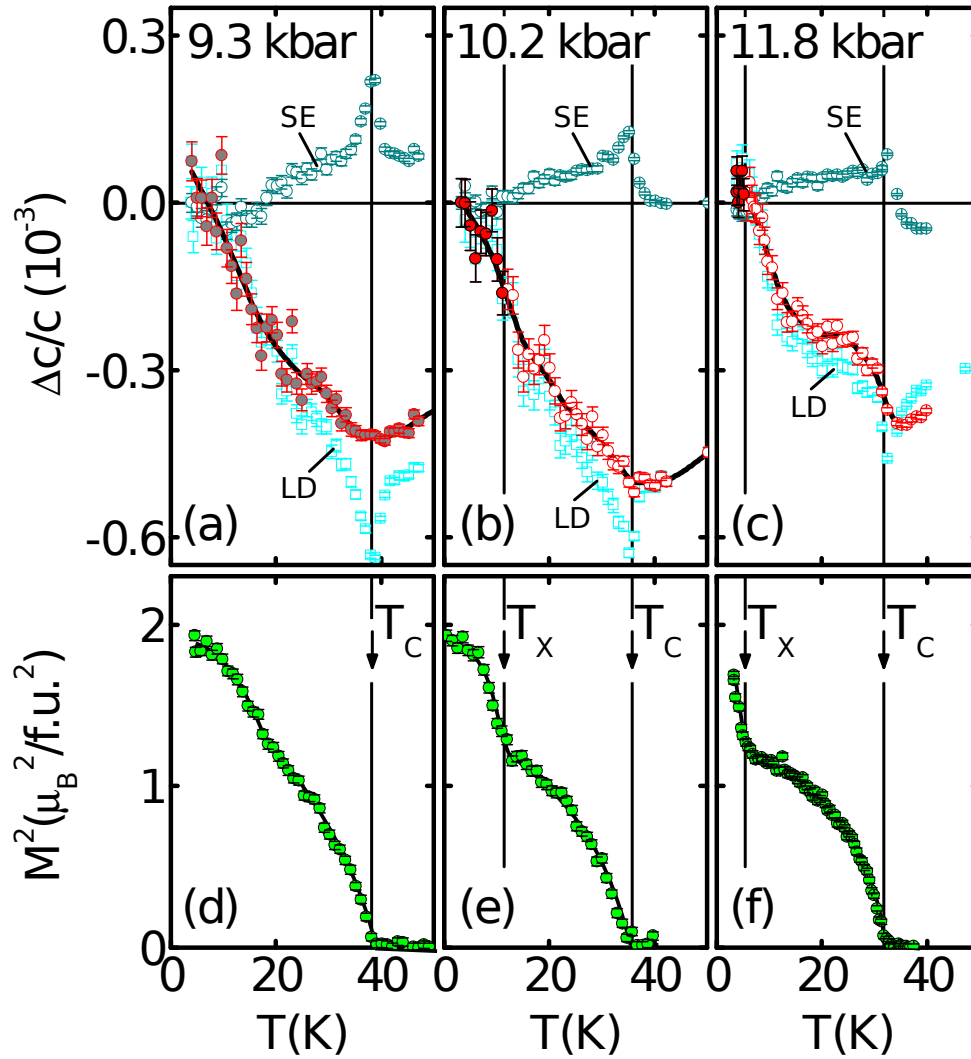


Figure 3.15: Thermal expansion of the c -axis and magnetization under pressure. Phase shifts measured in LD and SE geometry along the $(0,0,2)$ Bragg peak (top row) and the squared ordered moment inferred from the intensity of the $(0,4,0)$ magnetic peak (bottom row). The Larmor diffraction data (\square) is corrected by the spin echo phase (\circ) yielding $\Delta c/c$ (\bullet for $T < T_X$ and \circ for $T > T_X$). Black lines through the datapoints are guides to the eye.

Chapter 4

Results and Discussion

This chapter begins with a comparison of our Larmor diffraction (LD) data with thermal expansion data reported in the literature as LD is a relatively new technique and as we performed the first LD measurements on a ferromagnetic system (Sec. 4.1). Overall we find a good agreement of data recorded with the conventional methods of strain gauges and capacitive dilatometers with our LD data. The data reported in literature includes the thermal expansion along all crystalline axes at ambient pressure, however, under pressure only studies of either the a -axis, the b -axis, or volumetric thermal expansion were reported up to now. Our comprehensive study, presented in Sec. 4.2, including the thermal expansion of all crystalline axes under pressures up to 12.4 kbar together with the magnetization considerably extends the literature. The main result of our study is the observation of an additional transition T_L in the c -axis thermal expansion under pressure. As will be discussed in Sec. 4.3, the transition at T_L is not related to contributions by the crystal lattice or magnetostriction to the thermal expansion but has a different yet unknown origin. We speculate that T_L might be driven by a change in the Fermi surface topology, a so-called Lifshitz transition. However, further experiments are required to verify this hypothesis.

So far, all mechanism that are discussed to drive the superconductivity in UGe_2 relate to magnetism. Therefore, our finding of a non-magnetic transition close to the superconducting phase is an important evidence to also consider non-magnetic superconducting pairing mechanisms in UGe_2 and might be a first step to unravel the origin of the unconventional superconductivity in UGe_2 .

4.1 Comparison with literature

4.1.1 Ambient pressure

As a proof of principle we first measured the thermal expansion of UGe_2 with Larmor diffraction at ambient pressure for all three crystalline axes and compared our data with data reported in the literature. In general, we find good agreement of our data with the

literature.

Fig. 4.1 shows a comparison of our Larmor diffraction data recorded in sample s1 with strain gauge data from Nishimura *et al.* [101] (panel a and b) and capacitive dilatometry data from Hardy *et al.* [102] (panel c and d) at ambient pressure. Except for a temperature offset of +4.24 K, for which the strain gauge data was shifted in Figs. 4.1a and b, the datasets are in good agreement¹. The origin of the temperature offset is not clear. However, as will be seen below, since our temperature values agree well with other values reported in the literature (e.g. with [91, 102]), and since we used state of the art Cernox temperature sensors in combination with Lakeshore LS 340 temperature controllers, we are confident that our temperature values are reliable. Furthermore, capacitive dilatometry data also is in good agreement with our data (Figs. 4.1c and d). The α values displayed in Ref. [102] were extracted and integrated yielding the $\Delta d/d$ values used for the comparison.

4.1.2 Under pressure

Under pressure, several strain gauge measurements along the a - and b -axis [91, 92, 101–104] and volumetric strain gauge measurements [105, 106] have been reported. We find a very good agreement of our b -axis data with literature. Our a -axis data is in less good agreement with the literature which can be explained through the large spin-echo phase correction necessary in this measurement geometry. No c -axis data under pressure has been reported so far in the literature.

Fig. 4.2 shows the thermal expansion along the b -axis under pressure measured with strain gauges by Kabeya *et al.* [91] (SG1) and by Taufour shown in Ref. [102] (SG2) in comparison to our Larmor diffraction data recorded in sample s3. In general, all datasets are in good agreement. Only minor deviations are observed: In panel b and c the datasets match perfectly, while in panel a the slopes below T_C are slightly different. In panel d, deviations along the temperature axis can be seen between the LD and the SG1 data, both nominally at 12.3 kbar. This temperature difference (corresponding to $\Delta p \approx 0.7$ kbar) can be reasonably explained though uncertainties in determining the pressure. Considering T_C , the SG2 dataset indicated as 13 kbar is also shifted to higher temperatures by around 6 K. However, since no technical information is given in Ref. [92] about the measurements under pressure this issue cannot be resolved here.

A comparison of the thermal expansion along the a -axis between strain gauge data by Nishimura *et al.* [101] and Larmor diffraction data, acquired on sample s3, is displayed in Fig. 4.3. While the data matches quite good at ambient pressure (panel a), except the temperature offset discussed above (not corrected in this graph), the data under pressure matches less well (panel b). The different slopes between SG and LD data could be caused by the large spin-echo phase correction necessary in this measurement geometry. Larmor diffraction raw data, spin-echo phase, and $\Delta d/d$ at 9.3 kbar and 11.8 kbar are illustrated

¹In Ref. [101] the a - and c -axis are interchanged as a $Cmcm$ crystal structure instead of a $Cmmm$ crystal structure was assumed in studies before 1996 [95]. All labels shown here are corrected.

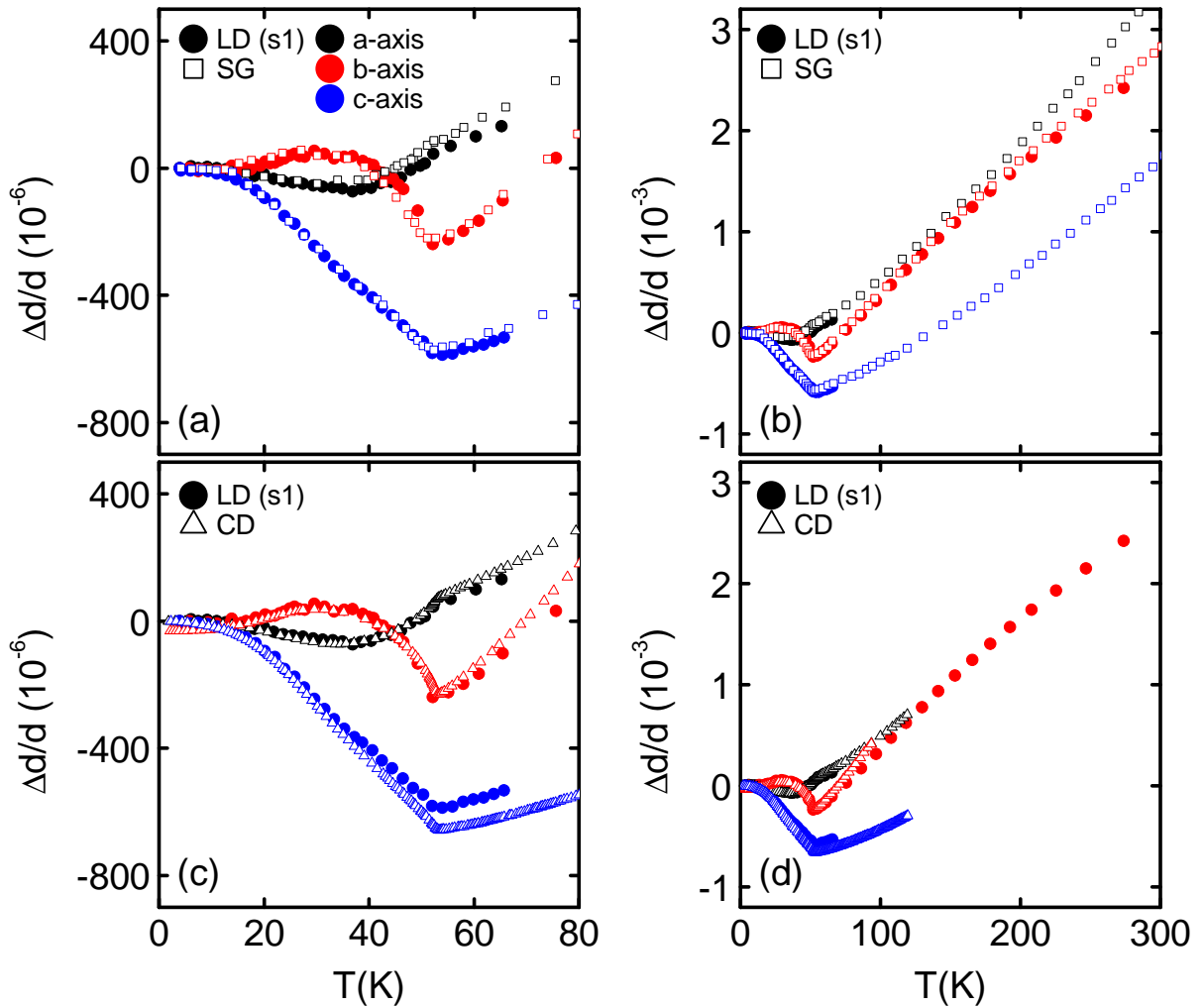


Figure 4.1: Comparison of Larmor diffraction data at ambient pressure with the literature. Comparison with strain gauge (SG) data from Nishimura *et al.* [101] at (a) low temperatures and (b) up to room temperature. The data from Ref. [101] was shifted by +4.24 K. See text for details. Comparison with capacitive dilatometry (CD) data from Hardy *et al.* [102] at (c) low temperatures and (d) up to room temperature. The shown Larmor diffraction (LD) data was taken on sample s1.

in Figs. A.2 and A.4 in the appendix. As can be seen, since the overall change in lattice constant along the a -axis is smaller compared to the other axes but the spin-echo phase contribution is of equal size, the spin-echo phase correction has a much larger effect on the $\Delta d/d$ curves and changes the slope of the raw data qualitatively. Considering the scattering of the raw data and the spin-echo phase, the differences between the SG data and the Larmor diffraction data along the a -axis under pressure appear plausible. However, it is important to note that the precise slope of the thermal expansion along the a -axis under pressure does not affect our main result in any way. That is, as our main result is inferred from the evolution of the transition temperatures T_C and T_X under pressure.

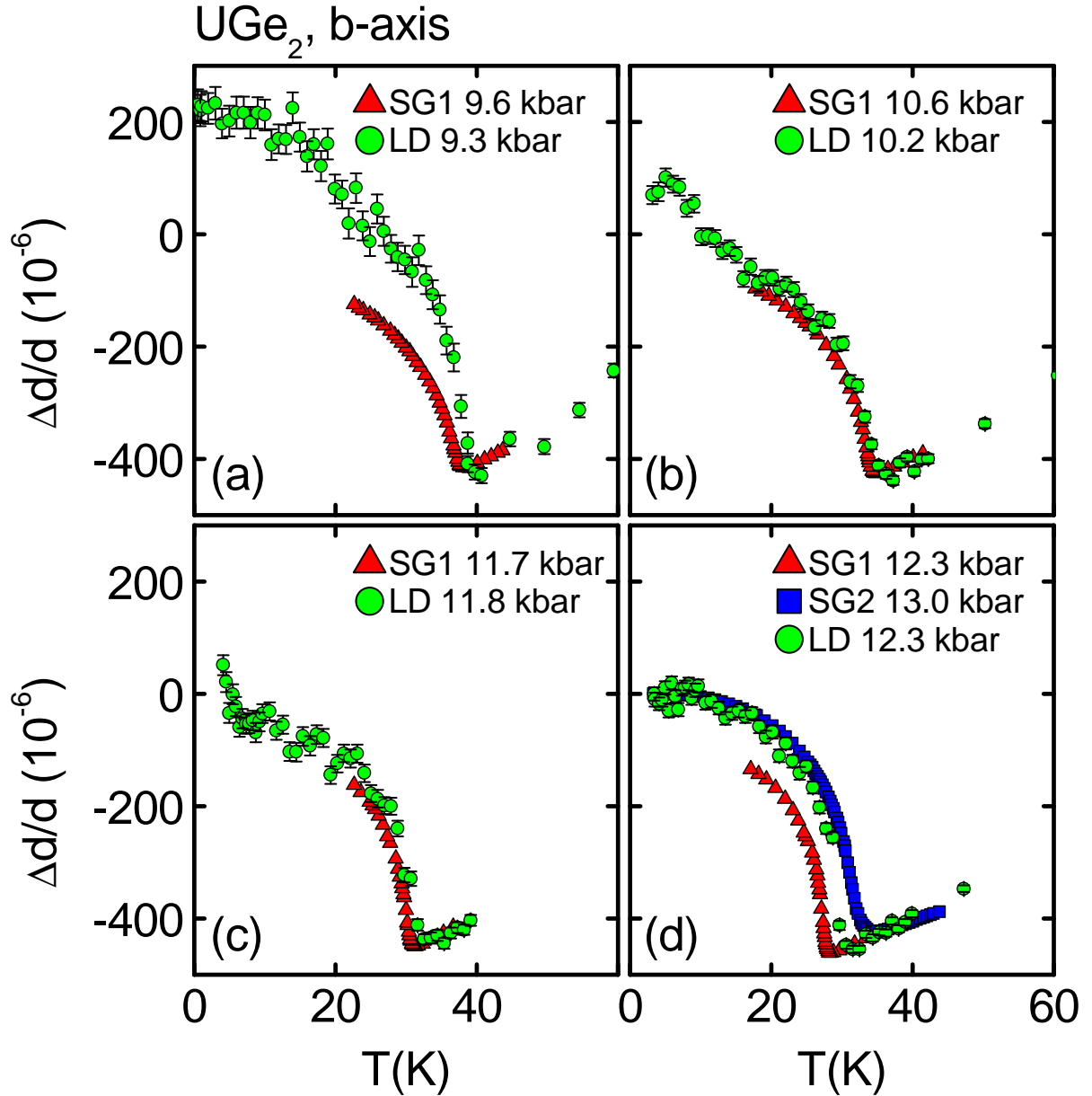


Figure 4.2: Comparison of thermal expansion data along the b -axis under pressure with the literature. Our Larmor diffraction (LD) data along the b -axis under pressure (taken on sample s3) in comparison with strain gauge data from Kabeya *et al.* [91] (SG1) and from Taufour shown in Ref. [102] (SG2).

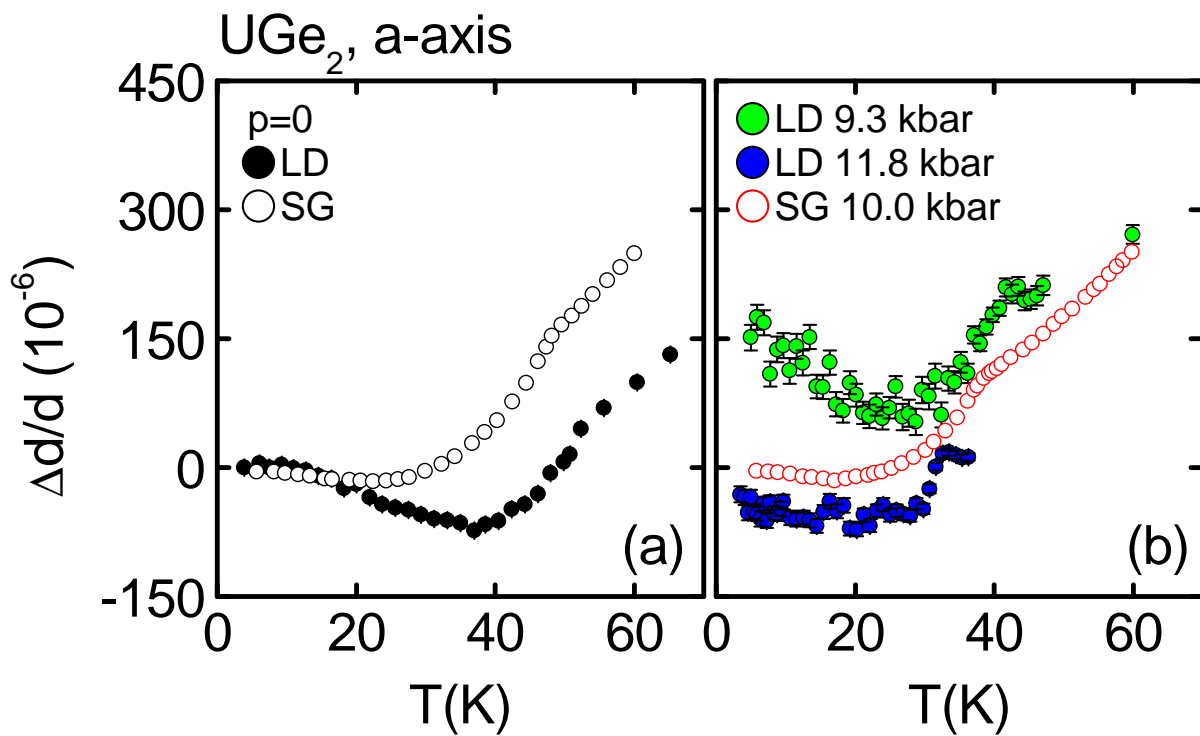


Figure 4.3: Comparison of thermal expansion data along the a -axis with the literature. (a) Larmor diffraction (LD) data at ambient pressure in comparison with strain gauge (SG) measurements reported by Nishimura *et al.* [101]. In panel b the datasets are shifted vertically for clarity.

4.2 Additional transition T_L

In the ferromagnetic regime of UGe_2 , a transition T_X between two ferromagnetic phases appears under pressure. T_X can be seen in the magnetization and the thermal expansion as the onset of a signal increase when coming from high temperatures. As discussed in Sec. 3.2, Larmor diffraction allows to directly compare the transition temperatures in the thermal expansion and in the magnetization as they are measured in the same setup. We find, that the T_X transition in the magnetization coincides with the thermal expansion along the a - and b -axis, as expected for standard magnetostriction. However, the T_X transition along the c -axis, labeled T_L in the following, lies several Kelvin higher. This implies that T_L is not driven by the magnetization but originates from a different mechanism.

In this chapter we first visualize the general behavior via $\Delta d_m/d$, which is the thermal expansion corrected for contributions from the crystal lattice, in comparison with the magnetization. $\Delta d_m/d$ displays all electronic contributions to the thermal expansion. Our main conclusion, that the T_L transition cannot be explained by magnetostriction is then deduced from $\Delta d/d$ as a function of the squared magnetization M^2 at temperatures below 30 K where the lattice contribution can be neglected. Therefore our conclusions are independent of the subtraction of the lattice contribution to the thermal expansion. While the experimental evidence is discussed below, physical implications concerning this new feature are discussed in Sec. 4.3.

For a closer look at the electronic contributions, we subtracted the lattice contribution to the thermal expansion $\Delta d_{\text{lattice}}/d$ from $\Delta d/d$ yielding a dataset $\Delta d_m/d$ which is mainly dominated by magnetostriction. To estimate $\Delta d_{\text{lattice}}/d$ for all our $\Delta d/d$ datasets we calculated the phonon contribution to the thermal expansion $\Delta d_{\text{ph}}/d$ from ambient pressure specific heat data via the Grüneisen relation

$$\Delta d_{\text{ph}}/d = \int dT \Gamma_d^{\text{ph}} C_{\text{ph}}(T) \quad (4.1)$$

assuming temperature and pressure independent Grüneisen parameters Γ_d^{ph} . We find that the high temperature part of $\Delta d/d$ can be accounted for reasonably well through $\Delta d_{\text{ph}}/d$ (see below). Therefore, we attribute $\Delta d_{\text{lattice}}/d$ to phonons and use $\Delta d_{\text{lattice}}/d \approx \Delta d_{\text{ph}}/d$ in the following.

As shown in Ref. [144], the phononic part to the specific heat of UGe_2 can be well described by the phenomenological Debye model. Hence, we first made a Debye fit of the ambient pressure specific heat of UGe_2 reported in Ref. [138] finding a Debye temperature $\Theta_D = 237 \text{ K}$ which is slightly lower than Θ_D in Ref. [144] (Fig. 4.4a). In a second step, this Debye fit was integrated according to Eq. 4.1, assuming temperature independent Grüneisen parameters. The result was then scaled to the high temperature part of the thermal expansion. As illustrated in Fig. 4.4b for the c -axis at 9.3 kbar as a typical example, we find that the high temperature part of the thermal expansion measurements under pressure can be described reasonably well with the $\Delta d_{\text{ph}}/d$ calculated from the ambient pressure specific heat data. The resulting datasets which are dominated by magnetostric-

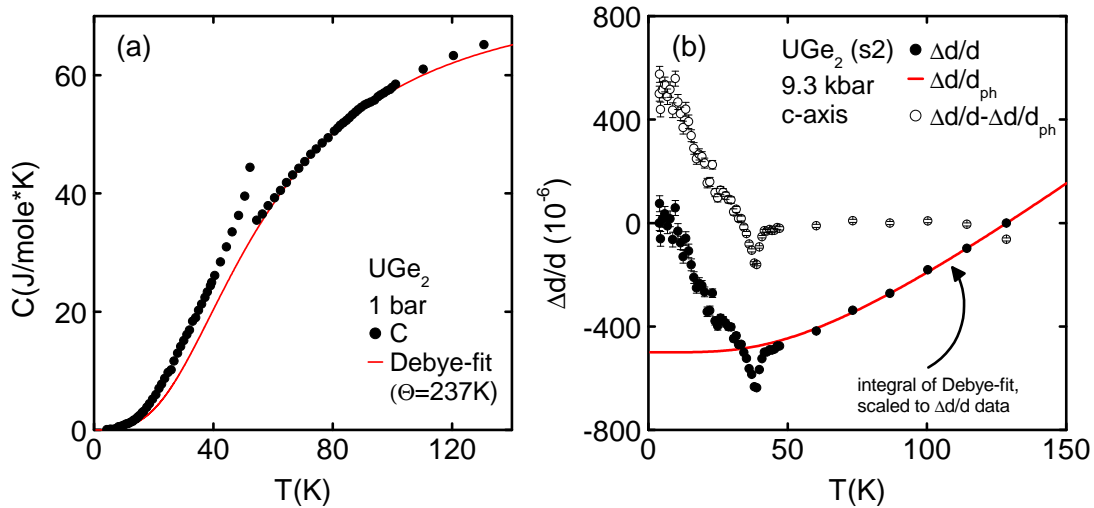


Figure 4.4: Subtraction of phonon contribution to the thermal expansion. (a) Temperature dependent specific heat of UGe_2 at ambient pressure from Ref. [138]. The red line is a Debye fit with $\Theta_D = 237 \text{ K}$. (b) Larmor diffraction raw data, i.e., without spin-echo phase correction, at 9.3 kbar as measured (closed datapoints) and with subtracted phonon part (open datapoints). The integrated specific heat was used to subtract the phonon contribution to the thermal expansion, according to the Grüneisen relation in Eq. 4.1.

tion are labeled $\Delta d_m/d = \Delta d/d - \Delta d_{\text{ph}}/d$ in the following.

Fig. 4.5 shows a comparison of all thermal expansion datasets with subtracted phonon contribution, $\Delta d_m/d$, and magnetization measurements acquired during this thesis. The upper row shows $\Delta d_m/d$ measured with Larmor diffraction for all crystalline axes for various pressures. The lower row shows the magnetization squared inferred from the intensity of a magnetic peak (under pressure) and VSM measurements from Ref. [93] (ambient pressure). The panels are shown in the order of increasing pressure from left to right. Concerning the spin-echo phase correction discussed in Sec. 3.5.2, it has to be noted that due to limited beamtime no spin-echo phase correction was measured and hence subtracted for several datasets. For the a -axis data at 10.2 kbar an estimated spin-echo phase was subtracted (open datapoints in panel e). However, this has no effect on the interpretation of our data. For details see Ref. [145].

The T_C and T_X transitions of the magnetization are seen as onsets of a signal increase (coming from high temperatures) and are marked through vertical lines. The b - and c -axes thermal expansion is qualitative comparable to the magnetization so that T_C and T_X also appear as a signal increase. The a -axis thermal expansion has a qualitatively different course and drops below zero between T_C and approximately T_X . With increasing pressure, the T_C and T_X transitions shift to lower temperatures. Above $p_X \approx 12 \text{ kbar}$ no T_X transition is observed in agreement with the literature. We find, that temperature dependent changes in $\Delta d_m/d$ along the a - and b -axes coincide with changes in the magnetization, and hence can be explained by standard magnetostriction. In contrast, along the c -axis a clear signal increase is observed several Kelvin above the T_X transition at a

temperature T_L . The signal increase at T_L is most clear at 11.8 kbar and is smeared out at lower pressures. The difference $T_L - T_X \approx 6$ K at 11.8 kbar, the highest pressure we measured below p_X , on approaching $p_X \approx 12$ kbar. This temperature difference is larger than any uncertainty in determining the transition temperatures or uncertainties related to pressure inhomogeneities².

To get a better insight in what features in the thermal expansion are driven by a changing magnetization independent of a phonon part subtraction, $\Delta d/d$ as a function of the magnetization squared, M^2 , is shown in Fig. 4.6 for the b - (panel a) and the c -axis (panel b) with temperature as an implicit parameter. Only data at temperatures $T < 30$ K are shown where the phonon contribution to the thermal expansion is negligibly small. Also, the spin-echo phases only have small temperature dependences in this temperature range so that our conclusions are independent of the SE phase correction (see Sec. 3.5.2). Open datapoints indicate $T > T_X$, closed datapoints indicate $T < T_X$. $\Delta b/b$ is a smooth function of M^2 . Even around T_X where both $\Delta b/b$ and M^2 show strong changes when plotted versus temperature (cf Fig. 4.5) no features are observed. This indicates that the b -axis thermal expansion is due to standard magnetostriction. $\Delta c/c$ exhibits a distinct step as a function of M^2 corresponding to the T_L transition discussed above. This implies that the c -axis thermal expansion cannot be explained by standard magnetostriction and that an additional mechanism is driving the T_L transition. The step is sharp at 11.8 kbar and smears out at lower pressures. At 10.2 kbar a broad cross-over is observed. At 9.3 kbar the T_L transition is completely smeared out. Physical interpretations about the origins of this feature are discussed in Sec. 4.3.

² M^2 and $\Delta c/c$ were measured on sample s3 and s2, respectively. However, the pressure inhomogeneity needed to shift T_X from 5.43 K up to $T_L = 12.16$ K is $\Delta p \approx 1.8$ kbar which is far greater than our estimated pressure inhomogeneity of $\Delta p \approx \pm 0.2$ kbar (see Sec. 3.4.1).

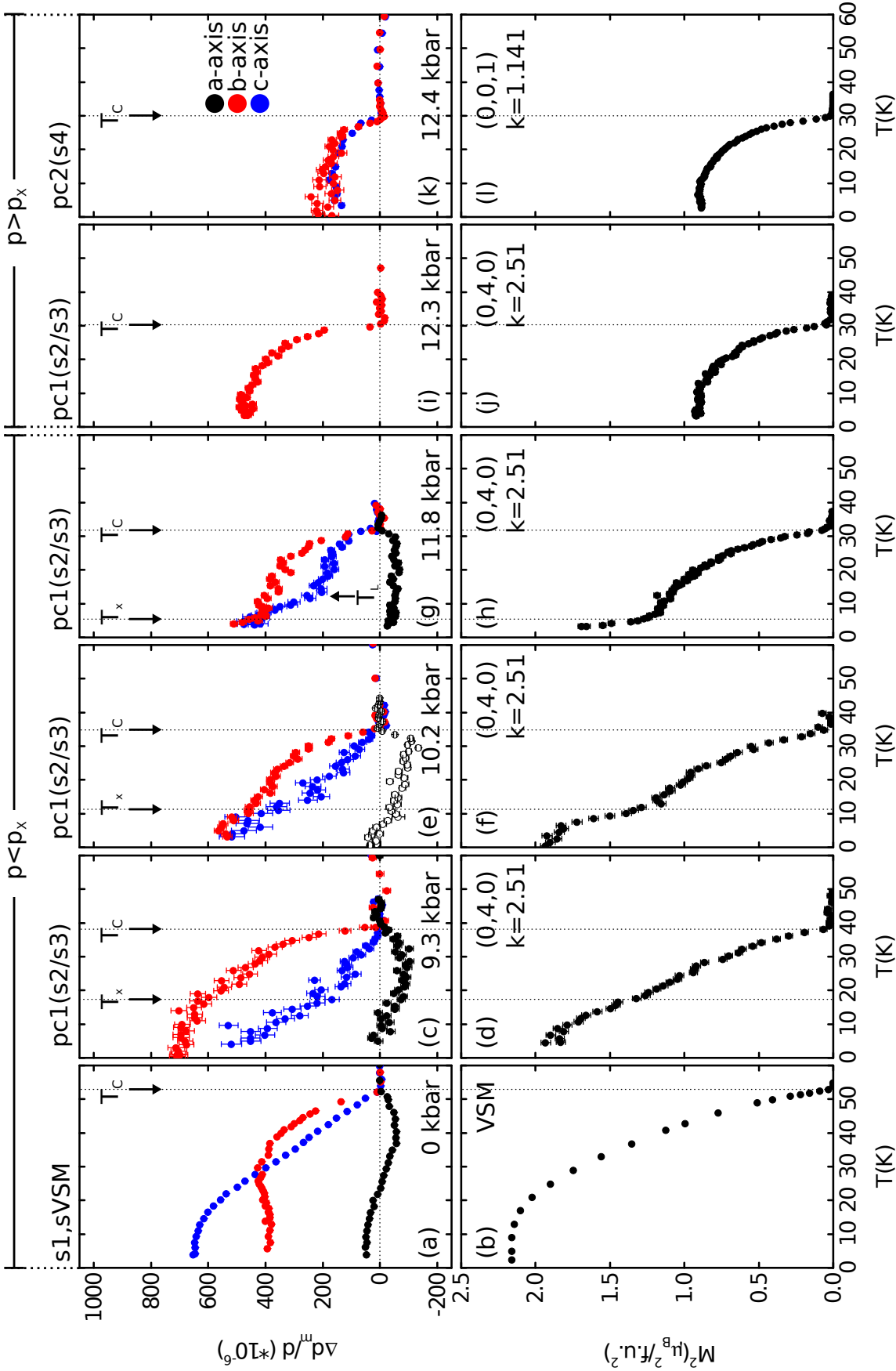


Figure 4.5: Comparison of $\Delta d_m/d(T)$ and $M^2(T)$ for all pressures measured. The transitions T_C and T_X in M^2 are indicated by dashed vertical lines. See text for details.

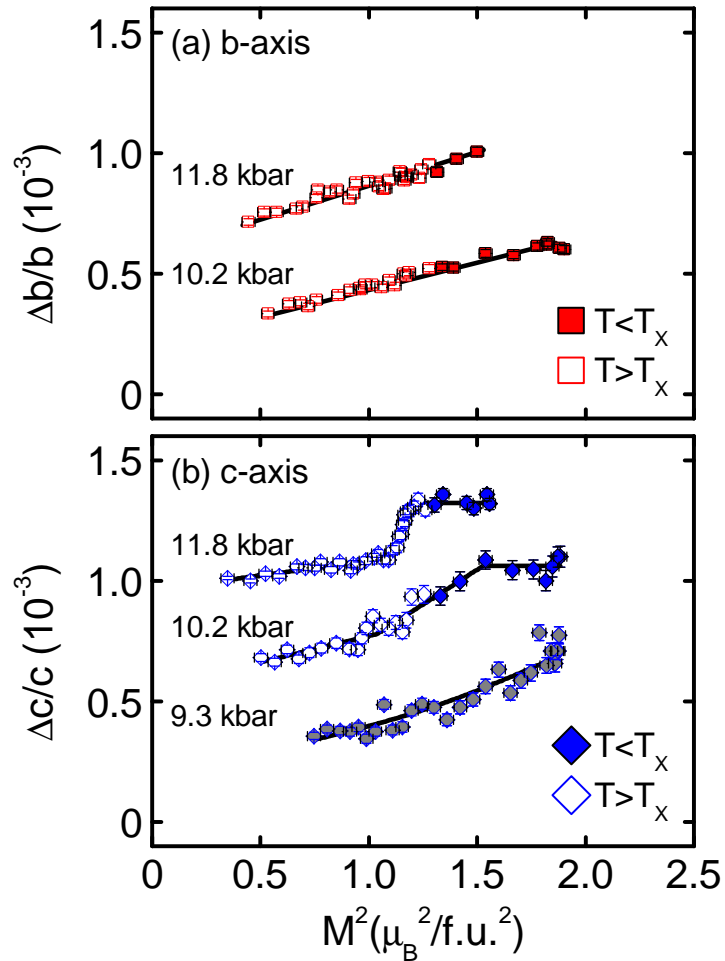


Figure 4.6: Thermal expansion $\Delta d/d$ versus the magnetization squared M^2 . (a) b -axis thermal expansion $\Delta b/b$ versus M^2 at 10.2 kbar and 11.8 kbar. Full and open symbols indicate datapoints below and above T_X determined from the magnetization, respectively. (b) c -axis thermal expansion $\Delta c/c$ versus M^2 at 9.3 kbar, 10.2 kbar, and 11.8 kbar. As the T_X transition is very broad at 9.3 kbar all symbols are shown gray at this pressure.

4.3 Discussion of the T_L transition

Our main result is summarized in the temperature-pressure phase diagram of UGe_2 in Fig. 4.7. Illustrated are the two ferromagnetic transitions T_C and T_X inferred from magnetization measurements of Ref. [93] (open green datapoints) together with T_C and T_X inferred from our magnetization measurements (full green datapoints) and thermal expansion data along the c -axis (blue datapoints), labeled T_L . It is important to note, that all T_X values in Fig. 4.7 were inferred from the raw Larmor diffraction data and hence are independent of spin-echo phase corrections or phonon part subtractions (see Fig. A.7). As known from the literature, T_C and T_X are suppressed to 0 under pressures of $p_c \approx 16$ kbar and $p_X \approx 12$ kbar. T_X is a crossover at low pressures and becomes a first order phase transition when approaching p_X . Around p_X , a superconducting dome emerges that has a maximum of the superconducting transition temperature T_{SC} at directly p_X . We find an additional transition T_L in the thermal expansion along the c -axis that lies several Kelvin above the T_X transition. With pressure approaching p_X , the difference $T_X - T_L$ increases, the transition at T_L becomes more pronounced and appears more and more as a jump in $\Delta c/c$ (see Fig. 4.6). Together, this marks T_L as a discrete transition which has a first order character close to p_X . In contrast to the a - and b -axis thermal expansion, the transitions in the c -axis do not coincide with transitions in the magnetization and thus cannot be accounted for by standard magnetostriction. Therefore, T_L has to originate from a different mechanism. To gain further insights of the mechanism driving the T_L transition, the relation between our findings and the scenarios proposed for the T_X transitions (see Sec. 2.2,p. 23) are discussed in the following.

The T_L transition and hence the finding of two transitions in the ferromagnetic phase in the vicinity of p_X is hard to reconcile with the first three scenarios discussed in Sec. 2.2: In scenario (i) the formation of a spin and charge density wave is proposed [107]. This implies the existence of a single temperature at which the SDW forms and not two. Besides, as discussed in Sec. 2.2 this scenario appears to be unlikely anyway. In scenario (ii) two almost degenerate ferromagnetic ground states are identified that differ in their orbital moment [108]. The T_X transition thus refers to the change from one to the other groundstate. Also here, two transitions in the ferromagnetic phase are hard to explain. In scenario (iii) it is shown that a double peak in the density of states can produce the transition at T_C and T_X [109]. A third transition at T_L can not be combined with this model in a simple manner.

Scenario (iv) and (v) both discuss the T_X transition in the context of a competition between Heisenberg and Kondo exchange interactions. Theoretical studies show that a breakdown of Kondo physics, where the shielding of local moments by conduction electrons suddenly ceases, can involve a drastic change of the topology of the Fermi surface, a so-called Lifshitz transition [147]. At a Lifshitz transition, the topology of the Fermi surface can change in two ways: Either the “neck” of the Fermi surface collapses, or a new split-off region of the Fermi surface appears/disappears (see Sec. 1.3). It is known that Lifshitz transitions can give sharp isotropic discontinuities in the thermal expansion [54, 148]. The fact that we observe this feature only in the c -axis and not concomitantly in the a -

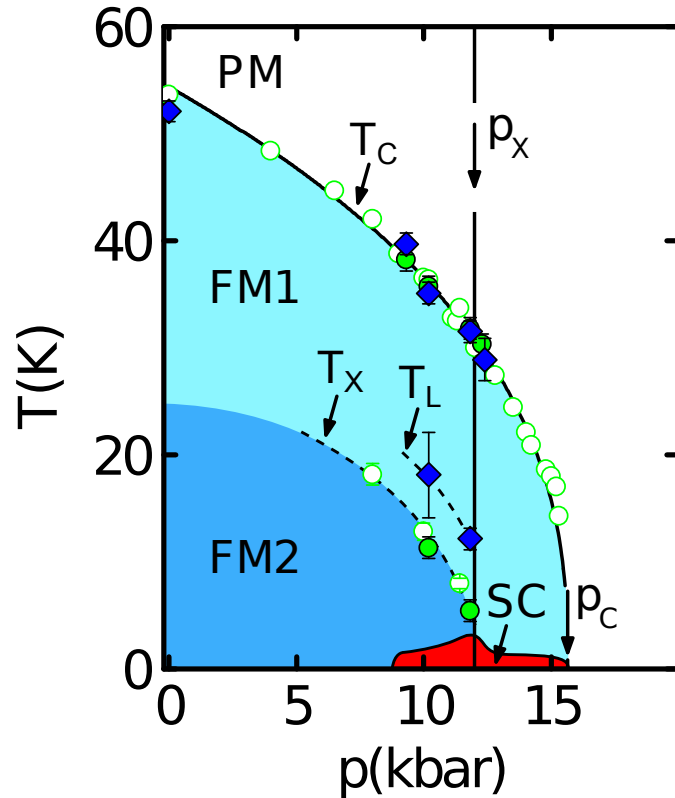


Figure 4.7: Temperature-pressure phase diagram of UGe_2 . Shown is T_C from magnetization measurements of Ref. [93] (\circ); T_C and T_X inferred from the magnetic peak intensity (\bullet); and T_C and T_X inferred from the thermal expansion measured with Larmor diffraction of the c -axis (\blacklozenge). The indicated superconducting region (red shading) follows the susceptibility data from Ref. [146]. The T_X transition in the c -axis lies several Kelvin above T_X in the magnetization and the a - and b -axis (not shown). The difference increases on approaching p_X .

and b -axis could be explained by a weak coupling of the crystal axes, i.e. a small Poisson ratio, as indicated by different sound velocities along the individual axes [144]. Furthermore, it is known from dHvA [94, 95] and Hall effect [86] measurements that the Fermi surface changes at T_X . Hackl and Vojta [147] showed that when the electronic degrees of freedom are coupled to the lattice degrees of freedom a Lifshitz transition is driven to first order and is accompanied by a discontinuous change in the volume. The dependence of the Kondo temperature T_K on the lattice parameters in combination with the Lifshitz transition can result in a second transition, as observed by us. This implies that if the T_L transition is indeed driven by a Lifshitz transition, it is in agreement with scenario (iv) and (v) where the T_X transition is explained through the sudden breakdown of the Kondo effect through an increasing ferromagnetic ordering of the unscreened local $5f$ moments when the temperature is lowered.

Considering the superconducting phase, the presence of a Lifshitz transition could lead to small Fermi surfaces that can indirectly promote superconducting pairing as discussed for UCoGe [149] and URhGe [58]. There, it is speculated that the presence of small Fermi surfaces could be important for the superconducting pairing mechanism since then the Fermi-wavevector can become of same magnitude as the short inverse-length scales of the magnetic correlations.

In conclusion, we find an additional transition T_L in the ferromagnetic phase of UGe₂ at pressures close to p_X that lies several Kelvin above the T_X transition in the magnetization. Comparison with the magnetization shows that T_L clearly has a non-magnetic origin. We speculate that T_L is the signature of a Lifshitz transition, i.e., a transition where the Fermi surface changes its topology. However, this is speculative so far and further experiments are required to proof this hypothesis. A Lifshitz transition at T_L can be reconciled with two scenarios proposed for the T_X transition in which T_X is attributed to the competition between Kondo and Heisenberg interaction. The finding of an additional, non-magnetic transition close to p_X shows that the phase diagram of UGe₂ is more complex than thought and that the superconducting pairing mechanism could be non-magnetic contrary to what has been discussed so far.

Part II

Skyrmions and the non-Fermi liquid puzzle of MnSi

The goal of this study was to investigate a possible connection between the magnetically non-trivial structure of the skyrmion lattice and the extended non-Fermi liquid (NFL) regime in the itinerant helimagnet MnSi. As method we chose simultaneous magnetoresistance and Hall effect measurements under pressure since the NFL behavior is characterized through an unusual temperature dependence of the resistivity and since the Hall effect shows distinct topological signatures in the presence of a skyrmion lattice. We find that indeed a topological Hall effect (THE) signal, signature of a nontrivial magnetic structure, survives the suppression of helimagnetic magnetic order with pressure and is observed inside the NFL state. The phase boundaries of NFL behavior and THE signal coincide suggesting skyrmionic textures as origin for the extended NFL behavior.

To set the stage for the new magnetoresistance and Hall effect data, acquired during this thesis, Secs. 5.1 and 5.2 will briefly introduce the basics about the itinerant helimagnet MnSi and summarize the current state of knowledge. Our results are presented and discussed in Chaps. 7 to 10 which closely follow our corresponding publications in Refs. [16] and [53],

Chapter 5

The helimagnet MnSi

5.1 MnSi at ambient pressure

MnSi is a weakly-magnetic itinerant electron system with a helical magnetic structure below an ordering temperature $T_c \approx 29.5$ K. The helical arrangement of the electron spins is due to three hierarchically ordered energy scales. (i) On the largest scale ferromagnetic exchange tends to align the electron spins parallel to each other. (ii) Since MnSi crystallizes in the non-centrosymmetric cubic B20 structure (space group $P2_13$) without inversion symmetry, a Dzyaloshinskii-Moriya interaction arises that tends to align the electron spins orthogonal to each other. The result of (i) and (ii) is a helical modulation of the electron spins with propagation length $\lambda_{helix} (T \rightarrow 0) \approx 180$ Å. The helices are pinned along the cubic space diagonal $\langle 111 \rangle$ due to magnetic anisotropies by higher order spin-orbit coupling [150].

This leads to the magnetic field-temperature phase diagram shown in Fig. 5.1. At temperatures below T_c two transitions are observed under magnetic field. Coming from the helical state at low magnetic fields, at $B_{c1} \approx 0.1$ T the propagation direction of the magnetic helices unpins from the $\langle 111 \rangle$ direction and aligns parallel to the applied magnetic field. The individual electron spins in the helix orient themselves more and more into the direction of the applied magnetic field forming a conical structure. The resulting phase is called conical phase. Depending on the field direction the transition at B_{c1} is a crossover or a symmetry breaking 2nd order phase transition. At $B_{c2} \approx 0.6$ T the magnetic structure makes a transition from the conical phase to a field polarized ferromagnetic state [151–153].

In a small phase pocket below T_c , called A-phase for historical reasons [152], the magnetic structure forms a lattice of magnetic whirls called skyrmions that is energetically stabilized through thermal fluctuations [15, 154–156]. A magnetic skyrmion is a whirl of the magnetization with a non-zero topological winding number (see Sec. 5.1.1). In MnSi those magnetic whirls consists of the superposition of three helices in a plane perpendicular to the applied magnetic field where the \vec{q} -vectors of the helices are oriented under an angle of 120° to each other. The skyrmions are arranged in a hexagonal lattice in a plane perpendicular to the applied magnetic field. Each skyrmion carries one quantum of emer-

gent flux per magnetic unit cell. In the direction parallel to the applied magnetic field the skyrmion lattice is translation invariant and forms so called skyrmions tubes analogous to vortex lines in type II superconductors (see Fig. 5.2). The skyrmion lattice is a generic feature of all helimagnetic B20 compounds ranging from high purity metals [154, 157] to semiconductors [158, 159] and insulators [160, 161].

The two most prominent experimental signatures of the skyrmion lattice in MnSi are a scattering pattern with six-fold-symmetry observed in small angle neutron scattering (SANS) [154, 155] and a topological Hall signal [15, 162] where the latter is of central interest for this thesis and will be discussed in Secs. 6.2.3 and 6.2.5 in detail. The topological Hall effect signal in MnSi shows up as a top-hat shaped signature that appears on top of the anomalous Hall effect signal (see Fig.6.7 c and d (p. 102)). It is caused by Berry phases that the conduction electrons pick up during their motion through the topologically non-trivial structure of the skyrmion lattice. The size of $4.5 \text{ n}\Omega\text{cm}$ reflects the density and the winding number of the skyrmion lattice in MnSi.

Under d.c. currents the skyrmion lattice in MnSi depins and begins to drift. The depinning transition can be observed at exceptionally low current densities of $j_c \approx 1 \text{ MA/m}^2$ that are five orders of magnitude smaller than observed in conventional spin transfer torque experiments [51, 52]. This is due to the very efficient gyromagnetic coupling of the electron spins to the magnetic structure via the Berry phases which also cause the topological Hall effect signal. As each skyrmion carries a quantum of magnetic flux, an emergent electric field is induced when the skyrmion lattice moves, following Faraday's law of induction [163]. Through the Hall effect, the emerging electric field can be directly measured and hence the motion of the skyrmions can be detected quantitatively. This direct control and quantitative detection of the motion of a magnetic structure combined with the depinning at ultra-low current densities promises to be interesting for spintronic devices like, e.g., racetrack memories.

5.1.1 More about skyrmions

Skyrmions are topologically stable field configurations that possess particle-like properties [154]. They are named after the particle physicist Tony Skyrme who developed a theory describing pions as topological solitons in the 1960s [165, 166]. Schematically a skyrmion can be depicted as the stereographic projection of a hairy ball or hedgehog who has been combed, where in our case the "hairs" consist of magnetic moments (Fig. 5.3). According to the hairy ball theorem [167, 168] the combing introduces vortices at the poles where then one vortex is projected into the center of the skyrmion and one on the rim. The resulting structure is topologically non-trivial in that it has a integer non-zero winding number which can be calculated through the integral

$$W = \frac{1}{4\pi} \int d^2r \hat{M} \left(\partial_x \hat{M} \times \partial_y \hat{M} \right). \quad (5.1)$$

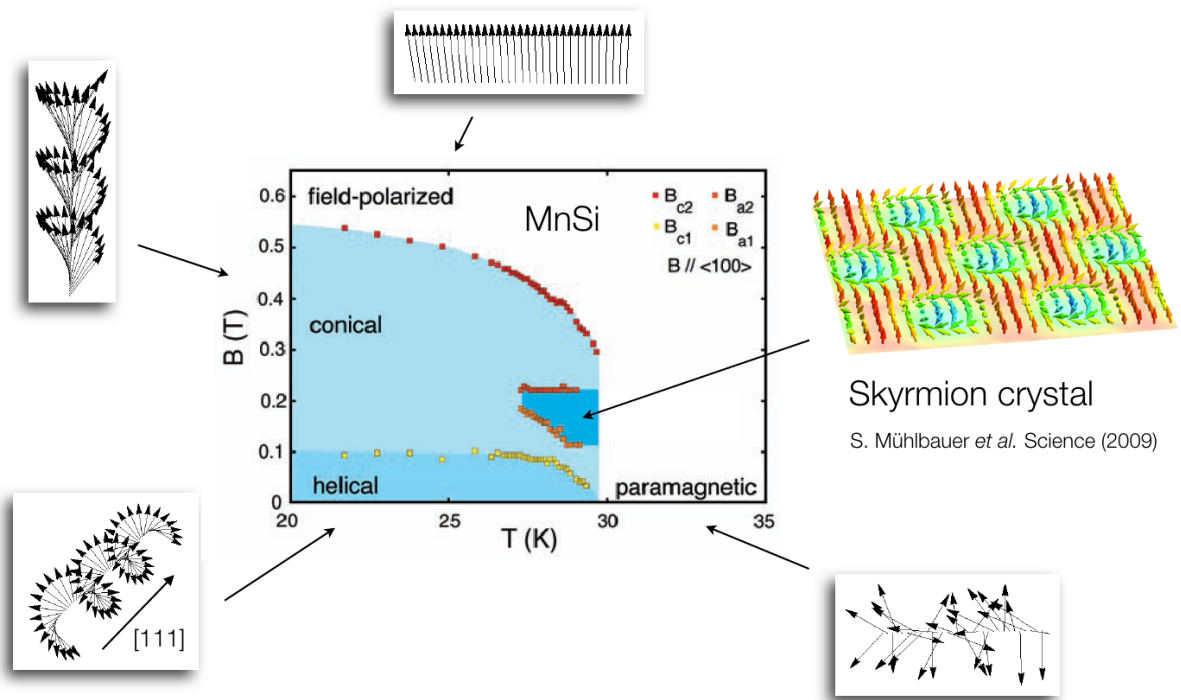


Figure 5.1: Magnetic field-temperature phase diagram of MnSi. The small illustrations around the phase diagram depict schematically the magnetic structure of the individual phases where arrows represent electron spins. Figure from [154, 164].

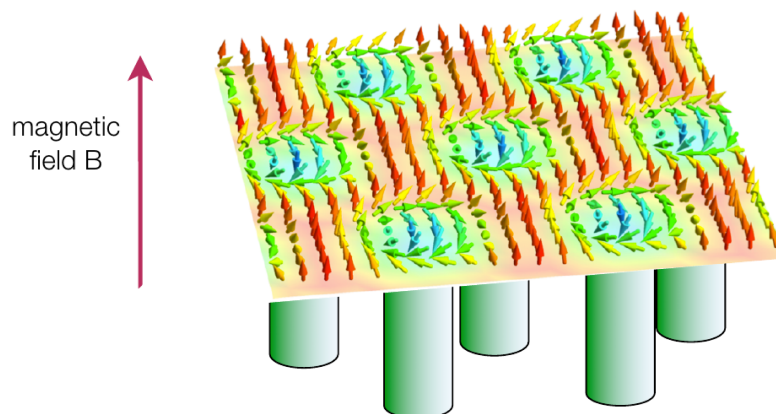


Figure 5.2: Schematic real space image of a skyrmion lattice. The skyrmions form in a plane perpendicular to the applied magnetic field. The skyrmions are arranged in a hexagonal lattice and propagate as skyrmion tubes in the direction parallel to the applied magnetic field, analogous to vortex lines in type II superconductors. Figure from [164].

In general, a structure cannot be continuously transformed in an object with a different winding number. Thus, a skyrmion is a topologically protected structure and stable against external influences until it is ultimately destroyed.

In the itinerant helimagnet MnSi the skyrmions are formed as whirls of the magnetization on top of a ferromagnetic background. Here, each whirl consists of the superposition of three helices that are oriented under an angle of 120° to each other. The skyrmions arrange themselves periodically in a hexagonal lattice in a plane perpendicular to the applied magnetic field (Fig. 5.4). In the direction parallel to the applied magnetic field the skyrmion lattice is translation invariant and forms so called skyrmions tubes analogous to vortex lines in type II superconductors (Fig. 5.2). The skyrmion density can be calculated as

$$\Phi^\mu = \frac{1}{8\pi} \epsilon_{\mu\nu\lambda} \hat{n} \cdot (\partial_\nu \hat{n} \times \partial_\lambda \hat{n}) \quad (5.2)$$

with the antisymmetric unit tensor $\epsilon_{\mu\nu\lambda}$ and $\hat{n} = \vec{M}/|M|$ [15, 169]. The integral of Φ^μ for each 2-dimensional magnetic unit cell is a measure for the winding number. In MnSi $\int dx dy \Phi^z = -1$, i.e., strictly speaking it is a lattice of anti-skyrmions where the magnetic moments in the center point in the opposite direction as the magnetic moments on the rim. As mentioned above, the skyrmion lattice can not be continuously transformed in a magnetic structure with a different winding number. Hence, the skyrmion lattice phase is separated from the conical state, which is topologically trivial and has a winding number zero, through a first order phase transition.

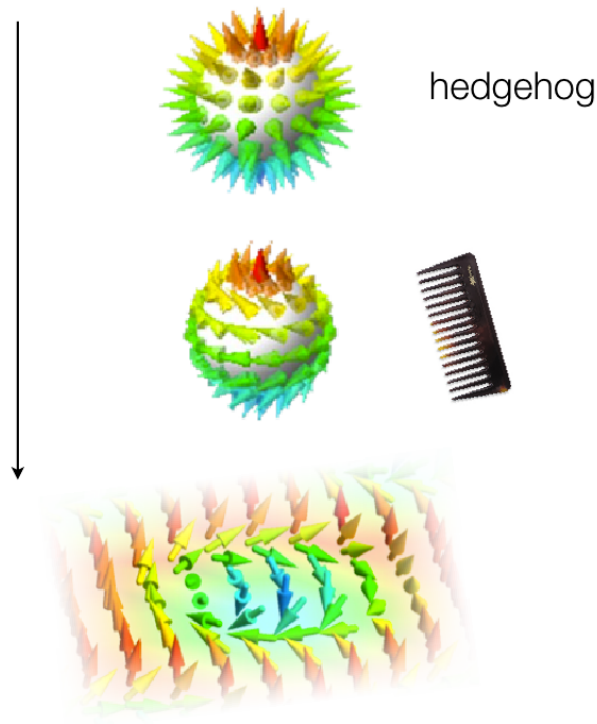


Figure 5.3: From a hedgehog to a skyrmion. A skyrmion can be depicted as stereographic projection of a combed hairy ball or hedgehog on a 2D plane. In our case the “hairs” represent magnetic moments. See text for details. Figure from [164].

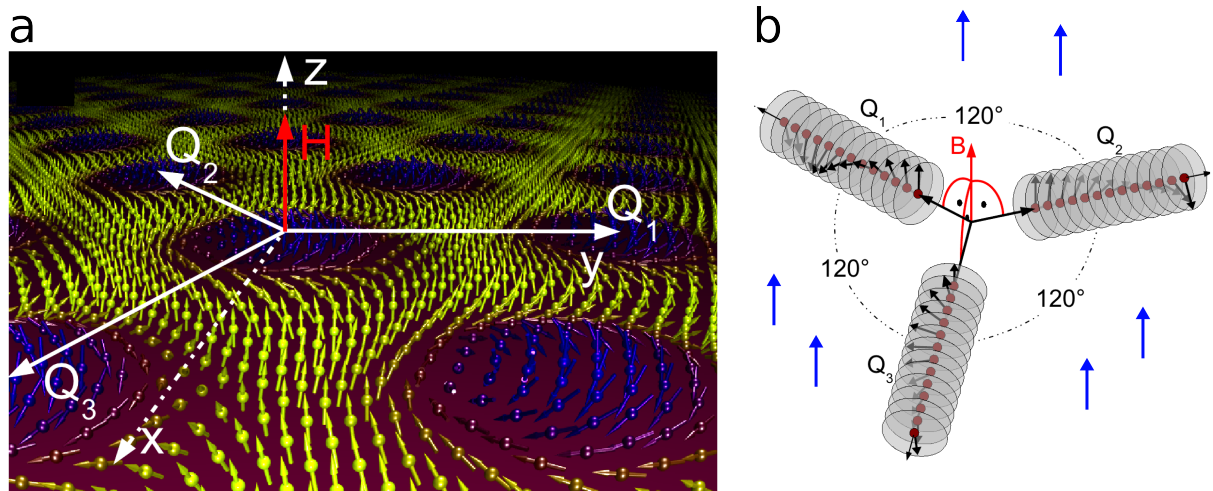


Figure 5.4: Skyrmion through superposition of helices. (a) Real space image of a skyrmion lattice which forms in a plane perpendicular to the applied magnetic field H . The vectors Q_1 , Q_2 , and Q_3 represent the propagation vectors of the three helices which form the indicated skyrmion. (b) Schematic image of the superposition of three helices in a plane under an angle of 120° to each other. Blue arrows indicate the ferromagnetic background. Figure from [170].

5.2 MnSi under hydrostatic pressure

Under hydrostatic pressure the phase diagram shown in Fig. 5.5a arises. The magnetic transition temperature T_c is shifted to lower temperatures with increasing pressure and is suppressed at a critical pressure $p_c \approx 14.6$ kbar [171, 172]. The transition at T_c becomes first order above $p^* \approx 12$ kbar, where T_c is already suppressed to $T^* \approx 12$ K, which can be seen, e.g., through a metamagnetic transition under applied magnetic field [74, 173, 174]. Therefore, the phase diagram of MnSi displays the tri-critical wings that are generically observed in ferromagnets in the vicinity of the critical pressure (cf Figs. 1.3c and 5.6d). In the ordered phase (light blue shading) MnSi follows the predictions of the Fermi liquid theory, the fundamental theory for metals at low temperatures, and can be described as a weakly spin-polarized ferromagnet¹ through an Ginzburg Landau theory accounting for the effects of spin fluctuations [14, 175].

In the pressure range $p^* < p < p_c$ a phase separation of the magnetic order is observed in NMR [36] and μ SR [176] experiments (dark blue shading) where one volume fraction tracks T_c as inferred from resistivity and susceptibility data. Above p_c , at temperatures below $T^* \approx 12$ K an extended non-Fermi liquid (NFL) regime with an unusual $T^{3/2}$ temperature dependence of the resistivity is observed down to the low mK range that extends up to at least $3 \times p_c$ (light green shading) [9, 10, 13, 177]. The exponent of the temperature dependence of the resistivity changes abruptly from the Fermi liquid value 2 to the non-Fermi liquid value 3/2 at the critical pressure p_c (Fig. 5.6 a). Through applying a magnetic field the Fermi liquid exponent can be recovered (Fig. 5.6 b). Above 48 kbar the exponent of the temperature dependence increases again from 1.5 [13]. The characteristic fields B_{c1} and B_{c2} do not change under pressure and survive even above p_c [178]. This indicates that the energy scales, ferromagnetism and Dzyaloshinskii-Moriya interaction, do not change with pressure.

In the pressure range $p_c < p < p_0 \approx 21$ kbar below a temperature T_0 , a smeared out scattering intensity in elastic neutron scattering emerges on a sphere in reciprocal space at the wavelength of the helical modulation (dark green shading) [50]. The broad scattering intensity above p_c is observed in $\langle 110 \rangle$ direction whereas below p_c the helices are pinned along the $\langle 111 \rangle$ direction (Fig. 5.5b and c). This implies that the helices survive above p_c into the NFL region but have lost their directional long-range order. In analogy to liquid crystals this is called partial order. Since above p_c a magnetic signal can be observed in neutron scattering [50] and NMR [36] experiments whereas no magnetic signal is observed in μ SR experiments [176] which probes slower timescales, this suggests that the magnetic moments are static on timescales between 10^{-10} s and 10^{-11} s. The temperature T_0 below which the partial order is observed represents a freezing temperature below which the fluctuations of the partial order become slow enough to be observed by elastic neutron scattering and NMR [67]. Since T_0 extrapolates to 0 at $p_0 \approx 21$ kbar a quantum critical point was suspected at p_0 . However, thermal expansion measurements under pressure performed by means of Larmor diffraction [49] could neither find a sign change in the Grüneisen parameter, that is expected at a pressure controlled quantum critical point

¹Since the helix length is comparatively long the magnetic structure locally resembles a ferromagnet.

(QCP) [120], at p_0 nor at p_c . Thus, neither p_c nor p_0 can be associated with a QCP.

Considering the experimental evidence, the NFL behavior observed in MnSi is remarkable in that it is in conflict with the present knowledge about normal metals [68,179]: On the one hand, a $T^{3/2}$ dependence of the resistivity has been observed in spin glasses and amorphous ferromagnets and can be explained through a diffusive motion of the charge carriers on length scales substantially larger than the mean free path [9,180,181]. However, this scenario is unrealistic considering the high-quality MnSi single crystals investigated and the extended temperature range in which the NFL behavior is observed. On the other hand, Fermi liquid theory is known to break down in the vicinity of QCPs where critical soft modes couple to the electron density. However, also this picture cannot explain the experimental observations. First, no QCP is found in MnSi at p_c and p_0 . Second, the NFL behavior extends over a very large pressure range, so that even if there would be a QCP, e.g. under field tuning, most of the NFL behavior would be far away from it. Third, T_c at low temperatures is first order, so that no critical soft modes are expected at this transition.

Theoretical models consider topological spin textures as origin for the partial order including an amorphous skyrmion ground state [179], short-ranged helical order [182] or periodic arrangement of double twist cylinders [183] both reminiscent of blue phases in liquid crystals and columnar fluctuations possibly realized in skyrmion lines [68]. It is speculated that these topological spin textures could be related to the NFL behavior. However, so far no experimental evidence has been reported for topologically spin textures in the NFL regime.

With the Hall effect measurements reported and discussed in Chaps. 7 to 10 and in our publications [16] and [53] we are able to present the first experimental evidence of topologically non-trivial spin textures in the NFL regime of MnSi. We are also able to directly link the topological Hall signal we observe at pressures $> p_c$ to the topological Hall signal caused by the skyrmion lattice at ambient pressure. We find that the boundaries of the NFL behavior and the topological Hall signal in the phase diagram coincide. This implies that the NFL behavior in MnSi is intimately linked to topologically non-trivial spin textures.

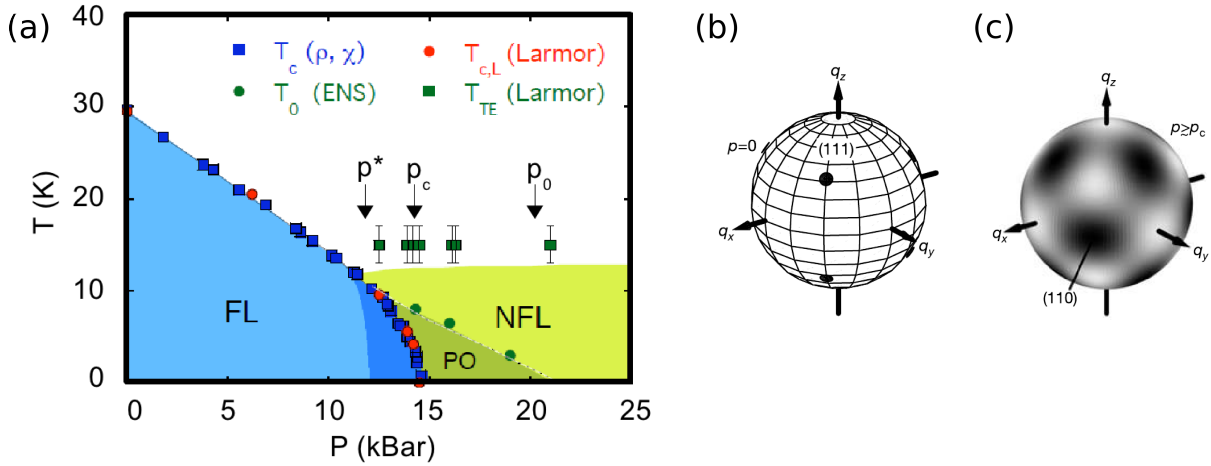


Figure 5.5: MnSi under pressure. (a) Temperature-pressure-phase diagram of MnSi as reported in [49]. The helical order in which MnSi shows a typical Fermi liquid (FL) behavior (light blue) is suppressed with pressure and vanishes at the critical pressure $p_c \approx 14.6$ kbar. Above a pressure $p^* \approx 12$ kbar a phase separation is observed in NMR [36] and μ SR [176] experiments (dark blue shading) where one volume fraction tracks T_c as inferred from resistivity, susceptibility and Larmor diffraction data [10, 49, 74, 173, 184, 185]. At higher pressures an extended non-Fermi liquid regime arises (light green) [9, 10, 13] up to a crossover temperature that can, e.g., be seen in Larmor diffraction as T_{TE} [49]. In a small region above p_c a partial magnetic order is observed up to $p_0 \approx 21$ kbar (dark green) where a broad scattering intensity along the $\langle 110 \rangle$ directions is observed in elastic neutron scattering (ENS) below a temperature T_0 (panel (c)) as opposed to the sharp scattering intensity observed along the $\langle 111 \rangle$ directions in the helical order (panel (b)) [50].

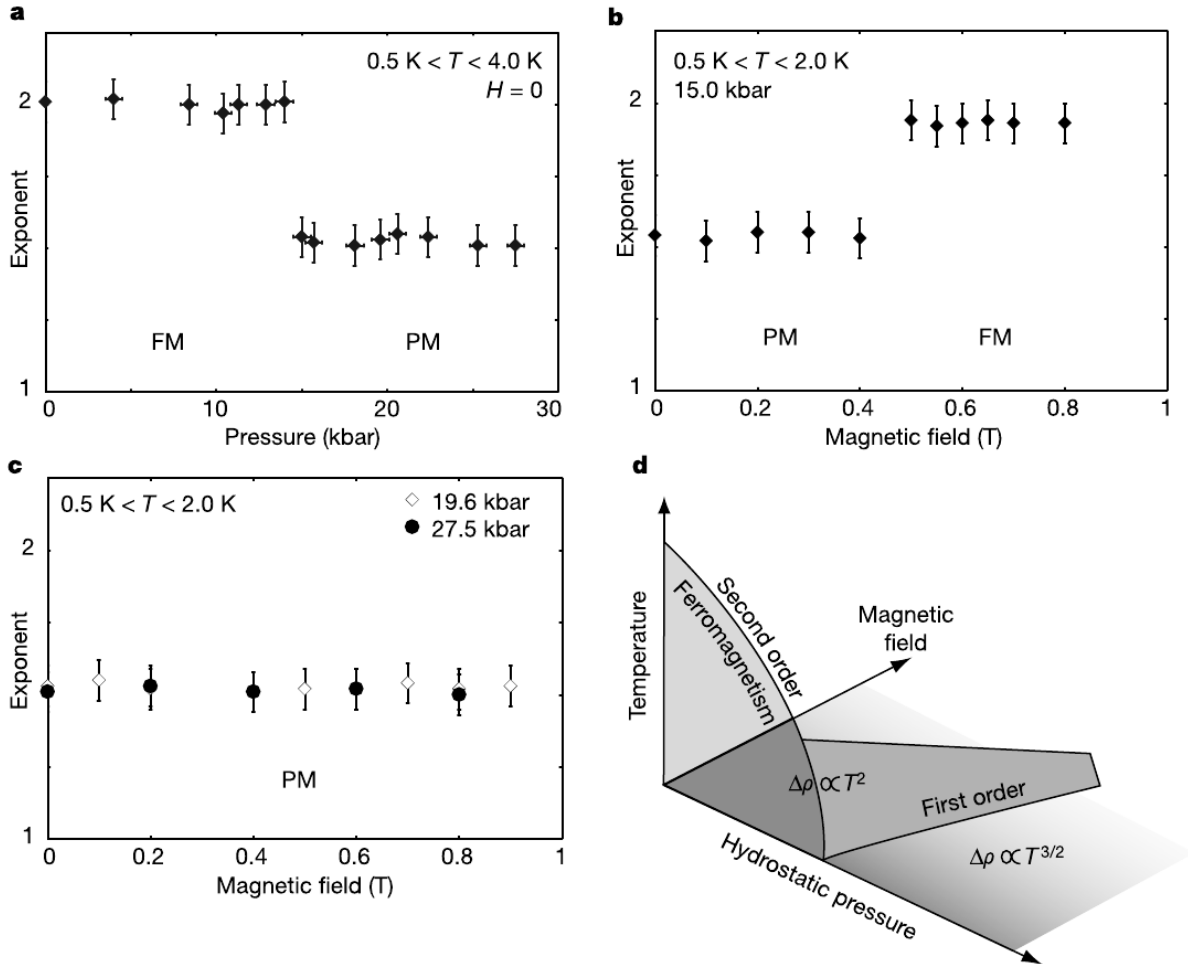


Figure 5.6: Non-Fermi liquid behavior in MnSi. (a) At the critical pressure the temperature exponent of the resistivity changes abruptly from the Fermi liquid value 2 to the non-Fermi liquid value $3/2$. (b) Under magnetic field the Fermi liquid exponent can be recovered, like shown here at ≈ 0.5 T at 15 kbar. (c) At higher pressures fields exceeding 1 T are needed to recover the Fermi liquid exponent. (d) Schematic temperature-pressure-magnetic field phase diagram of MnSi. Figure from [10].

Chapter 6

Experimental methods

6.1 Resistivity of metals at low temperatures

The electrical resistivity of metals is determined by the present scattering mechanisms through which the electron motion is disturbed. Scattering mechanisms include the interaction of electrons with excitations like phonons or magnons, defects in the crystalline lattice, and other electrons. Each scattering mechanism leads to a characteristic temperature dependence of the resistivity ρ . If several scattering mechanisms are present, their contributions to the total resistivity can be summed up according to Matthiessens rule $\rho_{total} = \rho_0 + \rho_{\text{phon.}} + \rho_{\text{el.-el.}} + \dots$, given that they are independent from each other.

The three most common forms of resistivity curves are illustrated in Fig. 6.1a: (1) The resistivity drops to a minimum and increases again logarithmically on cooling due to the Kondo effect. There, electrons scatter on screened local moments that form at low temperatures. (2) The resistivity drops continuously and converges against a residual resistivity ρ_0 . (3) On cooling, the resistivity drops discontinuously to zero at a critical temperature below which the material is superconducting. In this section scenario (2) will be discussed for non-magnetic (Sec. 6.1.1) and ferromagnetic (Sec. 6.1.2) metals summarizing the most important scattering mechanisms together with their temperature dependences. This is followed by a brief introduction on the magnetic field dependence of the resistivity, the so-called magnetoresistance in Sec. 6.1.3. Sec. 6.1.4 then discusses the resistivity and magnetoresistance of MnSi. More information about the resistivity of metals and magnetoresistive effects can, e.g., be found in Ref. [186].

6.1.1 Non-magnetic metals

In non-magnetic metals electrons are mainly scattered due to (i) defects in the crystal lattice, (ii) phonons, and (iii) electron-electron interactions. In the following the three contributions will be briefly discussed.

(i) Defects in the crystal lattice lead to a temperature independent contribution to the resistivity. At very low temperatures when other contributions become small, the resis-

tivity converges against a so-called residual resistivity ρ_0 . The ratio $\rho(300\text{ K})/\rho(T \rightarrow 0)$, the so-called residual resistivity ratio (RRR), is used as measure for the crystalline quality.

(ii) The phononic contribution to the resistivity depends on the considered temperature range. For $T \gg \Theta$ (Θ : Debye temperature) $\rho \propto T$ as all phonon states are occupied up to the Debye frequency ω_D and as the number of phonons per state are proportional to $k_B T$. For $T \ll \Theta$ one has to consider the occupied phonon states and a weighting factor that takes into account that at low temperatures only small scattering angles are possible due to the small momentum of the phonons. In total this yields $\rho \propto T^5$.

(iii) Electron-electron scattering gives a contribution $\rho \propto T^2$ due to simple phase-space arguments for electron energies close to the Fermi level in the independent electron approximation. The contribution from electron-electron scattering is small and can only be observed at low temperatures in clean samples where contributions from phonons and defects are negligible. According to the principle of adiabatic continuity stated in the Fermi-liquid theory, the predictions of the independent electron picture remain valid even when interactions between electrons become large. This is achieved through considering quasiparticles with a renormalized mass in place of electrons (see Sec. 1.4). The quasiparticle-quasiparticle scattering also yields a contribution $\rho \propto T^2$. In the rare cases where the Fermi liquid theory breaks down one talks about a non-Fermi liquid. Deviations from the Fermi liquid theory can be probed by tracking the temperature exponent α of the resistivity. For non-Fermi liquid behavior $\alpha \neq 2$.

6.1.2 Ferromagnetic metals

In addition to the scattering mechanisms present in non-magnetic metals, new behavior related to the electron spins arises in magnetic metals. In particular, in ferromagnetic transition metals the resistance below the Curie temperature T_C is usually lower than expected. At the Curie temperature T_C the resistance shows a characteristic decrease since the spin disorder and with it a scattering mechanism freezes out. In a simple scenario for band-ferromagnets, the majority d -band is shifted below the Fermi energy so that the s -electrons, that mainly carry the current, have less d -states in which they can scatter. Hence, the resistance drops (see Fig. 6.1b and c). This effect is called the negative magnetoresistance. From the change of slope in $\rho(T)$ the Curie temperature T_C can be determined.

At very low temperatures the electron-magnon scattering leads to a $\rho \propto T^2$ dependence of the resistivity as the number of magnons scales with $T^{3/2}$ and since $k_{\text{magnon}} \propto T^{1/2}$ due to the quadratic dispersion relation of magnons. Fig. 6.1d schematically shows the temperature dependent resistivity of a ferromagnetic metal with a drop at T_C and a $\rho \propto T^2$ behavior at low temperatures.

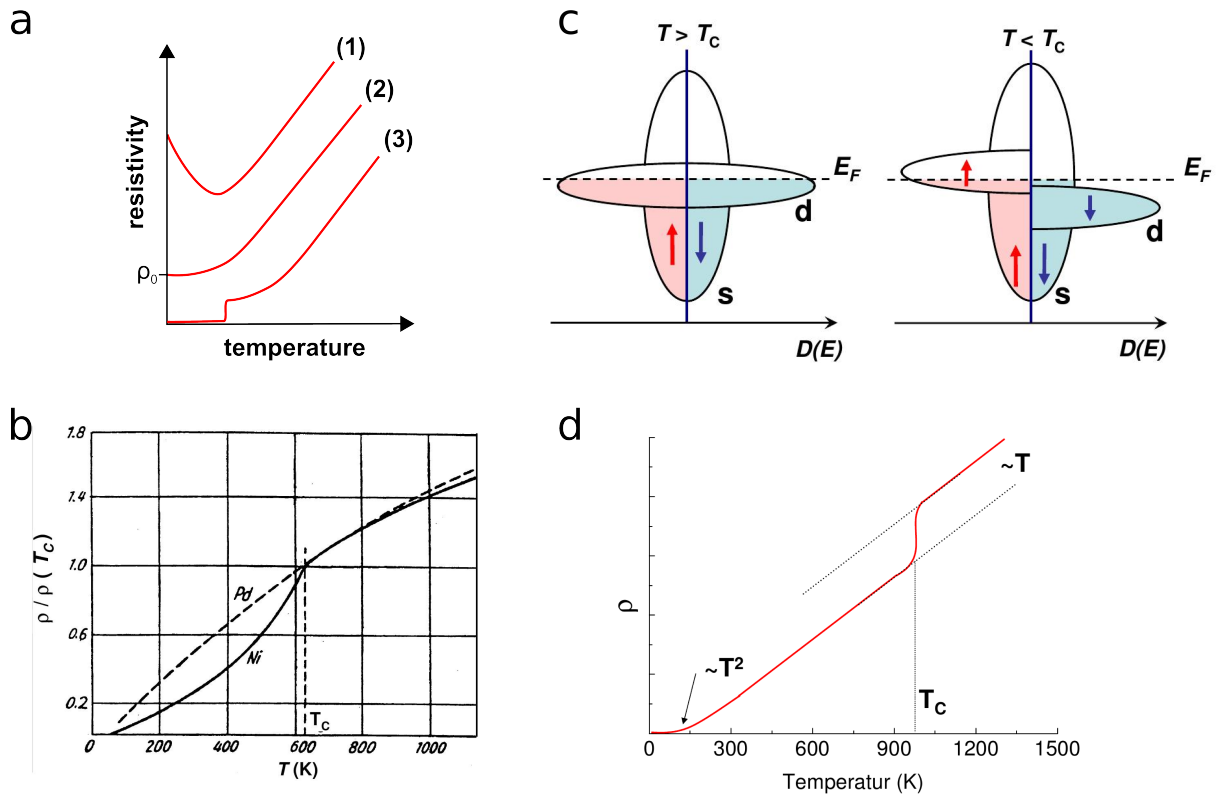


Figure 6.1: Resistivity of metals at low temperatures. (a) Schematic resistivity curves of metals showing (1) a Kondo effect at low temperatures, (2) the resistivity converging against the residual resistivity ρ_0 , and (3) a superconducting transition at low temperatures. (b) Resistance of Ni and Pd normalized to $\rho(T_C)$ (Coles, 1958). The electronic structure of the non-magnetic Pd resembles that of the ferromagnetic Ni. However, the resistance of Ni below T_C drops faster with decreasing temperature than that of Pd. At T_C the resistance of Ni shows a change of slope. (c) Below T_C the majority d-band is shifted below the Fermi energy E_F . (d) Typical resistivity curve of a ferromagnetic metal. Figures in (b),(c),(d) from Ref. [186].

6.1.3 Magnetoresistance

The resistivity of a material also shows a characteristic behavior when a magnetic field is applied. The simplest effect of the magnetic field is that the electrons are subject to a Lorentz force and move along curved trajectories. The effective path length between two scattering events increases and hence the overall resistance increases. This effect is called the positive magnetoresistance. When a phase transition into an ordered state, like the transition from a paramagnet into a ferromagnet, is crossed under an applied magnetic field, the magnetoresistance shows a change of slope as a scattering mechanism “freezes” out. This change of slope can be used to determine phase transition field values. Numerous magnetoresistance effects are known up to date, where an applied magnetic field changes the resistance of magnetic and non-magnetic conductors in bulk samples or heterostructures. In this thesis the magnetoresistance was only used to infer phase transition fields (see below). Therefore, we refer to the literature for more information about magnetoresistive effects (cf e.g. [186]).

6.1.4 Resistivity and magnetoresistance of MnSi

A typical example for the resistivity of MnSi below the critical pressure p_c is illustrated in Fig. 6.2. The resistivity has a characteristic drop at the transition T_c from the paramagnetic into the helimagnetic phase. In this thesis, we used the resulting maximum in $d\rho/dT(T)$ to infer the transition temperature T_c (see Fig. 6.16 (p.116)). At low temperatures Fermi liquid behavior with $\rho \propto T^2$ is observed. As was already discussed in Sec. 5.2, a non-Fermi liquid behavior with $\alpha = 3/2$ that extends over a wide region of the temperature-pressure phase diagram is observed in MnSi at pressures above p_c .

Fig. 6.3 shows the normalized magnetoresistance $\rho_{xx}(B)/\rho_{xx}(B=0)$ of MnSi up to 9 T between 10 K and 292 K (see also 6.6(b)). Below room temperature, MnSi shows a negative magnetoresistance. At temperatures below T_c the magnetoresistance shows distinct changes of slope at the transition fields B_{c1} and B_{c2} . The strongest suppression of the resistance ($\approx 50\%$ up to 9 T) is observed around $T_c \approx 29.5$ K. This implies that the resistance is dominated by magnetic fluctuations which are softest around T_c [187]. In our field dependent experiments we measured the magnetoresistance supplementary to the Hall effect and used the data to infer phase transition fields of MnSi. We tracked the magnetoresistance through measuring the voltage between the longitudinal contacts U_l in the typical Hall effect experiment geometry (Fig. 6.9 (p.105)) where the applied magnetic field is aligned orthogonal to the current direction. The magnetoresistance measured in this geometry is called the transverse magnetoresistance.

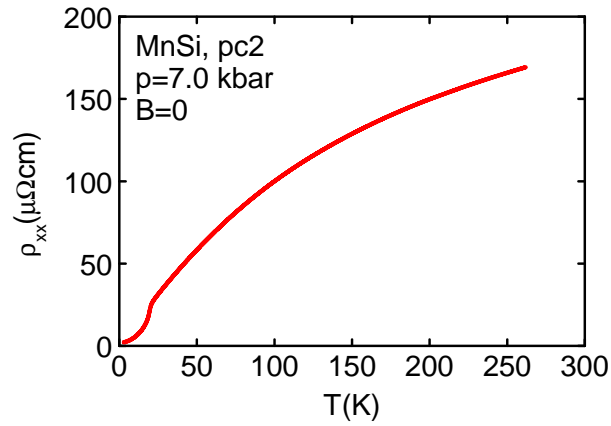


Figure 6.2: Resistivity of MnSi at 7.0 kbar.

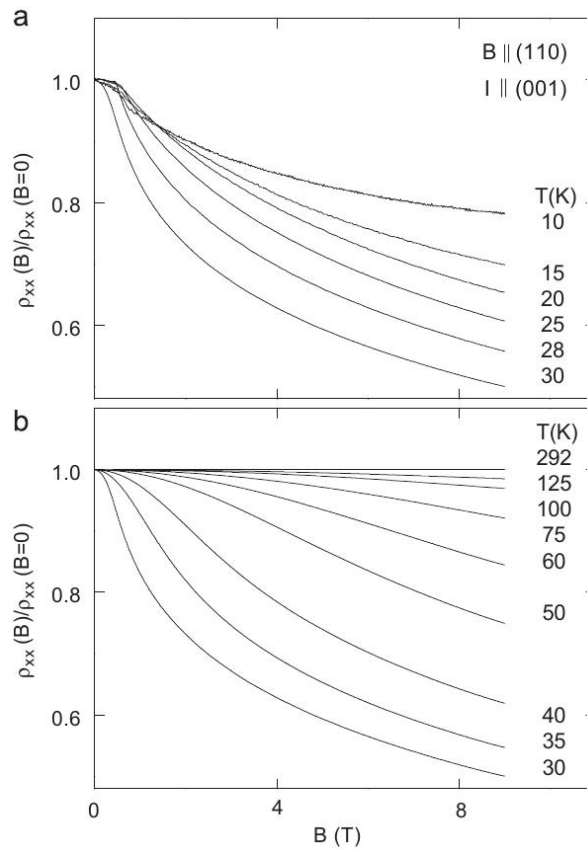


Figure 6.3: Magnetoresistance of MnSi. Normalized magnetoresistance $\rho_{xx}(B)/\rho_{xx}(B=0)$ of MnSi up to 9 T between 10 K and 292 K. See text for details. Figure from [187].

6.2 Hall effect

The Hall effect describes the appearance of a transverse voltage in a current-carrying conductor placed in a magnetic field. In the simplest scenario of a non-magnetic conductor, charge carriers are deflected due to a Lorentz force and accumulate on one side of the sample leading to a so-called Hall voltage that scales with the applied magnetic field, the charge carrier concentration, and a constant which is sensitive to the detailed band structure. In addition to this simple case discovered by Hall in 1879 [188] called the ordinary or the normal Hall effect (NHE) other mechanisms leading to a Hall effect have been identified during the past century. Here, we concentrate on Hall effect contributions observed in 3 dimensional magnetic metals. In ferromagnets like e.g. Fe, Ni, and Co an additional contribution to the Hall effect arises which scales with the magnetization. This contribution is called the anomalous Hall effect (AHE) [189]. Recently, a new type of Hall effect sensitive to the topology of non-coplanar spin structures was found. This so-called topological Hall effect (THE) was, e.g., identified in experiments on the frustration driven spin structure in 3D pyrochlore lattices and the skyrmion lattice in MnSi [15, 162, 169, 190, 191].

This section gives a short overview of basic concepts behind the NHE, the AHE, and the THE. Since one goal of this thesis was to study the evolution of the THE in the skyrmion lattice phase (A-phase) of MnSi under pressure, Sec. 6.2.5 describes the Hall effect features of MnSi known so far.

6.2.1 General remarks

Nomenclature

In a typical geometry of a Hall effect experiment, illustrated in Fig. 6.4, current is applied along the long side of a platelet shaped sample labeled x -direction. The magnetic field is applied perpendicular to the platelet along the z -direction. There, the longitudinal (magneto-)resistance ρ_l is labeled as ρ_{xx} and the transverse (Hall) resistance ρ_H as ρ_{xy} . Likewise, the conductivities are labeled σ_{xx} and σ_{xy} . Considering the tensorial relation between $\overset{\leftrightarrow}{\sigma}$ and $\overset{\leftrightarrow}{\rho}$ in two dimensions the Hall conductivity σ_{xy} can be expressed through ρ_{xx} and ρ_{xy} as

$$\sigma_{xy} = -\frac{\rho_{xy}}{\rho_{xx}^2 + \rho_{xy}^2} \approx -\frac{\rho_{xy}}{\rho_{xx}^2} \quad (6.1)$$

where the relation $\rho_{xy} = -\rho_{yx}$ and $\rho_{xx} = \rho_{yy}$ for isotropic materials was used (see e.g. [192]). Here, ρ_{xy}^2 can be neglected in the denominator when $\rho_{xx} \gg \rho_{xy}$ (like it is the case in MnSi).

The contributions to the Hall resistivity ρ_{xy} from the normal (NHE), the anomalous (AHE), and the topological (THE) Hall effect are labeled as ρ_{xy}^{NHE} , ρ_{xy}^{AHE} , and ρ_{xy}^{top} .

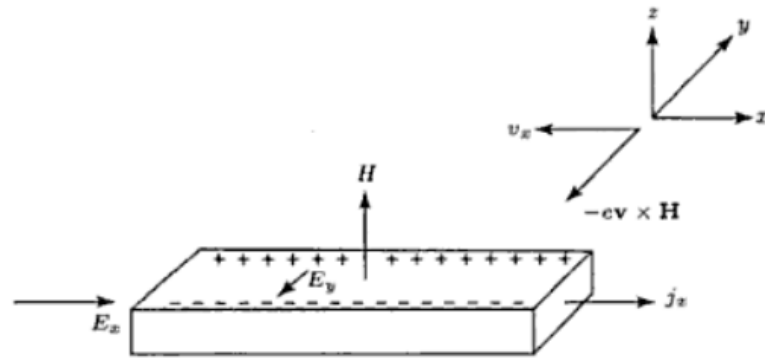


Figure 6.4: Geometry of a Hall effect experiment. Figure from [193].

Experimental evidence of the various Hall effect contributions

Fig. 6.5a - c illustrates schematically the experimental signatures of the NHE, the AHE, and the THE in $\rho_{xy}(B)$ together with the corresponding magnetization. The NHE is linearly proportional to the applied magnetic field B , with the slope of $\rho_{xy}(B)$ depending on the type of charge carriers. A positive (negative) slope of $\rho_{xy}(B)$ indicates a conduction dominated by electrons (holes), respectively¹. Fig. 6.5a illustrates the case of electron conduction.

In ferromagnetic materials an AHE contribution arises on top of the NHE. The AHE contribution scales with the magnetization M and thus leads to an increase in ρ_{xy} in field regions where the magnetization M is increasing with field (green shaded region in Fig. 6.5b). Once M is saturated, the AHE contribution remains constant and the slope of $\rho_H(B)$ is again determined by the NHE (blue shaded region). In materials with a non-trivial spin structure, a THE can arise in the AHE field region and yields an additional contribution to the Hall effect. In the case of MnSi the THE contribution is a top hat shaped signal on top of the AHE contribution (red region in Fig. 6.5c). In the corresponding field interval no additional feature is observed in the magnetization. Fig. 6.5d shows typical Hall effect data of MnSi under pressure where contributions from the NHE, the AHE, and the THE are observed. This will be discussed further in Sec. 6.2.5 and Chaps. 7-10.

¹Note, that the sign of ρ_{xy} is opposite to the sign of the Hall voltage U_H and the normal Hall constant R_0 : $U_H \propto R_H \propto -\rho_{xy}$ (see Eq. 6.34 and e.g. [192])

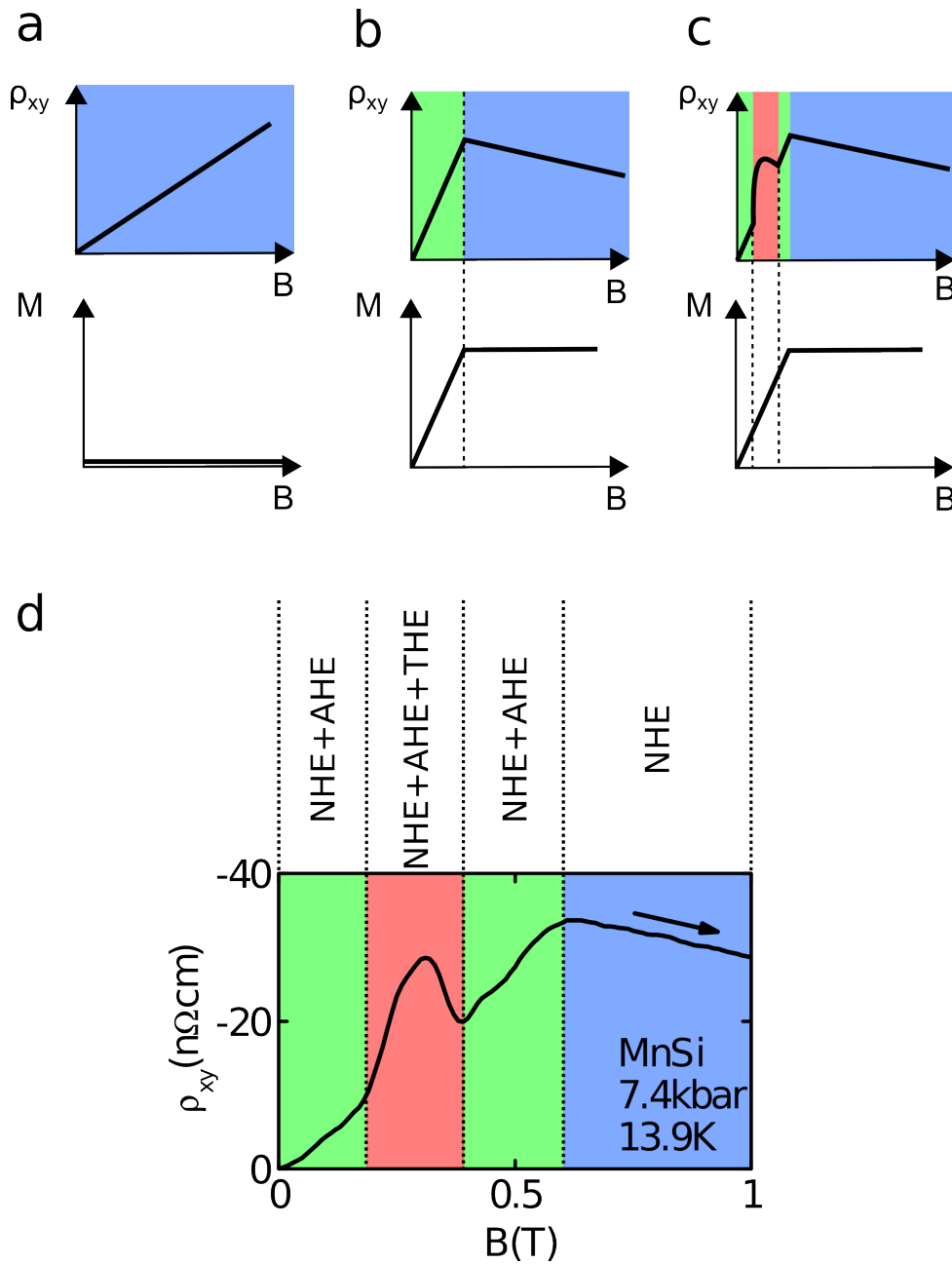


Figure 6.5: Examples of normal (NHE), anomalous (AHE), and topological Hall effect (THE). (a) NHE as observed in non-magnetic metals. The upper panel shows the Hall resistivity ρ_{xy} , the lower panel shows the corresponding magnetization M . (b) In ferromagnetic metals AHE and NHE are observed. In field regions where the magnetization is not saturated (green), the AHE contribution dominates ρ_{xy} . At fields where the magnetization is saturated (blue), the NHE contribution dominates the slope of ρ_{xy} . (c) In the helimagnet MnSi a THE signal corresponding to the skyrmion lattice is observed on top of the AHE contribution (red). In the same field region no signature is observed in the magnetization. (d) Hall resistivity of MnSi at 7.4 kbar and 13.9 K. The dominating Hall effect contributions in the different field ranges are indicated.

6.2.2 Normal Hall effect

When a current-carrying conductor is placed in a magnetic field the charge carriers are deflected by the Lorentz force to one side of the conductor. An electric field called Hall field builds up until the force of the Hall field on the charge carriers balances the Lorentz force. The Hall field and hence the observable Hall voltage is proportional to the charge carrier type and density.

In the Drude theory of metals this can be calculated as follows with electrons as charge carriers (cgs units) [193]: With the force $\vec{f} = -e \left(\vec{E} + \vec{v} \times \vec{H}/c \right)$ due to the applied electric and magnetic fields, \vec{E} and \vec{H} , acting on each electron, the momentum \vec{p} per electron becomes

$$\frac{d\vec{p}}{dt} = -e \left(\vec{E} + \frac{\vec{p}}{mc} \times \vec{H} \right) - \frac{\vec{p}}{\tau} \quad (6.2)$$

with the relaxation time τ . In a geometry as shown in Fig. 6.4 an electric field E_x is applied along the x -direction leading to a current density j_x flowing in the conductor. A magnetic field H along the z -direction leads to a Lorentz force $\frac{e}{c} \vec{v} \times \vec{H}$ on the electrons pointing in y -direction. Electrons accumulate on the lower sample edge and build up the Hall field E_y which is proportional to H and j_x . Therefore, a Hall coefficient can be defined as

$$R_H = \frac{E_y}{j_x H}. \quad (6.3)$$

With the current being time independent in the steady state $\frac{d\vec{p}}{dt} = 0$ and with $j_y = 0$, as no current is flowing in y -direction, the Hall coefficient becomes

$$R_H = -\frac{1}{nec}. \quad (6.4)$$

once E_y has built up. Therefore, the Hall coefficient depends on no parameter of the metal except the density of charge carriers n . In real materials R_H can be field and temperature dependent contrary to Eq. 6.3 when the Drude model is not sufficient to describe the actual situation. For example, n can vary with temperature due to the band structure yielding $R_H(T) = -\frac{1}{e \cdot n(T)c}$. In many metals the Drude result seems to be a limit value reached at very low temperatures in very pure samples at very high magnetic fields. Also, R_H can be positive or negative depending on the type of charge carrier.

In this thesis the SI-unit formulations of Eqs. 6.3 and 6.4, $R_0 = -\frac{1}{ne}$ and $\rho_{xy}^{\text{NHE}} = R_0 \cdot B$, will be used for data analysis. Here, R_0 and ρ_{xy}^{NHE} are labeled as normal Hall constant and normal Hall resistivity, respectively, to distinguish between the contributions from the different Hall effects.

6.2.3 Intrinsic anomalous and topological Hall effect

In ferromagnetic conductors an additional contribution to the Hall effect is observed that scales with the magnetization. This contribution is called the anomalous Hall effect (AHE). In fields where the magnetization increases the AHE contribution dominates the Hall signal. Early on, the empirical formula $\rho_{xy} = R_0 B + R_S M$ with the anomalous Hall coefficient R_S was established by Pugh and Lippert [194, 195]. Karplus and Luttinger (KL) formulated a first microscopic theory in which the electrons acquire an anomalous velocity perpendicular to the applied electric field and therefore contribute to the Hall effect [189, 196]. According to the KL theory this contribution depends only on the band structure, is largely independent of scattering and proportional to ρ_{xx}^2 . However, the KL theory describes only the situation in some materials and completely neglects scattering from disorder. Since then several AHE mechanisms have been proposed and only recently the AHE problem seems to become resolved.

The state of the art distinguishes between three AHE contributions: The two extrinsic contributions from (i) skew-scattering and (ii) side-jump scattering that describe the asymmetric scattering amplitudes for spin-up and spin-down electrons. And (iii) an intrinsic contribution due to an anomalous velocity caused by the Berry phase that the electrons acquire while moving in a curved band [197]. The conductivities can be added linearly to give the full AHE $\sigma_{xy}^{\text{AHE}} = \sigma_{xy}^{\text{AHE-skew}} + \sigma_{xy}^{\text{AHE-sj}} + \sigma_{xy}^{\text{AHE-int}}$. Recent experiments showed that electrons can not only acquire Berry phases when moving in a curved band in momentum space but also when moving through a topologically non-trivial magnetic structure in real space [15, 162, 169, 190, 191]. A topologically non-trivial structure is a structure with non-zero winding number (see Sec. 5.1.1). This leads to the so-called topological Hall effect (THE).

This section focuses on the intrinsic anomalous and the topological Hall effect which are closely connected to each other. The extrinsic contributions to the AHE will be covered in Sec. 6.2.4. The basic properties of the three contributions to the AHE are summarized in Table 6.2. The parts in the AHE follow the reviews of Nagaosa *et al.* [189] and Xiao *et al.* [197], and the paper of Ong *et al.* [198]. The presented theory of the THE and the interplay of intrinsic AHE and THE were developed by Rosch and collaborators along the experimental results on MnSi of this thesis and are published in our paper [16]. Earlier work on the THE in MnSi by Rosch and collaborators was presented in Ref. [15].

Intrinsic anomalous Hall effect

When electrons move in a conductor with broken time reversal or broken spatial inversion symmetry they pick up a transverse velocity that is connected to the topological properties of its Bloch states. This transverse velocity leads to dissipationless Hall currents that only dependent on the band structure. Hence, the resulting contribution to the Hall effect is called the intrinsic AHE. It is observed in, e.g., ferromagnets (broken time-reversal symmetry), in 2D conducting planes or at interfaces (broken spatial inversion symmetry). The intrinsic AHE dominates in materials with strong spin-orbit coupling. Since it

depends only on the band structure, the intrinsic AHE is independent of the transport lifetime τ , i.e., independent of σ_{xx} . With the concept of the Berry-phase [199] the intrinsic AHE contribution can be calculated.

The Berry concept states that a quantity $\vec{\Omega}(\vec{k})$, called the Berry curvature, exists and behaves like a magnetic field in momentum space with the Berry vector potential $\vec{X}(\vec{k})$. When electrons move adiabatically on the Fermi surface in the Berry vector potential, they accumulate a so-called Berry phase, analogous to the Aharonov-Bohm phase in momentum space. The Berry-phase is connected to the curvature of the bands in which the electrons move. An example is given below.

The semiclassical equation of motion for an electron in an electric field $\hbar\vec{v} = \nabla_{\vec{k}}\epsilon_n$ turns out to be incomplete. A term $e\vec{E} \times \vec{\Omega}$ called Luttinger term has to be added which takes accumulated Berry phases into account

$$\hbar\vec{v} = \nabla_{\vec{k}}\epsilon_n - e\vec{E} \times \vec{\Omega}. \quad (6.5)$$

The Luttinger terms yields a velocity that is transverse to the electric field and gives rise to a Hall current which can be calculated as (see [198] for details)

$$\vec{J}_H = \frac{e^2}{\hbar}\vec{E} \times \sum_{\vec{k}, \vec{s}} \vec{\Omega}(\vec{k}) f_{\vec{k}}^0 \quad (6.6)$$

with the equilibrium distribution function $f_{\vec{k}}^0$ ². Because \vec{J}_H derives from $f_{\vec{k}}^0$ it is independent of the transport lifetime τ . Furthermore, the Hall conductivity can be calculated as

$$\sigma_{xy} = n \frac{e^2}{\hbar} \langle \Omega \rangle \quad (6.7)$$

with the weighted average of the Berry curvature $\langle \Omega \rangle = n^{-1} \sum_{\vec{k}} \Omega_z(\vec{k}) f_{\vec{k}}^0$. And finally, the Hall resistivity can be calculated as

$$\rho_{xy} = \frac{e^2}{\hbar} \langle \Omega \rangle n \rho_{xx}^2. \quad (6.8)$$

A symmetry analysis yields that the Berry curvature vanishes in crystals with both time-reversal and spatial inversion symmetry (see [197]). Then the Luttinger term in Eq. 6.5 does not need to be considered. In systems with either broken time-reversal or inversion symmetries the Berry curvature does not vanish and the Luttinger term has to be considered. Examples for a broken time-reversal symmetry are crystals with ferromagnetic or antiferromagnetic order. An example for broken inversion symmetry is a single-layered graphene sheet.

² $f_{\vec{k}}^0$ implies a contribution of all electrons of the Fermi sea in contradiction to the Fermi liquid theory ideas where only electrons at the Fermi surface contribute. Haldane showed that the intrinsic anomalous Hall effect can also be expressed as a Fermi surface property [200].

The case when an electron moves along a curved band in momentum space is not the only case how it can accumulate a Berry-phase. Also nontrivial spin textures in real space give rise to a Berry phase yielding the topological Hall effect (THE). The THE will be covered below. It follows an example of the Berry phase an electron acquires when moving in a periodic potential.

Berry phase of an electron in a periodic potential

When an electrons drifts along a path C in momentum space it essentially moves through a curved parameter space. With the concept of parallel transport from differential geometry, the movement can be described through introducing a local coordinate system which has a lower dimension than the parameter space ³. Then one can calculate with the simpler local coordinates and introduce a phase factor, which is proportional to the curvature of the enclosed plane, when completing a closed path. In this case the phase factor is called Berry-phase.

For example (see [198] for details), for an electron in a periodic potential with the (Bloch) eigenstates

$$\Psi_{n\vec{k}}(\vec{r}) = \frac{1}{\sqrt{N}} e^{i\vec{k}\cdot\vec{r}} u_{n\vec{k}}(\vec{r}) \quad (6.9)$$

and a Hamiltonian perturbed by a static potential $V(\vec{r})$

$$H = V(\vec{r}) + \epsilon_n(\vec{k}) \quad (6.10)$$

the electron acquires a Berry-phase along C of

$$\chi(\vec{k}) = - \int_C d\vec{k}' \cdot \vec{X}(\vec{k}') \quad (6.11)$$

with the Berry vector potential

$$\vec{X}(\vec{k}) = \int_{cell} d^3r u_{n\vec{k}}^*(\vec{r}) i \nabla_{\vec{k}} u_{n\vec{k}}(\vec{r}). \quad (6.12)$$

Analog to the Aharonov-Bohm effect where electrons acquire a phase factor in real space due to a vector potential $\vec{A}(\vec{r})$, the phase factor χ can be viewed as the Aharonov-Bohm phase in momentum space acquired through the vector potential $\vec{X}(\vec{k})$ with the magnetic field

$$\vec{\Omega}(\vec{k}) = \nabla_{\vec{k}} \times \vec{X}(\vec{k}) \quad (6.13)$$

called the Berry curvature. Due to $\vec{\Omega}$ the way an electron reacts to a potential V is changed. This is expressed through a Luttinger term $e\vec{E} \times \vec{\Omega}$ that enters the group velocity so that the semiclassical equations of motion in real and momentum space become

³E.g. for a 3D sphere as parameter space the local coordinate system is a 2D plane which is spanned by two vectors tangential to the sphere.

$$\hbar\vec{k} = e\vec{E} + e\vec{v} \times \vec{B} \quad (6.14)$$

$$\hbar\vec{v} = \nabla\epsilon_n - e\vec{E} \times \vec{\Omega}. \quad (6.15)$$

Topological Hall effect (THE)

Like the intrinsic AHE, the topological Hall effect (THE) is due to Berry phases that are accumulated by electrons while moving through a crystal lattice with broken time-reversal symmetry. However, the Berry phases accumulated by electrons contributing to the intrinsic AHE are connected to the topology of the Fermi surface, where the Berry phases originate from the movement in a curved band in momentum space at wave vectors $\vec{k} \approx \vec{k}_f$. As discussed above, this can be interpreted as an effective magnetic field in momentum space $\vec{\Omega}$. Hence, the intrinsic AHE is due to momentum space Berry phases. The underlying driving force is spin-orbit coupling (SOC) which locks the orientation of the charge carrier spin to its momentum.

On the other hand the THE is due to electrons with wave vectors $\vec{k} \ll \vec{k}_f$ which are sensitive to the curvature of the spin structure in real space⁴. Again, this can be viewed as the movement in an effective magnetic field \vec{B}_{eff} but now in real space. Hence, the THE is due to real space Berry phases. The driving force here is the exchange splitting which aligns the electron spins parallel or antiparallel to the local magnetization. Therefore, the THE is independent of SOC. The ratio of SOC to exchange splitting determines if intrinsic AHE or THE dominates [201].

To summarize, electrons can also acquire Berry phases while their spins follow adiabatically the local magnetization in real space. For trivial spin-structures the Berry phases vanish but in cases where the spin-structure is topologically non-trivial, i.e., that is has a non vanishing winding number, a THE contribution arises.

So far a THE was reported for 3D pyrochlore lattices in $\text{Pr}_2\text{Ir}_2\text{O}_7$ [191] and $\text{Nd}_2\text{Mo}_2\text{O}_7$ [190] in which a non-coplanar spin structure is produced on short length scales by frustrated magnetic moments, and in the skyrmion lattice phase of B20 structures like MnSi [15] and MnGe [202]. In other materials like the perovskite SrFeO_3 [203], the manganite $\text{La}_{1-x}\text{Co}_x\text{MnO}_3$ [204], and the double-exchange ferromagnets CrO_2 [205] and Gd [206], a THE has been proposed.

In the following we concentrate on a THE invoked by the topologically non-trivial magnetic structure of a skyrmion lattice like it was developed by Rosch and collaborators along experimental results of MnSi at ambient pressure. Both theory and experimental results were reported in Ref. [15]. Triggered by the experimental results of this thesis, Rosch and collaborators derived a more detailed theory of the THE in a skyrmion lattice and the interplay between intrinsic AHE and THE [16, 201]. This will be covered in the

⁴given that the variations of the spin structure are large compared to the mean free path so that modifications of the band structure due to the spin order may be ignored [189].

next section. All relations below are also valid for other materials of the B20 family in which a skyrmion lattice phase can be observed.

The case of a conduction electron moving through a magnetic skyrmion is illustrated in Fig. 6.7a. The electron spin follows the local magnetization and hence begins to twist. The sideward deflection is caused by the Berry phase accumulated by moving in the effective magnetic field of the skyrmion \vec{B}_{eff} . In case of a skyrmion lattice \vec{B}_{eff} is proportional to the skyrmion density given in Eq. 5.2:

$$\Phi^\mu = \frac{1}{8\pi} \epsilon_{\mu\nu\lambda} \hat{n} \cdot (\partial_\nu \hat{n} \times \partial_\lambda \hat{n})$$

with the antisymmetric unit tensor $\epsilon_{\mu\nu\lambda}$ and $\hat{n} = \vec{M}/|M|$. \vec{B}_{eff} can be calculated as $\vec{B}_{\text{eff}} = \Phi_0 \vec{\Phi}$ with the flux quantum for a single electron $\Phi_0 = h/e$ and $\vec{\Phi}$ being the integrated skyrmion density [15, 169]. The latter is a measure for the winding number if taken per unit cell. E.g., for the lattice of anti-skyrmions in MnSi $\int dx dy \Phi^z = -1$ for each 2-dimensional magnetic unit cell [154]. In turn, for a single Q -structure $\vec{\Phi} = 0$ and hence $\vec{B}_{\text{eff}} = 0$ which illustrates that only for a non-trivial spin-texture with non-zero winding number a THE can be observed.

In a semiquantitative approach the size of $\Delta\rho_{xy}^{\text{top}}$ in MnSi can be calculated taking into account several factors [15]: (i) As MnSi is a multiband system the size of $\Delta\rho_{xy}^{\text{top}}$ depends on details of the bandstructure and the relative size of scattering rates. As these values enter the normal Hall constant R_0 it can be used for a semiquantitative prediction. (ii) An adiabatic limit is assumed in which the charge carriers smoothly follow the texture \vec{M} with infinite lifetime. Spin-flip scattering is neglected. (iii) As majority and minority charge carriers collect Berry phases of opposite signs the local spin polarization P has to be considered. It is $\Delta\rho_{xy}^{\text{top}} \rightarrow 0$ for $P \rightarrow 0$ and $\Delta\rho_{xy}^{\text{top}}$ maximal for $P = 1$. Taken together,

$$\Delta\rho_{xy}^{\text{top}} = PR_0 B_{\text{eff}}^z \quad (6.16)$$

with \hat{z} being the direction of the applied magnetic field. From Eqs. 5.2 and 6.16 it becomes clear that the size of $\Delta\rho_{xy}^{\text{top}}$ scales with the skyrmion density which itself scales with the helix length λ_{helix} of the underlying host material. Hence, a large $\Delta\rho_{xy}^{\text{top}}$ is expected for a small λ_{helix} and vice versa. Table 6.1 summarizes λ_{helix} and $\Delta\rho_{xy}^{\text{top}}$ for several materials of the B20 family.

Since the applied magnetic field is needed to induce a non-zero spin chirality but as it also destroys the spin texture when increased above a certain threshold (because all moments will align along the direction of the applied field), the THE is a non-monotonic contribution to the Hall conductivity and only takes place in a certain interval of magnitude of the applied magnetic field like seen in Fig. 6.7b,c, and d [169].

Table 6.1: Topological Hall effect in various materials. Length of magnetic helix λ_{helix} , corresponding size of the THE $\Delta\rho_{xy}^{\text{top}}$, and effective magnetic field B_{eff} for materials of the B20 family. B_{eff} was calculated with Eq. 6.30.

material	λ_{helix} [nm]	$\Delta\rho_{xy}^{\text{top}}$ [n Ω cm]	B_{eff} [T]
FeGe [157]	≈ 60	$\ll 1$	-0.99
Fe _{1-x} Co _x Si, x=0.2%	38.7 [207]	$\ll 1$ [208]	-2.39
MnSi	18 [154]	4.5 [15]	-13.15
MnSi, p ≈ 11 kbar	≈ 16 [50]	≈ 40 [16, 162]	-13.15
Mn _{1-x} Fe _x Si, x=0.08%	10.5 [207]	≈ 40 [208]	-32.49
Mn _{1-x} Co _x Si, x=0.04%	9.7 [207]	≈ 32 [208]	-38.07
MnGe [202]	3	200	-397.95

Interplay of intrinsic anomalous and topological Hall effect

Discussions about the size of the giant topological Hall signal under pressure that was discovered in this thesis (see Chaps. 7 and 8) revealed that the complicated band structure of MnSi with many bands at the Fermi level needs to be taken into account. Where in Neubauer *et al.* [15] all bands were treated equally, a closer inspection shows that different bands contribute differently to the THE depending on the competition of spin-orbit coupling (SOC) and exchange splitting (see below). The contribution of each band to the THE scales with the relative size of its scattering rates while the THE is approximately independent of the total scattering rate. In the following the interplay of the contributions from intrinsic AHE and THE to the Hall effect are discussed along the corresponding section in our paper that was developed by Rosch and collaborators [16].

In magnetic metals without inversion symmetry the orientation of the electron spins is determined through exchange splitting and SOC. Exchange splitting of the bands is caused by magnetism and is described by a Zeeman field $b^{\text{ex}}(\vec{r})$ in real space (real space coordinate \vec{r}). It leads to a parallel or antiparallel alignment of the electron spins with respect to the local magnetic field. When exchange splitting is the dominant interaction, the electron spins smoothly follow the magnetic structure and pick up Berry phases in real space which leads to a THE.

SOC also leads to a splitting of the bands and is described by $\vec{g}^{\text{SO}}(\vec{p})$ (momentum space coordinate \vec{p}). SOC locks the electron spins to its momentum. When SOC is the dominant interaction the electrons pick up Berry phases in momentum space which leads to an intrinsic AHE.

In cases where SOC is of the same order of magnitude as the exchange splitting both real and momentum space movements of the electrons need to be considered. I.e., the general description is in the 6-dimensional phase space with coordinate $\vec{x} = (\vec{r}, \vec{p})$. For weak SOC and smooth magnetic textures the two interactions can be added up to obtain a single

band model Hamiltonian

$$H = \epsilon_{\vec{p}} \mathbf{1} + \vec{g}^{SO}(\vec{p}) \vec{\sigma} + \vec{b}^{ex}(\vec{r}) \vec{\sigma}. \quad (6.17)$$

The sign of the electron charge $e < 0$ is taken into account, so that the spin (magnetic moment) of an electron orients preferentially antiparallel (parallel) to the Zeeman field, respectively. The direction of the local magnetization can be defined in the semiclassical limit as

$$\hat{n} = \frac{\vec{g}^{SO}(\vec{p}) + \vec{b}^{ex}(\vec{r})}{|\vec{g}^{SO}(\vec{p}) + \vec{b}^{ex}(\vec{r})|}. \quad (6.18)$$

Accordingly, spin up \uparrow can be defined as parallel to \hat{n} , and spin down \downarrow as antiparallel to \hat{n} . Spin down \downarrow is the state with the lower energy and carried by the majority electrons. In the following, we concentrate on cases where the exchange fields vary on length scales much longer than the Fermi wavelength, like it is the case in MnSi.

The Berry phases picked up by electrons with majority (\downarrow) and minority (\uparrow) spins have opposite signs. To take this into account it is useful to introduce the emergent charges $q_{\downarrow}^e = 1/2$ and $q_{\uparrow}^e = -1/2$. For the majority spins then the Berry vector potential

$$q_{\downarrow}^e A_j(x) = i\hbar \left\langle u(\vec{x}) \left| \frac{\partial}{\partial x_j} \right| u(\vec{x}) \right\rangle, j = 1 \dots 6 \quad (6.19)$$

arises (cf Eq. 6.12). Here, $|u(\vec{x})\rangle$ is the local wave function of the majority spin defined through the relation $(\hat{n}(\vec{x}) \vec{\sigma}) |u(\vec{x})\rangle = -|u(\vec{x})\rangle$. With the Berry vector potential, the effective magnetic fields Ω_{ij} (Berry curvature) can be calculated. Where for the intrinsic AHE discussed above the effective magnetic field was only considered in momentum space, the effective fields here are in momentum and real space. Correspondingly, the effective fields Ω_{ij} are represented though an antisymmetric 6×6 matrix $\overset{\leftrightarrow}{\Omega}$

$$\Omega_{ij} = \frac{\partial A_j}{\partial x_i} - \frac{\partial A_i}{\partial x_j} = \hbar \hat{n} \left(\frac{\partial}{\partial x_i} \hat{n} \times \frac{\partial}{\partial x_j} \hat{n} \right). \quad (6.20)$$

The components $i \in \{1, 2, 3\}$ (3×3 submatrix in the upper left) of $\overset{\leftrightarrow}{\Omega}$ describe the effective field in real space

$$B_i^e(\vec{x}) = \left| \frac{e}{q_{\sigma}^e} \right| B_i^{\text{eff}}(\vec{x}) = \frac{1}{2} \sum_{j,k=1 \dots 3} \epsilon_{ijk} \Omega_{jk} \quad (6.21)$$

where the emergent field B^e , in units \hbar/area , is related to the effective field B^{eff} , measured in the unit Tesla, by the factor $|e/q_{\sigma}^e|$. The components $i, j, k \in \{4, 5, 6\}$ (3×3 submatrix in the lower right) of $\overset{\leftrightarrow}{\Omega}$ describe the effective field in momentum space. The remaining 9 independent components are mixed terms. Geometrically, $\Omega_{ij} dx_i dx_j$ is the Berry phase (times \hbar) accumulated along an infinitesimal loop in the ij -plane with area $dx_i dx_j$. The area $dx_i dx_j$ is defined by the solid angle enclosed by the vector $\hat{n}(\vec{x})$ when moving around this loop.

As described above, due to $\overleftrightarrow{\Omega}$ a Luttinger term has to be added to the semiclassical equations of motions (see Eqs. 6.14 and 6.15). It is important to note that other than in the discussion about the intrinsic AHE, phase space coordinates are used here.

The emergent flux Φ^e can be calculated by integrating \vec{B}^e over a magnetic unit cell of the skyrmion lattice in real space. The result is \hbar times the total solid angle covered by \hat{n} . The total solid angle has to be a multiple of $4\pi = 2\pi/|q^e|$ due to the periodic boundary condition. Thus, the emergent flux is quantized and $n(p)$ is an integer.

$$\Phi^e(\vec{p}) = \int_{UC} \vec{B}^e(\vec{x}) d^2\vec{r} = \frac{2\pi\hbar}{|q^e|} n(p) = \begin{cases} 0 & |\vec{g}^{SO}(\vec{p})| > |\vec{b}^{ex}(\vec{r}_0)| \\ -\frac{2\pi\hbar}{|q^e|} & |\vec{g}^{SO}(\vec{p})| < |\vec{b}^{ex}(\vec{r}_0)| \end{cases} \quad (6.22)$$

Two regimes have to be distinguished: (i) When the exchange splitting is larger than the SOC ($|\vec{b}^{ex}(\vec{r}_0)| > |\vec{g}^{SO}(\vec{p})|$) the electron spins follows the magnetic structure, i.e., \vec{b}^{ex} . The emergent flux is then determined by the winding number of the magnetic structure. In the case of the SLP of MnSi the winding is -1 and thus the emergent flux is $-\hbar 4\pi$. (ii) When the SOC is larger than the exchange splitting ($|\vec{g}^{SO}(\vec{p})| > |\vec{b}^{ex}(\vec{r}_0)|$) the electron spins follow the direction of \vec{g}^{SO} . In this case \vec{b}^{ex} leads only to small deviations from the dominant direction of \vec{g}^{SO} . The winding number and with it the emergent flux vanishes.

For the case of negligible SOC ($|\vec{g}^{SO}(\vec{p})| \ll |\vec{b}^{ex}(\vec{r}_0)|$) the topological contribution to the Hall conductivity σ_{xy}^{top} can be estimated from the Boltzmann equation in the relaxation time approximation. The following assumptions are used: The relaxation time is spin dependent with τ_{\uparrow} for minority spin and τ_{\downarrow} for majority spin electrons; \vec{B}^e points in z -direction; the scattering rates are independent of \vec{k} . This leads to

$$\sigma_{xy}^{\text{top}} \approx B^e \sum_{\sigma n} \int e^2 q_{\sigma}^e \tau_{\sigma n}^2 \left(\frac{(\vec{v}_{kn}^y)^2}{m_{kn}^{xx}} - \frac{\vec{v}_{kn}^x \vec{v}_{kn}^y}{m_{kn}^{xy}} \right) \times \frac{\partial f_0(\epsilon_{k\sigma n})}{\partial \epsilon} \frac{d^3 k}{(2\pi)^3} \quad (6.23)$$

$$= B^e \sum_{\sigma n} \int e^2 q_{\sigma}^e w_{k\sigma n} \frac{d^3 k}{(2\pi)^3} \quad (6.24)$$

with \vec{v}_{kn} velocity in band n , $m_{kn}^{ij} = (\partial^2 \epsilon_{k\sigma n} / \hbar^2 \partial k_i \partial k_j)^{-1}$ being elements of the effective mass tensor, and the spin dependent scattering rates $w_{k\sigma n}$ (see below). A Hall conductivity due to orbital magnetic fields leads to the exact same formula if the emergent charge q_{σ}^e is replaced by the electron charge $e < 0$. Hence, the topological Hall resistivity $\Delta\rho_{yx}^{\text{top}}$ can be expressed through the normal Hall constant R_0 as

$$\Delta\rho_{yx}^{\text{top}} \approx R_0 B^e \left\langle \frac{q_{\sigma}^e}{e} \right\rangle_{\text{FS}} = R_0 B^{\text{eff}} P. \quad (6.25)$$

$P = \left| \frac{e}{q_{\sigma}^e} \right| \left\langle \frac{q_{\sigma}^e}{e} \right\rangle_{\text{FS}}$ is an effective polarization. $\langle \dots \rangle_{\text{FS}}$ is an average over all Fermi surfaces weighted by the square of spin dependent scattering rates $w_{k\sigma n}$:

$$\langle \dots \rangle_{FS} = \frac{\sum_{n\sigma} \int \dots w_{\vec{k}\sigma n}}{\sum_{n\sigma} \int w_{\vec{k}\sigma n}} \quad (6.26)$$

$$w_{\vec{k}\sigma n} = \tau_{\sigma n}^2 \left(\frac{\left(\frac{\vec{v}_{kn}^y}{m_{kn}^{xx}} \right)^2 - \frac{\vec{v}_{kn}^x \vec{v}_{kn}^y}{m_{kn}^{xy}}}{m_{kn}^{xy}} \right) \frac{\partial f_0(\epsilon_{\vec{k}\sigma n})}{\partial \epsilon} \quad (6.27)$$

The difference to Neubauer *et al.* [15] is that each band is considered individually weighted by its scattering rate instead of just taking one single estimated value for the polarization P . So it is possible that some bands do not contribute or that the contribution of some bands cancel each other. In MnSi the effective magnetic field is $B_{\text{eff}} \approx -13.15$ T (see Eq. 6.30).

6.2.4 Extrinsic anomalous Hall effect

In this section the two extrinsic contributions to the anomalous Hall effect (AHE) from skew-scattering and side-jump scattering will be briefly introduced. Whereas the intrinsic AHE and THE relate to the band structure and the magnetic structure, respectively, both extrinsic contributions relate to asymmetric scattering amplitudes for spin-up and spin-down electrons. The basic properties of all contributions to the AHE are summarized in Table 6.2.

Skew scattering contribution

The skew scattering contribution of the AHE first proposed by Smit [209, 210] arises due to asymmetric scattering processes of the charge carriers on, e.g., impurities in the presence of spin-orbit coupling.

When a charge carrier is scattered at a potential V from, e.g., a magnetic impurity, it undergoes a transition between two states m and n with wave vector \vec{k} and \vec{k}' , respectively. The principle of detailed balance states that the transition probability between these two states is identical in both directions $W_{n \rightarrow m}$ and $W_{m \rightarrow n}$, like it is assumed in semiclassical Boltzmann transport theory. This assumption is not valid anymore in the presence of spin-orbit coupling. In a simple model a term

$$W_{\vec{k}\vec{k}'}^A = -\tau_A^{-1} \vec{k} \times \vec{k}' \cdot \vec{M}_s \quad (6.28)$$

can be introduced in the transition probability to describe the effect of spin-orbit coupling. According to this term, a transition which is right handed with respect to the magnetization direction has a different transition probability than the corresponding left handed one. The wave vector \vec{k}' of the scattered charge carrier is orthogonal to both the incident wave vector \vec{k} and the magnetization \vec{M}_s and hence leads to a transverse current

Table 6.2: Properties of the anomalous Hall effect contributions. τ is the transport lifetime and l is the carrier mean free path. The approximation $\rho_{xy} \ll \rho_{xx}$ was used, so that, e.g., $\sigma_{xy} = -\frac{\rho_{xy}}{\rho_{xx}^2 + \rho_{xy}^2} \approx -\frac{\rho_{xy}}{\rho_{xx}^2}$.

contribution			dominant regime
intrinsic	$\sigma_{xy} \propto \tau^0, \propto l^0, \propto \sigma_{xx}^0, \propto \rho_{xx}^0$	$\rho_{xy} \propto \rho_{xx}^2$	strong spin-orbit coupling, $10^4(\Omega m)^{-1} < \sigma_{xx} < 10^6(\Omega m)^{-1}$
skew-scattering	$\sigma_{xy} \propto \tau^1, \propto l^1, \propto \sigma_{xx}^1, \propto \rho_{xx}^{-1}$	$\rho_{xy} \propto \rho_{xx}$	high conductivity, $\sigma_{xx} > 10^6(\Omega m)^{-1}$
side-jump	$\sigma_{xy} \propto \tau^0, \propto l^0, \propto \sigma_{xx}^0, \propto \rho_{xx}^0$	$\rho_{xy} \propto \rho_{xx}^2$	$10^4(\Omega m)^{-1} < \sigma_{xx} < 10^6(\Omega m)^{-1}$ (if not intrinsic)

orthogonal to the applied electric field \vec{E} .

When skew scattering dominates the AHE the Hall conductivity $\sigma_{xy}^{\text{AHE-skew}}$ and the conductivity σ_{xx} are both proportional to the transport lifetime τ . Hence, $\rho_{xy}^{\text{AHE-skew}} = \sigma_{xy}^{\text{AHE-skew}} \rho_{xx}^2$ is proportional to the longitudinal resistivity ρ_{xx} .

Side-jump contribution

The side-jump mechanism describes a microscopic displacement $\Delta y \approx 10^{-10} - 10^{-11}$ m of charge carriers scattering from a magnetic impurity [211, 212].

In the theoretical picture charge carriers treated as Gaussian wave packets with wave vector \vec{k} scatter from a spherical impurity with spin-orbit interaction $H_{SO} = (1/2m^2c^2)(r^{-1}\partial V/\partial r)S_zL_z$. The impurity distorts the wave function locally and creates a local current density. This leads to a displacement transverse to \vec{k} of size $\frac{1}{6}k\hbar^2/m^2c^2$. With the strict definitions for the intrinsic and the skew-scattering contribution from Nagaosa *et al.* [189], the side-jump contribution can also be defined as $\sigma_{xy}^{\text{AHE-sj}} = \sigma_{xy}^{\text{AHE}} - \sigma_{xy}^{\text{AHE-int}} - \sigma_{xy}^{\text{AHE-skew}}$. The side-jump contribution is independent of the transport lifetime τ , i.e., $\sigma_{xy}^{\text{AHE-sj}}$ independent of σ_{xx} , and hence hard to distinguish from the intrinsic contribution which is also independent of τ (see below). When a σ_{xy}^{AHE} independent of σ_{xx} is observed, the intrinsic contribution is usually calculated and compared to the experimental data. In most cases the intrinsic contribution accounts for the AHE. In the other cases the AHE is attributed to side-jump scattering.

6.2.5 Hall Effect in MnSi

Three contributions to the Hall effect could be identified in MnSi: (i) A NHE contribution $\rho_{xy}^{\text{NHE}} = R_0 B$ which scales linearly with the applied magnetic field B . (ii) An intrinsic AHE contribution to the conductivity below $T_c = 29.5 \text{ K}$ which scales with the magnetization $\sigma_{xy}^{\text{AHE-int}} = S_H M$ [187, 213]. (iii) A THE contribution $\Delta\rho_{xy}^{\text{top}}$ in the regime of the skyrmion lattice phase which reflects the non-zero topological winding number of the spin structure [15, 16]. The three contributions are summarized in Fig. 6.5.

Normal Hall effect & intrinsic anomalous Hall effect in MnSi

For a ferromagnet, MnSi has a low resistivity of $\rho_{xx} \approx 2 - 5 \mu\Omega\text{cm}$ at 4 K and an unusually large charge carrier mean free path l up to $\approx 240 \text{ \AA}$ at 4 K. σ_{xy} proves to be independent of l which hints at the intrinsic AHE as dominating contribution [187, 213]. Furthermore, band structure calculations show that both extrinsic contributions to the AHE, i.e., side-jump and skew scattering, are not relevant in MnSi [214].

With a large magnetoresistance (up to $\approx 40\%$ up to $\approx 5 \text{ T}$ near T_c), as expected in a high purity metal, the empirical formula $\rho_{xy} = R_0 B + R_S M$ cannot account for the experimental data, for M fails to match $\rho'_{xy} = \rho_{xy} - R_0 B$ (Fig. 6.6). The data can rather be explained with

$$\rho_{xy} = R_0 B + S_H \rho_{xx}^2 M \quad (6.29)$$

at temperatures below T_c where the scaling factor S_H derives from the Hall conductivity $\sigma_{xy}^{\text{AHE}} = S_H M \approx \frac{\rho_{xy}^{\text{AHE}}}{\rho_{xx}^2}$. S_H proves to be temperature independent below T_c so that σ_{xy}^{AHE} is only determined by $M(T, H)$ and hence independent of l [213].

At high ($T \gtrsim 100 \text{ K}$) and low ($T \lesssim 5 \text{ K}$) temperatures, $\rho_{xy}(B)$ is linear indicating that the NHE contribution dominates (Fig. 6.6c). The positive slope above 150 K hints at positive charge carriers with density between $n \approx 3.78 \cdot 10^{22} \text{ cm}^{-3}$ and $n \approx 8.5 \cdot 10^{22} \text{ cm}^{-3}$ [187, 213]. At intermediate temperatures ρ_{xy} has a “knee” feature due to a dominating AHE contribution. For $T < T_c$ the “knee” feature tracks the upper critical field B_{c2} .

Above T_c , Eq. 6.29 fails to describe the experimental data which can rather be fitted with the empirical relationship $\rho'_{xy} = \rho_{xy} - R_0 B = \alpha \rho_{xx}^2 M^{1.5}$ with the temperature dependent parameter α . However, the mechanism behind this relation is unclear up to now [187].

Topological Hall effect in MnSi

In the skyrmion lattice phase (A-phase) of MnSi, a THE contribution arises due to the non-zero winding number of the spin-structure. Fig. 6.7c and d shows the data of Ref. [15] where the topological contribution $\Delta\rho_{xy}^{\text{top}}$ can be seen as a top hat shaped additional signal that rides on top of the AHE. The THE signal occurs in the field and temperature interval of the skyrmion lattice phase of MnSi ($B \approx 0.15 - 0.2 \text{ T}$, $T \approx 28.0 - 28.8 \text{ K}$, see Fig. 6.7b). As discussed in Sec. 6.2.3, the size of $\Delta\rho_{xy}^{\text{top}}$ can be estimated by Eq. 6.25:

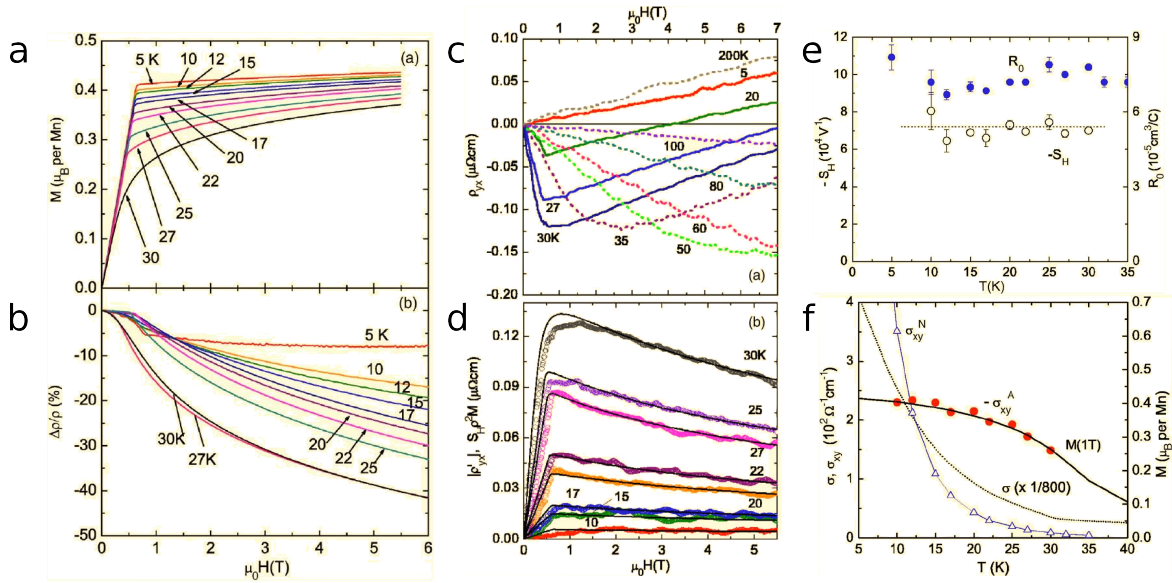


Figure 6.6: Magnetoconductance and Hall effect in MnSi. (a) Magnetization up to 5 T between 5 K and 30 K. (b) Magnetoconductance $\Delta\rho/\rho$. (c) $\rho_{yx}(B)$ up to 5 T and in a temperature range 5 K - 200 K. At highest and lowest temperatures, ρ_{yx} is linear indicating that NHE contributions dominate. At intermediate temperatures ρ_{yx} has a “knee” feature indicating dominating AHE contributions that scale with the magnetization. (d) The solid lines calculated with Eq. 6.29 nicely describe $\rho'_{yx} = \rho_{yx} - R_0 B$ below T_c . (e) Below T_c the parameters S_H and R_0 prove to be temperature independent. (f) With decreasing temperature the normal Hall conductivity σ_{xy}^{NHE} and the conductivity σ which is $\propto l$ increase strongly while the σ_{xy}^{AHE} changes only slightly with the magnetization. All figures from [213].

$$\Delta\rho_{yx}^{\text{top}} \approx R_0 B^c \left\langle \frac{q_\sigma^e}{e} \right\rangle_{\text{FS}} = R_0 B^{\text{eff}} P$$

The magnitude of the effective magnetic field B_{eff}^z can be derived from the proposed magnetic structure of a lattice of anti-skyrmions with winding number $\int dx dy \Phi^z = -1$ for each 2-dimensional magnetic unit cell [15]. The skyrmion lattice is a hexagonal lattice with lattice vectors $2\pi/\lambda_S$ in reciprocal and $\lambda_S/\sin(2\pi/3)$ in real space, respectively. The size of the unit cell is $\lambda_S^2/\sin(2\pi/3)$ which leads to

$$B_{\text{eff}} = -\frac{h}{e} \left(\frac{\sqrt{3}}{2\lambda_S^2} \right) \approx -13.15 \text{ T}. \quad (6.30)$$

Here, λ_S is approximately the helix length in the helical phase close to T_c , $\lambda_{\text{helix}} \approx \lambda_S \approx 165 \text{ \AA}$ [16]⁵.

The polarization $P = \mu_{spo}/\mu_{sat}$ represents the ratio of ordered magnetic moment in the skyrmion-lattice-phase (A-phase) $\mu_{spo} \approx 0.2 \pm 0.05 \mu_B/\text{f.u.}$ to the saturated magnetic moment $\mu_{sat} \approx 2.2 \pm 0.2 \mu_B/\text{f.u.}$ which can be taken from the Curie-Weiss moment in the paramagnetic state or the free Mn moment and has the magnitude $P \approx 0.1 \pm 0.02$. The normal Hall constant $R_0 = 1.7 \cdot 10^{-10} \Omega \text{mT}^{-1}$ can be inferred from the Hall signal at room temperature. Due to a calculation mistake the effective magnetic field was calculated as $B_{\text{eff}} \approx -2.5 \text{ T}$ in Neubauer *et al.* [15] leading to $\Delta\rho_{xy}^{\text{top}} = (4 \pm 1) \text{ n}\Omega\text{cm}$. With B_{eff} from Eq. 6.30 $\Delta\rho_{xy}^{\text{top}} \approx 21 \text{ n}\Omega\text{cm}$ is estimated which is approximately five times larger than the experimental value of $\Delta\rho_{xy}^{\text{top}} = 4.5 \text{ n}\Omega\text{cm}$. However, considering the uncertainties of R_0 and P and the possibility that some bands do not contribute to the THE depending on the competition of exchange splitting and SOC, which will be discussed in Chap. 8, that were not considered in Neubauer *et al.* [15], this seems plausible.

At the same time as Neubauer *et al.* [15] showed that the top hat shaped signal in $\rho_{xy}(B)$ at ambient pressure is a THE due to the skyrmion lattice in MnSi, Lee *et al.* [162] found a 10 times larger signature in $\rho_{xy}(B)$ at hydrostatic pressures between 6 kbar and 12 kbar in a field range of 0.1 T to 0.5 T, i.e., from B_{c1} to B_{c2} (see Fig. 6.8). However, both the size and the field range of the signature seemed puzzling. The field range is several 100 mT larger than found for the skyrmion lattice phase at ambient pressure. Also, the tenfold size compared to ambient pressure measurements could not be explained, since, with what was known, the parameters in Eq. 6.16 are only weakly pressure dependent. (i) B_{eff} : The helix length and hence the density of the skyrmion lattice is known to be almost unchanged under pressure, implying an approximately pressure independent B_{eff} [50]. (ii) P : The polarization decreases slightly with pressure as the ordered moment in the helimagnetic state decreases by 10% up to 12 kbar and as the Curie-Weiss moment in the paramagnetic state also remains unchanged. The decreased P would even lead to a reduced $\Delta\rho_{xy}^{\text{top}}$. (iii) R_0 : Neither the electrical resistivity ρ_{xx} nor the Hall effect ρ_{xy} shown in Ref. [162] suggest a change of R_0 with pressure. (iv) The critical fields B_{c1} and B_{c2} do not change with pressure [173, 178] and hence the field range of the skyrmion lattice is

⁵The helix length changes from $\lambda_{\text{helix}} \approx 180 \text{ \AA}$ for $T \rightarrow 0$ to $\lambda_{\text{helix}} \approx 165 \text{ \AA}$ for $T \rightarrow T_c$ (cf [40, 215, 216])

expected to be similar as compared with ambient pressure.

One goal of this thesis was to track the evolution of the THE in MnSi under pressure and establish a connection between the data of Neubauer *et al.* [15] and Lee *et al.* [162] if possible. As will be shown, $\Delta\rho_{xy}^{\text{top}}$ evolves from 4.5 n Ω cm at ambient pressure to ≈ 40 n Ω cm at 12 kbar with a field range consistent with the ambient pressure skyrmion lattice phase due to an unexpected conspiracy of mechanisms. The large field range seen by Lee *et al.* [162] can be identified to originate from low sample qualities (low RRR $\rho_{xx}(300\text{ K})/\rho_{xx}(4.2\text{ K}) \approx 50$) and pressure inhomogeneities. This will be discussed in Chap. 7 and 8.

Furthermore, a major goal was to study the Hall effect at pressures above the critical pressure p_c . Signatures linking the skyrmion lattice phase seen at ambient pressure to the non-Fermi-Liquid regime (NFL) at high pressures were found. The top hat shaped $\Delta\rho_{xy}^{\text{top}}$ seen at $p < p_c$ evolves into a broad peak whose phase boundaries coincide with the phase boundaries of the $\rho_{xx} \propto T^{3/2}$ temperature dependence of the NFL regime. This will be discussed in Chaps. 9 and 10.

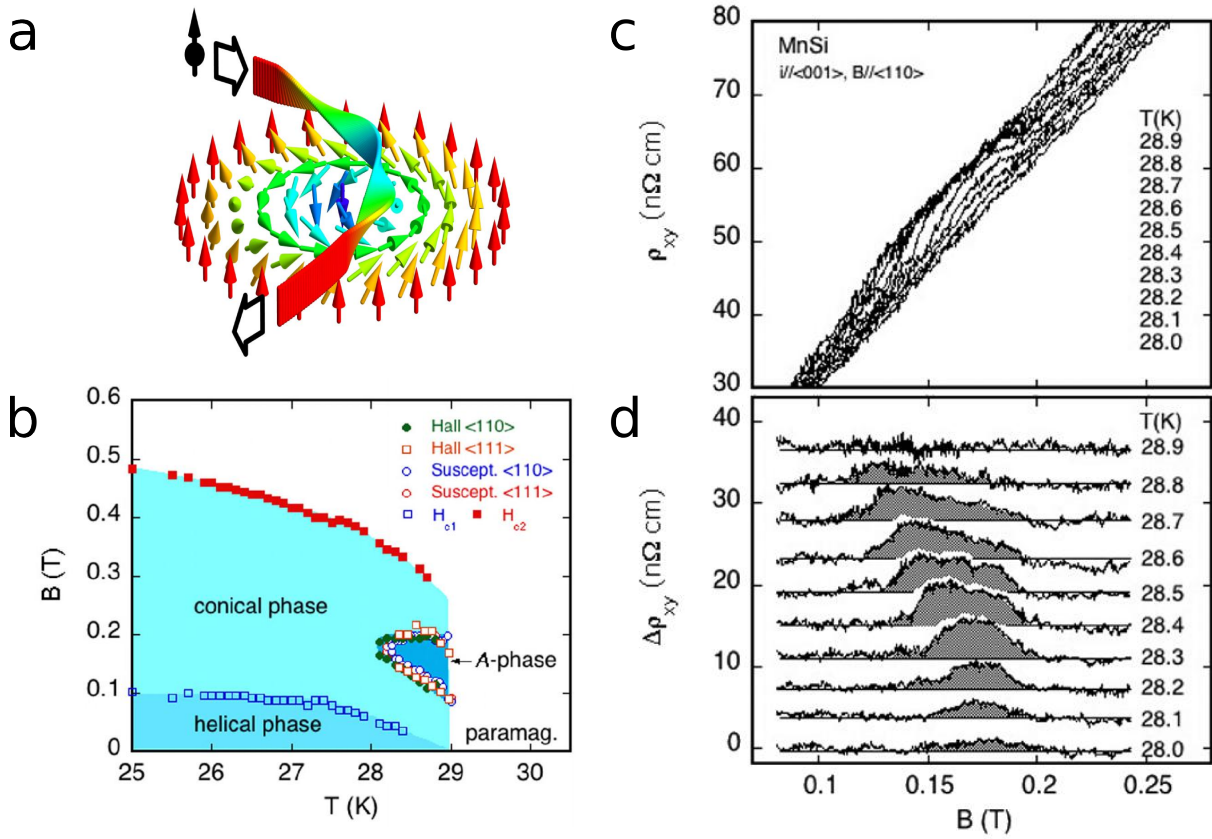


Figure 6.7: Topological Hall effect in MnSi. (a) Electron moving through a skyrmion. The electron spin follows the local magnetization and hence twists. The accumulated Berry phase leads to a sideways deflection and is the origin of the THE. Picture from [165]. (b) Magnetic phase diagram of MnSi [15]. (c) The THE in MnSi is seen as an increase in ρ_{xy} riding on top of the AHE. (d) After subtracting the AHE the THE becomes clear as top hat shaped signal (gray shading). Picture from [15].

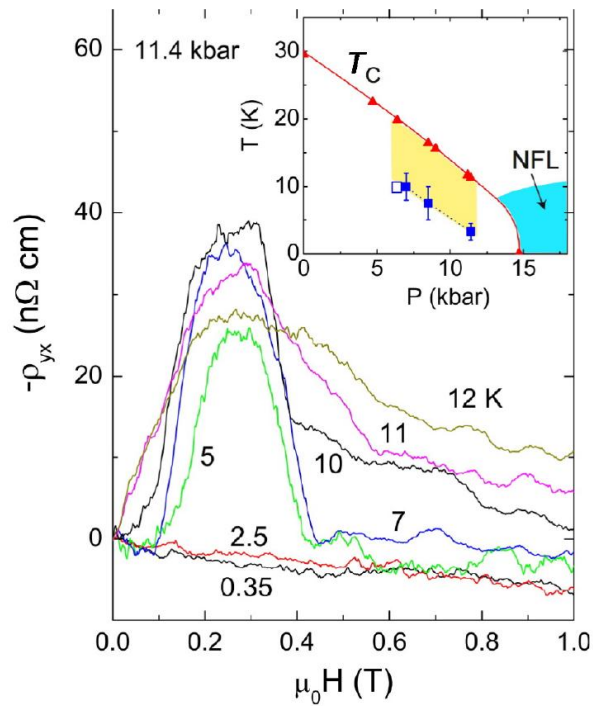


Figure 6.8: Signature in the Hall effect of MnSi under pressure. ρ_{xy} in the pressure range between 6 kbar and 12 kbar measured by Lee *et al.* [162]. A large, top-hat shaped signature ($\approx 40 \text{ n}\Omega\text{cm}$) in the field range of 0.1 T to 0.5 T is observed. However, both size and field range are larger than the topological Hall effect contribution seen at ambient pressure and cannot be explained with what is known so far.

6.3 Experimental setup

6.3.1 Crystals

MnSi samples for this study were grown by Neubauer, Münzer, and Bauer in a three-step procedure: (i) purification of the starting elements, (ii) preparation of polycrystalline rods, and (iii) single-crystal growth by optical float zoning. After purifying the starting elements via etching and ultrasonic cleaning, polycrystalline rods were casted using a water-cooled Huykin crucible with radio-frequency heating inside an all-metal sealed furnace. The polycrystalline rods were subsequently mounted in an ultrahigh vacuum compatible four-mirror image furnace where they were float-zoned into single crystals [217, 218].

Float-zoned rods were characterized via x-ray Laue diffraction in backscattering geometry. Samples were cut out of the identified single crystalline regions with a wire saw. Subsequent grinding with abrasive paper of fineness up to 4000 yielded samples with dimensions $2.8 \times 1 \times 0.2 \text{ mm}^3$.

As summarized in table 6.3, the MnSi samples had residual resistivity ratios (RRR) between ≈ 40 and ≈ 150 and were oriented with magnetic field B pointing along the crystalline $\langle 110 \rangle$ and applied current I pointing along either the $\langle 100 \rangle$ or $\langle 110 \rangle$ direction (see Fig. 6.9). All samples agreed well with the literature in terms of temperature, field, and pressure dependence of resistivity and Hall effect in regions known so far.

6.3.2 Magnetcryostat

All measurements on MnSi shown in this thesis were performed with a continuous-flow cryostat from Oxford Instruments containing a 14/16 T superconducting magnet with a temperature range 1.5 K - 300 K. Pressure cells were attached to a sample stick which was mounted inside a variable temperature insert (VTI) and cooled through a Helium gas-flow.

The Helium gas flowing around the pressure cell was heated to the desired temperatures with a resistive heater during the intake from the Helium bath to the VTI. The intake pathway with which the flowing gas thermalized consisted of a capillary and a copper block. The latter contained a Cernox thermometer (control thermometer) and the afore-said resistive heater for a PID temperature control through a Oxford Instruments ITC503 temperature controller. A pressure in the mbar range inside the VTI allowed access to temperatures down to 1.5 K.

The sample stick we used is based on a tube made from stainless steel (diameter 10 mm) with attached radiation shields. Electric wiring consisted of twisted pairs of $80 \mu\text{m}$ thick copper wires running along the outside of the sample stick. Pressure cells were tightly screwed to a copper block ($20 \times 15 \times 15 \text{ mm}^3$) via a copper adapter piece at the end of the sample stick yielding a good thermal contact. The sample temperature was determined with a calibrated Lakeshore Cernox thermometer CX-1030-AA mounted inside a bore in

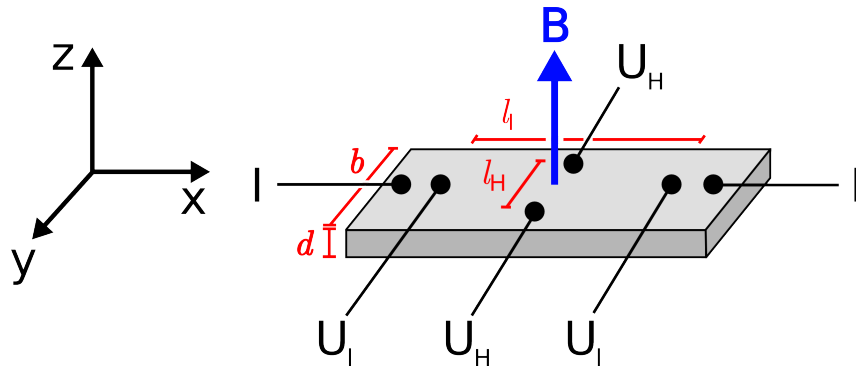


Figure 6.9: Measurement geometry. Geometry used for Hall effect measurements with current I flowing along the x -direction, magnetic field B pointing along the z -direction, U_l being the longitudinal and U_H being the Hall voltage. Directions $B \parallel \langle 110 \rangle$ and $I \parallel \langle 110 \rangle$ or $\langle 100 \rangle$ were used. Samples were contacted in a 6-terminal-configuration. b and d are the width and the thickness of the sample, respectively. l_l and l_H are the distances between the longitudinal and the Hall voltage contacts.

the copper block mentioned before (sample thermometer).

Temperature sweeps were performed with slow rates of 0.2 K/min and 0.3 K/min to minimize the sample temperature lagging behind the control temperature. Before magnetic field sweeps a waiting time between 60 min and 120 min allowed the sample temperature to converge against the desired control temperature. Despite careful measurement procedures samples were subject to temperature drifts of around 0.14 K during ± 2 T magnetic field sweeps leading to small offsets of the measured data. However these offsets did not have any relevance for the interpretation of our data.

Magnetic field sweeps up to ± 14 T were performed in continuous ramps with 0.2 T/min. Due to the induction of the magnet recorded field values which were calculated from the current applied with an Oxford Instruments IPS 120 current source were lagging behind the actual field values in the magnet bore. This led to a systematic error of 0.14 T and was corrected before symmetrization and antisymmetrization (see Sec. 6.4.1).

Small magnetic field sweeps up to ± 2 T were performed through changing the field in 10 mT steps with a 20 s waiting time per step during which data was recorded. This procedure was not subject to systematic errors like described above.

6.3.3 Measurement electronics

Magnetoresistance and Hall effect measurements were performed through application of an ac current to our samples while tracking the corresponding voltages U_l and U_H along the longitudinal and the Hall contacts with a Lock-In amplifier. Fig. 6.9 shows a sketch of a sample contacted in a 6-terminal-configuration. Fig. 6.10 shows a sketch of the

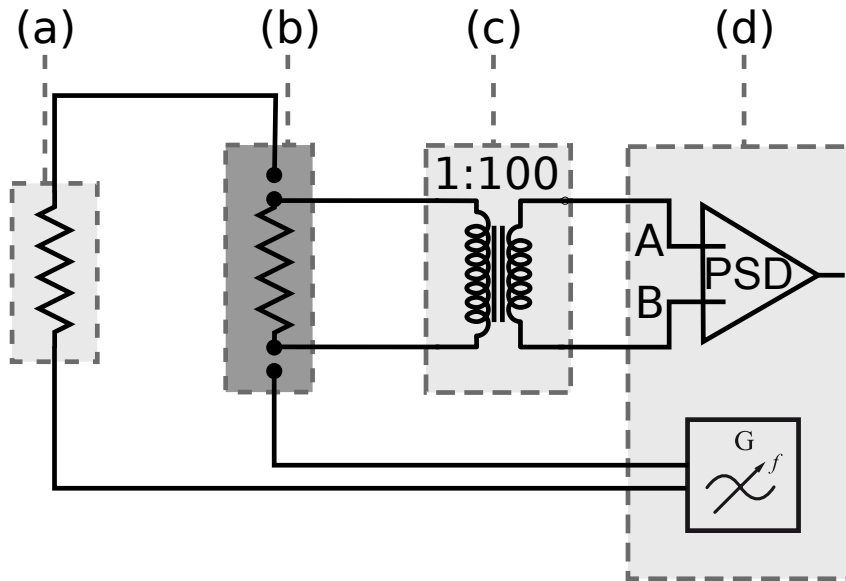


Figure 6.10: Sketch of the measurement setup. (a) $1\text{ k}\Omega$ current limiting resistor. (b) Sample. (c) Signal Recovery Model 1900 Precision Low-Noise Signal Transformer with amplification 1:100. (d) SR830 Lock-In amplifier with phase sensitive detector (PSD) and sine generator (G) operating at $V_{\text{rms}} = 5\text{ V}$ and 22.08 Hz . For clarity, only the measurement setup for the longitudinal resistance U_l is shown. The voltage along the Hall contacts U_H is simultaneously recorded with a similar setup of transformer and Lock-In amplifier.

measurement setup.

The ac current applied to the sample was produced by a sinusoidal signal of $V_{\text{rms}} = 5\text{ V}$ of the internal oscillator of a Stanford Research SR830 Lock-In amplifier together with a current limiting resistor of $1\text{ k}\Omega$. As the $1\text{ k}\Omega$ resistor was about two orders of magnitudes larger than the sample with connected wiring ($\approx 16\ \Omega$) this yielded a current of $I_{\text{rms}} = 5\text{ mA}$. A frequency of 22.08 Hz was chosen to operate the Signal Recovery Model 1900 Precision Low-Noise Signal Transformer, which was used to amplify U_l and U_H by a factor of 100, in a range with less than 1 dB attenuation. The wiring consisted of coaxial cables outside of the cryostat, and $80\ \mu\text{m}$ thick copper wires arranged in twisted pairs inside the cryostat. Typical signal sizes at the Lock-In amplifier were $U_l(T = 280\text{ K}, B = 0\text{ T}) \approx 7\text{ mV}$, $U_l(T = 5\text{ K}, B = 0\text{ T}) \approx 90\ \mu\text{V}$, $U_l(T = 3\text{ K}, B = 14\text{ T}) \approx 60\ \mu\text{V}$ for the longitudinal voltage, and $U_H(T = 280\text{ K}, B = 0\text{ T}) \approx 160\ \mu\text{V}$, $U_H(T = 5\text{ K}, B = 0\text{ T}) \approx 3\ \mu\text{V}$, $U_H(T = 3\text{ K}, B = 14\text{ T}) \approx 4\ \mu\text{V}$ for the Hall voltage.

6.3.4 Pressure cells

Hydrostatic pressures up to the critical pressure $p_c \approx 14.6\text{ kbar}$ of MnSi and above were generated with piston-cylinder cells as described in Ref. [140] (Fig. 6.11).

Samples were mounted inside a Teflon capsule filled with liquid pressure medium, where the lower end was sealed with an obturator also acting as a wire-feedthrough. Hydrostatic pressure was created through compressing the Teflon capsule with a non-magnetic

tungsten-carbide (WC) anvil while the obturator was held in place by a locknut. A cell-body of hardened Berylco 25, Copper with 2.5% Beryllium (Cu:Be), prevented bagging of the Teflon capsule. Locknuts, obturators, and sealing rings were also manufactured from hardened Berylco 25.

With this kind of setup with bore diameter 5 mm, pressures of about 25 kbar can be reached. The maximum pressure is limited through the yield strength of 960 N/mm^2 - 1460 N/mm^2 of hardened Berylco 25 [219]. For experiments requiring higher pressures, the pressure limit can be increased up to 35 kbar by placing a cartridge of hard metal like NiCrAl in the bore of the pressure cell [220].

The tungsten-carbide (WC) anvils which were labeled non-magnetic nonetheless carried a small magnetic moment originating from Cobalt or Nickel used as binder in the sintering process. This led to a systematic error of about 15 mT at the sample position. As all features of interest in MnSi are field dependent in the order of 10^2 mT this systematic error had no impact on any interpretation and could be neglected.

Fig. 6.12 shows pictures of the sample as set up inside the pressure cell. Twisted pairs of copper wire with diameter of either $80 \mu\text{m}$ or $120 \mu\text{m}$ were glued in the obturator feedthrough with Stycast 2850 FT epoxy and checked for pressure tightness. A hat shaped Teflon sample holder was mounted holding wires in a defined position. The sample was then suspended in a defined orientation through soldering both ends onto the $120 \mu\text{m}$ copper wires used as current contacts. Hence, the pressure medium could completely flow around the sample reducing uniaxial strains.

As voltage contacts $25 \mu\text{m}$ Pt wires were spot welded directly onto the sample surface with a Schmidt Instruments Model UIP 1000 digital spot-welding-apparatus. The contacts were arranged in a 6-terminal-configuration for magnetoresistance and Hall effect measurements as shown in Fig. 6.9. The Pt wires were then soldered onto the $80 \mu\text{m}$ copper wires. A thin piece of tin was soldered directly onto two pairs of $80 \mu\text{m}$ copper wire and used as pressure gauge (see Sec. 6.4.4).

For first experiments, a Fluorinert FC72:FC84 mixture with volume ratio 1:1 (FC) was used. As a dependence of the topological Hall signal on the cooling procedure was observed (see Sec. 6.4.5), all further experiments were performed with a methanol:ethanol mixture with volume ratio 4:1 (ME) known to have a higher hydrostatic limit (≈ 100 kbar [221]) than Fluorinert mixtures (≈ 20 kbar [141]). Table 6.3 summarizes all pressure cells assembled for this project.

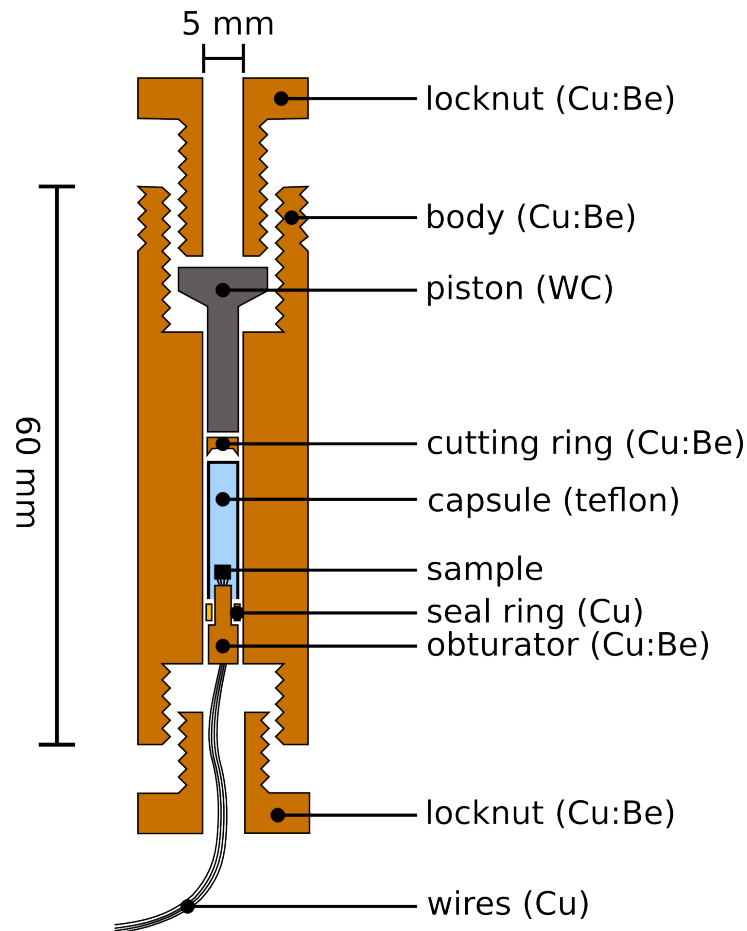


Figure 6.11: Pressure cell. Sketch of a piston-cylinder-cell with a 5 mm bore. The sample is mounted inside a Teflon capsule filled with liquid pressure medium. The lower end of the Teflon capsule is sealed by an obturator which is held in place by a locknut. Pressure transmitted through a WC piston compresses the Teflon capsule and hence leads to a hydrostatic pressure acting on the sample. See text for details.

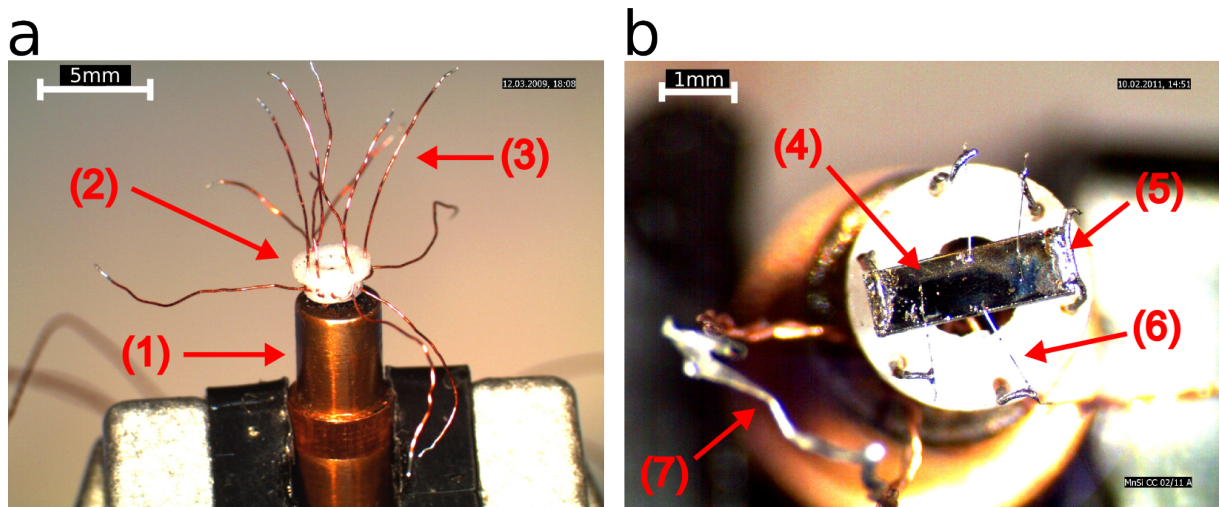


Figure 6.12: Setup inside of the clampcell. (a) Obturator (1) with $80 - 120 \mu\text{m}$ Cu wires (3) glued in with Stycast 2850 FT epoxy. On top of the obturator a hat shaped sample holder (Teflon) is mounted (2). The Cu wires are led through holes in the sample holder and shortened subsequently. (b) Top view of a MnSi sample (4) mounted on the sample holder. The small faces of the sample are soldered onto two $120 \mu\text{m}$ Cu wires (used as current leads) and thus held in a defined orientation (5). As voltage contacts $25 \mu\text{m}$ Pt wires (6) are spot welded onto the up side of the sample. The other ends of the Pt wires are soldered onto $80 \mu\text{m}$ Cu wires exiting the pressure cell. Geometry factors were determined optically via microscope as a first approach (see Sec. 6.4.2). On the bottom left a piece of Sn soldered between Cu leads can be seen (7). The Sn is used as pressure gauge

Table 6.3: Overview of samples and pressure cells. Pressure cells used for magneto-transport and magnetization measurements under pressure. The individual pressure cells will be referred to as pc1, pc2, etc. in the following. ¹ RRR (=residual resistivity ratio) was determined at the lowest pressure available as the ratio $\rho_{xx}(T = 280 \text{ K}) / \rho_{xx}(T \rightarrow 0)$. ² FI: Fluorinet FC72:FC84 (1:1) mixture. ME: methanol:ethanol (4:1) mixture.

pressure cell (pc)	RRR ¹	sample size (m^3)	orientation	pressure medium ²	pressures (kbar)
1	≈93	$2.9 \times 1.0 \times 0.22$	$B \parallel \langle 110 \rangle, I \parallel \langle 100 \rangle$	FI	6.6
2	≈92	$2.8 \times 1.0 \times 0.25$	$B \parallel \langle 110 \rangle, I \parallel \langle 100 \rangle$	FI	7.0, 10.0
3	≈300	$2.5 \times 1.0 \times 0.20$	$B \parallel \langle 110 \rangle, I \parallel \langle 100 \rangle$	ME	10.7
4	≈300	$2.7 \times 0.9 \times 0.20$	$B \parallel \langle 110 \rangle, I \parallel \langle 100 \rangle$	ME	8.1
5	≈45	$2.8 \times 1.0 \times 0.20$	$B \parallel \langle 110 \rangle, I \parallel \langle 110 \rangle$	ME	7.6, 6.7, 5.9, 5.7, 5.1, 4.6, 3.4, 2.9, 2.6, 2.2, 0.3
6	≈40	$2.7 \times 1.0 \times 0.20$	$B \parallel \langle 110 \rangle, I \parallel \langle 100 \rangle$	ME	5.2, 7.4, 9.6, 11.0, 11.2, 12.8, 12.8, 0.4
7	≈45	$2.8 \times 1.0 \times 0.20$	$B \parallel \langle 110 \rangle, I \parallel \langle 110 \rangle$	ME	18.1, 13.7
8	≈150	$2.9 \times 1.1 \times 0.20$	$B \parallel \langle 110 \rangle, I \parallel \langle 100 \rangle$	ME	15.7, 14.7, 13.7, 13.2, 12.3, 11.5, 10.3, 9.3, 7.8, 6.1, 4.9, 3.7, 0.5
M	≈70	$6.0 \times 1.0 \times 1.0$	$B \parallel \langle 100 \rangle$	ME	0.0, 4.05, 7.50, 10.13, 11.80

6.4 Data analysis

6.4.1 Symmetrization & antisymmetrization

Due to unavoidable misalignments of the contact positions there is always a transverse voltage pick-up in the voltage U_l measured along the longitudinal contacts. Vice versa, longitudinal contributions to the voltage U_H are measured along the Hall contacts. Assuming that the magnetoresistance is symmetric and the Hall effect antisymmetric to $B = 0$, the data can be corrected for these misalignment contributions. Through measuring a magnetic field interval of a field sweep ($\rho_{xx}(B), \rho_{xy}(B)$) two times with the field being swept upwards and downwards the relation

$$\rho_{xx} = F_{xx} U_{xx} = F_{xx} \frac{1}{2} (U_l(+B) + U_l(-B)) \quad (6.31)$$

$$\rho_{xy} = -F_{xy} U_{xy} = -F_{xy} \frac{1}{2} (U_H(+B) - U_H(-B)) \quad (6.32)$$

called symmetrization and antisymmetrization, respectively, can be applied. F_{xx} and F_{xy} are geometry factors (see 6.4.2)⁶.

Fig. 6.13 illustrates the application of Eqs. 6.31 and 6.32 to a magnetic field sweep. Panel a and d show raw data of U_l and U_H with measurement directions up (red) and down (blue). The downsweeps (blue) are mirrored about $B = 0$ (panel b and e) and then added to (panel c) or subtracted from (panel f) the upsweeps. The result is one dataset with an effective measurement direction (black curves).

The same relations can be used for temperature sweeps ($\rho_{xx}(T), \rho_{xy}(T)$). There, the temperature sweep is measured two times at magnetic field values $+B$ and $-B$ and Eqs. 6.31 and 6.32 applied subsequently. The resulting dataset refers to a magnetic field with absolute value $|B|$.

6.4.2 Geometry factors

For a quantitative comparison of the data from different pressure cells, the specific resistivities were calculated through multiplying the measured voltages U_{xx} and U_{xy} with geometry factors F_{xx} and F_{xy}

$$\rho_{xx} = \frac{bd}{l_l} \frac{1}{T} \frac{1}{I} U_{xx} = F_{xx} U_{xx} \quad (6.33)$$

$$\rho_{xy} = -\frac{E_{xy}}{J} \frac{1}{T} = -\frac{bd}{l_H} \frac{1}{T} \frac{1}{I} U_{xy} = -F_{xy} U_{xy} \quad (6.34)$$

with sample width b , sample thickness d , distance of transport contacts l_l , distance of Hall contacts l_H , and amplification through a transformer T ⁷ (see Fig. 6.9). In a first

⁶ The minus sign of ρ_{xy} originates from general considerations about the experimental set up (see [192]).

⁷ see footnote 6.

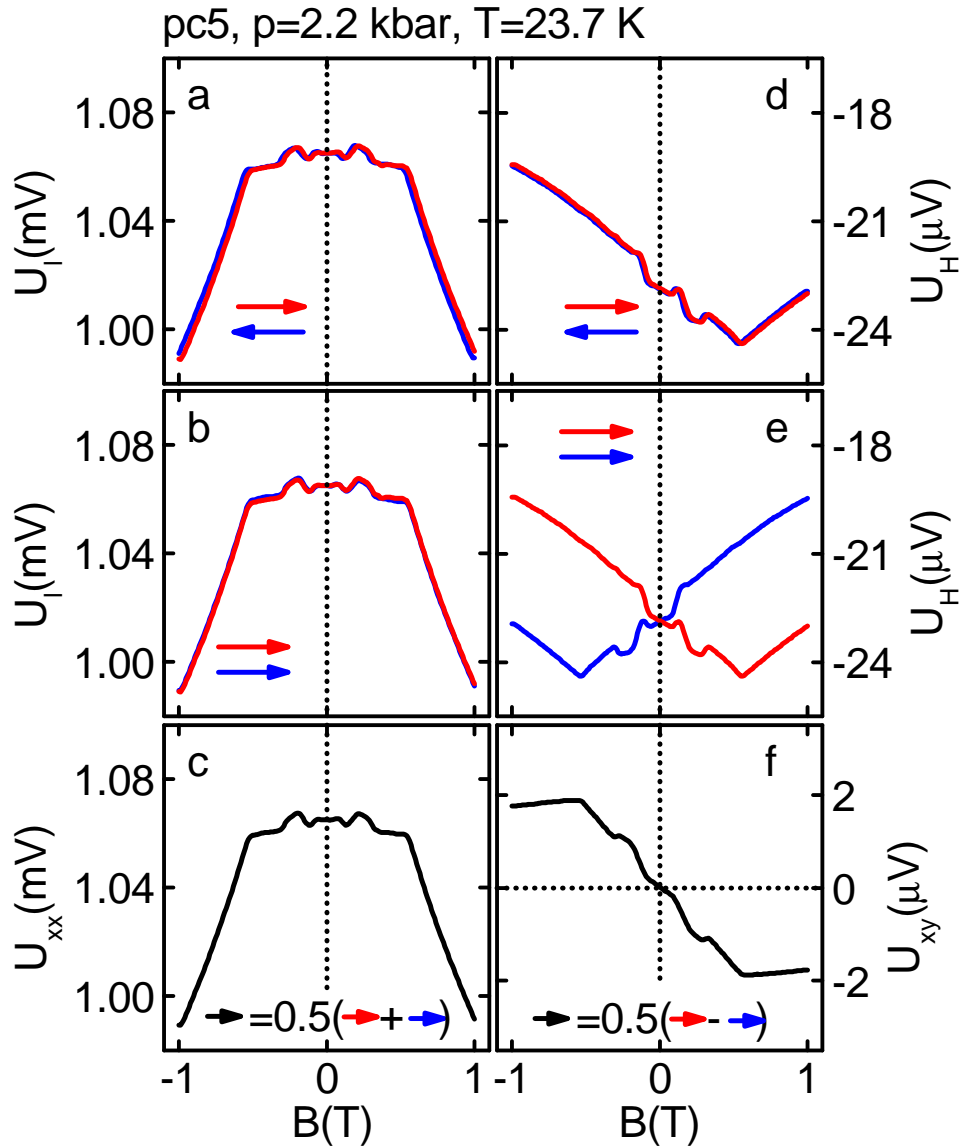


Figure 6.13: Symmetrization and antisymmetrization. (a),(b),(c) Symmetrization of voltages U_l measured along the longitudinal contacts during field sweeps. (d),(e),(f) Antisymmetrization of voltages U_H measured simultaneously along the Hall contacts during the same field sweeps. The arrows indicate the measurement direction of each field sweep.

approach, b , d , l_l and l_H were determined optically through a microscope to calculate the geometry factors $F_{xx,\text{opt}}$ and $F_{xy,\text{opt}}$ (see fig 6.12b). Subsequently, the geometry factors were adjusted via scaling $\rho_{xx}(p)$ and $\rho_{xy}(p)$ data to a reference to achieve a higher accuracy (see below).

As shown in Fig. 6.14a, the pressure dependence of the longitudinal resistance at 35 K, $\rho_{xx}(p, T = 35 \text{ K}, B = 0)$, was extracted from temperature sweeps evaluated with $F_{xx,\text{opt}}$ (full data points). A linear fit of data from Pfeiderer *et al.* [74] and pressure cell pc5, yielding $\rho_{xx}(p, T = 35 \text{ K}, B = 0) = 48 \mu\Omega\text{cm} - 0.8 \mu\Omega\text{cm}/\text{kbar} \cdot p$, was then used as reference to adjust the geometry factors F_{xx} from the other pressure cells. The corresponding scaled $\rho_{xx}(p, T = 35 \text{ K}, B = 0)$ data is shown as open data points.

Analogously, the pressure dependence of the Hall resistance at 2.8 K and 13.5 T, $\rho_{xy}(p, T = 2.8 \text{ K}, B = 13.5 \text{ T})$, was extracted from field sweeps evaluated with $F_{xy,\text{opt}}$ (full data points in Fig. 6.14b). A linear fit of data from pressure cells pc5 and pc6, yielding $\rho_{xy}(p, T = 2.8 \text{ K}, B = 13.5 \text{ T}) = 0.19 \mu\Omega\text{cm} - 0.002 \mu\Omega\text{cm}/\text{kbar} \cdot p$, was then used as reference to adjust the geometry factors F_{xy} from the other pressure cells. The corresponding scaled $\rho_{xy}(p, T = 2.8 \text{ K}, B = 13.5 \text{ T})$ data is shown as open data points.

6.4.3 Demagnetization factors

When a sample is brought into an external magnetic field B_{ext} the actual field at the sample position B_{int} is reduced due to stray fields created by the magnetization M of the sample. This demagnetizing field, which depends on the sample geometry and its magnetization M , can be subtracted from the external field through the relation

$$B_{\text{int}} = B_{\text{ext}} - \mu_0 N M (B_{\text{ext}}) \quad (6.35)$$

with the demagnetizing factor N [222]. For the case of rectangular shaped ferromagnetic samples N can be calculated with the formulas given in Ref. [223] which show that a sample configuration with the long edge parallel and the short edges orthogonal to B_{ext} , as ideally suited for magnetization measurements, yields the smallest N . A Configuration with the shortest edge parallel to B_{ext} , as ideally suited for Hall effect measurements, yields the highest N . In our case, with Hall effect configuration and sample dimensions $0.2 \times 2.8 \times 1 \text{ mm}^3$ $N_H = 0.760$. Magnetization measurements by Halder [224] could be used to determine B_{int} . There, $N_M = 0.079$ with sample dimensions $5.6 \times 1 \times 1 \text{ mm}^3$.

To simplify calculations, we used that in MnSi $\chi = \mu_0 dM/dB$ can be approximated by a constant $\chi_{\text{con}}^{\text{ext}}$ in the field interval $B < B_{c2}$ which contains all features of interest (see Fig. 6.15). For $B > B_{c2}$ the approximation $B_{\text{int}} \approx B_{\text{ext}} - \mu_0 M^{\text{sat}}$ was used as χ becomes small, i.e., the magnetization nearly saturates [225]. With $\mu_0 M(B_{\text{ext}}) \approx \chi_{\text{con}}^{\text{ext}} B_{\text{ext}}$ and $M(B_{c2}^{\text{int}}) = M(B_{c2}^{\text{ext}}) = M^{\text{sat}}$:

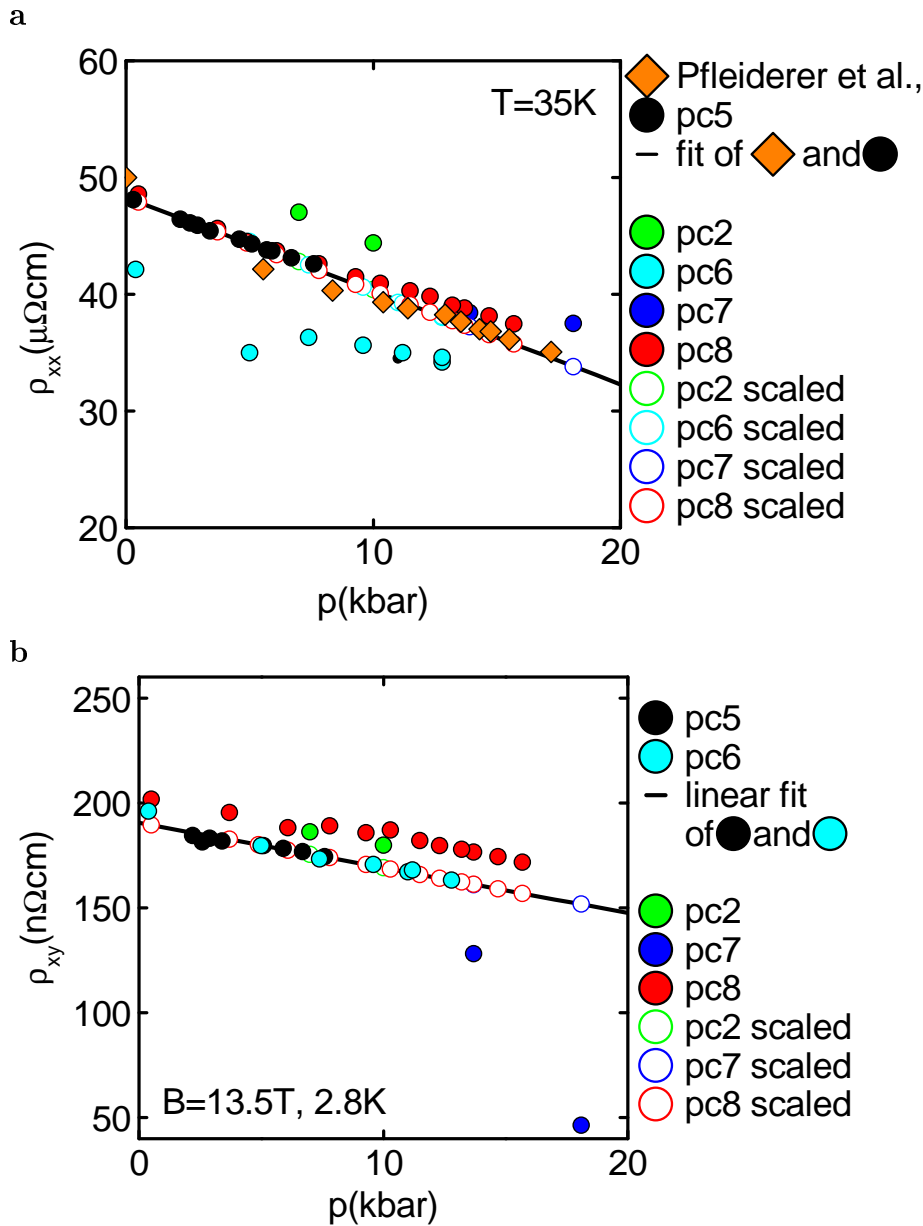


Figure 6.14: Geometry factors. The shown data was used to determine the geometry factors F_{xx} and F_{xy} . (a) ρ_{xx} vs. p taken at 35 K and 0 T for each pressure point. Data calculated with optically determined geometry factor F_{xx} (full data points) was scaled to a linear fit of data from Pfleiderer *et al.* [74] and pressure cell pc5 (open data points). (b) ρ_{xy} vs. p taken at 13.5 T and 2.8 K for each pressure point. Data calculated with optically determined geometry factor F_{xy} (full data points) was scaled to a linear fit of data from pressure cells pc5 and pc6 (open data points).

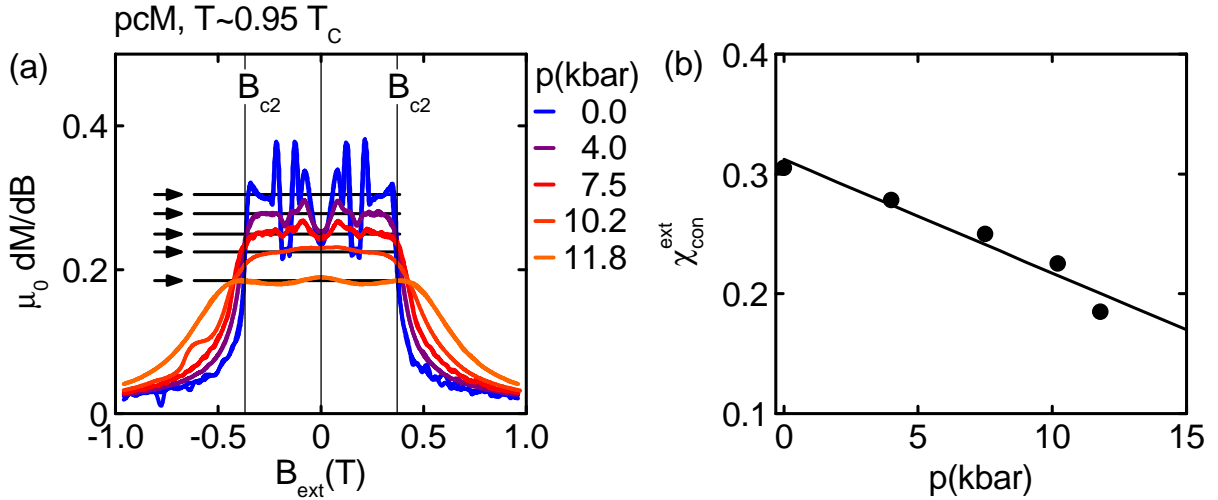


Figure 6.15: Susceptibility under pressure. (a) $\mu_0 dM/dB$ calculated from magnetization measurements from Halder [224]. The plateau values $\chi_{\text{con}}^{\text{ext}}$ of $\mu_0 dM/dB$ for $B < B_{c2}$ indicated by the arrows were fitted linearly to receive an approximation for $\chi_M(p)$ for demagnetization calculations (shown in panel (b)).

$$B_{\text{int}} = B_{\text{ext}} (1 - N\chi_{\text{con}}^{\text{ext}}) \quad (6.36)$$

$$\Rightarrow \chi_{\text{con}}^{\text{int}} = \frac{\mu_0 M^{\text{sat}}}{B_{c2}^{\text{int}}} = \underbrace{\frac{\mu_0 M^{\text{sat}}}{B_{c2}^{\text{ext}}}}_{=\chi_{\text{con}}^{\text{ext}}} \frac{1}{1 - N\chi_{\text{con}}^{\text{ext}}} = \frac{1}{\frac{1}{\chi_{\text{con}}^{\text{ext}}} - N} \quad (6.37)$$

With $\chi_M := \chi_{\text{con},M}^{\text{ext}}$ for magnetization and $\chi_H := \chi_{\text{con},H}^{\text{ext}}$ for Hall effect samples

$$\chi_{\text{con}}^{\text{int}} = \frac{1}{\frac{1}{\chi_M} - N_M} = \frac{1}{\frac{1}{\chi_H} - N_H} \quad (6.38)$$

$$\Rightarrow \chi_H = \frac{\chi_M}{1 - \chi_M(N_M - N_H)} \quad (6.39)$$

$$\text{Magnetization : } B_{\text{int}} = B_{\text{ext}} (1 - N_M \chi_M) \quad (6.40)$$

$$\text{Halleffect : } B_{\text{int}} = B_{\text{ext}} \left(1 - N_H \frac{\chi_M}{1 - \chi_M(N_M - N_H)} \right) \quad (6.41)$$

For $B < B_{c2}$ the field reduction of B_{ext} in the Hall effect experiments ranged between 12% at 11.8 kbar and 19% at ambient pressure.

6.4.4 Determination of pressures

For each pressure point the pressure value was determined through a comparison of the transition temperature T_c , inferred from the position T_{max} of the maximum in $dU_l(T)/dT$,

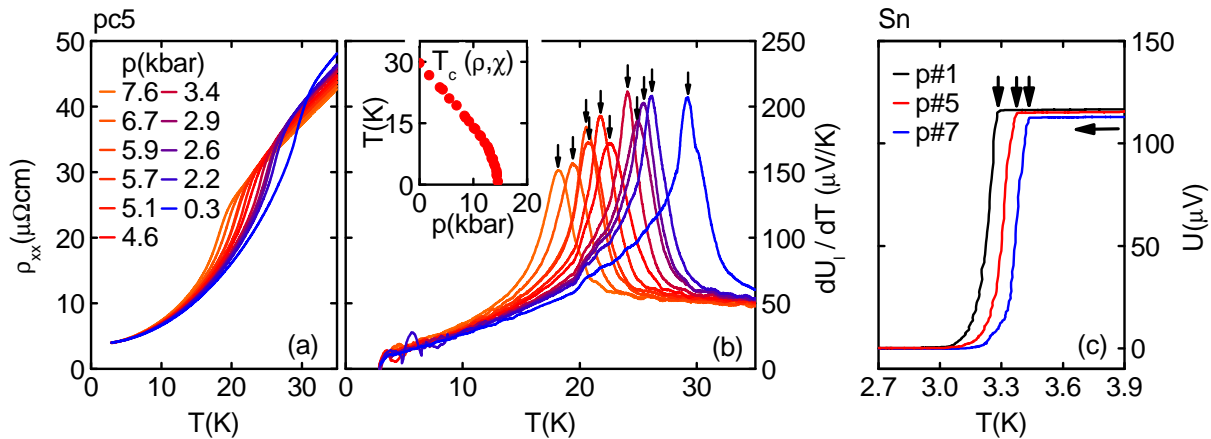


Figure 6.16: Determination of pressure values. (a) $\rho_{xx}(T)$ and (b) $dU_l(T)/dT$ from pressure cell pc5 where U_l is the raw signal measured along the longitudinal voltage contacts. The transition temperature T_c was inferred from the position T_{\max} of the peak in $dU_l(T)/dT$. The inset shows $T_c(p)$ inferred from ρ and χ data from Pfeleiderer *et al.* [74]. (c) Pressure dependent superconducting transition of a piece of Sn inside the same pressure cell.

with $T_c(p)$, inferred from ρ and χ data, from Pfeleiderer *et al.* [74]. Fig. 6.16 illustrates this for pressure cell pc5 as a showcase. The consistency between the pressure value inferred from $dU_l(T_{\max})/dT$ and the pressure value inferred from the pressure dependent superconducting transition of a piece of Sn, mounted inside the same pressure cell, was checked for several pressures and was in good agreement [226].

Pressure values above p_c , where T_c is suppressed, were determined through the Sn-transition and alternatively through extrapolating the characteristic pressure dependence of $\rho_{xx}(T = 35 \text{ K}, B = 0)$ and $\rho_{xy}(T = 2.8 \text{ K}, B = 13.5 \text{ T})$ in cases where the Sn could not be measured due to, e.g., broken contact wires (see Sec. 6.4.2).

The accuracies lie around $\pm 0.5 \text{ kbar}$ for absolute pressure values and around $\pm 0.2 \text{ kbar}$ for relative pressure values between different pressure points of the same pressure cell.

6.4.5 Influence of pressure media and cooling procedures

The size and occurrence of the topological Hall signal ρ_{xy}^{top} in MnSi showed differences depending on (i) the pressure transmitting medium and (ii) the cooldown procedure consistent with uniaxial strains in the sample produced by non-hydrostatic components in the pressure transmitting medium.

(i) As shown in Fig. 7.10a (p. 134), experiments performed with a Fluorinert FC72:FC84 mixture with volume ratio 1:1 (FC) as pressure transmitting medium produced an A-phase extending over a much wider temperature region as opposed to experiments with a methanol:ethanol mixture with volume ratio 4:1 (ME). ME is known to provide better hydrostatic pressure conditions than Fluorinert mixtures. This is, e.g., reflected in a much higher hydrostatic limit of $\approx 100 \text{ kbar}$ [221] of ME as compared to a hydrostatic

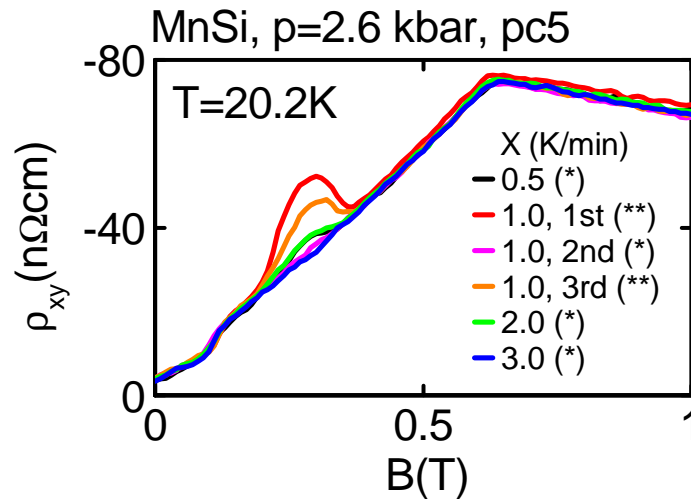


Figure 6.17: Effect of cooling procedure on THE. The same field-sweep measured after cooldown procedures with different cooling rates X through the solidification points of methanol (175 K) and ethanol (159 K). The following cooling procedures were used: 300 K/250 K \rightarrow 200 K @ 3 K/min, 200 K \rightarrow 100 K @ X K/min, 100 K \rightarrow 15 K @ 3 K/min, 15 K \rightarrow 3 K @ 1 K/min with X values given in the graph. (*) After sample was heated to 250 K with 1 h waiting time for thermalization. (**) After sample-stick was removed from cryostat for complete warm-up. The topological Hall signal ρ_{xy}^{top} depends sensitively on the cooling procedure. See text for details.

limit of ≈ 20 kbar [141] of Fluorinert mixtures. As discussed later in Sec. 7.3, the extended A-phase is consistent with typical anisotropies ($\lesssim 10^{-1}$ kbar) reported to occur in Fluorinert mixtures. As a consequence all experiments, following the first ones, were performed with ME as pressure transmitting medium.

(ii) When cooling a pressure cell, the liquid pressure medium solidifies which potentially leads to non-hydrostatic pressure components. Like shown by Sidorov *et al.* [141], for Fluorinert mixtures a hydrostatic pressure can be retained when cooling with a small rate of 1 K/min. Hence, all experiments were performed with a cooling rate of 1 K/min through the interval 200 K-100 K containing the solidification points of methanol (175 K) and ethanol (159 K). Fig. 6.17 shows the Hall effect $\rho_{xy}(B)$ of MnSi at 2.6 kbar for different cooldown procedures in a pressure cell with ME as pressure transmitting medium (pc5). The largest topological Hall signals ρ_{xy}^{top} are observed for the initial cooldowns from room temperature with a rate of 1 K/min through the interval 200 K-100 K. Heating the pressure cell to 250 K and cooling down again at different rates between 0.5 K/min and 3 K/min produces a reduced ρ_{xy}^{top} illustrating the dependence on the cooling procedure.

It is important to note that earlier Hall effect measurements on MnSi under pressure by Lee *et al.* [162] were performed with a single component Fluorinert FC77, known to have poor hydrostatic pressure properties. We believe that this produced the unusual topological Hall signal smeared out over a wide field region (up to B_{c2}) they observed.

Chapter 7

Results $p < p^*$

7.1 Magnetic field dependence

The Hall effect $\rho_{xy}(B)$ shows a pressure dependent top-hat shaped signal whose size increases up to $\approx 40 \text{ n}\Omega\text{cm}$ with pressures up to 12 kbar. As shown below, through studying field boundaries, pressure dependence, and the evolution of its size, the top-hat signal in $\rho_{xy}(B)$ can be attributed to the topological Hall effect (THE) signal $\Delta\rho_{xy}^{\text{top}} \approx 4.5 \text{ n}\Omega\text{cm}$ seen at ambient pressures [15]. Measurements on samples with different qualities and the usage of different pressure transmitting media suggest that the large top-hat signal reported by Lee *et al.* [162] also represents a THE signal. However, as we can show, the signal they observed is broadened due to low sample quality and pressure inhomogeneities and hence emerges in an unexpected field range.

Fig. 7.1 shows the magneto-transport properties of MnSi at 2.8 K for pressures up to 11.5 kbar and fields up to 14 T. With increasing field the magnetoresistance $\rho_{xx}(B)$ normalized to $\rho_{xx}(B=0)$ drops, i.e., shows a negative magnetoresistance, from the sharp maximum at $B=0$ by about 9% up to B_{c2} , shows a shallow minimum and increases again to higher fields, i.e., shows a positive magnetoresistance at high fields. With pressure increasing up to ≈ 12 kbar the same qualitative behavior is observed (Fig. 7.1a). The Hall resistivity $\rho_{xy}(B)$ decreases down to $\approx -190 \text{ n}\Omega\text{cm}$ with increasing field and displays only a small increase with increasing pressure by about 10% at 14 T from 0.5 kbar to 11.5 kbar (Fig. 7.1b). Its slope, and hence the charge carrier concentration, does essentially not change with pressure, and with it the normal Hall constant $R_0(p, T=2.8 \text{ K})$ derived from the slope of $\rho_{xy}(B)$ above 10 T as shown later in Fig. 8.1b. The Hall conductivity $\sigma_{xy} = -\frac{\rho_{xy}}{\rho_{xx}^2 + \rho_{xy}^2} \approx -\frac{\rho_{xy}}{\rho_{xx}^2}$ is practically featureless and shows only small non-linear contributions due to the AHE. σ_{xy} has only a small pressure dependence and drops by about 5% at 14 T from 0.5 kbar to 11.5 kbar (Fig. 7.1c).

The magneto-transport properties at small fields up to 1 T are shown in Fig. 7.2 for a pressure of 7.0 kbar and at various temperatures below and above $T_c = 19.2 \text{ K}$. At temperatures above T_c , $\rho_{xx}(B)$ displays a featureless negative magnetoresistance (Fig. 7.2a). Below T_c , $\rho_{xx}(B)$ rises up to B_{c1} before it drops with distinct changes of slope at B_{c1} and B_{c2} . In a field and temperature range somewhat larger than the skyrmion lattice phase

(SLP) at ambient pressure, $\rho_{xx}(B)$ displays a shallow maximum. In the same range a top-hat shaped signal can be observed in the Hall resistivity $\rho_{xy}(B)$ on top of NHE and AHE contributions to the Hall effect (Fig. 7.2b). The size of $\approx 40 \text{ n}\Omega\text{cm}$, which is tenfold the size of $\Delta\rho_{xy}^{\text{top}} \approx 4.5 \text{ n}\Omega\text{cm}$ at ambient pressure, is in agreement with the signal reported by Lee *et al.* [162].

The top-hat signal appears and vanishes abruptly at certain fields B_{a1} and B_{a2} as it is expected of a THE contribution. However, the field range does not expand all the way from B_{c1} to B_{c2} , as reported by Lee *et al.* [162], but is smaller. Through studying samples of different qualities, i.e. different RRRs, we can show that the extended field range is an effect seen in low quality samples as used by Lee *et al.* [162]. Higher quality samples show the top-hat signal in a smaller field range as will be discussed in Fig. 7.5. In the temperature range where the top-hat signal can be observed, the size of the Hall conductivity $\sigma_{xy} = -\frac{\rho_{xy}}{\rho_{xx} + \rho_{xy}^2} \approx -\frac{\rho_{xy}}{\rho_{xx}^2}$ increases with decreasing temperature before vanishing like $\Delta\rho_{xy}^{\text{top}}$ at ambient pressure when exiting the SLP (Fig. 7.2c). Also, the signal increase in σ_{xy} on cooling is expected for a THE since the polarization increases with the magnetization as opposed to a temperature independent $\sigma_{xy}^{\text{AH-int}} \propto \rho_{xx}^0$ expected for the intrinsic AHE seen otherwise in MnSi (see Sec. 6.2.3). Thus, the data suggests that the top-hat signal can be identified with a THE.

Fig. 7.3 shows examples of typical $\rho_{xx}(B)$ curves for $T < T_c$ (panels a and c) and $\rho_{xy}(B)$ curves at temperatures where the top-hat signal is observed under pressures up to 12 kbar (panels b and d). The transition fields B_{c1} , B_{c2} and B_{a1} , B_{a2} , identified by distinct changes of slope, are indicated by arrows. As explained in Sec. 6.4.1, symmetrization/antisymmetrization yields datasets with an effective measurement direction from negative to positive field, i.e., here from -1 T to 1 T. Hence, transition fields at negative (positive) effective fields were measured at decreasing (increasing) fields and are labeled with the superscript “-” (“+”). The data for pressures $p > p_c$ shown in panels e to i will be covered in Chap. 9.

The fields B_{c1} and B_{c2} can be identified in $\rho_{xx}(B)$ where the signatures of B_{c1} and B_{c2} change qualitatively with temperature and pressure. At lower pressures $\rho_{xx}(B)$ displays a maximum at $B = 0$ whereas it displays a shallow minimum up to B_{c1} at higher pressures. With increasing temperature, the curvature $d^2\rho_{xx}(B = B_{c2})/dB^2$ changes from positive to negative. The fields B_{c2} , B_{a1} and B_{a2} can be identified in $\rho_{xy}(B)$ which shows the same qualitative field dependence at all pressures up to 12 kbar. In contrast to B_{c1} and B_{c2} a hysteresis is observed for B_{a1} and B_{a2} (see below).

Fig. 7.4a shows the Hall resistivity $\rho_{xy}(B)$ at 7.4 kbar in the temperature range of the top-hat signal for increasing (red curve) and decreasing (blue curve) fields. B_{a1} and B_{a2} show a hysteresis indicating a first order transition into the SLP whereas no hysteresis is observed outside of it. The size $\Delta\rho_{xy}^{\text{top}}$ of the top-hat signal can be determined after subtracting NHE and AHE contributions from $\rho_{xy}(B)$ (Fig. 7.4b). The slope of the NHE is determined at fields $B > B_{c2}$ and subtracted from $\rho_{xy}(B)$ first. In a second step the AHE contribution, assumed linearly in B up to B_{c2} , is subtracted yielding

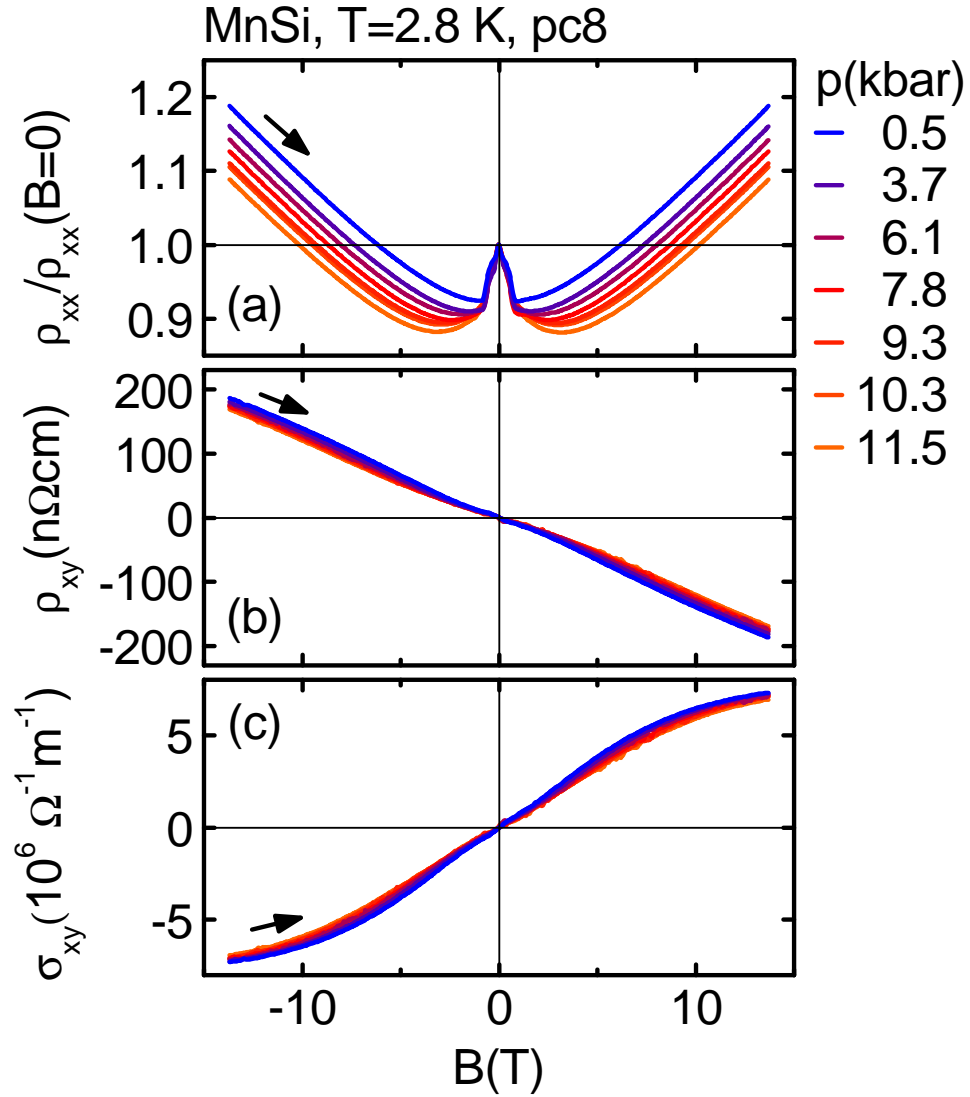


Figure 7.1: Magneto-transport properties at 2.8 K up to 14 T for pressures up to 11.5 kbar. (a) Magnetoresistance $\rho_{xx}(B)$ normalized to $\rho_{xx}(B=0)$. (b) Hall resistivity $\rho_{xy}(B)$. (c) Hall conductivity $\sigma_{xy} = -\frac{\rho_{xy}}{\rho_{xx}^2 + \rho_{xy}^2} \approx -\frac{\rho_{xy}}{\rho_{xx}^2}$.

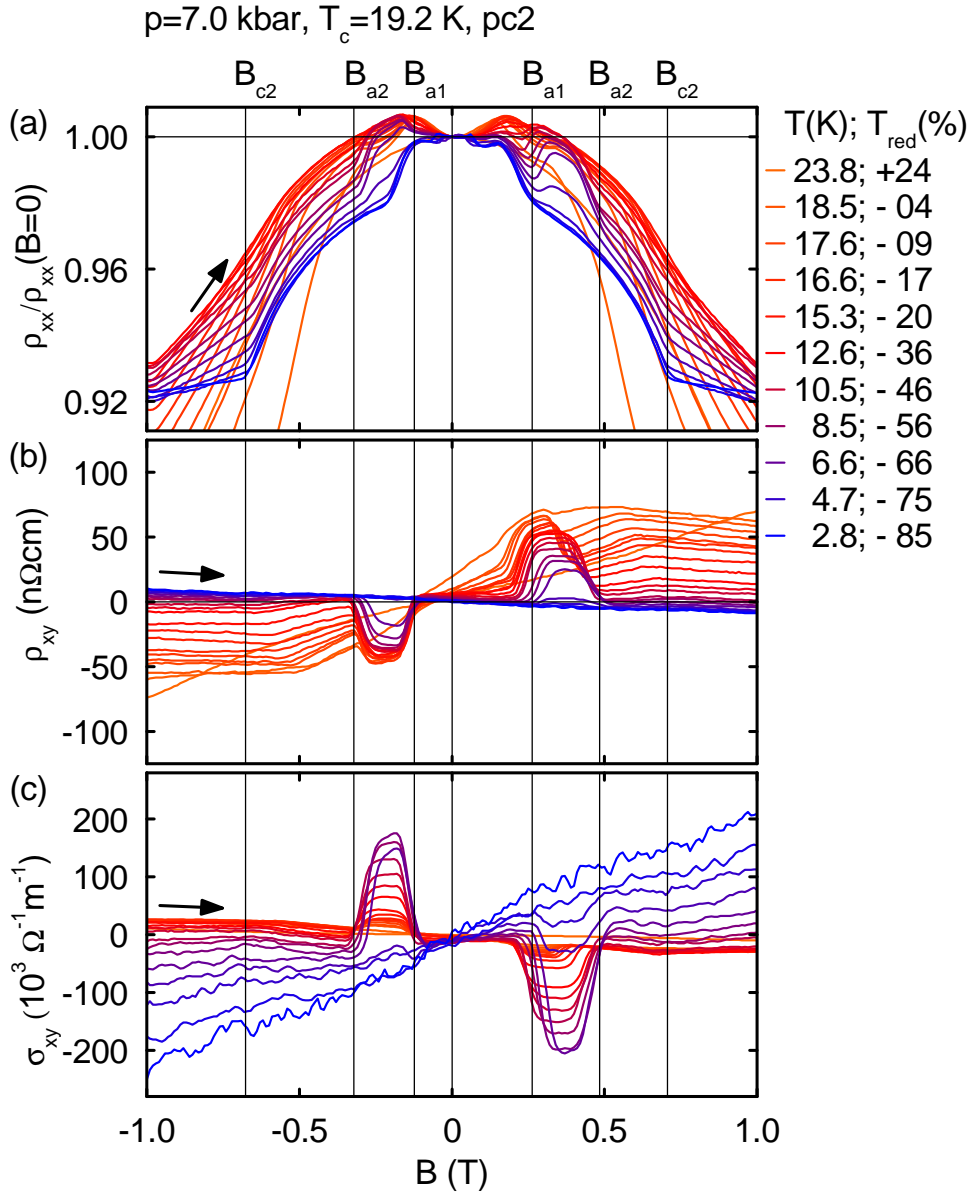


Figure 7.2: Magneto-transport properties at 7.0 kbar for various temperatures below and above $T_c = 19.2$ K for small magnetic fields up to 1 T. (a) Magnetoresistance $\rho_{xx}(B)$ normalized to $\rho_{xx}(B=0)$. (b) Hall resistivity $\rho_{xy}(B)$. On top of the NHE and AHE contributions to the Hall effect a top-hat shaped signal can be observed in $\rho_{xy}(B)$ in a field and temperature range somewhat larger than the skyrmion lattice phase (SLP) at ambient pressure. (c) Hall conductivity $\sigma_{xy} = -\frac{\rho_{xy}}{\rho_{xx}^2 + \rho_{xy}^2} \approx -\frac{\rho_{xy}}{\rho_{xx}^2}$.

$\rho_{xy}^* = (\rho_{xy} - \rho_{xy}^{NHE}) - \rho_{xy}^{AHE}$ in which a clear peak can be seen. $\Delta\rho_{xy}^{\text{top}}$ is then estimated as the peak height as illustrated.

When considering the evolution of the top-hat signal in the Hall resistivity $\rho_{xy}(B)$, the peak height increases up to $\approx 50 \text{ n}\Omega\text{cm}$ at 12 kbar, i.e., to the tenfold size of the THE signal at ambient pressure (Fig. 7.5). A comparison with the magnetization $M(B)$ from Halder [224] shows that the boundaries of the top-hat signal coincide with that of the SLP, and that it cannot originate from a feature in the uniform magnetization $M(B)$. Thus, an AHE can be ruled out as origin suggesting a THE. Furthermore, the field and temperature range of the top-hat signal proves to be dependent on the sample quality and explains the wide field range reported by Lee *et al.* [162].

Fig. 7.5a and b show the Hall resistivity $\rho_{xy}(B)$ at low fields in two samples of different quality, $\text{RRR}\approx 45$ and $\text{RRR}\approx 150$, at a reduced temperature $T_{\text{red}} = (T - T_c)/T_c$ where the top-hat signal becomes maximal ($T_{\text{red,max}}$). Dependent on the sample quality $\rho_{xy}(B)$ exhibits changes. First, the top-hat signal peaks at different reduced temperatures. For the low quality sample $T_{\text{red,max}} \approx -0.17$, i.e., the largest top-hat signal is observed at $T = 0.83 T_c$. For the high quality sample $T_{\text{red,max}} \approx -0.04$, i.e., the largest top-hat signal is observed at $T = 0.96 T_c$. However, the size of the top-hat signal proves to be independent of sample quality. Second, in the high quality sample the temperature and field range coincides well with the SLP at ambient pressure, whereas in the low quality sample the field range of the top-hat signal is much wider and also a different temperature dependence is observed. Experiments with a FC72:FC84 Fluorinert mixture (FI) as pressure transmitting medium (instead of a Methanol:Ethanol mixture (ME) used otherwise), known to provide much less isotropic pressure conditions, also lead to an extended temperature and field range of the top-hat signal (see Fig. 7.10a). The changed top-hat signal in low quality samples suggests that local differences of the compressibility of MnSi in the vicinity of defects and inhomogeneities leads to pressure inhomogeneities and local uniaxial strain. Taken together, the top-hat signal reported by Lee *et al.* [162], which extended up to B_{c2} , seems to be due to a combination of a low sample quality ($\text{RRR}\approx 50$) and inhomogeneous pressure conditions. In Ref. [162] a single component Fluorinert FC:77 was used, known to yield even less favorable pressure homogeneity than Fluorinert mixtures [141]. Third, the non-top-hat signal part of $\rho_{xy}(B)$ of the low quality sample is much less pressure dependent than the high quality sample. Since the dominant AHE contribution follows the relation $\rho_{xy} = R_0 B + S_H \rho_{xx}^2 M$ [213], the decrease in ρ_{xy} reflects the decrease in ρ_{xx} as the temperature range of the magnetic phase is shifted to lower temperatures with increasing pressure. The decrease is larger in the high quality sample in which ρ_{xx} converges against a lower residual resistance as compared to the low quality sample.

Fig. 7.5c illustrates magnetization data in a sample with $\text{RRR}\approx 70$ at a reduced temperature 5% below T_c , according to $T_{\text{red,max}}$ observed in the high quality Hall effect sample. $M(B)$ qualitatively tracks $\rho_{xy}(B)$ outside the top-hat signal region as expected for a dominating AHE contribution. In turn, inside the field region of the top-hat signal in $\rho_{xy}(B)$ the magnetization $M(B)$ does not show a comparable signature and even decreases by $\approx 20\%$ with pressure increasing up to 12 kbar, whereas the size of the top-hat

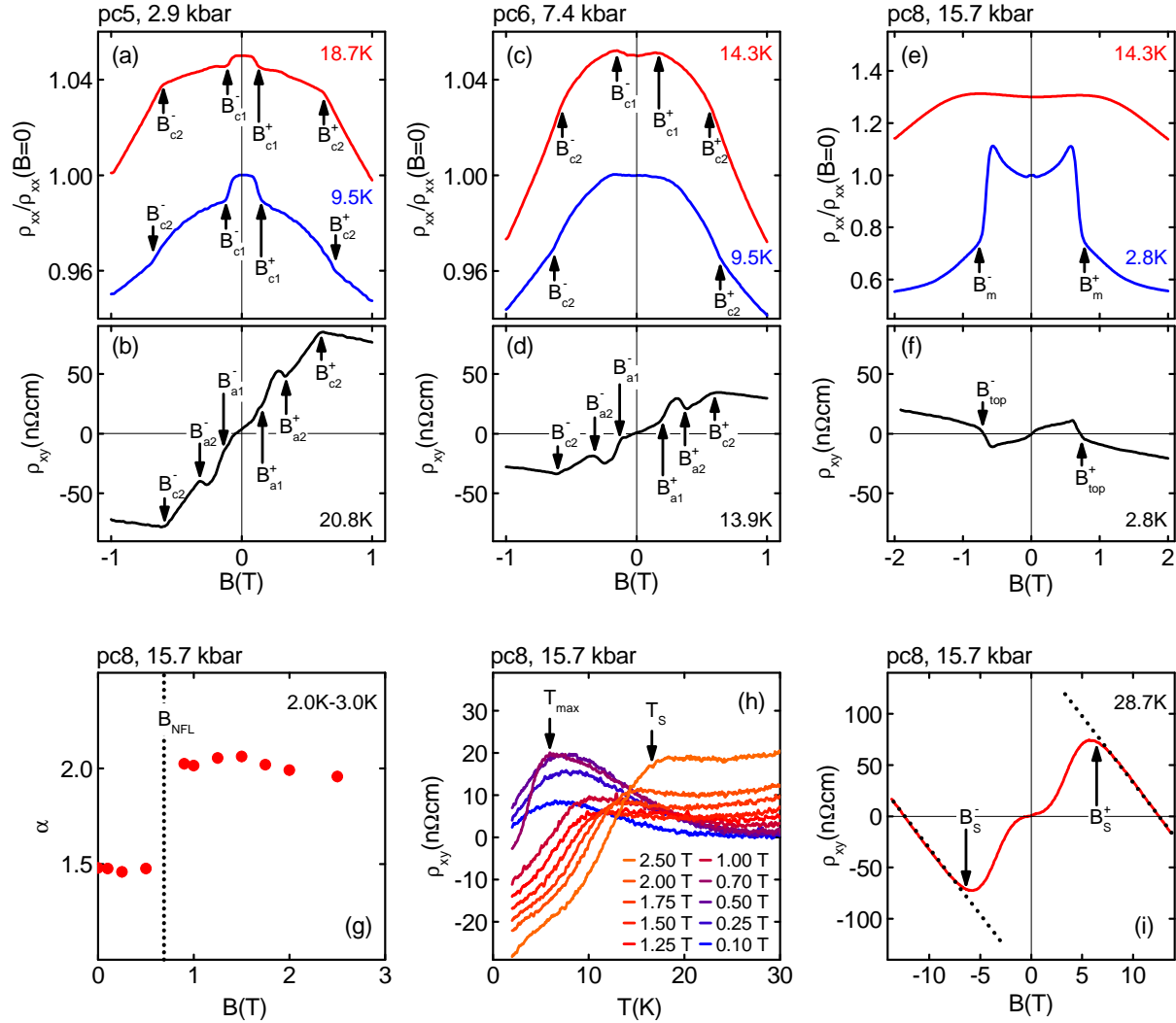


Figure 7.3: Typical Hall effect and magnetoresistance of MnSi under pressure. Examples of typical $\rho_{xx}(B)$ curves for $T < T_c$ (panels a,c,e), $\rho_{xy}(B)$ curves at temperatures where the top-hat signal is observed for pressures $< p_c$ (panels b,d), and $\rho_{xy}(B)$ at 2.8 K for $p > p_c$ where a broad feature emerges in the Hall effect (panel f). The transition fields B_{c1} , B_{c2} and B_{a1} , B_{a2} for $p < p_c$, and B_m , B_{top} for $p > p_c$, that are identified by distinct changes of slope, are indicated by arrows. (g) Exponent α from $\rho_{xx}(T)$. (h) Temperature dependent Hall resistivity $\rho_{xy}(T)$. (i) Hall resistivity $\rho_{xy}(B)$ up to high fields.

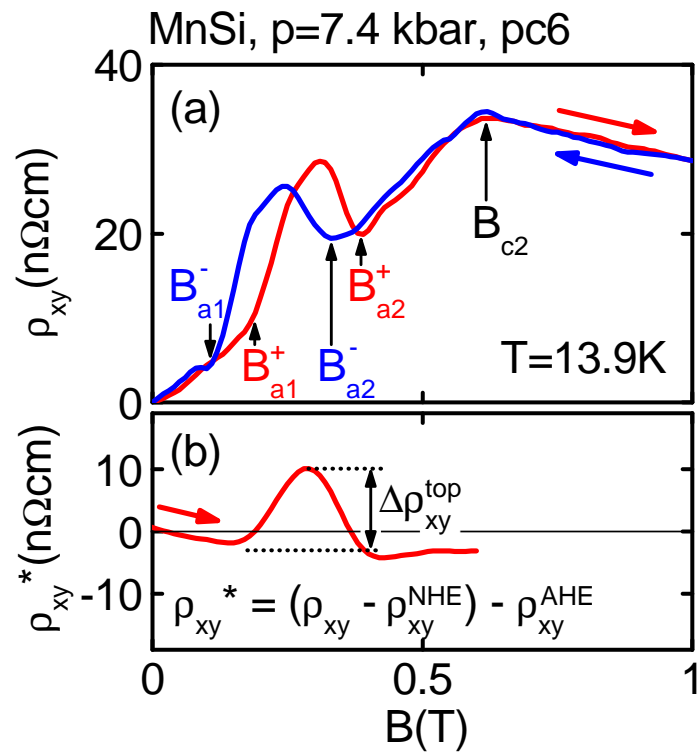


Figure 7.4: Field range and size of the THE signal. (a) Hall resistivity $\rho_{xy}(B)$ at 7.4 kbar in the temperature range of the top-hat signal for increasing (red curve) and decreasing (blue curve) fields. B_{a1} and B_{a2} show a clear hysteresis. (b) The size $\Delta\rho_{xy}^{\text{top}}$ of the top-hat signal can be determined after subtracting NHE and AHE contributions from $\rho_{xy}(B)$. The size of $\Delta\rho_{xy}^{\text{top}}$ was estimated as the peak height as illustrated.

signal increases. Hence, the top-hat signal does not derive from an AHE contribution tracking a feature in the magnetization. This supports a THE contribution as origin.

Susceptibility dM/dH data calculated from the magnetization (Fig. 7.5d) allows to visualize even small changes in $M(B)$ as well as to track transition fields as a comparison with AC susceptibility data recently showed [153]. The phase boundaries of the SLP at ambient pressure are clearly visible as spikes, indicating a first order transition, and coincide with the field region of the top-hat signal in $\rho_{xy}(B)$ (Fig. 7.5d). Under pressure, the transition fields are unchanged while the spike signatures smear out. The presence of the top-hat signal in $\rho_{xy}(B)$ in the same pressure region suggests that the spikes in dM/dH smear out due to small pressure inhomogeneities while the SLP remains.

In summary, the field dependence of Hall resistivity, Hall conductivity, magnetization and susceptibility at various pressures and temperatures allows us to attribute the top-hat signal in $\rho_{xy}(B)$ and $\sigma_{xy}(B)$ to the THE signal at ambient pressure. Hence, the top-hat signal will be referred to as $\Delta\rho_{xy}^{\text{top}}$ in the following. Its size increases by a factor of ≈ 10 from $4.5 \text{ n}\Omega\text{cm}$ at ambient pressure to $\approx 40 \text{ n}\Omega\text{cm}$ at 12 kbar. The field and temperature range of $\Delta\rho_{xy}^{\text{top}}$ does not change with pressure, however, it depends on sample quality and pressure conditions. The top-hat signal reported by Lee *et al.* [162] can be identified as a $\Delta\rho_{xy}^{\text{top}}$ broadened due to poor sample quality and pressure conditions.

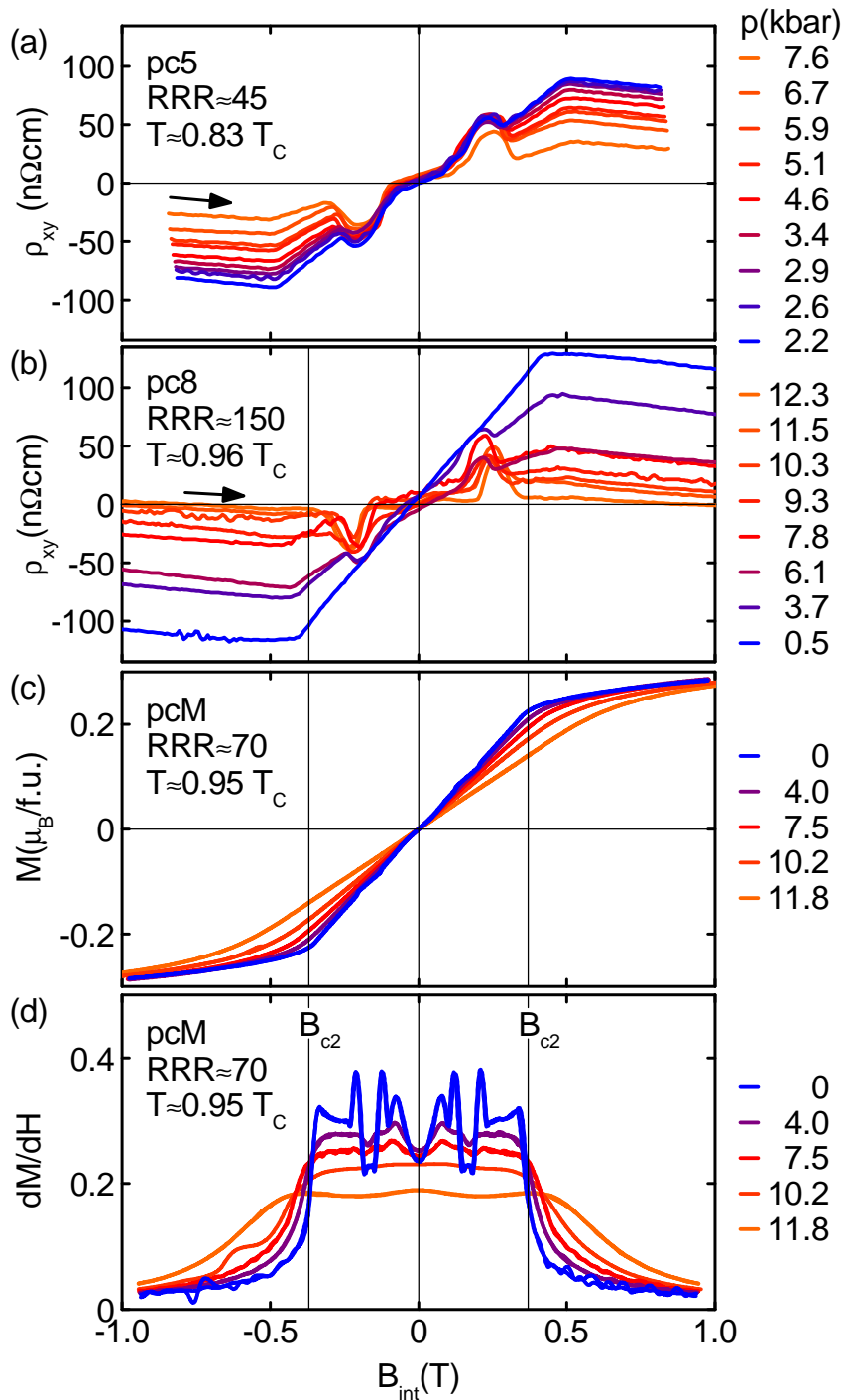


Figure 7.5: Hall effect and magnetization at small fields under pressure. Hall resistivity $\rho_{xy}(B)$ for a low and a high quality sample in comparison to magnetization data from Halder [224] at various pressures up to 12.3 kbar. The data was taken at comparable reduced temperatures below T_c where a maximal top-hat signal was observed (see text). All field values were corrected for demagnetization effects (see Sec. 6.4.3). The Hall effect data has an effective field sweep direction from negative to positive fields indicated by arrows, whereas for the magnetization data both field sweep directions are shown. (a) $\rho_{xy}(B)$ in a low quality sample with $\text{RRR} \approx 45$ at $T \approx 0.83 T_c$. (b) $\rho_{xy}(B)$ in a high quality sample with $\text{RRR} \approx 150$ at $T \approx 0.96 T_c$. (c) Magnetization $M(B)$ in a sample with $\text{RRR} \approx 70$. (d) Susceptibility dM/dH calculated from the magnetization.

7.2 Temperature dependence

The temperature dependent Hall resistivity $\rho_{xy}(T)$ shows a metastable high value down to the lowest temperatures measured after field cooling at fields where a top-hat $\Delta\rho_{xy}^{\text{top}}$ signal is seen in $\rho_{xy}(B)$. A comparison with the magnetization identifies the metastable signal as THE, implying a metastable skyrmion lattice phase (SLP) as origin, like it was seen in $\text{Fe}_{1-x}\text{Co}_x\text{Si}$ in small angle neutron scattering studies [159]. Furthermore, a dependence on sample quality is discussed.

Typical $\rho_{xy}(T)$ data at pressures up to $\approx 12 \text{ kbar}$ is illustrated in Fig. 7.6a,b,c. Two different measurement procedures were performed: (i) Data recorded on heating in a magnetic field after cooling in zero field, labeled as “zfc/fh”. (ii) Data recorded on heating in a magnetic field after cooling down in the same unchanged field, labeled as “fc/fh”. As a crosscheck, data recorded while cooling in a field yielded the same results as recording on heating in the same field after field cooling, thereby justifying the fc/fh procedure. The lowest temperature accessible was typically 2K.

At pressures below p_c and magnetic fields outside the SLP, $\rho_{xy}(T)$ behaves as expected for a dominating AHE contribution, following the relation $\rho_{xy} = R_0 B + S_H \rho_{xx}^2 M$ [213]. $\rho_{xy}(T)$ shows a maximum at T_c and becomes small for both low and high temperatures due to the dropping resistivity ρ_{xx} and magnetization M , respectively. Fc/fh and zfc/fh yield the same results (Fig. 7.6a and c). However, for fields inside the SLP a high Hall signal remains below T_c for fc/fh while zfc/fh curves drop to low temperatures as seen at other field values (Fig. 7.6b). This implies a metastable SLP down to the lowest temperatures measured. So once the SLP is prepared, thermal fluctuations cannot unwind the magnetic structure. Further tests show that the fc/fh procedure is the only way to obtain a high Hall signal down to lowest temperatures. $\rho_{xy}(T)$ at pressures above p_c illustrated in Fig. 7.6d,e,f will be covered in Chap. 9.

When studying $\rho_{xy}(T)$ at various pressures in samples of different quality, a considerable variation can be seen in the metastable Hall signal that emerges under pressure at temperatures below T_c for field cooled measurements. Fig. 7.7 shows $\rho_{xy}(T)$ for a high quality sample with $\text{RRR} \approx 150$ in the panels on the left hand side and for a low quality sample with $\text{RRR} \approx 45$ on the right hand side. Panel a and d display field cooled measurements, panel b and e display the corresponding zero field cooled measurements, and finally panel c and f display the differences between field and zero field cooled measurements. The metastable Hall signal shows much less variation in the low quality sample than in the high quality sample, suggesting that pinning at defects is needed to stabilize the field cooled SLP at low temperatures. At all pressures and for all samples studied the metastable Hall signal converges against a limit of $\approx 50 \text{ n}\Omega\text{cm}$.

A comparison of the Hall resistivity $\rho_{xy}(T)$ with the magnetization $M(T)$ allows to distinguish between AHE and a THE contributions, since the AHE scales with the uniform magnetization whereas the THE does not. Fig. 7.8 shows magnetization measurements under pressure from Halder [224] which were performed following the same zfc/fc and fc/fh

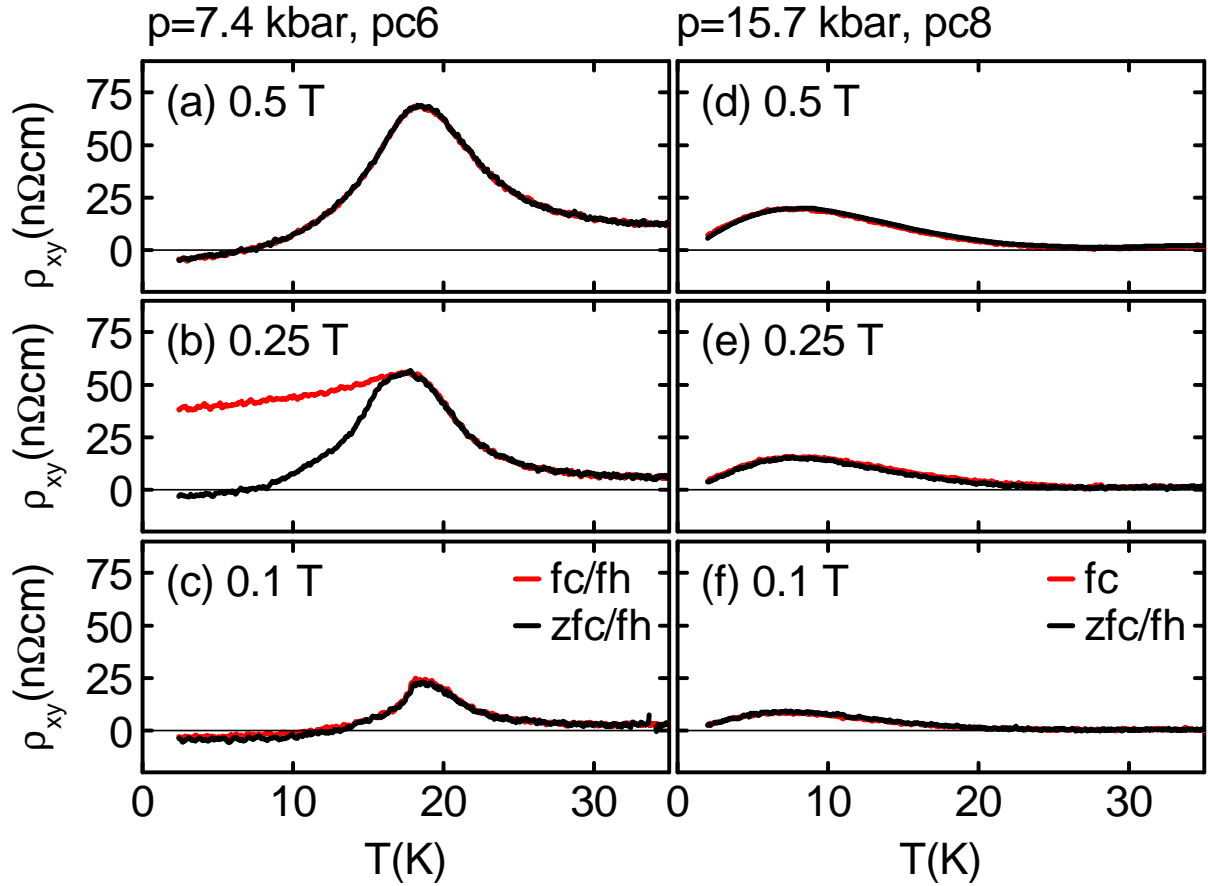


Figure 7.6: Temperature dependent Hall effect below and above the critical pressure. Temperature dependent Hall resistivity $\rho_{xy}(T)$ at 7.4 kbar (panels a,b,c) and 15.7 kbar (panels d,e,f), i.e. below and above p_c at various magnetic fields. Curves obtained for two different measurement procedures are shown: Black curves were measured while heating in a field after cooling in zero-field (zfc/fh). Red curves were measured while heating in a field after cooling in the same field (fc/fh) or while cooling in a field (fc) which was checked to yield the same results as fc/fh. At fields above and below the field range of the SLP no difference between zfc/fh and fc/fh,fc is observed. At pressures below p_c , $\rho_{xy}(T)$ is governed by a broad peak around T_c while above p_c a small smeared out peak emerges below ≈ 15 K, i.e. in the NFL region. In the field region of the SLP a metastable Hall signal is observed down to the lowest temperatures for fc/fh measured curves at pressures below p_c (panel b). At pressures above p_c , no difference is observed at the same field (panel e).

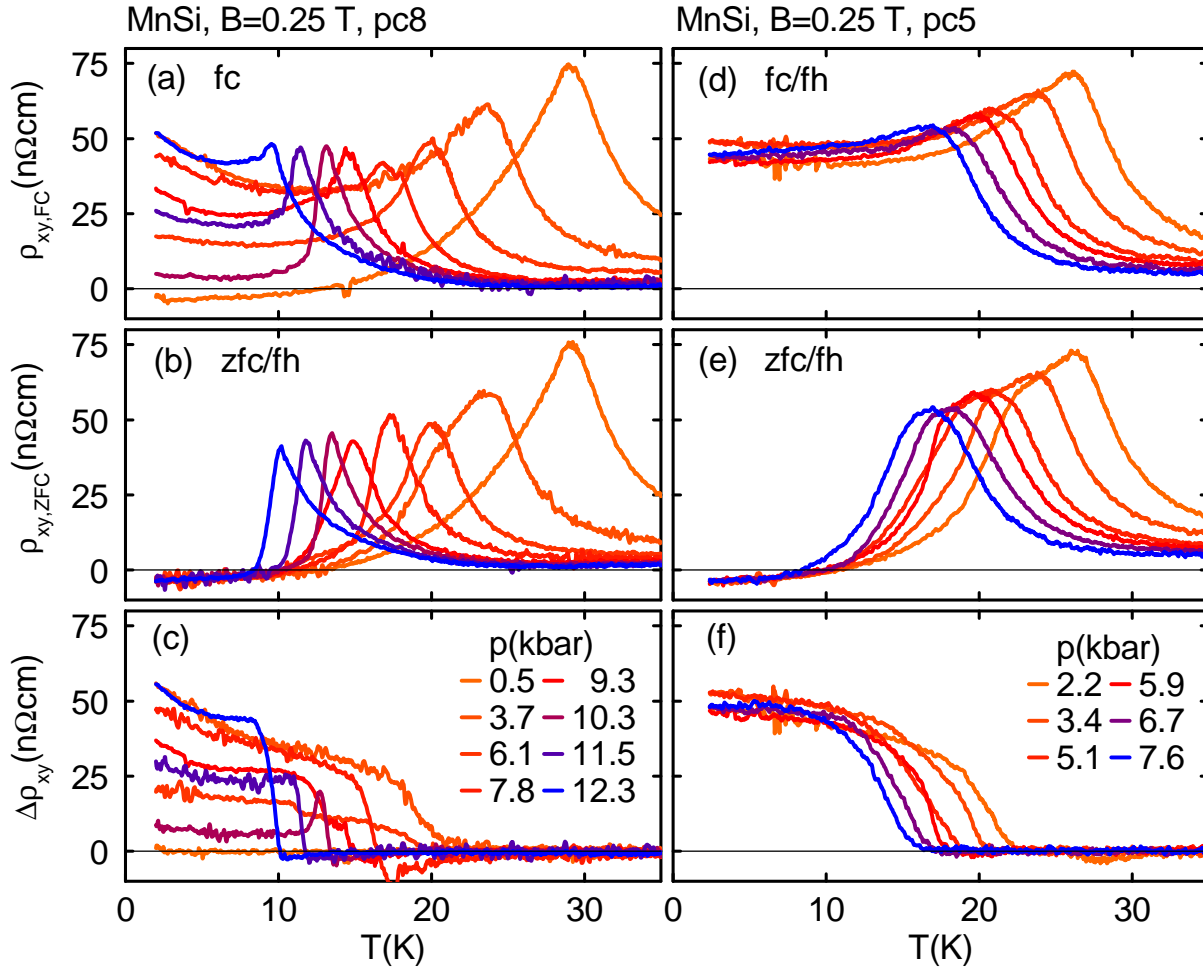


Figure 7.7: Field cooled THE. Temperature dependent Hall resistivity $\rho_{xy}(T)$ at field values inside the SLP, for two samples of different quality, $\text{RRR} \approx 150$ (left side panels) and $\text{RRR} \approx 45$ (right side panels), at various pressures up to 12.3 kbar. Panel a and d show curves measured on field cooling (fc) and field heating after field cooling (fc/fh), respectively. Panel b and e show the corresponding curves on heating after zero field cooling (zfc/fh). The differences of field cooling and zero field cooling, i.e. $\Delta\rho_{xy}(T) = \rho_{xy}^{\text{fc}}(T) - \rho_{xy}^{\text{zfc}}(T)$, are finally shown in panel c and f. Under pressure, a metastable high Hall signal emerges down to the lowest temperatures measured on field cooling.

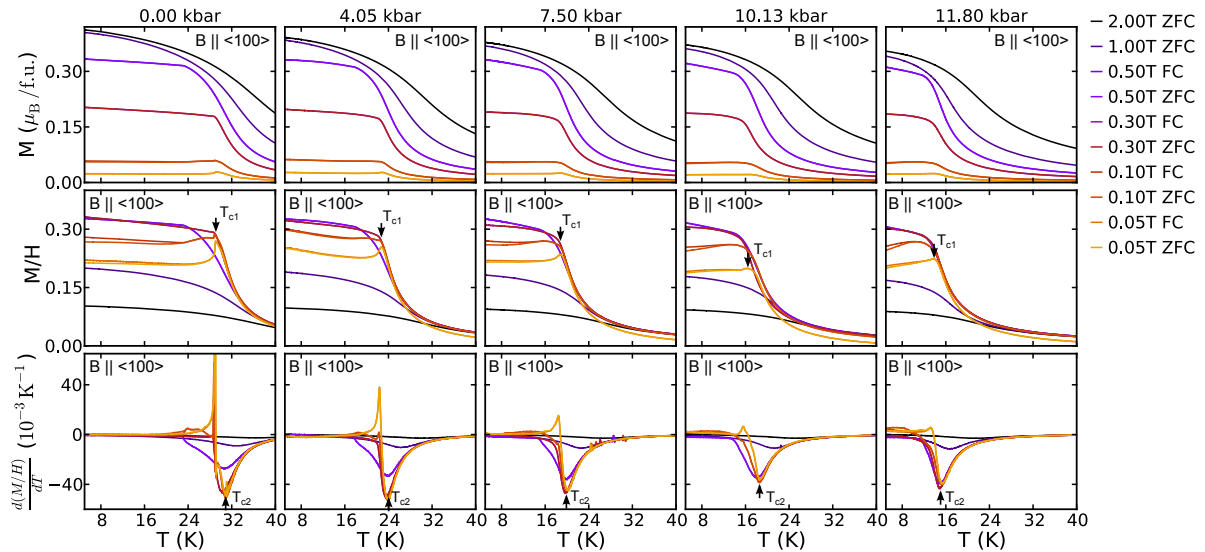


Figure 7.8: Temperature dependent magnetization under pressure. Magnetization measurements under pressure from Halder [224] performed on pressure cell pcM following the same zfc/fc and fc/fh procedures as for the Hall effect measurements shown above. *First row:* No significant differences between field and zero field cooling can be observed in the magnetization $M(T)$. *Second row:* $M/H(T)$ plotted to reveal better differences between zfc and fc curves. Also no significant differences can be observed. *Third row:* $\frac{d(M/H)}{dT}(T)$ permits to determine T_c accurately and corresponds to the magnetocaloric effect $\frac{dM}{dT} = dS/dB$. The sharp spike near T_c for $p = 0$ vanishes with increasing pressure. The qualitative behavior remains unchanged.

procedures as for the Hall effect measurements shown above. No significant differences between field and zero field cooling can be observed in the magnetization $M(T)$ shown in the panels of the first row, in $M/H(T)$ shown in the second row, and in $\frac{d(M/H)}{dT}(T)$ shown in the third row. Hence, the metastable Hall signal seems to represent a THE.

Summarized, a metastable Hall signal emerges in the temperature dependent Hall effect $\rho_{xy}(T)$ under pressure after field cooling. The metastable Hall signal does not follow the uniform magnetization and hence seems to represent a THE contribution. At all pressures and for all samples studied the metastable Hall signal converges against a limit of $\approx 50 \text{ n}\Omega\text{cm}$ at 2.0 K, the lowest temperature measured. This value seems to be the generic THE value in MnSi that is reached once the effects of finite temperatures are switched off.

7.3 Magnetic phase diagram

At ambient pressure the phase boundaries of the magnetic phase diagram inferred from magneto-transport measurements are consistent with susceptibility data from Bauer *et al.* [153, 218]. Under pressure, the magnetic phase diagram inferred from magneto-transport measurements does not change qualitatively, except an emerging metastable skyrmion lattice phase (SLP) under field cooling. Therefore, the observed top-hat Hall

signal under pressure is linked to the THE of the SLP seen at ambient pressure. Pressure inhomogeneities influence the field boundaries of the SLP, whereas no dependence on the current direction can be seen.

Fig. 7.9a shows the magnetic phase diagram inferred from magneto-transport measurements (full data points) in comparison to susceptibility data from Bauer *et al.* [153, 218] (open data points). All phase boundaries prove to be consistent. Furthermore, the magneto-transport data allows to track the evolution of the phase diagram under pressure (Fig. 7.9b, c, d, e). With increasing pressure the helimagnetic transition T_c is suppressed to lower temperatures. The transition B_{c2} from the conical (spin-flop) phase to a spin polarized state does not change with pressure, consistent with SANS data from Pfeleiderer *et al.* [178]. In contrast to Ref. [178], the transition B_{c1} from the helical to the conical phase slightly increases with pressure. However, this reflects mainly the changing form of the magnetoresistance (see Fig. 7.3).

In contrast to Lee *et al.* [162], the THE signal forms a well-defined phase pocket below T_c (red shading). As discussed in Sec. 7.2, a metastable THE signal emerges under field cooling, so that the phase pocket is then extended down to the lowest temperatures measured (bright red shading). Taken together, the phase diagram under pressure remains qualitatively unchanged, except the emerging metastable region under field cooling. The small phase pocket below T_c at ambient pressure, related to the SLP, evolves continuously with pressure into a phase pocket with a larger field and temperature range. Therefore, we also identify the phase pocket under pressure as a SLP (denoted “A-phase”). As will be discussed in Chap. 8, the THE signal in the SLP under pressure can also be quantitatively linked to the THE signal at ambient pressure.

To determine the role of pressure inhomogeneities and local strains on the SLP under pressure, further studies were performed with a FC72:FC84 Fluorinert mixture with volume ratio 1:1 (FI) as pressure transmitting medium, known to provide less uniform pressure conditions than the methanol:ethanol mixture with volume ratio 4:1 (ME) used otherwise. A comparison at pressures around 7 kbar in Fig. 7.10a shows a significantly larger SLP in a high quality sample ($RRR \approx 92$) with FI as pressure transmitting medium than in a low quality sample ($RRR \approx 40$) with ME. Since $\rho_{xy}(T)$ data in Sec. 7.2 suggested that pinning at defects stabilize the SLP at low temperatures, the extended range seems to be completely caused through the usage of FI consistent with typical anisotropies reported to be $\lesssim 10^{-1}$ kbar. However, those anisotropies are tiny as compared to the overall pressure of order ≈ 10 kbar.

Furthermore, as expected, no significant difference was observed in the Hall signal for the current being applied along different directions, i.e., $I \parallel \langle 100 \rangle$ and $\langle 110 \rangle$ with field $B \parallel \langle 110 \rangle$ (Fig. 7.10b).

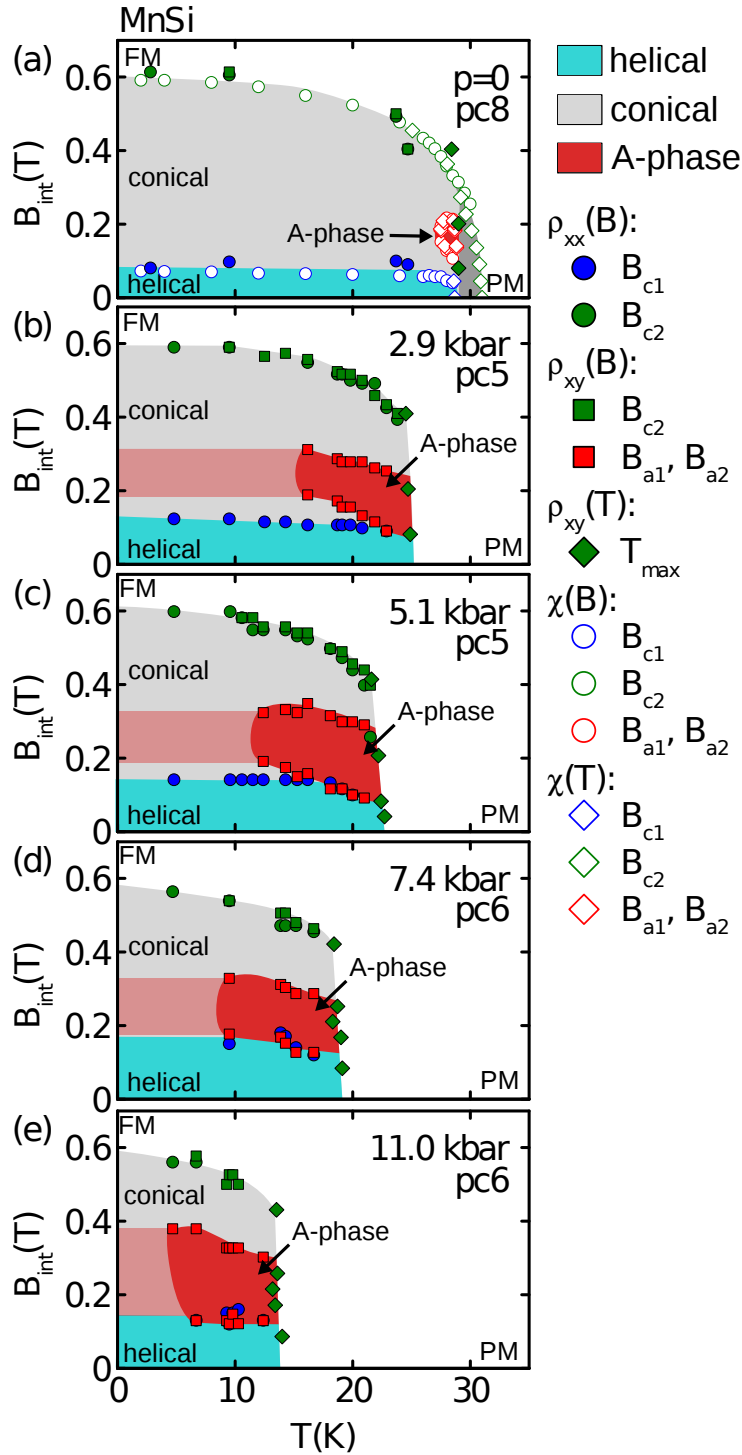


Figure 7.9: Magnetic field-temperature phase diagram of MnSi under pressure. Magnetic phase diagram at various pressures for $B \parallel \langle 110 \rangle$. The data was recorded on samples with $RRR \approx 40-45$ and with ME as pressure transmitting medium. B_{c1} , B_{c2} , B_{a1} , and B_{a2} refer to B_{c1}^+ , B_{c2}^+ , B_{a1}^+ , and B_{a2}^+ in Fig. 7.3. T_{max} represents the temperature dependent maximum in $\rho_{xy}(T)$ (see Figs. 7.3h, 7.6, 7.7). (a) At ambient pressure magneto-transport data (full data symbols) is consistent with susceptibility data of Bauer *et al.* [153, 218] (empty symbols). (b),(c),(d),(e) Phase diagram under pressure inferred from magneto-transport data. Except a metastable SLP observed under field cooling (bright red shading) the phase diagram remains qualitatively the same.

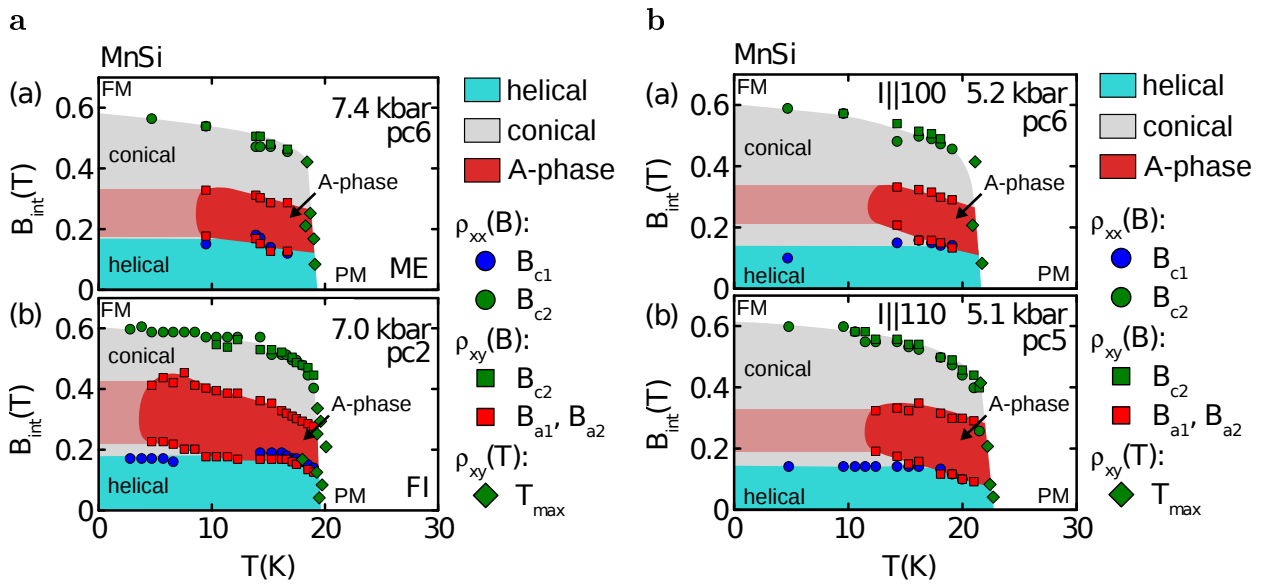


Figure 7.10: Effect of pressure medium and crystalline direction on the B - T -phase diagram. (a) Magnetic phase diagram around 7kbar in a high quality sample ($RRR \approx 92$) with FI as pressure transmitting medium compared to a low quality sample ($RRR \approx 40$) with ME. Due to the less uniform pressure conditions in FI, a SLP (denoted as “A-phase”) with a significantly larger temperature and field range is observed (bottom panel). (b) Magnetic phase diagram around 5 kbar for the orientations $I \parallel \langle 100 \rangle$ and $\langle 110 \rangle$ with field $B \parallel \langle 110 \rangle$. No significant differences are observed.

Chapter 8

Discussion $p < p^*$

As seen in the previous chapter, the size of the topological Hall effect (THE) in the skyrmion lattice phase (SLP) of MnSi increases from $\Delta\rho_{xy}^{\text{top}} \approx 4.5 \text{ n}\Omega\text{cm}$ to $\approx 40 \text{ n}\Omega\text{cm}$ with pressure up to $\approx 12 \text{ kbar}$. Furthermore, a large Hall signal $\approx 50 \text{ n}\Omega\text{cm}$ is observed at low temperatures in field cooled temperature sweeps that could be identified as THE. In this chapter we will first summarize the behavior of the THE under pressure in Sec. 8.1. Furthermore, we will show in Sec. 8.2 that size and pressure dependence of the large Hall signal observed in field cooled temperature sweeps can be described by Eq. 6.25:

$$\Delta\rho_{yx}^{\text{top}} \approx R_0 B^e \left\langle \frac{q_\sigma^e}{e} \right\rangle_{\text{FS}} = R_0 B^{\text{eff}} P.$$

This confirms that the Hall signal truly represents a THE whose size represents the generic size of the THE in MnSi that can be seen when the effects of finite temperature are essentially switched off. A discussion about how the factors in Eq. 6.25 evolve with pressure reveals that the decreased THE size at ambient pressure and high temperatures can be attributed to the change of the local polarization close to T_c for the most important part (Sec. 8.3). The remaining part is most likely due to one or a combination of several mechanisms including changes of the Fermi surface, change of scattering processes, competition between exchange splitting and spin-orbit coupling, and spin-flip scattering. All conclusions will be summarized in Sec. 8.4.

8.1 $\Delta\rho_{xy}^{\text{top}}$ under pressure

The key features that we find of the THE signal $\Delta\rho_{xy}^{\text{top}}$ under pressure are illustrated in Fig. 8.1a. (i) We find that $\Delta\rho_{xy}^{\text{top}}$ observed in magnetic field sweeps (cf Fig. 7.5a and b) increases under pressure by roughly a factor of ten from $\approx 4.5 \text{ n}\Omega\text{cm}$ at ambient pressure to $\approx 40 \text{ n}\Omega\text{cm}$ at $\approx 12 \text{ kbar}$ (full data points). In the following we will refer to this signal as $\Delta\rho_{xy,\text{BS}}^{\text{top}}$. The size of $\Delta\rho_{xy,\text{BS}}^{\text{top}}$ was estimated as shown in Fig. 7.4 at temperatures close to T_c where it becomes maximal. The solid line is a guide to the eye and illustrates an upper boundary. As T_c is suppressed to lower temperatures with increasing pressure, the increase in $\Delta\rho_{xy,\text{BS}}^{\text{top}}$ also means an increase with decreasing temperature. Since sample

quality only affects the reduced temperature at which the maximal THE signal is observed but not the size of $\Delta\rho_{xy,BS}^{\text{top}}$, we do not distinguish between different pressure cells here.

(ii) The metastable THE signal observed in field cooled temperature sweeps at $B = 0.25$ T (see Fig. 7.7) allows to study the generic size of the THE in MnSi in the low temperature limit, i.e., without the effects of finite temperature. The open data points in Fig. 8.1a correspond to the difference of field and zero-field cooled $\rho_{xy}(T)$, i.e., THE of the metastable SLP, at 2K, the lowest temperature measured. In the following we refer to this signal as $\Delta\rho_{xy,TS}^{\text{top}}$. Here, only data from low quality samples is shown for clarity since they exhibit a more stable field cooled SLP at low temperatures (cf Fig. 7.7c and f). With increasing pressure, the metastable THE signal decreases slightly. The decrease agrees with the relative pressure dependence of the magnetization $dm_{\text{red}}/dp \approx -0.02 \text{ kbar}^{-1}$, with $m_{\text{red}} = m(p)/m(p=0)$, as extrapolated for zero field from fields above B_{c2} [174] (solid straight line). At pressures above 12 kbar, T_c is sufficiently suppressed so that $\Delta\rho_{xy,BS}^{\text{top}}$ from field sweeps reach the size of those from metastable temperature sweeps, $\Delta\rho_{xy,TS}^{\text{top}}$, and the full and open datapoints overlap. When extrapolated to ambient pressure, $\Delta\rho_{xy,TS}^{\text{top}}$ runs against a value of $\approx 50 \text{ n}\Omega\text{cm}$.

Considering the key features above, two questions arise: Can the size of $\Delta\rho_{xy,TS}^{\text{top}}$ be successfully described by Eq. 6.25 which implies that it truly represents the generic size of the THE in MnSi caused by a skyrmion lattice? Why is $\Delta\rho_{xy,BS}^{\text{top}}$ at ambient pressure so much smaller? These two questions will be discussed in Secs. 8.2 and 8.3.

8.2 Generic size of $\Delta\rho_{xy}^{\text{top}}$

In this section we clarify that the THE signal observed in the low temperature limit, $\Delta\rho_{xy,TS}^{\text{top}}$, can be described by Eq. 6.25 and therefore represents the generic THE size in MnSi caused by a skyrmion lattice. First, we will see that Eq. 6.25 yields a reasonable value for the polarization P at ambient pressure where $\Delta\rho_{xy,TS}^{\text{top}}$, R_0 , and B^{eff} are known. Second, through a comparison with the magnetization we will see that the pressure dependence of $\Delta\rho_{xy,TS}^{\text{top}}$ can be described quantitatively by Eq. 6.25. There, the main contribution to the pressure dependence relates to a decreasing polarization. With this knowledge we are then able to discuss the mechanisms behind the pressure dependence of $\Delta\rho_{xy,BS}^{\text{top}}$ observed in field sweeps in Sec. 8.3.

According to Eq. 6.25 the local spin polarization can be calculated as

$$P = \left| \frac{e}{q_{\sigma}^e} \right| \left\langle \frac{q_{\sigma}^e}{e} \right\rangle_{FS} \approx \frac{\Delta\rho_{yx}^{\text{top}}}{R_0 B^{\text{eff}}}. \quad (8.1)$$

At ambient pressure we can insert the values known from our experiments and the literature. With $\Delta\rho_{xy,TS}^{\text{top}} \approx -50 \text{ n}\Omega\text{cm}$, $B^{\text{eff}} \approx -13.15$ T, and $R_0 = 17 \text{ n}\Omega\text{m/T}$ the polarization becomes $P \approx 0.22$. This is of the same order of magnitude as the ratio of local magnetization to the saturated magnetic moment of the Mn ions $P = \mu_{spo}/\mu_{sat} \approx \frac{0.4 \mu_B}{2.2 \mu_B} \approx 0.18$,

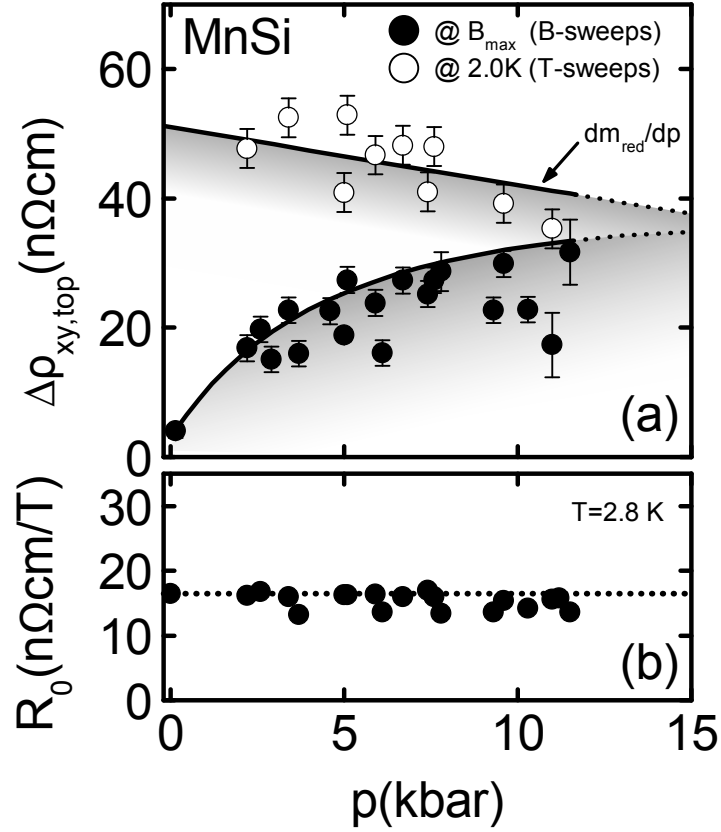


Figure 8.1: Evolution of the THE and the normal Hall constant R_0 under pressure. (a) *full data points*: $\Delta\rho_{xy}^{\text{top}}(p)$ inferred from magnetic field sweeps at temperatures where it becomes maximal (see Fig. 7.4). Data from pressure cells pc5, pc6, pc8 and at ambient pressure from Neubauer *et al.* [15] is shown. *open data points*: $\Delta\rho_{xy}^{\text{top}}(p)$ inferred from the difference of field cooled and zero-field cooled temperature sweeps at 2 K (see Fig. 7.7). For clarity, only data from pressure cells pc5 and pc6 are shown since they exhibit a more stable field cooled SLP at low temperatures due to low quality samples. (b) Normal Hall constant inferred from the slope of $\rho_{xy}(B)$ at fields larger 10 T (see Fig. 7.1). Data from pressure cells pc5, pc6, pc8 and at ambient pressure from Neubauer *et al.* [15] is shown.

and hence a reasonable value. Considering the complex band-structure of MnSi, where for both majority and minority charge carriers electron-like and hole-like parts of the Fermi surfaces exist [227, 228], and the complicated $\langle q_\sigma^e/e \rangle_{FS}$ that determines P , Eq. 6.25 yields a quantitative result that explains the large Hall signal under pressure. Furthermore, it confirms that the large Hall signal can be explained by a THE contribution caused by a skyrmion lattice.

As illustrated by the open datapoints in Fig. 8.1a, $\Delta\rho_{xy,TS}^{\text{top}}$ decreases linearly with increasing pressure. Since R_0 is only weakly pressure dependent in the low temperature limit and since B^e is in general only weakly pressure dependent as will be discussed below, the decrease in $\Delta\rho_{xy,TS}^{\text{top}}$ has to originate from the change of the Fermi surface average of the emergent charge $\langle q_\sigma^e/e \rangle_{FS}$. To test this, we compare the pressure dependence of $\Delta\rho_{xy,TS}^{\text{top}}$ with that of the magnetization. As the emergent charge is of opposite sign for majority and minority spins, one expects a linear dependence of $\langle q_\sigma^e/e \rangle_{FS}$ on the local spin polarization¹ and hence on the magnetization. The straight solid line in Fig. 8.1a shows the slope of the relative pressure dependence of the magnetization $dm_{\text{red}}/dp \approx -0.02 \text{ kbar}^{-1}$, with $m_{\text{red}} = m(p)/m(p=0)$, as extrapolated for zero field from fields above B_{c2} [174]. The rate of decrease is also consistent with the ordered magnetic moment inferred from SANS data [50, 178]. We find that the pressure dependence of $\Delta\rho_{xy,TS}^{\text{top}}$ and equivalently the pressure dependence of $\langle q_\sigma^e/e \rangle_{FS}$ quantitatively coincides with that of the magnetization. This shows that the pressure dependence of the generic THE can be described by Eq. 6.25 and is dominated by $\langle q_\sigma^e/e \rangle_{FS}$.

The check of the consistency at ambient pressure and the quantitative agreement with the pressure dependence show that Eq. 6.25 can describe the large Hall signal observed in the low temperature limit. Therefore, $\Delta\rho_{xy,TS}^{\text{top}}$ represents the generic size of the THE in MnSi caused by the skyrmion lattice. The pressure dependence of the normal Hall constant R_0 and the emergent magnetic field B^e will be discussed below. The pressure dependence of the THE inferred from field sweeps, $\Delta\rho_{xy,BS}^{\text{top}}$, will be discussed in Sec. 8.3.

8.2.1 Normal Hall constant R_0 under pressure

At low temperatures and high magnetic fields the normal Hall constant R_0 is approximately independent of pressure as seen in Fig. 8.1b where R_0 , inferred from the slope of $\rho_{xy}(B)$ at 2.8 K at fields larger 10 T (see Fig. 7.1), is shown. The value is in agreement with the ambient pressure value evaluated at room temperature of $R_0 \approx 16.5 \text{ n}\Omega\text{cm/T}$ corresponding to a charge carrier concentration of $n \approx 3.78 \times 10^{22} \text{ cm}^{-3}$ [187]. However, it is difficult to evaluate R_0 at small fields where the local magnetization is small, like it is the case close to T_c , since the AHE contribution dominates in this regime. Non-relativistic band-structure calculations by Jeong *et al.* [227], which reproduce in all details the experimentally observed Fermi surfaces at large fields as De-Haas van-Alphen measurements showed [228], allow to deduce that R_0 is only weakly pressure dependent at fixed magne-

¹if there are no strong changes in the band-structure

tizations, but might have sizable changes when the magnetization is small and changes. From Jeong *et al.* [227] it can be seen that topology, shape, size and sign of effective masses of minority and majority Fermi surfaces in MnSi change strongly when the magnetization is increased from 0 to $0.4\mu_{\text{B}}$, i.e., the size of ordered moment at low T .

Taken together, R_0 does essentially not change with pressure at fixed magnetizations. Close to T_c where the magnetization is small, however, R_0 might have sizable changes.

8.2.2 Emergent magnetic field B^e under pressure

There are two possibilities how the emergent magnetic field B^e can change with pressure. First, the winding number per magnetic unit cell can change when the spin-orbit coupling becomes of a size comparable to the exchange splitting. However, for low temperatures and deep in the ordered phase we can assume that the exchange splitting is larger than the spin-orbit coupling, ruling out a change of the winding number.

Second, the length of the helical magnetic modulation can change with pressure and with it the magnetic unit cell of the skyrmion lattice. So far, no data exists about the size of the helix length in the SLP in MnSi under pressure. However, since in all B20 structures studied so far the helix length had the same value in the SLP and in the helimagnetic state, as expected from theory [154], it seems sufficient to consider existing data of the change of the helix length in the helimagnetic state under pressure to determine changes of the helix length in the SLP. Studies under uniaxial pressure show that one does not have to worry about uniaxial pressure components inside the pressure cells as the helix length remains unchanged under uniaxial pressure [229]. Neutron scattering studies show that the helix length remains essentially unchanged in the helimagnetic state under pressure [50, 230] which is also reflected by the fact that the transition field B_{c2} proves to be pressure independent [178]. Therefore, the size of the magnetic unit cell in the SLP in MnSi does not change with pressure.

Taken together, the emergent magnetic field remains unchanged under pressure and is given by one flux quantum per magnetic unit cell. The magnitude of the effective magnetic field remains $B_{\text{eff}} \approx -13.15 \text{ T}$ and may at best increase at the percent level.

8.3 Temperature dependence of $\Delta\rho_{xy}^{\text{top}}$

While the last section discussed whether the large Hall signal $\Delta\rho_{xy,\text{TS}}^{\text{top}}$ observed in field cooled temperature sweeps at low temperatures truly represents a THE that can be described by Eq. 6.25, this section focuses on the question why a considerably smaller THE signal $\Delta\rho_{xy,\text{BS}}^{\text{top}}$ is observed in magnetic field sweeps at ambient pressure and at high temperatures. The most important part of the decreased size can be attributed to the change of the local spin polarization at temperatures close to T_c compared to $T \rightarrow 0$. The remaining part is most likely due to one or a combination of several mechanisms including changes of the Fermi surface, change of scattering processes, competition between

exchange splitting, and spin-orbit coupling and spin-flip scattering.

As seen in Fig. 8.1 and discussed in Sec. 8.2, the polarization scales linearly with the magnetization. Hence, the decrease of the magnetization with increasing temperature explains part of the decreased size of $\Delta\rho_{xy,BS}^{\text{top}}$ at temperatures close to T_c compared to $\Delta\rho_{xy,TS}^{\text{top}}$ in the low temperature limit. In Neubauer *et al.* [15] the polarization in the SLP was estimated as $P = \mu_{spo}/\mu_{sat} \approx \frac{0.2\mu_B}{2.2\mu_B} \approx 0.09$ being a factor two smaller than at zero temperature $P \approx \frac{0.4\mu_B}{2.2\mu_B} \approx 0.18$ and therefore accounts for a factor of two in the change of $\Delta\rho_{xy}^{\text{top}}$. Although the reduction of P was certainly underestimated in [15] this does not explain the difference by a factor of ten in $\Delta\rho_{xy}^{\text{top}}$ between $\Delta\rho_{xy,TS}^{\text{top}}$ at $T \rightarrow 0$ and $\Delta\rho_{xy,BS}^{\text{top}}$ in the temperature range of the SLP. The remaining factor of five is most probably due to one of or a combination of the following five scenarios:

1. *Changes of Fermi surface:* Band-structure calculations suggest strong changes of Fermi surface for small local magnetizations. These would modify R_0 and the Fermi surface averages $\langle q_\sigma^e/e \rangle_{FS}$.
2. *Scattering processes:* Close to T_c the scattering processes are completely different than at low temperatures. This can strongly affect the Fermi surface averages $\langle q_\sigma^e/e \rangle_{FS}$ as different Fermi surfaces are weighted by the square of the scattering time.
3. *Spin-orbit coupling:* Close to T_c the exchange splitting becomes small and might give way to spin-orbit coupling as the dominating interaction. This implies that electron spins do not follow the magnetic texture completely anymore reducing the real space Berry phase pick up. For some bands the topological contribution may be switched off completely. Also only a part of a Fermi surface can be affected by the real space Berry phases while for other parts the emergent magnetic flux vanishes.
4. *Spin-flip scattering:* Close to T_c it is possible that the adiabatic approximation is not valid anymore and electrons are subject to spin-flip scattering. Hence the electrons lose the accumulated Berry phase when they scatter from a majority to a minority electron and vice versa. This is especially the case when the spin-flip scattering length is smaller than the distance between the skyrmions.
5. *Competition of momentum and phase-space Berry phases:* When exchange splitting and spin-orbit coupling become of the same order of magnitude, besides real-space Berry phases momentum-space Berry phases (intrinsic AHE) and even phase-space Berry phases can arise.

8.4 Conclusions

Taken together, our comprehensive studies of the Hall effect of MnSi at low temperatures and pressures up to 12 kbar show that the top-hat shaped THE seen in the SLP at ambient pressure increases by a factor of ten from $\approx 4.5 \text{ n}\Omega\text{cm}$ to $\approx 40 \text{ n}\Omega\text{cm}$ at $\approx 12 \text{ kbar}$.

The large top-hat shaped Hall effect signal observed under pressure clearly evolves out of the SLP at ambient pressure and, therefore, can be attributed to a THE arising from a SLP. As T_c is sufficiently suppressed to lower temperatures under pressure, effects of finite temperatures are essentially switched off revealing the generic size of the THE. Furthermore, the metastable SLP under field cooling allows to directly observe the generic size of the THE of $\approx 50 \text{ n}\Omega\text{cm}$ which depends only weakly on sample quality and pressure.

Exploring samples of different qualities and pressure cells with different pressure media, we can show that the signal observed by Lee *et al.* [162] represents a THE signal broadened by defect induced pinning and pressure inhomogeneities.

The tenfold increase in size of the THE is mainly determined by how the scattering rates average over the various Fermi surfaces. The reduced size observed at ambient pressure is due to a unusual combination of mechanisms including changes of the polarization, changes of the Fermi surface, change of scattering processes, competition between exchange splitting and spin-orbit coupling and spin-flip scattering, where the most important contribution is the reduction of the polarization close to T_c .

The Hall effect experiments up to $\approx 12 \text{ kbar}$, presented here in Chaps. 7 and 8, allow to unambiguously link the large Hall effect signal under pressure to a skyrmion lattice. This establishes a sound basis for the experiments at pressures exceeding p^* and p_c presented in the following Chaps. 9 and 10. There, it will be shown that the THE signal survives up into the non-Fermi liquid (NFL) phase, however, in a broadened field and temperature range that coincides with the boundaries of the NFL regime. This implies that skyrmionic textures exist in, and potentially are the reason for, the extended NFL regime observed in MnSi.

Chapter 9

Results $p > p^*$

For pressures exceeding $p^* \approx 12$ kbar, an extended non-Fermi liquid (NFL) regime appears above T_c and p_c in the phase diagram of MnSi (cf Fig. 5.5a). The top-hat shaped topological Hall effect (THE) signal observed in the skyrmion lattice phase (SLP) survives in the NFL regime. Compared to pressures $p < p^*$ the THE signal exists in a broadened field and temperature range whose boundaries coincide with that of the NFL regime. Here, we present resistivity and Hall effect measurements up to 18.1 kbar. First, we reproduce the temperature and field boundaries of the NFL regime shown in the literature by Pfeleiderer *et al.* [9] and Doiron-Leyraud *et al.* [10] through the temperature dependent longitudinal resistivity $\rho_{xx}(T)$. Furthermore, we show magnetoresistance and field dependent Hall effect data across a wide field range, up to 14 T, of the magnetic phase diagram to be able to unambiguously distinguish between AHE, NHE, and THE contributions. Our main result is then inferred from magnetic field sweeps at small fields where the THE signal is observed. Finally, the magnetic phase diagram is discussed at various pressures.

9.1 Temperature dependence

The longitudinal resistivity $\rho_{xx}(T)$ shows an abrupt transition from a Fermi liquid (FL) T^2 to a non-Fermi liquid (NFL) $T^{3/2}$ temperature dependence on crossing the critical pressure p_c , consistent with literature [9, 10]. Also, the return of $\rho_{xx}(T)$ to a FL temperature dependence when crossing the metamagnetic transition under an applied magnetic field is reproduced. Contrary to data at pressures below p_c , no metastable Hall effect signal can be observed above p_c in field cooled temperature sweeps of $\rho_{xy}(T)$.

Fig. 9.1a shows the temperature dependence of the longitudinal resistance $\rho_{xx}(T)$ at $B = 0$ for pressures up to 15.7 kbar. The transition temperature T_c , seen as change of slope, is suppressed from ≈ 30 K to lower temperatures with increasing pressure and vanishes at a critical pressure $p_c \approx 14.6$ kbar. At p_c , the T^2 dependence at low temperatures changes abruptly into a $T^{3/2}$ dependence that is observed up to $T^* \approx 12$ K. This is further illustrated in the inset which shows the exponent α from low temperature fits of $\rho_{xx}(T)$ with the formula $T = AT^\alpha + \rho_0$. $\alpha = 2$ is associated with a Fermi liquid behavior (blue

shading) whereas $\alpha = 3/2$ is associated with a non-Fermi liquid behavior (orange shading).

Fig. 9.1b shows $\rho_{xx}(T)$ at 15.7 kbar for various magnetic fields up to 2.5 T. As illustrated in the inset, when applying a magnetic field the $\alpha = 3/2$ NFL behavior abruptly reverts to $\alpha = 2$ FL behavior at the field $B_{\text{NFL}} \approx 0.7$ T which coincides with the itinerant metamagnetic transition at B_m . Exponents close to B_{NFL} in the center of the crossover are not shown.

At pressures below p_c , the temperature dependent Hall resistivity $\rho_{xy}(T)$ is governed by a broad peak around T_c , while at pressures above p_c , a small broad peak emerges below ≈ 15 K, i.e. in the NFL regime. As will be discussed in Sec. 9.3 along magnetic field sweeps, the broad peak is due to a THE contribution. However, unlike at pressures below p_c , no metastable Hall signal is observed in field cooled temperature sweeps at pressures above p_c . This is illustrated in Fig. 7.6 (p.129) where $\rho_{xy}(T)$ at 7.4 kbar ($< p_c$) is shown in comparison to $\rho_{xy}(T)$ at 15.7 kbar ($> p_c$). The data in panels a,c,d, and f was measured at fields outside of the field range of the SLP. Field cooled and zero field cooled data display no difference. Data in panel b and e was measured at fields inside the field range of the SLP. For field cooled data at 7.4 kbar a metastable Hall signal emerges. This was already discussed in Sec. 7.2. In turn, for data at 15.7 kbar no metastable Hall signal can be observed. As for lower pressures a slight dependence of the metastable Hall signal on the sample quality was observed, we checked a high ($RRR \approx 150$) and a low quality ($RRR \approx 45$) sample at pressures above p_c . Neither showed a metastable Hall signal.

9.2 Magnetic field dependence at high fields

At low temperatures, the magnetoresistance exhibits distinct drops at the transition fields B_{c2} for pressures below p_c and at B_m , the itinerant metamagnetic transition, for $p > p_c$. At higher temperatures, the magnetoresistance shows no distinct features. The Hall effect is dominated by the NHE and hence shows a linear slope at low temperatures. At higher temperatures a large AHE contribution arises as a “knee” shaped feature that is accompanied by a shoulder sitting on top of the AHE contribution. The shoulder vanishes above ≈ 70 K and can be clearly distinguished from the THE signals at small fields that represent our main result and will be presented in the next section.

Fig. 9.2a shows the magnetoresistance $\rho_{xx}(B)$ at pressures up to 15.7 kbar at fields up to 14 T for temperatures of 2.8 K (upper panel) and 28.7 K (lower panel). At 2.8 K and $p < p_c$, $\rho_{xx}(B)$ drops by about 10% up to B_{c2} before increasing again monotonously up to high fields. For $p > p_c$, $\rho_{xx}(B)$ increases by about 10% up to B_m , the itinerant metamagnetic transition, then drops by about 40% before increasing again monotonously up to high fields. At higher temperatures (cf 28.7 K) the drop in $\rho_{xx}(B)$ evolves into a broad crossover. The drop at low temperatures resembles a magnetic scattering mechanism that is quenched by the applied field. At higher temperatures higher fields are needed to

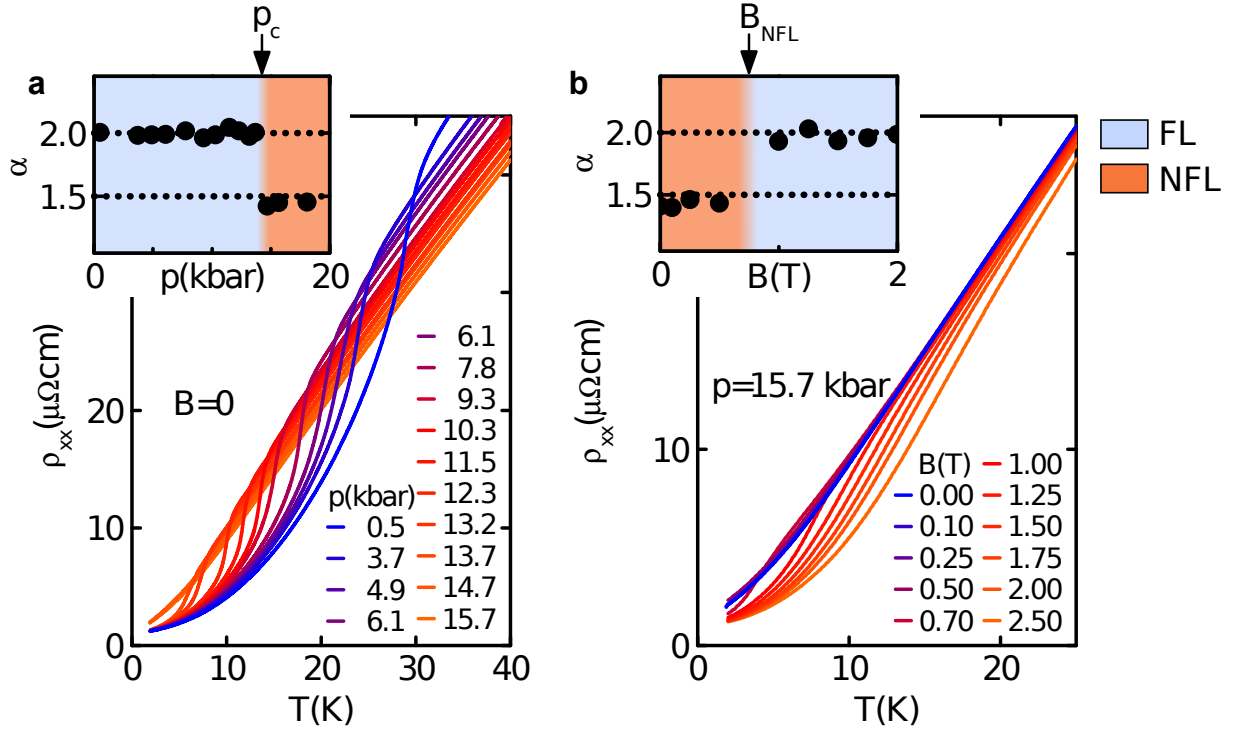


Figure 9.1: Non-Fermi liquid behavior of the resistivity under pressure. (a) $\rho_{xx}(T)$ at $B = 0$ for pressures up to 15.7 kbar in pressure cell pc8. The inset shows the exponent α from low temperature fits of $\rho_{xx}(T)$. At the critical pressure $p_c \approx 14.6$ kbar a T^2 dependence (blue shading) at low temperatures changes abruptly into a $T^{3/2}$ dependence (orange shading). (b) $\rho_{xx}(T)$ at 15.7 kbar for various magnetic fields up to 2.5 T. At an applied field $B_{\text{NFL}} \approx 0.7$ T, the $T^{3/2}$ dependence switches back to a T^2 dependence. This is again illustrated by the exponent α in the inset.

quench those spin excitations.

Fig. 9.2b shows the Hall resistivity $\rho_{xy}(B)$ at pressures up to 15.7 kbar at fields up to 14 T for temperatures of 2.8 K (upper panel) and 28.7 K (lower panel). At 2.8 K, $\rho_{xy}(B)$ decreases monotonously, almost linear to higher fields down to $\approx -180 \text{ n}\Omega\text{cm}$ without notable features, i.e., $\rho_{xy}(B)$ is dominated by the NHE. We neglect the THE contributions at small fields for now as they will be discussed in detail below. At 28.7 K, $\rho_{xy}(B)$ is dominated by the AHE at fields up to a “knee” shaped features above which $\rho_{xy}(B)$ reverts to the linear slope, determined through the NHE, as observed at low temperatures. On top of the AHE contribution a shoulder emerges below fields B_S that coincides with the itinerant metamagnetic transition at B_m (see Fig. 7.3 for the definition of B_S and B_m). The shoulder can neither be observed in the magnetoresistance ρ_{xx} nor in the magnetization [16, 173, 174].

The temperature dependence of the shoulder in ρ_{xy} is shown in Fig. 9.3 at 15.7 kbar and temperatures up to 97 K. At low temperatures, ρ_{xy} is dominated by the NHE and has a linear slope. Again, we neglect the THE contributions at small fields for now as they will be discussed in detail below. With increasing temperature, a strong AHE contribution emerges along with the shoulder. The AHE contribution and the shoulder both vanish for temperatures above $\approx 70 \text{ K}$. For now, the origin of the shoulder emerging below B_S is unclear. The corresponding transition fields B_S and B_m imply a connection to the itinerant metamagnetic transition. However, as the THE features of interest can be clearly distinguished from the emerging shoulder on top of the AHE, the interpretation of our data is not affected in any way.

9.3 Magnetic field dependence at small fields

The Hall effect data at small fields shows that the THE signal, observed in the SLP of MnSi, survives above p_c/T_c and is seen as a broad peak across the entire NFL regime of the phase diagram. The boundaries in which the THE signal emerges coincide with the boundaries of the NFL behavior. These findings represent the main result of our data at high pressures.

Fig. 9.4 shows the field dependent Hall resistivity $\rho_{xy}(B)$ at various pressures and temperatures at small magnetic fields inferred from high-quality samples ($RRR > 92$). From left to right the columns show selected pressures covering the range from below p^* to pressures above p_c ($p = 7.0 \text{ kbar}, 10.3 \text{ kbar}, 13.7 \text{ kbar}, 15.7 \text{ kbar}$). The color shadings illustrate the different metallic states in the phase diagram inferred from the longitudinal resistance ρ_{xx} (cf Fig. 9.1 and 9.5 discussed below). White shading corresponds to the paramagnetic region, blue shading to regions where Fermi liquid behavior (FL) is observed and orange shading to regions where non-Fermi liquid behavior (NFL) is observed. The top-hat shaped THE signal seen in the FL regions below T_c survives into the NFL regime (red shading). On crossing the boundary to the NFL regime, the

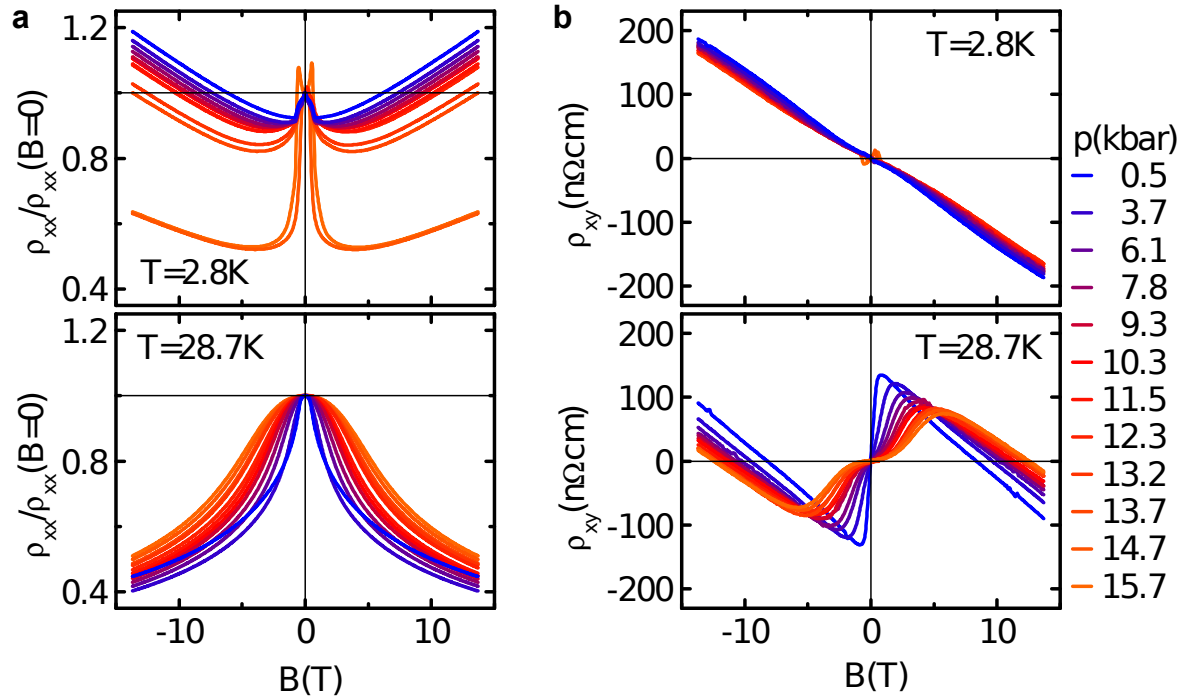


Figure 9.2: Hall effect and magnetoresistance at high magnetic fields. (a) Normalized magnetoresistance $\rho_{xx}(B)/\rho_{xx}(B=0)$ at pressures up to 15.7 kbar at fields up to 14 T at 2.8 K (upper panel) and at 28.7 K (lower panel) in pressure cell pc8. The most notable feature is the $\approx 40\%$ drop at B_m for low temperatures and for $p > p_c$. (b) Hall resistivity $\rho_{xy}(B)$ at pressures up to 15.7 kbar at fields up to 14 T at 2.8 K (upper panel) and 28.7 K (lower panel) in pressure cell pc8. At 2.8 K ρ_{xy} is dominated by the NHE, i.e. it decreases monotonously without notable features (the THE signal seen at small fields will be discussed later). At 28.7 K ρ_{xy} is dominated by a AHE contribution, i.e., it shows a distinct “knee” shaped feature. On top of the AHE contribution a shoulder appears.

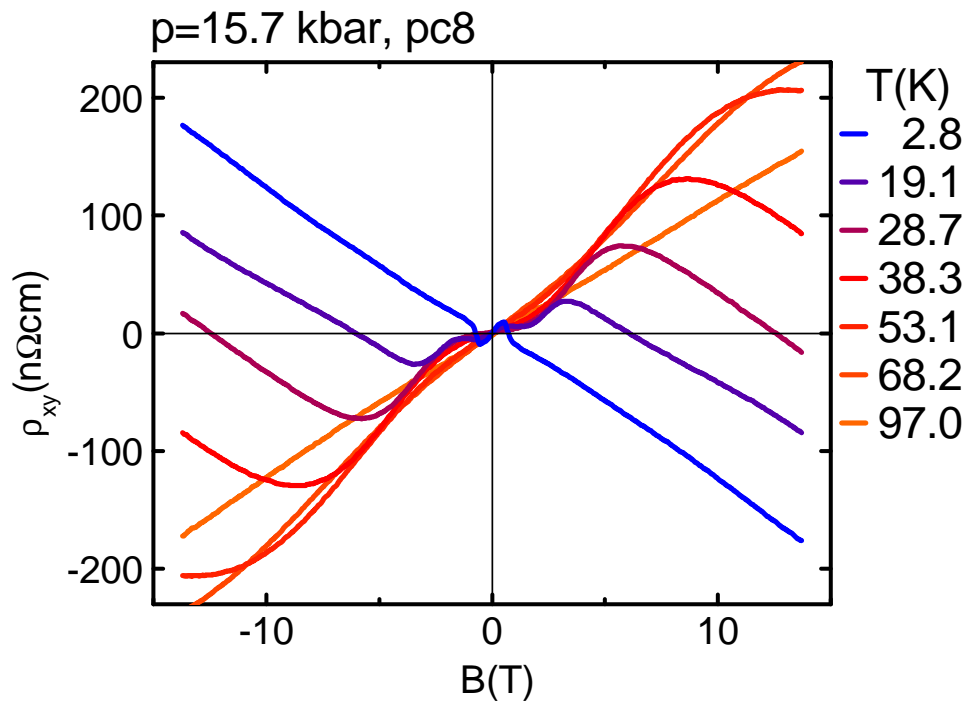


Figure 9.3: Shoulder in the Hall effect at high fields. Hall resistivity ρ_{xy} at 15.7 kbar for fields up to 14 T and temperatures up to 97 K. On top of the AHE signal a shoulder emerges that vanishes above ≈ 70 K.

rather sharp THE signal in the FL phase evolves into a broad peak of the same sign and roughly the same size which, however, extends over a larger field region from $B = 0$ to B_{top} (see Fig. 7.3 for the definition of B_{top}). The evolution of the THE signal across T_c can be seen at $p^* < 13.7 \text{ kbar} < p_c$, where NFL behavior is observed at temperatures above T_c up to $T^* \approx 12 \text{ K}$ (cf Fig. 5.5a). With increasing temperature (coming from low temperatures) the top-hat shaped THE signal emerges in the SLP. On crossing T_c , the THE signal becomes a broad peak ranging from $B = 0$ to B_{top} with the same sign and the same order of magnitude as below T_c . Above $T^* \approx 12 \text{ K}$ the THE signal vanishes together with the NFL behavior. At pressures above p_c , the THE signal appears at all temperatures below $T^* \approx 12 \text{ K}$ across the entire NFL regime.

The field boundaries of the NFL region and the THE signal coincide as illustrated in Fig. 9.5 where a comparison of the normalized magnetoresistance $\rho_{xx}(B)/\rho_{xx}(B=0)$ with the Hall resistivity $\rho_{xy}(B) - \rho_{xy, \text{norm}}(B)$ (corrected for the NHE contribution) and the exponent α of the temperature dependence of $\rho_{xx}(T)$ at 14.7 kbar ($> p_c$) is shown. The columns correspond to different temperatures between 1.6 K and 9.6 K . The NFL-FL transition at B_{NFL} , inferred from the jump in α , coincides with the drop in the magnetoresistance at B_m and a vanishing of the broad maximum in the Hall effect at B_{top} (see Fig. 7.3 for the definitions of B_{NFL} , B_m , and B_{top}).

Low quality samples with $RRR \approx 40 - 45$ show a similar behavior (Fig. 9.6). However, as it was observed for lower pressures, the THE signal in the low quality samples is overall broadened and appears to be bigger in the NFL region compared to the signal in the high quality samples. Also, a strong hysteresis is observed at 13.7 kbar and 2.8 K , i.e. very close to p_c , in a region of the phase diagram where a phase segregation was reported in neutron scattering [49, 50], μ -SR [176], and NMR [36].

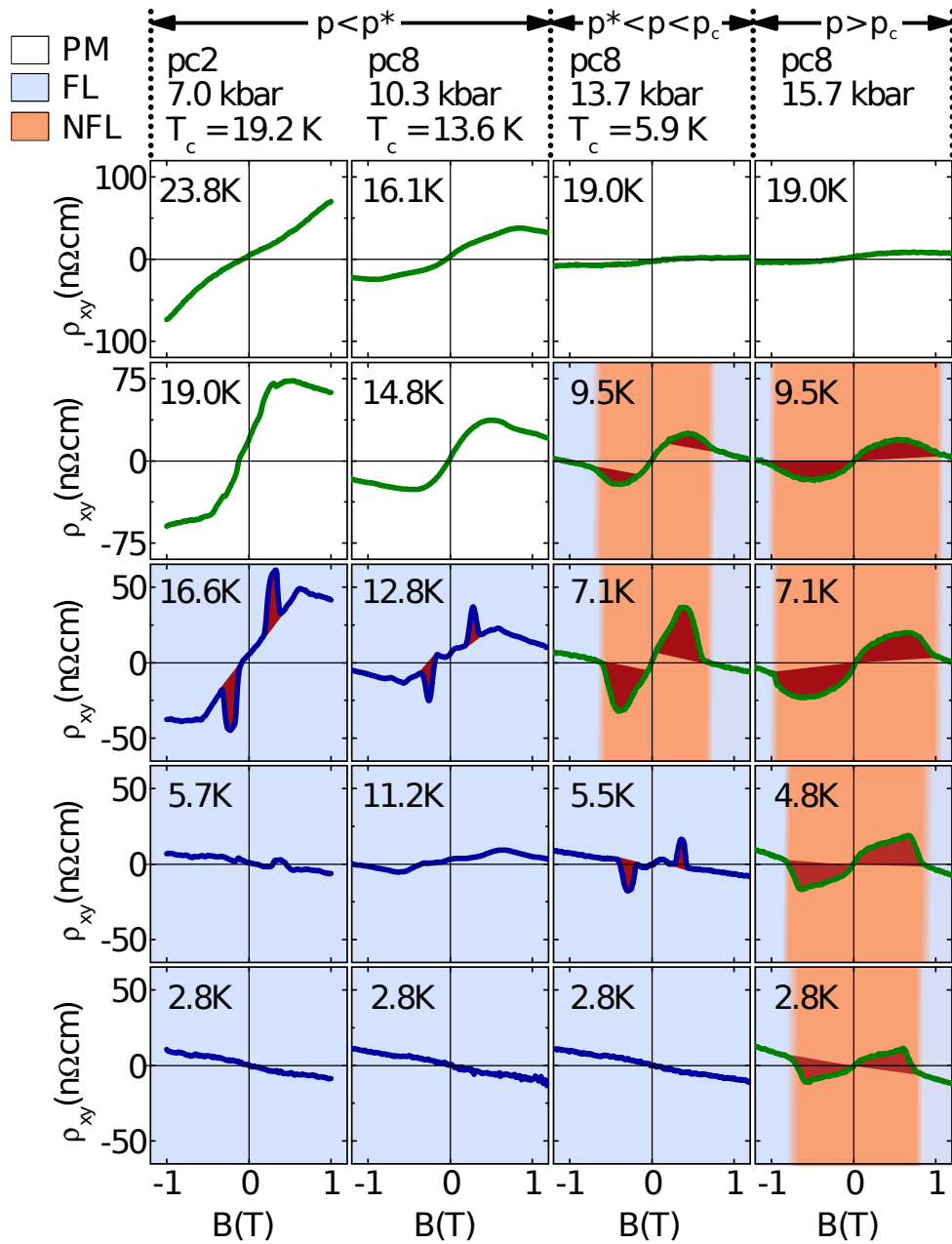


Figure 9.4: THE below and above the critical pressure. Field dependent Hall resistivity $\rho_{xy}(B)$ at various pressures and temperatures from high-quality samples ($RRR > 92$). From left to right the columns are at $p = 7.0$ kbar, 10.3 kbar, 13.7 kbar, 15.7 kbar. White shading corresponds to the paramagnetic region of the phase diagram, blue shading to regions where Fermi liquid behavior (FL) is observed and orange shading to regions where non-Fermi liquid behavior (NFL) is observed. The top-hat shaped topological Hall signal seen in the FL regions evolves into a broad maximum in the NFL regions (red shading).

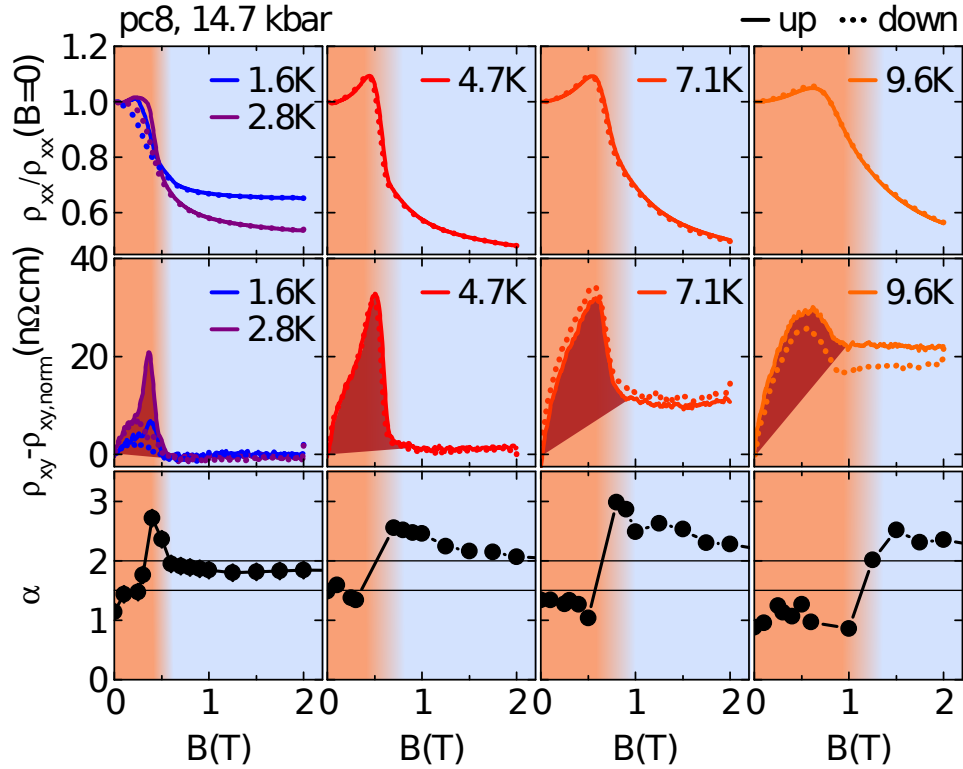


Figure 9.5: Boundaries of THE and NFL regime. Comparison of the normalized magnetoresistance $\rho_{xx}(B)/\rho_{xx}(B=0)$ with the Hall resistivity $\rho_{xy}(B) - \rho_{xy,norm}(B)$ (corrected for the NHE contribution) and the exponent α of the temperature dependence of $\rho_{xx}(T)$ at $p = 14.7$ kbar ($> p_c$). FL and NFL behavior are indicated by blue and orange shading. The columns correspond to different temperatures between 1.6 K and 9.6 K. The NFL-FL transition inferred from α coincides with a drop in the magnetoresistance and a vanishing of the broad maximum in the Hall effect.

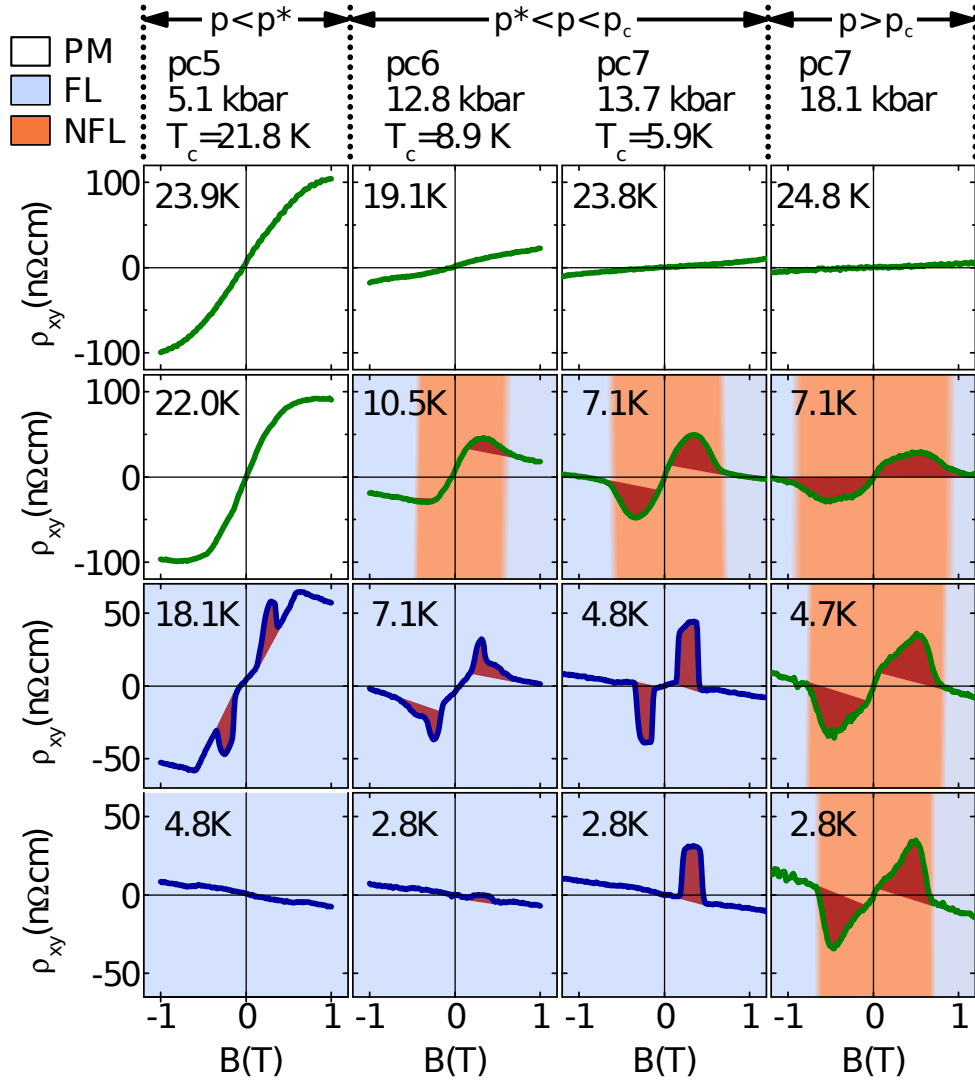


Figure 9.6: THE below and above the critical pressure in low quality samples. Field dependent Hall resistivity $\rho_{xy}(B)$ at various pressures and temperatures for low-quality samples with $RRR \approx 40 - 45$. The graph is arranged similar to Fig. 9.4 where data from high-quality samples ($RRR > 92$) is shown. As it was observed for lower pressures in Chap. 7, the topological Hall signal in low-quality samples extends over a broader field region and appears to be slightly larger in comparison with high-quality samples.

9.4 Magnetic phase diagram under pressure

Finally, we sum up the results obtained from field and temperature dependent measurements of the longitudinal resistance and the Hall effect in temperature-pressure and magnetic field-temperature phase diagrams. All transition fields and temperatures used in the phase diagrams will be introduced in Sec. 9.4.1. The phase diagrams will be discussed in Sec. 9.4.2.

9.4.1 Definition of transition fields and temperatures

The definition of all transition fields and temperatures is illustrated in Fig. 7.3 (p. 124). Panels a,b,c,d show typical $\rho_{xx}(B)$ and $\rho_{xy}(B)$ data for pressures below p_c , as already discussed in Sec. 7.1. Panels e to i show typical $\rho_{xx}(B)$, $\rho_{xy}(B)$, α , and $\rho_{xy}(T)$ data at 15.7 kbar ($> p_c$). When the pressure is increased above p_c , the magnetoresistance $\rho_{xx}(B)$ shows only one characteristic field B_m at low temperatures, where the magnetoresistance shows a large drop of $\approx 40\%$ that indicates an itinerant metamagnetic transition (Fig. 7.3e). At higher temperatures (above T^*), the drop in $\rho_{xx}(B)$ evolves into a broad crossover. The Hall resistivity $\rho_{xy}(B)$ displays the THE signal below $T^* \approx 12$ K discussed above ranging from $B = 0$ to a field B_{top} that coincides with B_m (Fig. 7.3f). However, the change of $\rho_{xx}(B)$ at B_m does not account for changes in $\rho_{xy}(B)$ through an intrinsic AHE contribution which is very small at these low temperatures and has an entirely different temperature dependence. This can be seen, e.g., through the fact that samples of different quality, and hence different residual resistivities, display a similar THE contribution. If the feature we identified as THE signal had its origin in an intrinsic AHE, it would scale with ρ_{xx} and thus would strongly depend on the sample quality.

The temperature exponent α of $\rho_{xx}(T)$ switches abruptly from from a $T^{3/2}$ (NFL) to a T^2 (FL) dependence at a field B_{NFL} (Fig. 7.3g), as already shown in the inset of Fig. 9.1. Here, α was evaluated in a temperature range between 2.0 K and 3.0 K. α values in the center of the crossover close to B_{NFL} are not shown. The temperature dependent Hall resistivity $\rho_{xy}(T)$ at numerous magnetic fields is shown in Fig. 7.3h. The maximum of $\rho_{xy}(T)$ is due to the intrinsic AHE that scales with $\rho_{xy} = R_0 B + S_H \rho_{xx}^2 M$ as shown in Eq. 6.29 [213]. At high temperatures, $\rho_{xy}(T)$ decreases due to a decreasing magnetization. At low temperature two regimes have to be distinguished. First, at low fields the downturn of $\rho_{xy}(T)$ is due to a decreasing ρ_{xx} . Here, the maximum of $\rho_{xy}(T)$ is labeled T_{max} . At high fields ($\gtrsim 1$ T), the downturn below T_S is due to a shoulder in the field dependence of ρ_{xy} at B_S (see below). Here, the maximum of $\rho_{xy}(T)$ is labeled T_S . At high magnetic fields and temperatures between ≈ 10 K and ≈ 70 K, a shoulder emerges on the Hall resistivity on top of the AHE contribution (Fig. 7.3i). The onset of the shoulder, where $\rho_{xy}(T)$ leaves a linear slope (coming from high fields), is marked as the field B_S .

9.4.2 Phase diagrams

Fig. 9.7a shows the temperature-pressure phase diagram inferred from the longitudinal resistivity $\rho_{xx}(T)$. As known from the literature, T_c is suppressed with increasing pressure and vanishes at $p_c \approx 14.6$ kbar. The color shading refers to the underlying nature of the metallic state like it was used in Secs. 9.1, 9.2, and 9.3. The phase diagram reproduces the one shown in Pfeiderer *et al.* [49] (see Fig. 5.5a). As discussed above, the NFL regime (orange shading) is accompanied by a THE signal.

Fig. 9.7b - e shows the magnetic phase diagram at selected pressures covering the ranges $p < p^*$ (7.4 kbar), $p^* < p < p_c$ (13.7 kbar), and $p > p_c$ (15.7 kbar and 18.1 kbar). For pressures below p^* , the magnetic phase diagram is qualitatively as seen at ambient pressure. However, the A-phase (SLP) is extended over a larger temperature range and displays a larger THE signal compared to ambient pressure as already discussed in Chaps. 7 and 8. Above p^* , where T_c is suppressed below $T^* \approx 12$ K, NFL behavior is observed above T_c at temperatures up to T^* . As discussed along the field dependent data (see Sec. 9.3), a THE signal is observed in the entire NFL regime. The boundaries of the NFL regime (B_{NFL}) and the THE signal (B_{top}) coincide. Above p_c , the magnetic phases are suppressed and an extended NFL region accompanied by a THE signal is seen up to $T^* \approx 12$ K and up to fields B_{top} , B_{NFL} .

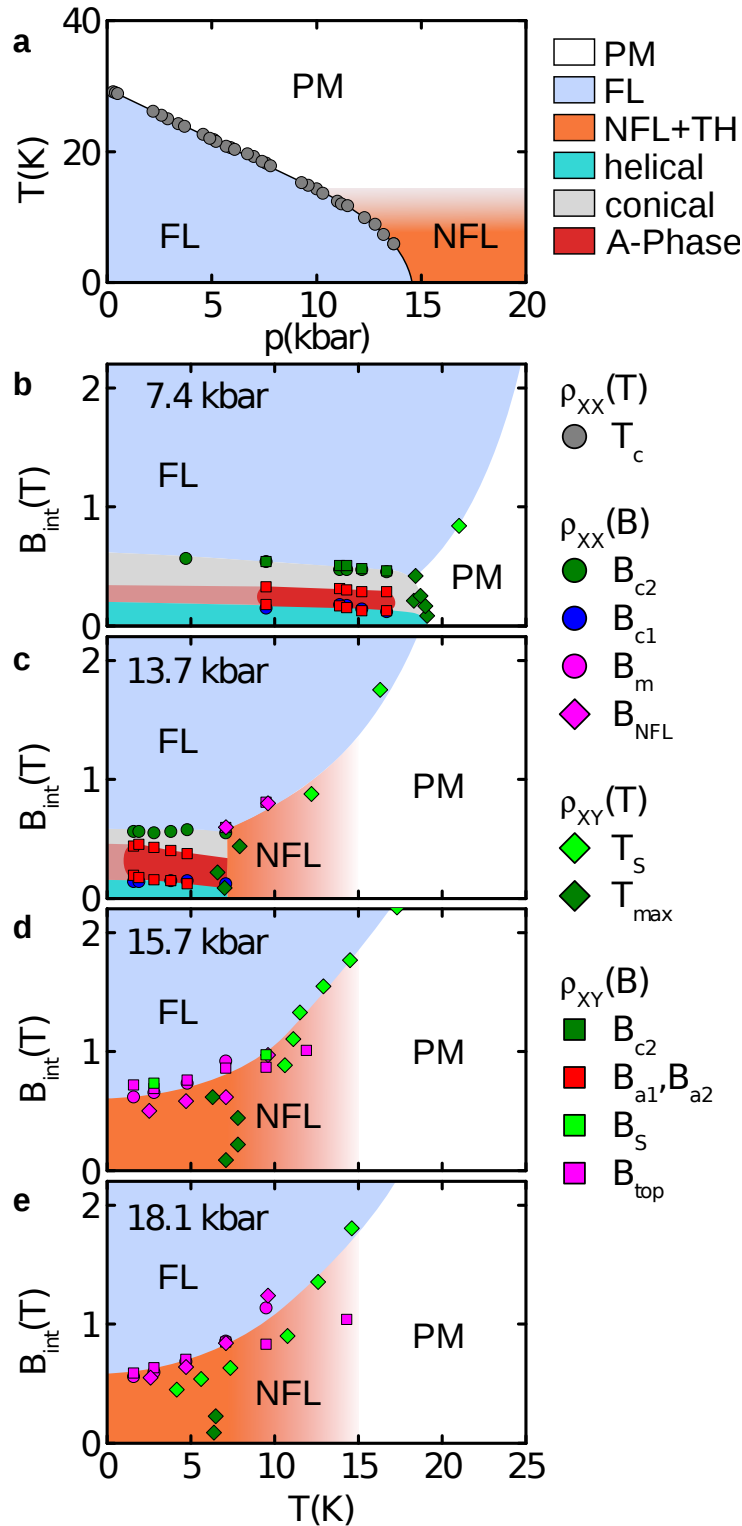


Figure 9.7: Phase diagrams at high pressures. Phase diagrams inferred from field and temperature dependent resistivity ρ_{xx} and Hall resistivity ρ_{xy} data. The shown features were measured at an increasing field (labeled with the superscript “+” in Fig. 7.3). (a) Temperature-pressure phase diagram. The solid black line through the datapoints is a guide to the eye. (b)-(e) Magnetic field-temperature phase diagrams at various pressures below and above p_c .

Chapter 10

Discussion $p > p^*$

As seen in the last chapter, the extended non-Fermi liquid (NFL) regime in MnSi is accompanied by a topological Hall effect (THE) signal. The THE signal clearly evolves from the THE signal seen in the skyrmion lattice phase (SLP) of MnSi at ambient pressure. On crossing T_c/p_c , i.e., the phase boundaries to the NFL state, the top-hat shaped THE signal, observed within the field range of the SLP, becomes a broad peak with a much broader field range. Already at tiny fields a THE appears. The field boundaries of the THE, B_{top}^+ and B_{top}^- , coincide with the metamagnetic transition where the NFL behavior abruptly switches back to Fermi liquid (FL) behavior under applied magnetic field at B_{NFL} .

The missing dependence on sample quality, the different temperature dependence than ρ_{xx} , the absence of comparable features in the magnetization, and the connection to the THE of the SLP clearly indicate that the broad peak in the Hall signal in the NFL regime is a THE. The fact that the THE signal in the FL and NFL regime evolve into each other, and the fact that sign and the order of magnitude of the THE in the FL and NFL regimes are the same - pointing at an unchanged winding number of -1 - imply that in the NFL regime skyrmionic textures are the reason for the THE signal. As the temperature, field and pressure boundaries of the NFL state and the THE coincide, the magnetic textures and the NFL are clearly linked to each other.

Several theoretical studies [179, 182, 183, 231] propose topologically non-trivial spin textures as the origin of the partial order in MnSi, where elastic neutron scattering studies show that helices - with an unchanged pitch compared to the helical phase at low pressures - exist above p_c below a temperature T_0 but have lost their directional dependence. However, the partial order, as observed by elastic neutron scattering and NMR, appears only in a small phase pocket within the NFL regime whereas the THE signal covers the entire NFL regime.

Kirkpatrick *et al.* [68] proposed columnar fluctuations of chiral spin textures as origin of the partial order and the extended NFL regime. While this theory is in contrast to some experimental observations, i.e., the prefactor of the $T^{3/2}$ dependence of the resistivity, a lot of aspects fit nicely to our observations of a THE signal across the entire NFL

regime. According to Ref. [68] chiral spin textures, possibly realized through skyrmions, exist above p_c and can be viewed as a columnar chiral fluid which exhibits a first order phase transition at T_0 from a chiral liquid to a chiral gas. The soft modes of this chiral fluid are columnar fluctuations, possibly skyrmion lines, that are slow enough below T_0 to be observed by elastic neutron scattering [50] and NMR [36]. If soft modes of this spin texture couple to the charge density this could explain the extended NFL behavior in MnSi. Combined with our results this implies that those soft modes can be observed on timescales probed by the Hall effect across the entire NFL regime.

Taken together, our observations support one of or combinations of the following three scenarios: (i) Spontaneously forming randomly oriented skyrmions at $B = 0$ that are stratified in a magnetic field. (ii) Formation of skyrmions already at tiny fields. (iii) Strong fluctuations between helical modulations and skyrmionic textures.

In a more general context it was proposed that when itinerant ferromagnetism is suppressed fluctuations arise that can lead to the formation of complex spin structures [11, 12]. In turn, those complex spin structures could lead to a breakdown of the Fermi liquid behavior. For example, in the ferromagnets $ZrZn_2$ [48] and Ni_3Al [232] a $T^{3/2}$ temperature dependence of the resistivity extending over a larger range of the temperature-pressure phase diagram has also been observed in connection with the suppression of a magnetic phase. However, so far no complex spin structures have been observed in $ZrZn_2$ and Ni_3Al . Since both materials are ferromagnets one would expect complex spin structures with a zero winding number, unlike the topologically non-trivial spin structures we observe in MnSi. In principle, MnSi could be an first example of these complex spin structures at the border of itinerant magnetism. Since MnSi exhibits a Dzyaloshinskii-Moriya interaction those spin structures are topologically non-trivial, i.e., they have a non-zero winding number.

In conclusion, our observation of a THE signal across the entire NFL regime, that clearly evolves from the THE connected to the SLP at low pressures, is the first experimental evidence of topological non-trivial spin textures within the NFL regime. Sign and size of the THE remain unchanged below and above p_c pointing at skyrmion structures. As the phase boundaries of NFL regime and THE coincide, this skyrmion structures are a good candidate for the long-sought intrinsic mechanism behind the NFL behavior.

Part III

Summary and outlook

In this thesis the two itinerant ferromagnets UGe_2 and MnSi were studied around the critical pressures. In both materials the considered phase transitions turn first order before they are suppressed giving rise to quantum critical behavior without the presence of a quantum critical point. In the superconducting ferromagnet UGe_2 we performed measurements of the thermal expansion under pressure concomitant with the magnetization using the neutron spin echo technique called Larmor diffraction. We concentrated on the pressure range around the pressure p_X where a phase transition T_X between two ferromagnetic phases is suppressed and a superconducting dome emerges. Experimental results reported so far imply that the suppression of the T_X transition, whose origin is yet unclear, is intimately connected to the emerging superconductivity. In the helimagnet MnSi we studied the evolution of a topological Hall effect signal, that is signature of a lattice of magnetic whirls, a so-called the skyrmion lattice, under pressure. We covered the pressure range from ambient pressure to pressures above the critical pressure where an extended non-Fermi liquid phase was reported in earlier studies. The main results of the two projects are summarized below.

Thermal expansion of UGe_2 under pressure [137]

For our project on UGe_2 we performed the neutron spin echo technique Larmor diffraction for the first time on a ferromagnet. We overcame the experimental difficulties resulting from a neutron depolarization when the sample is in the ferromagnetic state through applying an demagnetizing AC magnetic field when cooling through the Curie temperature yielding equally populated domains. Furthermore, we could straight forward correct our raw data for contributions to the phase rotations not related to a change in lattice constant, so-called spin-echo phases, that are observed in our high-pressure experiments. The origin of the spin-echo phases is still unclear and further experiments are required to settle this issue. However, the interpretation of our data is completely independent from any spin-echo phase corrections. In total we measured six pressure points between ambient pressure and 12.4 kbar. Our data matches well with thermal expansion data acquired with the established methods of capacitive dilatometry and strain gauges that was reported in literature so far.

Through concomitant measurements of the thermal expansion and the magnetization we were able to separate contributions from the crystal lattice and magnetostriction to the thermal expansion from other contributions. We find that under pressure the a - and b -axis thermal expansion can be well accounted for by the lattice contribution and magnetostriction while an additional contribution emerges at a transition temperature T_L several Kelvin above T_X . We speculate that the T_L transition could be signature of a change in the Fermi surface topology at a Lifshitz transition. However, more experimental information is needed to proof this hypothesis. This could be an important piece of information for identifying the mechanism behind the unconventional superconductivity found in UGe_2 .

Topological Hall effect in MnSi under pressure

We performed a comprehensive study of the Hall effect in MnSi where we measured a total of 38 pressure points. We carefully checked the influence of various experimental parameters as sample quality, sample orientation, pressure media, and cooling procedures. We were able to track the evolution of the topological Hall effect (THE) up to pressures above p_c . The results for the pressure ranges $p < p^* \approx 12$ kbar and $p > p^*$ are summarized below.

$p < p^*$ - Giant generic topological Hall effect signal [16]

With increasing pressure the size of the THE increases tenfold from $\Delta\rho_{xy}^{\text{top}}(p=0) \approx 4.5$ n Ω cm up to $\Delta\rho_{xy}^{\text{top}}(p \approx 12$ kbar) ≈ 40 n Ω cm. The THE signature clearly evolves from the THE signal of the skyrmion lattice phase at ambient pressure and can furthermore be unambiguously identified as THE through its temperature dependence and through a comparison with magnetization measurements under pressure. We are able to identify the signature reported in the Hall effect between 6 and 12 kbar in a wide field interval by Lee *et al.* [162] as THE broadened due to a low sample quality and poor pressure conditions.

The large THE signal can be conserved down to the lowest temperatures measured (typically ≈ 2 K) when cooling down in a magnetic field. The THE reveals its generic size in the low temperature limit as $\Delta\rho_{xy}^{\text{top}} \approx 50$ n Ω cm where finite temperature effects are essentially switched off.

The size of the THE can be explained quantitatively through a theoretical analysis by Rosch and collaborators in our paper [16]. The decreased THE signal size at ambient pressure and high temperatures can be attributed to the change of the local polarization close to T_c for the most important part. The remaining part is most likely due to one or a combination of several mechanisms including changes of the Fermi surface, change of scattering processes, competition between exchange splitting and spin-orbit coupling, and spin-flip scattering.

Our results imply that the large THE reported in other materials as MnGe [202] and SrFeO₃ [203] with ≈ 200 n Ω cm could generically be much larger when finite temperature effects can essentially be switched off through suppressing the skyrmion lattice phase to lower temperatures with pressure or doping. As the THE is the mechanism that couples current to the magnetic structure, the critical current j_c in spin transfer torque experiments, that was found to be ultralow in MnSi [51, 52, 233], is expected to decrease with increasing THE. Studies on iron doped MnSi with THE signals up to ≈ 40 n Ω cm show that j_c decreases with the THE size, however, in these systems the disorder introduced pinning on iron sites which leads to an increased j_c has to be overcompensated first [234]. Therefore, spin transfer torque experiments on MnSi under pressure are currently on its way where the influence of the THE size on j_c can be studied directly without the effect of pinning at impurities. These results are of great interest for applications of skyrmions

in spintronic devices that seem to become more and more achievable [235].

$p > p^*$ - Topological non-Fermi liquid [53]

We find a THE in the non-Fermi liquid region above the critical pressure p_c where magnetic order is already suppressed. The THE signal clearly evolves from the THE signal seen in the skyrmion lattice phase of MnSi at ambient pressure. Sign and size of the THE remain unchanged below and above p_c pointing at skyrmion structures. The field boundaries of the THE coincide with the metamagnetic transition where the NFL behavior abruptly switches back to Fermi liquid behavior under applied magnetic field. Also the temperature and pressure boundaries of the NFL state and the THE coincide. Thus, the magnetic textures and the NFL are clearly linked to each other. This could be a first example of a more general phenomenon where magnetic textures form on the border of ferromagnetism [11, 12]. Those complex spin structures could be the long-sought intrinsic mechanism driving the breakdown of Fermi liquid behavior in MnSi.

Publications

- **Formation of a topological non-Fermi liquid in MnSi.** R. Ritz, M. Halder, M. Wagner, C. Franz, A. Bauer, C. Pfleiderer. *Nature* **497**, 231 (2013)
- **Giant generic topological Hall resistivity in MnSi under pressure.** R. Ritz, M. Halder, C. Franz, A. Bauer, M. Wagner, R. Bamler, A. Rosch, C. Pfleiderer. *Physical Review B* **87**, 13, 134424 (2013)
- **Thermal expansion of UGe₂ under pressure.** D.A. Sokolov, R. Ritz, C. Pfleiderer, T. Keller, A.D. Huxley. *submitted to Physical Review Letters*
- **Emergent electrodynamics of skyrmions in a chiral magnet.** T. Schulz, R. Ritz, A. Bauer, M. Halder, M. Wagner, C. Franz, C. Pfleiderer, K. Everschor, M. Garst, A. Rosch. *Nature: Physics* **8**, 4, 301 (2012)
- **Neutron scattering studies of the lattice expansion in a ferromagnetic superconductor UGe₂ under pressure.** D.A. Sokolov, R. Ritz, C. Pfleiderer, T. Keller, A.D. Huxley. *Journal of Physics: Conference Series* **273**, 012085 (2011)
- **Distribution of Lattice Constants in CePt₃Si Observed by Larmor Diffraction and SANS.** R. Ritz, S. Mühlbauer, C. Pfleiderer, T. Keller, J. White, M. Laver, E.M. Forgan, R. Cubitt, C. Dewhurst, P.G. Niklowitz, A. Prokofiev, E. Bauer. *Journal of Physics: Conference Series* **200**, 012165 (2010)
- **Skyrmion lattices in metallic and semiconducting B20 transition metal compounds.** C. Pfleiderer, T. Adams, A. Bauer, W. Biberacher, B. Binz, F. Birkelbach, P. Böni, C. Franz, R. Georgii, M. Janoschek, F. Jonietz, T. Keller, R. Ritz, S. Mühlbauer, W. Münzer, A. Neubauer, B. Pedersen, A. Rosch. *Journal of Physics: Condensed Matter* **22**, 16, 164207 (2010)
- **Topological Hall Effect in the A Phase of MnSi.** A. Neubauer, C. Pfleiderer, B. Binz, A. Rosch, R. Ritz, P.G. Niklowitz, P. Böni. *Physical Review Letters* **102**, 18, 186602 (2009)
- **Hall effect and magnetoresistance in MnSi.** A. Neubauer, C. Pfleiderer, R. Ritz, P.G. Niklowitz, P. Böni. *Physica B: Condensed Matter* **404**, 19, 3163 (2009)
- **Quantum order in the chiral magnet MnSi.** C. Pfleiderer, A. Neubauer, S. Mühlbauer, F. Jonietz, M. Janoschek, S. Legl, R. Ritz, W. Münzer, C. Franz, P.G.

Niklowitz, T. Keller, R. Georgii, P. Böni, B. Binz, A. Rosch, U.K. Rössler, A.N. Bogdanov. *Journal of Physics: Condensed Matter* **21**, 16, 164215 (2009)

Acknowledgements

During my time as diploma and doctoral student at the institute E21 I received great support and had the luck of working with the greatest colleagues imaginable. I also enjoyed the support from my family, relatives and friends. For this I would like thank everyone at this point. This personal part will be in German.

Prof. Christian Pfeiderer Vielen Dank für die tolle Zeit in Deiner Gruppe! Vielen Dank für all die guten Gespräche, Ratschläge, Motivation, die Freiheiten, die interessantesten Projekte und die vielen Möglichkeiten an Konferenzen, Workshops und Austauschprogrammen teilzunehmen. Es war schön mit Dir zusammenzuarbeiten.

Prof. Peter Böni Vielen Dank für die interessanten Gespräche, Deine Expertise in Neutronenstreuung und die guten Bedingungen am E21.

Meine Mitstreiter und Freunde am Lehrstuhl Vielen Dank für Eure Unterstützung, das Teamwork und den ganzen Spaß, den wir zusammen hatten - im Labor, auf Konferenzen, Workshops, Urlauben und Partys. Es war toll, Euch als Kollegen zu haben und in einem so zusammengeschweißten Team zu arbeiten! Ich würde sagen: "Es geht in die richtige Richtung!"

Die alte Garde: Marc Janoschek, Sebastian Mühlbauer, Andreas Neubauer, Stefan Legl. *Die mittlere Generation:* Alexander Regnat, Tim Adams, Christian Franz, Florian Bernlocher, Andreas Bauer, Michael Wagner, Stefan Giemsa, Wolfgang Münzer, Florian Jonietz, Felicitas Birkelbach, Christopher Duvinage, Michael Schulz, Birgit Wiedemann, Saskia Gottlieb-Schönmeyer, Hubert Ceeh, Benjamin Rohrmoser. *Junges Gemüse:* Tomek Schulz, Ralf Korntner, Christoph Schnarr, Jonas Kindervater, Marco Halder, Philipp Schmakat, Ralitsa Bozhanova, Dorothea Mallinger, Katharina Lochner, Maximilian Hirschberger, Jan Spallek, Markus Strobl, Marein Rahn, Felix Rucker, Alfonso Chacon, Georg Benka, Patrick Ziegler, ... und alle, die ich vergessen habe.

Die “Erwachsenen” am Lehrstuhl: Barbara Russ, Astrid Mühlberg, Christoph Morkel und Sarah Dunsiger Vielen Dank für viele interessante Gespräche über Physik, Politik und das Leben im Allgemeinen... und für den ein oder anderen Kuchen.

Achim Rosch, Markus Garst und Robert Bamler Vielen Dank für die gute “theoretische” Unterstützung bei unseren MnSi-Projekten.

Andrew Huxley and Dmitry Sokolov Thank you for the close cooperation and all the support on our UGe₂-project.

Das TRISP-Team: Thomas Keller und Kathrin Buchner Vielen Dank für die gute Unterstützung bei den vielen Messzeiten am TRISP!

Das PANDA-Team: Astrid Schneidewind, Enrico Faulhaber und Dirk Etdorf Vielen Dank für die Unterstützung bei unseren inelastischen Experimenten.

Technische Unterstützung: Andreas Mantwill, Zentralwerkstatt, Kühlmitteleinheit, Kristalllabor Vielen Dank für die Unterstützung und für die “Schwätzchen zwischendurch auf dem Gang“.

Meine Familie Papa, Mama, Gabi, Susi, Tina, Hartwig & Johanna, Klaus & Bruni + Familie, Dorothee + Familie, Alex, Matthias ... Vielen Dank für die ganze Unterstützung, die ich von Euch bekommen habe. Ihr seid super!

WG-Mitbewohner, Mitphysiker, Wohnheimkollegen und Schulfreunde Andi H., Josch, Uli T., Peter, Andi B., Martin, Anso, Julius, Uli W., Jürgen, Sarah, Prombi, Hans, Dieter, Franz, Schink, Pfister, Sabine, Timo, Arne, Ralph, ... Auch Euch vielen Dank für die gute Zeit.

Kerstin - Das Beste sollte man sich immer für den Schluß aufheben. Ich genieße jeden Moment, den wir zusammen verbringen und freue mich auf eine schöne gemeinsame Zukunft!

Appendix A

Overview LD and SE scans

In this section all UGe₂ data recorded in Larmor diffraction (LD) and spin-echo (SE) geometry are summarized in Figs. A.1 - A.6. In each figure, the upper row shows $\Delta d_{\text{raw-data}}/d$ (black datapoints) and the SE phase (red datapoints) calculated according to Eq. 3.12:

$$I = I_0 \left(1 + P \cos \left(2\pi \frac{x_{\text{TC4}} - x_{\text{TC4},0}}{\Delta L} \right) \right)$$

The SE phase corrected $\Delta d_{\text{raw-data}}/d$ is illustrated when available (green datapoints). The middle row shows the corresponding polarization P , and the bottom row shows the intensity I_0 normalized to the intensity at base temperature. At 10.2 kbar, the a -axis SE phase was estimated from the corresponding polarization (open red datapoints) as it was found empirically, that the a -axis SE phase at 9.3 kbar and 11.8 kbar resembles the corresponding polarization curves (Fig. A.3a).

Fig. A.7 illustrates how the T_X and T_L transitions were determined in the magnetization and in the $\Delta d_{\text{raw-data}}/d$ at 9.3 kbar, 10.2 kbar, and 11.8 kbar.

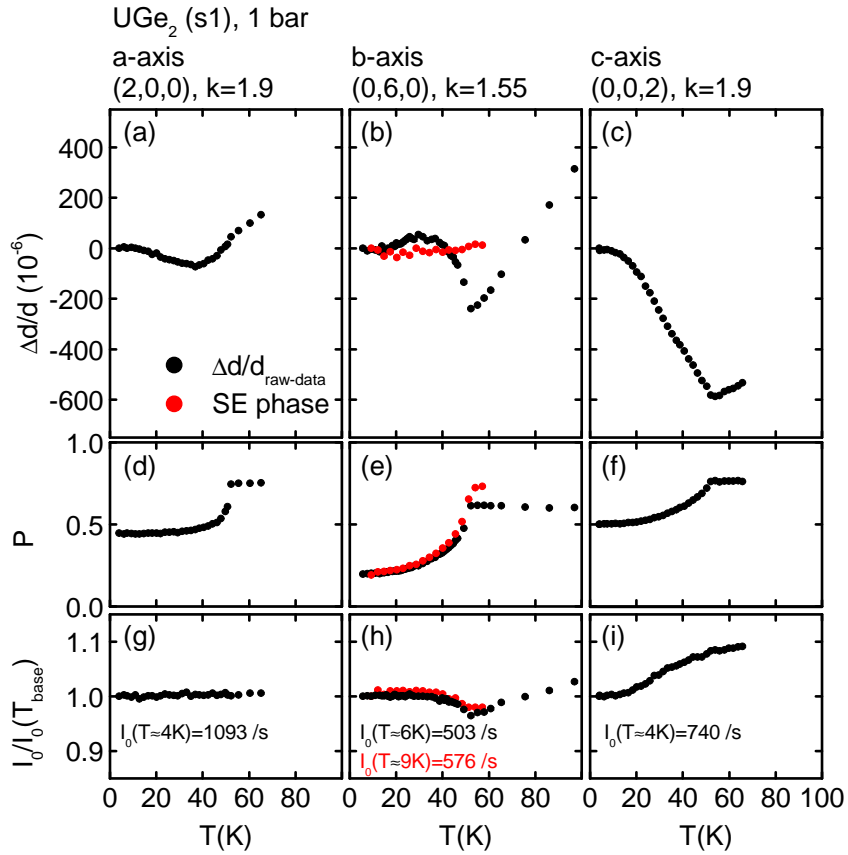


Figure A.1: Phase, intensity and polarization of all LD and SE scans at ambient pressure. The parameters $\Delta d/d$, I_0 , and P refer to equation 3.12 with which the raw data was fitted.

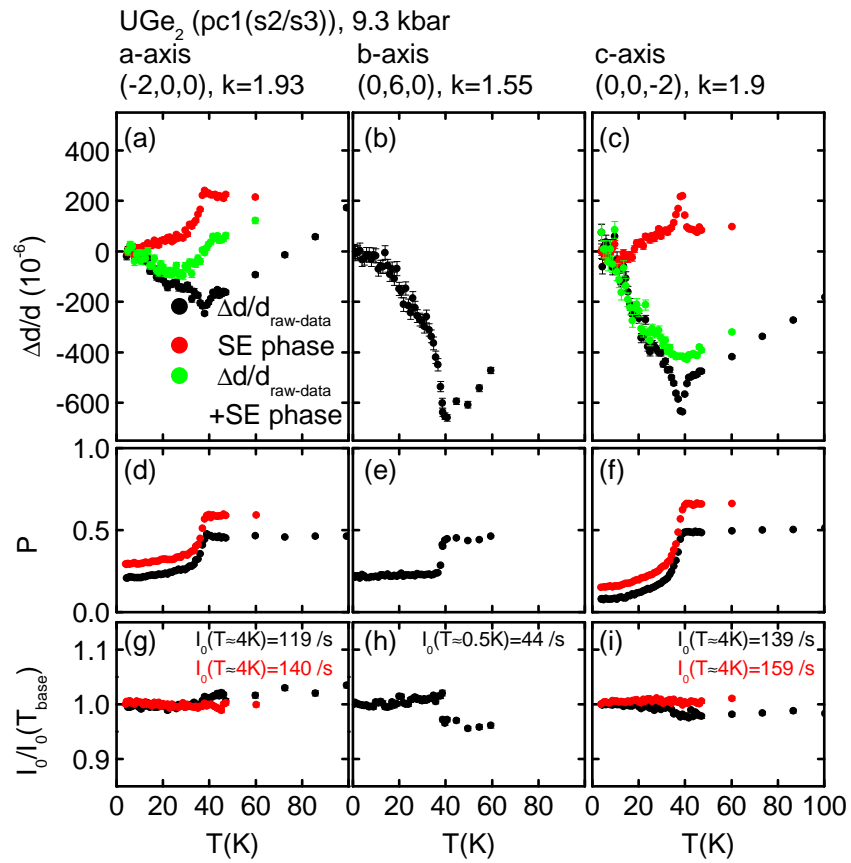


Figure A.2: Phase, intensity and polarization of all LD and SE scans at 9.3 kbar. The parameters $\Delta d/d$, I_0 , and P refer to equation 3.12 with which the rawdata was fitted.

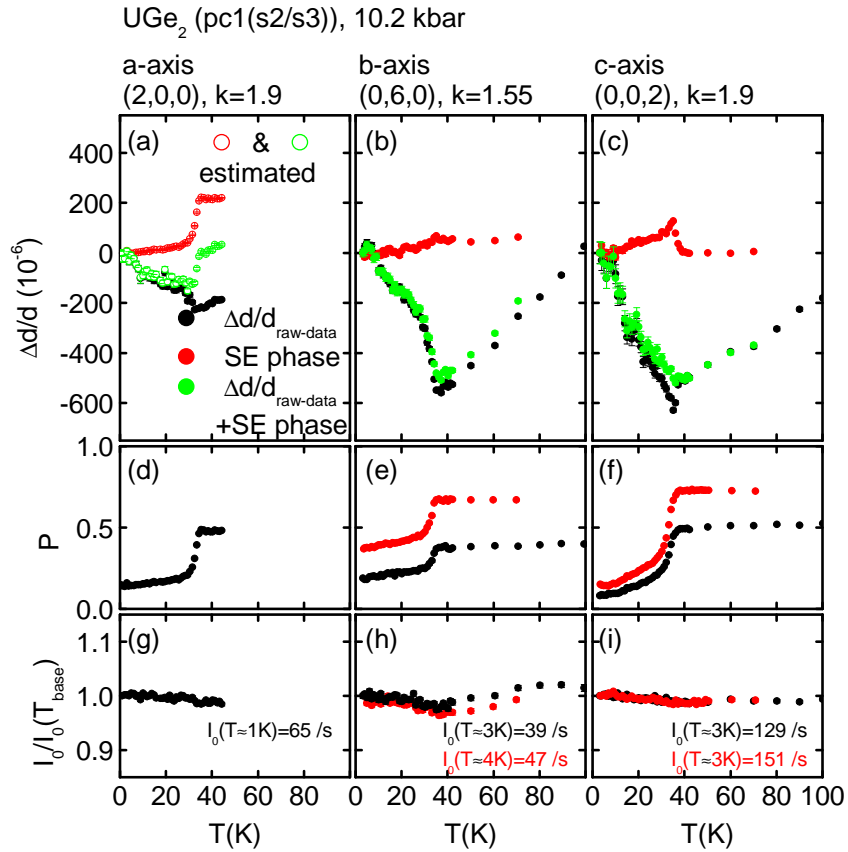


Figure A.3: Phase, intensity and polarization of all LD and SE scans at 10.2 kbar. The parameters $\Delta d/d$, I_0 , and P refer to equation 3.12 with which the raw data was fitted. In panel a the a -axis SE phase was estimated from the corresponding polarization curve.

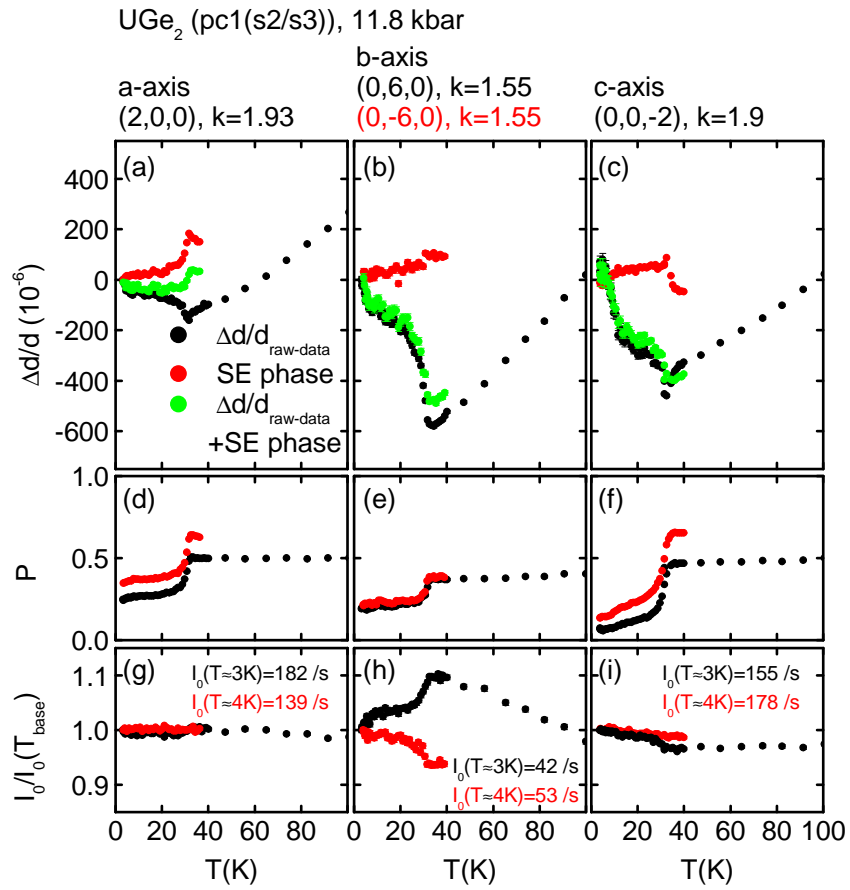


Figure A.4: Phase, intensity and polarization of all LD and SE scans at 11.8 kbar. The parameters $\Delta d/d$, I_0 , and P refer to equation 3.12 with which the raw data was fitted.

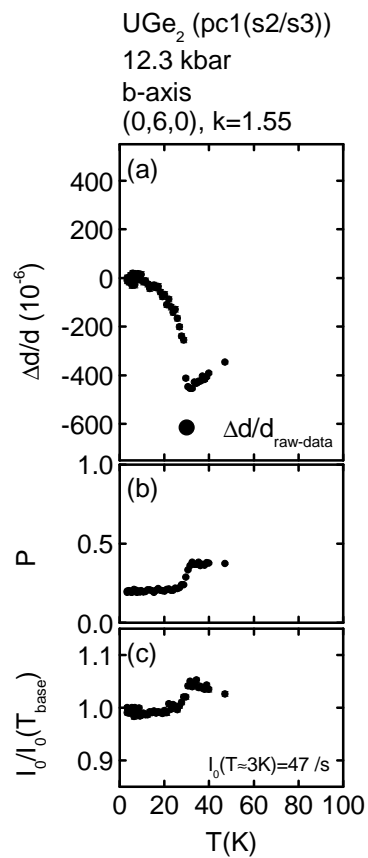


Figure A.5: Phase, intensity and polarization of all LD and SE scans at 12.3 kbar. The parameters $\Delta d/d$, I_0 , and P refer to equation 3.12 with which the raw data was fitted.

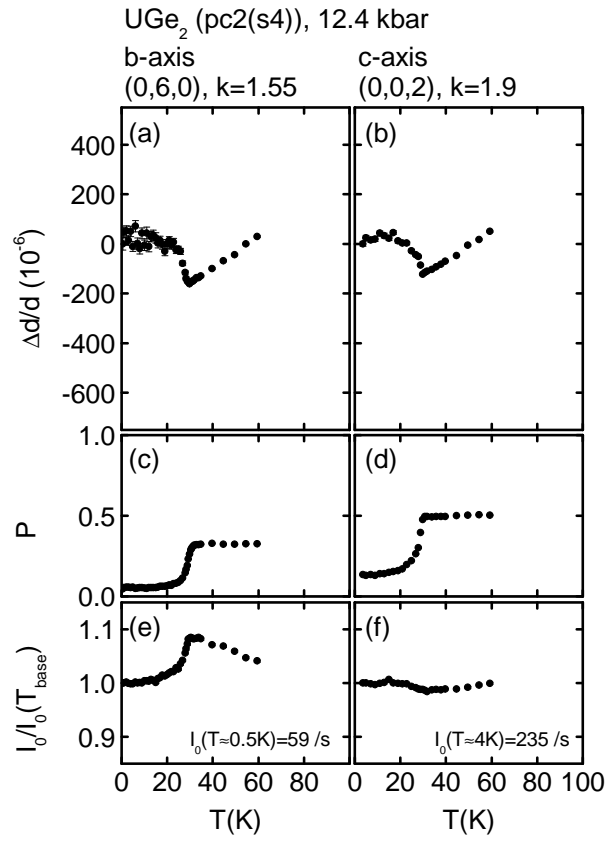


Figure A.6: Phase, intensity and polarization of all LD and SE scans at 12.4 kbar. The parameters $\Delta d/d$, I_0 , and P refer to equation 3.12 with which the raw data was fitted.

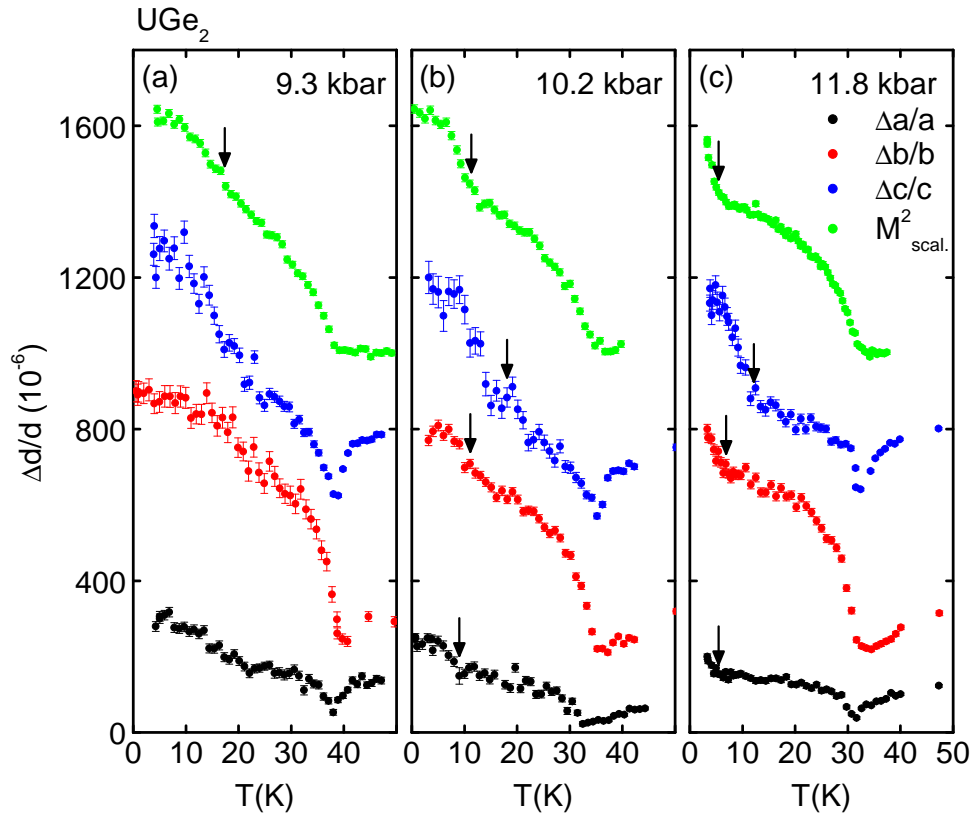


Figure A.7: Thermal expansion raw data at 9.3 kbar, 10.2 kbar and 11.8 kbar together with the scaled magnetization. The transitions at T_X are seen as onsets of signal increases in the individual axes and the magnetization that are marked through arrows. Since the T_X transitions are very broad in the thermal expansion at 9.3 kbar, no arrows are inserted in panel a.

Bibliography

- [1] T. Vojta. Quantum phase transitions in electronic systems. *Annalen der Physik*, 9(6):403–440, 2000.
- [2] N. D. Mathur, F. M. Grosche, S. R. Julian, I. R. Walker, D. M. Freye, R. K. W. Haselwimmer, and G. G. Lonzarich. Magnetically mediated superconductivity in heavy fermion compounds. *Nature*, 394(6688):39–43, 1998.
- [3] R. Movshovich, T. Graf, D. Mandrus, J. D. Thompson, J. L. Smith, and Z. Fisk. Superconductivity in heavy-fermion CeRh₂Si₂. *Phys. Rev. B*, 53:8241–8244, 1996.
- [4] E. Vargoz, P. Link, D. Jaccard, T. Le Bihan, and S. Heathman. Is CeCu₂ a pressure-induced heavy-fermion superconductor? *Physica B: Condensed Matter*, 229(3–4):225 – 232, 1997.
- [5] I. R. Walker, F. M. Grosche, D. M. Freye, and G. G. Lonzarich. The normal and superconducting states of CeIn₃ near the border of antiferromagnetic order. *Physica C: Superconductivity*, 282–287(0):303 – 306, 1997.
- [6] J. Custers, P. Gegenwart, H. Wilhelm, K. Neumaier, Y. Tokiwa, O. Trovarelli, C. Geibel, F. Steglich, C. Pepin, and P. Coleman. The break-up of heavy electrons at a quantum critical point. *Nature*, 424:524–527, 2003.
- [7] H. v. Löhneysen, T. Pietrus, G. Portisch, H. G. Schlager, A. Schröder, M. Sieck, and T. Trappmann. Non-Fermi-liquid behavior in a heavy-fermion alloy at a magnetic instability. *Phys. Rev. Lett.*, 72:3262–3265, 1994.
- [8] S. S. Saxena, P. Agarwal, K. Ahilan, F. M. Grosche, R. K. W. Haselwimmer, M. J. Steiner, E. Pugh, I. R. Walker, S. R. Julian, P. Monthoux, et al. Superconductivity on the border of itinerant-electron ferromagnetism in UGe₂. *Nature*, 406(6796):587–592, 2000.
- [9] C. Pfleiderer, S. R. Julian, and G. G. Lonzarich. Non-Fermi-liquid nature of the normal state of itinerant-electron ferromagnets. *Nature*, 414:427–430, 2001.
- [10] N. Doiron-Leyraud, I. R. Walker, L. Taillefer, M. J. Steiner, S. R. Julian, and G. G. Lonzarich. Fermi-liquid breakdown in the paramagnetic phase of a pure metal. *Nature*, 425:595–599, 2003.
- [11] G. J. Conduit, A. G. Green, and B. D. Simons. Inhomogeneous phase formation on the border of itinerant ferromagnetism. *Phys. Rev. Lett.*, 103:207201, 2009.

- [12] D. Belitz and T. R. Kirkpatrick. Fluctuation-driven quantum phase transitions in clean itinerant ferromagnets. *Phys. Rev. Lett.*, 89:247202, 2002.
- [13] P. Pedrazzini, D. Jaccard, G. Lapertot, J. Flouquet, Y. Inada, H. Kohara, and Y. Onuki. Probing the extended non-Fermi liquid regimes of MnSi and Fe. *Physica B*, 378-380:165–166, 2006.
- [14] G. G. Lonzarich and L. Taillefer. Effect of spin fluctuations on the magnetic equation of state of ferromagnetic or nearly ferromagnetic metals. *Journal of Physics C: Solid State Physics*, 18:4339–4371, 1985.
- [15] A. Neubauer, C. Pfleiderer, B. Binz, A. Rosch, R. Ritz, P. G. Niklowitz, and P. Böni. Topological Hall effect in the A-phase of MnSi. *Phys. Rev. Lett.*, 102(18):186602, 2009.
- [16] R. Ritz, M. Halder, C. Franz, A. Bauer, M. Wagner, R. Bamler, A. Rosch, and C. Pfleiderer. Giant generic topological Hall resistivity of MnSi under pressure. *Phys. Rev. B*, 87:134424, 2013.
- [17] S. L. Sondhi, S. M. Girvin, J. P. Carini, and D. Shahar. Continuous quantum phase transitions. *Rev. Mod. Phys.*, 69:315–333, 1997.
- [18] G. R. Stewart. Non-Fermi-liquid behavior in d - and f -electron metals. *Rev. Mod. Phys.*, 73(4):797–855, 2001.
- [19] G. R. Stewart. Addendum: Non-Fermi-liquid behavior in d - and f -electron metals. *Rev. Mod. Phys.*, 78:743–753, 2006.
- [20] M. Vojta. Quantum phase transitions. *Reports on Progress in Physics*, 66(12):2069, 2003.
- [21] D. Belitz, T. R. Kirkpatrick, and T. Vojta. How generic scale invariance influences quantum and classical phase transitions. *Rev. Mod. Phys.*, 77:579–632, 2005.
- [22] H. v. Löhneysen, A. Rosch, M. Vojta, and P. Wölfle. Fermi-liquid instabilities at magnetic quantum phase transitions. *Rev. Mod. Phys.*, 79:1015–1075, 2007.
- [23] D. M. Broun. What lies beneath the dome? *Nature Physics*, 4(3):170–172, 2008.
- [24] S. Sachdev. Quantum magnetism and criticality. *Nature Physics*, 4(3):173–185, 2008.
- [25] P. Gegenwart, Q. Si, and F. Steglich. Quantum criticality in heavy-fermion metals. *Nature Physics*, 4(3):186–197, 2008.
- [26] S. Sachdev and B. Keimer. Quantum criticality. *Physics Today*, 64:29, 2011.
- [27] W. Gebhardt and U. Krey. *Phasenübergänge und kritische Phänomene: Eine Einführung für Physiker im Hauptstudium*. Friedrich Vieweg, 1980.

-
- [28] J. J. Binney, N. J. Dowrick, A. J. Fisher, and M. Newman. *The theory of critical phenomena: An introduction to the renormalization group*. Oxford University Press, Inc., 1992.
- [29] C. Pfleiderer. Why first order quantum phase transitions are interesting. *Journal of Physics: Condensed Matter*, 17(11):987, 2005.
- [30] J. A. Hertz. Quantum critical phenomena. *Phys. Rev. B*, 14:1165–1184, 1976.
- [31] S. E. Rowley, L. J. Spalek, R. P. Smith, M. P. M. Dean, G. G. Lonzarich, J. F. Scott, and S. S. Saxena. Quantum criticality in ferroelectrics. *arXiv preprint*, 0903.1445, 2009.
- [32] R. Coldea, D. A. Tennant, E. M. Wheeler, E. Wawrzynska, D. Prabhakaran, M. Telling, K. Habicht, P. Smeibidl, and K. Kiefer. Quantum criticality in an Ising chain: experimental evidence for emergent E8 symmetry. *Science*, 327(5962):177–180, 2010.
- [33] D. Bitko, T. F. Rosenbaum, and G. Aeppli. Quantum critical behavior for a model magnet. *Phys. Rev. Lett.*, 77(5):940, 1996.
- [34] M. Uhlarz, C. Pfleiderer, and S. M. Hayden. Quantum phase transitions in the itinerant ferromagnet ZrZn_2 . *Phys. Rev. Lett.*, 93(256404), 2004.
- [35] A. Huxley, I. Sheikin, and D. Braithwaite. Metamagnetic behavior near the quantum critical point in UGe_2 . *Physica B: Condensed Matter*, 284:1277–1278, 2000.
- [36] W. Yu, F. Zamborszky, J. D. Thompson, J. L. Sarrao, M. E. Torelli, Z. Fisk, and S. E. Brown. Phase inhomogeneity of the itinerant ferromagnet MnSi at high pressures. *Phys. Rev. Lett.*, 92:086403, 2004.
- [37] M. Otero-Leal, F. Rivadulla, M. Garcia-Hernandez, A. Pineiro, V. Pardo, D. Baldomir, and J. Rivas. Identification of a marginal Fermi-liquid in itinerant ferromagnet CoS_2 . *arXiv preprint*, 0806.2819, 2008.
- [38] D. Belitz, T. R. Kirkpatrick, and J. Rollbühler. Tricritical Behavior in Itinerant Quantum Ferromagnets. *Phys. Rev. Lett.*, 94(247205), June 2005.
- [39] D. Belitz and T. R. Kirkpatrick. A compilation of metallic systems that show a quantum ferromagnetic transition. *arXiv preprint*, 1204.0873, 2012.
- [40] M. Janoschek, M. Garst, A. Bauer, P. Krautscheid, R. Georgii, P. Böni, and C. Pfleiderer. Fluctuation-induced first-order phase transition in Dzyaloshinskii-Moriya helimagnets. *Phys. Rev. B*, 87:134407, 2013.
- [41] S. A. Brazovskii. Phase transition of an isotropic system to a nonuniform state. *Sov. Phys. JETP*, 41:85, 1975.

- [42] N. T. Huy, A. Gasparini, D. E. de Nijs, Y. Huang, J. C. P. Klaasse, T. Gortenmulder, A. de Visser, A. Hamann, T. Görlach, and H. v. Löhneysen. Superconductivity on the Border of Weak Itinerant Ferromagnetism in UCoGe. *Phys. Rev. Lett.*, 99:067006, Aug 2007.
- [43] D. Belitz, T. R. Kirkpatrick, and T. Vojta. Nonanalytic behavior of the spin susceptibility in clean Fermi systems. *Physical Review B*, 55(15):9452, 1997.
- [44] T. Vojta, D. Belitz, R. Narayanan, and T. R. Kirkpatrick. Quantum critical behavior of clean itinerant ferromagnets. *Zeitschrift für Physik B Condensed Matter*, 103(3):451–461, 1997.
- [45] D. Belitz, T. R. Kirkpatrick, and T. Vojta. First order transitions and multicritical points in weak itinerant ferromagnets. *Phys. Rev. Lett.*, 82:4707–4710, 1999.
- [46] W. J. Duncan. Quantum phase transitions in NbFe₂ and BaFe₂As₂. PhD thesis, Royal Holloway, University of London, 2010.
- [47] W. J. Duncan. Quantum phase transitions and quantum criticality in NbFe₂. *Seminar talk, Munich, Germany.*, 2009.
- [48] R. P. Smith, M. Sutherland, G. G. Lonzarich, S.S. Saxena, N. Kimura, S. Takashima, M. Nohara, and H. Takagi. Marginal breakdown of the Fermi-liquid state on the border of metallic ferromagnetism. *Nature*, 455(7217):1220–1223, 2008.
- [49] C. Pfleiderer, P. Böni, T. Keller, U. K. Rößler, and A. Rosch. Non-Fermi liquid metal without quantum criticality. *Science*, 316:1871–1874, 2007.
- [50] C. Pfleiderer, D. Reznik, L. Pintschovius, H. v. Löhneysen, M. Garst, and A. Rosch. Partial order in the non-Fermi-liquid phase of MnSi. *Nature*, 427:227–231, 2004.
- [51] F. Jonietz, S. Mühlbauer, C. Pfleiderer, A. Neubauer, W. Münzer, A. Bauer, T. Adams, R. Georgii, P. Böni, R. A. Duine, et al. Spin transfer torques in MnSi at ultralow current densities. *Science*, 330(6011):1648–1651, 2010.
- [52] T. Schulz, R. Ritz, A. Bauer, M. Halder, M. Wagner, C. Franz, C. Pfleiderer, K. Everschor, M. Garst, and A. Rosch. Emergent electrostatics of skyrmions in a chiral magnet. *Nature Physics*, 8(4):301–304, 2012.
- [53] R. Ritz, M. Halder, M. Wagner, C. Franz, A. Bauer, and C. Pfleiderer. Formation of a topological non-Fermi liquid in MnSi. *Nature*, 497(7448):231–234, 2013.
- [54] I. M. Lifshitz. Anomalies of electron characteristics of a metal in the high pressure region. *Sov. Phys. JETP*, 11(5):1130–1135, 1960.
- [55] D. Koudela. Lifshitz transitions in RCo₅ (R=Y,La) and in Osmium. PhD thesis, TU Dresden, 2007.
- [56] Ya. M. Blanter, M. I. Kaganov, A. V. Pantsulaya, and A. A. Varlamov. The theory of electronic topological transitions,. *Physics Reports*, 245(4):159 – 257, 1994.

-
- [57] H. Rosner, D. Koudela, U. Schwarz, A. Handstein, M. Hanfland, I. Opahle, K. Koepernik, M. D. Kuz'min, K.-H. Müller, J. A. Mydosh, et al. Magneto-elastic lattice collapse in YCo_5 . *Nature Physics*, 2(7):469–472, 2006.
- [58] E. A. Yelland, J. M. Barraclough, W. Wang, K. V. Kamenev, and A. D. Huxley. High-field superconductivity at an electronic topological transition in URhGe. *Nature Physics*, 7(11):890–894, 2011.
- [59] J. Betouras. Lifshitz topological transition in interacting fermion systems. *Talk at 4th Hubbard theory consortium London summer programme in condensed matter physics, Royal Holloway, University of London.*, 2013.
- [60] C. Liu, T. Kondo, R. M. Fernandes, A. D. Palczewski, E. D. Mun, N. Ni, A. N. Thaler, A. Bostwick, E. Rotenberg, J. Schmalian, et al. Evidence for a Lifshitz transition in electron-doped iron arsenic superconductors at the onset of superconductivity. *Nature Physics*, 6(6):419–423, 2010.
- [61] Y. Okamoto, A. Nishio, and Z. Hiroi. Discontinuous Lifshitz transition achieved by band-filling control in Na_xCoO_2 . *Phys. Rev. B*, 81:121102, Mar 2010.
- [62] A. Hackl and M. Vojta. Zeeman-driven Lifshitz transition: A model for the experimentally observed Fermi-surface reconstruction in YbRh_2Si_2 . *Phys. Rev. Lett.*, 106:137002, Mar 2011.
- [63] L. D. Landau. The theory of a Fermi liquid. *Sov. Phys. JETP*, 3(6):920, 1957.
- [64] D. Pines and P. Nozières. *The theory of quantum fluids*. W. A. Benjamin, New York, 1966.
- [65] P. Nozières. *Interacting Fermi systems*. W. A. Benjamin, New York, 1964.
- [66] P. Coleman, C. Pépin, Q. Si, and R. Ramazashvili. How do Fermi liquids get heavy and die? *Journal of Physics: Condensed Matter*, 13(35):723, 2001.
- [67] B. M. Maple, R. E. Baumbach, N. P. Butch, J. J. Hamlin, and M. Janoschek. Non-Fermi liquid regimes and superconductivity in the low temperature phase diagrams of strongly correlated d- and f-electron materials. *Journal of Low Temperature Physics*, 161(1):4–54, 2010.
- [68] T. R. Kirkpatrick and D. Belitz. Columnar fluctuations as a source of non-Fermi-liquid behavior in weak metallic magnets. *Phys. Rev. Lett.*, 104:256404, 2010.
- [69] P. Coleman. Theories of non-Fermi liquid behavior in heavy fermions. *Physica B: Condensed Matter*, 259:353–358, 1999.
- [70] A. J. Schofield. Non-Fermi liquids. *Contemporary Physics*, 40(2):95–115, Apr 1999.
- [71] O. Trovarelli, C. Geibel, S. Mederle, C. Langhammer, F. M. Grosche, P. Gegenwart, M. Lang, G. Sparn, and F. Steglich. YbRh_2Si_2 : Pronounced non-Fermi-liquid effects above a low-lying magnetic phase transition. *Phys. Rev. Lett.*, 85:626–629, Jul 2000.

- [72] P. Gegenwart, J. Custers, C. Geibel, K. Neumaier, T. Tayama, K. Tenya, O. Trovarelli, and F. Steglich. Magnetic-field induced quantum critical point in YRh_2Si_2 . *Phys. Rev. Lett.*, 89:056402, Jul 2002.
- [73] V. S. Zapf, N. A. Frederick, K. L. Rogers, K. D. Hof, P.-C. Ho, E. D. Bauer, and M. B. Maple. Magnetic and non-Fermi-liquid phases in $\text{Ce}_{1-x}\text{Y}_x\text{RhIn}_5$. *Phys. Rev. B*, 67:064405, Feb 2003.
- [74] C. Pfleiderer, G. J. McMullan, S. R. Julian, and G. G. Lonzarich. Magnetic quantum phase transition in MnSi under hydrostatic pressure. *Phys. Rev. B*, 55:8330–8338, 1997.
- [75] N. Tateiwa, T. Kobayashi, K. Hanazono, K. Amaya, Y. Haga, R. Settai, and Y. Onuki. Pressure-induced superconductivity in a ferromagnet UGe_2 . *Journal of Physics: Condensed Matter*, 13(1):L17, 2000.
- [76] T. Muramatsu, T. C. Kobayashi, K. Shimizu, K. Amaya, D. Aoki, Y. Haga, and Y. Onuki. Electrical resistivity of CeTIn_5 ($T = \text{Rh, Ir}$) under high pressure. *Physica C: Superconductivity*, 388:539–540, 2003.
- [77] A. de Visser. Superconducting ferromagnets. *Encyclopedia of Materials: Science and Technology*, Eds K.H.J. Buschow et al. (Elsevier, Oxford), pages 1–6, 2010.
- [78] C. Pfleiderer. Superconducting phases of f -electron compounds. *Rev. Mod. Phys.*, 81:1551–1624, 2009.
- [79] D. Aoki and J. Flouquet. Ferromagnetism and superconductivity in uranium compounds. *J. Phys. Soc. Jpn.*, 81(1):011003, 2012.
- [80] K. Oikawa, T. Kamiyama, H. Asano, Y. Ōnuki, and M. Kohgi. Crystal structure of UGe_2 . *J. Phys. Soc. Jpn.*, 65(10):3229–3232, 1996.
- [81] P. Boulet, A. Daoudi, M. Potel, H. Noël, G. M. Gross, G. André, and F. Bourée. Crystal and magnetic structure of the uranium digermanide UGe_2 . *Journal of Alloys and Compounds*, 247(1–2):104 – 108, 1997.
- [82] Y. Ōnuki, I. Ukon, S. W. Yun, I. Umehara, K. Satoh, T. Fukuhara, H. Sato, S. Takayanagi, M. Shikama, and A. Ochiai. Magnetic and electrical properties of U–Ge intermetallic compounds. *J. Phys. Soc. Jpn.*, 61(1):293–299, 1992.
- [83] G. Oomi, T. Kagayama, K. Nishimura, S. W. Yun, and Y. Onuki. Electrical resistivity of single crystalline UGe_2 at high pressure and high magnetic field. *Physica B: Condensed Matter*, 206–207(0):515 – 518, 1995.
- [84] G. Oomi, K. Nishimura, Y. Onuki, and S. W. Yun. Anomalous thermal expansion of single-crystalline UGe_2 . *Physica B: Condensed Matter*, 186–188(0):758 – 760, 1993.
- [85] H. Misiorek, J. Mucha, R. Troć, and B. Coqblin. Thermal conductivity anisotropy in a ferromagnetic superconductor, UGe_2 . *Journal of Physics: Condensed Matter*, 17(4):679, 2005.

-
- [86] V. H. Tran, S. Paschen, R. Troć, M. Baenitz, and F. Steglich. Hall effect in the ferromagnet UGe₂. *Phys. Rev. B*, 69:195314, 2004.
- [87] A. Huxley, I. Sheikin, E. Ressouche, N. Kernavanois, D. Braithwaite, R. Calemczuk, and J. Flouquet. UGe₂: A ferromagnetic spin-triplet superconductor. *Phys. Rev. B*, 63:144519, 2001.
- [88] Y. Ōnuki, S. W. Yun, I. Ukon, I. Umehara and K. Satoh, I. Sakamoto, M. Hunt, P. Meeson, P.-A. Probst, and M. Springford. High field magnetoresistance and de Haas-van Alphen effect in UGe₂. *J. Phys. Soc. Jpn.*, 60(7):2127–2130, 1991.
- [89] A. B. Shick and W. E. Pickett. Magnetism, spin-orbit coupling, and superconducting pairing in UGe₂. *Phys. Rev. Lett.*, 86:300–303, 2001.
- [90] V. Taufour, D. Aoki, G. Knebel, and J. Flouquet. Tricritical point and wing structure in the itinerant ferromagnet UGe₂. *Phys. Rev. Lett.*, 105:217201, 2010.
- [91] N. Kabeya, R. Iijima, E. Osaki, S. Ban, K. Imura, K. Deguchi and N. Aso, Y. Homma, Y. Shiokawa, and N. K. Sato. Tricritical point of a ferromagnetic transition in UGe₂. *Journal of Physics: Conference Series*, 200(3):032028, 2010.
- [92] V. Taufour, A. Villaume, D. Aoki, G. Knebel, and J. Flouquet. Magnetic field evolution of critical end point in UGe₂. *Journal of Physics: Conference Series*, 273(1):012017, 2011.
- [93] C. Pfleiderer and A. D. Huxley. Pressure dependence of the magnetization in the ferromagnetic superconductor UGe₂. *Phys. Rev. B*, 89(147005), 2002.
- [94] T. Terashima, T. Matsumoto, C. Terakura, S. Uji, N. Kimura, M. Endo, T. Komatsubara, and H. Aoki. Evolution of quasiparticle properties in UGe₂ with hydrostatic pressure studied via the de Haas-van Alphen effect. *Phys. Rev. Lett.*, 87:166401, 2001.
- [95] R. Settai, M. Nakashima, S. Araki, Y. Haga, T. C. Kobayashi, N. Tateiwa, H. Yamagami, and Y. Onuki. A change of the Fermi surface in UGe₂ across the critical pressure. *Journal of Physics: Condensed Matter*, 14(1):L29, 2002.
- [96] H. Kotegawa, V. Taufour, D. Aoki, G. Knebel, and J. Flouquet. Evolution toward quantum critical end point in UGe₂. *J. Phys. Soc. Jpn.*, 80(8):083703, 2011.
- [97] A. D. Huxley, S. Raymond, and E. Ressouche. Magnetic excitations in the ferromagnetic superconductor UGe₂. *Phys. Rev. Lett.*, 91:207201, 2003.
- [98] A. Huxley, E. Ressouche, B. Grenier, D. Aoki, J. Flouquet, and C. Pfleiderer. The coexistence of superconductivity and ferromagnetism in actinide compounds. *Journal of Physics: Condensed Matter*, 15(28):1945, 2003.

- [99] I. Sheikin, E. Steep, D. Braithwaite, J.-P. Brison, S. Raymond, D. Jaccard, and J. Flouquet. Superconductivity, upper critical field and anomalous normal state in CePd_2Si_2 near the quantum critical point. *Journal of Low Temperature Physics*, 122(5-6):591–604, 2001.
- [100] I. Sheikin, A. Huxley, D. Braithwaite, J. P. Brison, S. Watanabe, K. Miyake, and J. Flouquet. Anisotropy and pressure dependence of the upper critical field of the ferromagnetic superconductor UGe_2 . *Phys. Rev. B*, 64:220503, 2001.
- [101] K. Nishimura, G. Oomi, S. W. Yun, and Y. Onuki. Effect of pressure on the Curie temperature of single-crystal UGe_2 . *Journal of Alloys and Compounds*, 213–214(0):383 – 386, 1994.
- [102] F. Hardy, C. Meingast, V. Taufour, J. Flouquet, H. v. Löhneysen, R. A. Fisher, N. E. Phillips, A. Huxley, and J. C. Lashley. Two magnetic Grüneisen parameters in the ferromagnetic superconductor UGe_2 . *Phys. Rev. B*, 80:174521, 2009.
- [103] G. Oomi, T. Kagayama, and Y. Onuki. Critical electron scattering in UGe_2 near the magnetic phase transition induced by pressure. *Journal of Alloys and Compounds*, 271–273(0):482 – 485, 1998.
- [104] G. Oomi, M. Ohashi, F. Honda, Y. Haga, and Y. Onuki. Anomalous pressure dependence of the electrical resistance and thermal expansion of UGe_2 in the paramagnetic state. *Journal of Physics: Condensed Matter*, 15(28):2039, 2003.
- [105] G. Oomi, M. Ohashi, K. Nishimura, and Y. Onuki. Precursor phenomena to pressure-induced superconductivity in the thermal expansion of UGe_2 . *J. Nucl. Sci. Technol.*, Supplement 3:90–93, 2002.
- [106] Y. Ushida, H. Nakane, T. Nishioka, G. Motoyama, S. Nakamura, and N. K. Sato. Thermal expansion measurement under pressure of UGe_2 . *Physica C: Superconductivity*, 388–389(0):525 – 526, 2003.
- [107] S. Watanabe and K. Miyake. Coupled CDW and SDW fluctuations as an origin of anomalous properties of ferromagnetic superconductor UGe_2 . *J. Phys. Soc. Jpn.*, 71(10):2489–2499, 2002.
- [108] A. B. Shick, V. Janiš, V. Drchal, and W. E. Pickett. Spin and orbital magnetic state of UGe_2 under pressure. *Phys. Rev. B*, 70:134506, 2004.
- [109] K. G. Sandeman, G. G. Lonzarich, and A. J. Schofield. Ferromagnetic superconductivity driven by changing Fermi surface topology. *Phys. Rev. Lett.*, 90:167005, 2003.
- [110] N. B. Perkins, M. D. Núñez Regueiro, B. Coqblin, and J. R. Iglesias. Underscreened Kondo lattice model applied to heavy fermion uranium compounds. *Phys. Rev. B*, 76:125101, 2007.

-
- [111] C. Thomas, A. S. da Rosa Simões, J. R. Iglesias, C. Lacroix, N. B. Perkins, and B. Coqblin. Application of the $S = 1$ underscreened Anderson lattice model to Kondo uranium and neptunium compounds. *Phys. Rev. B*, 83:014415, 2011.
- [112] S. Hoshino and Y. Kuramoto. Itinerant versus localized heavy-electron magnetism. *Phys. Rev. Lett.*, 111:026401, 2013.
- [113] G. H. Lander, E. S. Fisher, and S. D. Bader. The solid-state properties of Uranium. A historical perspective and review. *Advances in Physics*, 43(1):1–111, 1994.
- [114] G. H. Lander, M. S. S. Brooks, and B. Johansson. Orbital band magnetism in actinide intermetallics. *Phys. Rev. B*, 43:13672–13675, 1991.
- [115] D. Fay and J. Appel. Coexistence of p -state superconductivity and itinerant ferromagnetism. *Phys. Rev. B*, 22:3173–3182, 1980.
- [116] K. Kuwahara, H. Sagayama, K. Iwasa, M. Kohgi, Y. Haga, Y. Onuki, K. Kakurai, M. Nishi, K. Nakajima, N. Aso, and Y. Uwatoko. Magnetic form factor of UGe_2 under high pressure. *Physica B: Condensed Matter*, 312–313(0):106 – 108, 2002.
- [117] T. H. K. Barron and G. K. White. *Heat capacity and thermal expansion at low temperatures*. Kluwer Academic New York, 1999.
- [118] C. Y. Ho and R. E. Taylor. *Thermal expansion of solids*, volume 4. ASM international, 1998.
- [119] L. Zhu, M. Garst, A. Rosch, and Q. Si. Universally diverging grüneisen parameter and the magnetocaloric effect close to quantum critical points. *Phys. Rev. Lett.*, 91:066404, 2003.
- [120] M. Garst and A. Rosch. Sign change of the Grüneisen parameter and magnetocaloric effect near quantum critical points. *Phys. Rev. B*, 72:205129, 2005.
- [121] K. Grube, W. H. Fietz, U. Tutsch, O. Stockert, and H. v. Löhneysen. Suppression of the structural phase transition in CeCu_6 by pressure and Au doping. *Phys. Rev. B*, 60:11947–11953, 1999.
- [122] G. Motoyama, T. Nishioka, and N. K. Sato. Phase transition between hidden and antiferromagnetic order in URu_2Si_2 . *Phys. Rev. Lett.*, 90:166402, 2003.
- [123] M. T. Rekveldt. High-resolution diffraction using Larmor precession of polarised neutrons. *Materials Science Forum*, 321-324:258–263, 2000.
- [124] M. T. Rekveldt, T. Keller, and R. Golub. Larmor precession, a technique for high-sensitivity neutron diffraction. *Europhys.Lett.*, 54(3):342, 2001.
- [125] F. Mezei, C. Pappas, and T. Gutberlet. *Neutron spin echo spectroscopy: Basics, trends and applications*, volume 601. Springer, 2003.

- [126] T. Keller, R. Golub, F. Mezei, and R. Gähler. Recent developments and results from the neutron resonance spin-echo spectrometer (NRSE) at BENSC Berlin. *Physica B: Condensed Matter*, 234–236(0):1126 – 1127, 1997.
- [127] T. Keller, R. Gähler, H. Kunze, and R. Golub. Features and performance of an NRSE spectrometer at BENSC. *Neutron News*, 6(3):16–17, 1995.
- [128] F. R. Kroeger and C. A. Swenson. Absolute linear thermal-expansion measurements on copper and aluminum from 5 to 320 K. *Journal of Applied Physics*, 48(3):853–864, 1977.
- [129] J. Repper, T. Keller, M. Hofmann, C. Kremaszky, W. Petry, and E. Werner. Neutron Larmor diffraction measurements for materials science. *Acta Materialia*, 58(9):3459 – 3467, 2010.
- [130] J. Repper, T. Keller, M. Hofmann, C. Kremaszky, W. Petry, and E. Werner. Neutron Larmor diffraction for the determination of absolute lattice spacing. *JCPDS-International Centre for Diffraction Data*, 2009.
- [131] T. Keller, M. Th. Rekveldt, and K. Habicht. Neutron Larmor diffraction measurement of the lattice-spacing spread of pyrolytic graphite. *Applied Physics A*, 74:127–129, 2002.
- [132] P. G. Niklowitz, C. Pfeiderer, T. Keller, M. Vojta, Y.-K. Huang, and J. A. Mydosh. Parasitic small-moment antiferromagnetism and nonlinear coupling of hidden order and antiferromagnetism in URu₂Si₂ observed by Larmor diffraction. *Phys. Rev. Lett.*, 104:106406, 2010.
- [133] T. Keller, K. Habicht, H. Klann, M. Ohl, H. Schneider, and B. Keimer. The NRSE-TAS spectrometer at the FRM-2. *Applied Physics A*, 74:332–335, 2002.
- [134] <http://www2.fkf.mpg.de/keimer/groups/frm/methods.html>.
- [135] F. Mezei. Neutron spin echo and polarized neutrons. *Neutron Inelastic Scattering (IAEA, Vienna)*, pages 125–134, 1978.
- [136] P. Böni, D. Clemens, M. S. Kumar, and C. Pappas. Applications of remanent supermirror polarizers. *Physica B: Condensed Matter*, 267–268(0):320 – 327, 1999.
- [137] D. A. Sokolov, R. Ritz, C. Pfeiderer, T. Keller, and A. D. Huxley. Thermal expansion of UGe₂ under pressure. Submitted to PRL.
- [138] D. A. Sokolov. Private communication.
- [139] <http://www.frm2.tum.de/wissenschaftliche-nutzung/zentrale-servicegruppen/probenumgebung/ausstattung/index.html>.
- [140] C. Pfeiderer, A. D. Huxley, and S. M. Hayden. On the use of Cu:Be clamp cells in magnetization and neutron scattering studies. *Journal of Physics: Condensed Matter*, 17(40):3111, 2005.

-
- [141] V. A. Sidorov and R. A. Sadykov. Hydrostatic limits of fluorinert liquids used for neutron and transport studies at high pressure. *J. Phys.: Condens. Matter*, 17(40):3005–3008, 2005.
- [142] S. Sakarya, N. H. van Dijk, and E. Brück. Determination of the magnetic domain size in the ferromagnetic superconductor UGe₂ by three-dimensional neutron depolarization. *Phys. Rev. B*, 71:174417, 2005.
- [143] M. Wagner. Private communication.
- [144] S. Raymond and A. Huxley. Phonon spectrum of the ferromagnetic superconductor UGe₂ and consequences for its specific heat. *Phys. Rev. B*, 73:094420, 2006.
- [145] Under pressures up to p_X , all curves except two are corrected for the measured spin-echo phase: (i) The b -axis at 9.3 kbar is not spin-echo phase corrected (see Fig. A.2). However, as seen at 10.2 kbar and 11.8 kbar (see Figs.A.3 and A.4) the spin-echo phase correction does only minor changes to $\Delta b/b$ that do not affect the qualitative course. (ii) For the a -axis at 10.2 kbar (shown as open datapoints in panel e) an estimated spin-echo phase correction was subtracted. Thereby, the spin-echo phase was estimated from the scaled polarization curve (see Fig. A.3) as the spin-echo phase along the a -axis at 9.3 kbar and 11.8 kbar empirically resemble the scaled polarization curves. Compared to the corrected a -axis curves at 9.3 kbar and 11.8 kbar, the 10.2 kbar curve appears reasonable. At pressures above p_X , that are not relevant for our main results, no spin-echo phase was measured and corrected (see Figs.A.5 and A.6).
- [146] H. Nakane, G. Motoyama, T. Nishioka, and N. K. Sato. Correlation between superconductivity and ferromagnetism in UGe₂. *J. Phys. Soc. Jpn.*, 74(3):855–858, 2005.
- [147] A. Hackl and M. Vojta. Kondo volume collapse, Kondo breakdown, and Fermi surface transitions in heavy-fermion metals. *Phys. Rev. B*, 77:134439, 2008.
- [148] V. P. Antropov, M. I. Katsnelson, V. G. Koreshkov, A. I. Likhtenstein, A. V. Trefilov, and V. G. Vaks. On anomalies of anisotropic thermal expansion near points of electronic topological transitions in noncubic metals. Applications to Zn, Cd and Cd-Mg alloys. *Physics Letters A*, 130(3):155 – 160, 1988.
- [149] C. Stock, D. A. Sokolov, P. Bourges, P. H. Tobash, K. Gofryk, F. Ronning, E. D. Bauer, K. C. Rule, and A. D. Huxley. Anisotropic critical magnetic fluctuations in the ferromagnetic superconductor UCoGe. *Phys. Rev. Lett.*, 107:187202, 2011.
- [150] L. D. Landau and E. M. Lifshitz. *Course of theoretical physics, vol. 8*. Pergamon Press, 1980.
- [151] S. Kusaka, K. Yamamoto, T. Komatsubara, and Y. Ishikawa. Ultrasonic study of magnetic phase diagram of MnSi. *Solid State Communications*, 20(9):925–927, 1976.

- [152] K. Kadowaki, K. Okuda, and M. Date. Magnetization and magnetoresistance of MnSi. *J. Phys. Soc. Jpn.*, 51(8):2433–2438, 1982.
- [153] A. Bauer and C. Pfleiderer. Magnetic phase diagram of MnSi inferred from magnetization and ac susceptibility. *Phys. Rev. B*, 85:214418, 2012.
- [154] S. Mühlbauer, B. Binz, F. Jonietz, C. Pfleiderer, A. Rosch, A. Neubauer, R. Georgii, and P. Böni. Skyrmion lattice in a chiral magnet. *Science*, 323(5916):915–919, 2009.
- [155] T. Adams, S. Mühlbauer, C. Pfleiderer, F. Jonietz, A. Bauer, A. Neubauer, R. Georgii, P. Böni, U. Keiderling, K. Everschor, M. Garst, and A. Rosch. Long-Range crystalline nature of the skyrmion lattice in MnSi. *Phys. Rev. Lett.*, 107:217206, 2011.
- [156] A. Tonomura, X. Yu, K. Yanagisawa, T. Matsuda, Y. Onose, N. Kanazawa, H. S. Park, and Y. Tokura. Real-space observation of skyrmion lattice in helimagnet MnSi thin samples. *Nano Letters*, 12(3):1673–1677, 2012.
- [157] X. Z. Yu, N. Kanazawa, Y. Onose, K. Kimoto, W. Z. Zhang, S. Ishiwata, Y. Matsui, and Y. Tokura. Near room-temperature formation of a skyrmion crystal in thin-films of the helimagnet FeGe. *Nature Mater.*, 10(2):106–109, 2010.
- [158] X. Z. Yu, Y. Onose, N. Kanazawa, J. H. Park, J. H. Han, Y. Matsui, N. Nagaosa, and Y. Tokura. Real-space observation of a two-dimensional skyrmion crystal. *Nature*, 465(7300):901–904, 2010.
- [159] W. Münzer, A. Neubauer, T. Adams, S. Mühlbauer, C. Franz, F. Jonietz, R. Georgii, P. Böni, B. Pedersen, M. Schmidt, A. Rosch, and C. Pfleiderer. Skyrmion lattice in the doped semiconductor $\text{Fe}_{1-x}\text{Co}_x\text{Si}$. *Phys. Rev. B*, 81:041203, 2010.
- [160] S. Seki, X. Z. Yu, S. Ishiwata, and Y. Tokura. Observation of skyrmions in a multiferroic material. *Science*, 336(6078):198–201, 2012.
- [161] T. Adams, A. Chacon, M. Wagner, A. Bauer, G. Brandl, B. Pedersen, H. Berger, P. Lemmens, and C. Pfleiderer. Long-wavelength helimagnetic order and skyrmion lattice phase in Cu_2OSeO_3 . *Phys. Rev. Lett.*, 108(23):237204, 2012.
- [162] M. Lee, W. Kang, Y. Onose, Y. Tokura, and N. P. Ong. Unusual Hall effect anomaly in MnSi under pressure. *Phys. Rev. Lett.*, 102(18):186601, 2009.
- [163] J. Zang, M. Mostovoy, J. H. Han, and N. Nagaosa. Dynamics of skyrmion crystals in metallic thin films. *Phys. Rev. Lett.*, 107:136804, 2011.
- [164] M. Garst. Spin-transfer torques and emergent electrodynamics in magnetic skyrmion crystals. *Talk at Newspin2 conference, College Station, Texas.*, 2011.
- [165] C. Pfleiderer and A. Rosch. Condensed-matter physics: Single skyrmions spotted. *Nature*, 465(7300):880–881, 2010.

-
- [166] T. H. R. Skyrme. A unified field theory of mesons and baryons. *Nuclear Physics*, 31:556–569, 1962.
- [167] M. Eisenberg and R. Guy. A proof of the hairy ball theorem. *The American Mathematical Monthly*, 86(7):pp. 571–574, 1979.
- [168] R. Abraham, J. E. Marsden, and T. S. Ratiu. *Manifolds, tensor analysis, and applications*, volume 75. Springer, 1988.
- [169] B. Binz and A. Vishwanath. Chirality induced anomalous-Hall effect in helical spin crystals. *Physica B*, 403(5-9):1336–1340, 2008.
- [170] S. Mühlbauer. Vortex lattices in superconducting niobium and skyrmion lattices in the chiral magnet MnSi investigated by neutron scattering. PhD Thesis, TU München, 2009.
- [171] J. D. Thompson, Z. Fisk, and G. G. Lonzarich. Perspective on heavy-electron and Kondo-lattice systems from high pressure studies . *Physica B*, 161(1-3):317–323, 1989.
- [172] C. Pfleiderer, R. H. Friend, G. G. Lonzarich, N. R. Bernhoeft, and J. Flouquet. Transition from a magnetic to a nonmagnetic state as a function of pressure in MnSi. *International Journal of Modern Physics B*, 07:887–890, 1993.
- [173] C. Thessieu, C. Pfleiderer, A. N. Stepanov, and J. Flouquet. Field dependence of the magnetic quantum phase transition in MnSi. *J. Phys.: Condens. Matter*, 9:6677, 1997.
- [174] K. Koyama, T. Goto, T. Kanomata, and R. Note. Observation of an itinerant metamagnetic transition in MnSi under high pressure. *Phys. Rev. B*, 62:986–991, 2000.
- [175] T. Moriya. Spin fluctuations in itinerant electron magnetism. *Springer, Heidelberg, Berlin*, 1985.
- [176] Y. J. Uemura, T. Goko, I. M. Gat-Malureanu, J. P. Carlo, P. L. Russo, A. T. Savici, A. Aczel, G. J. MacDougall, J. A. Rodriguez, G. M. Luke, et al. Phase separation and suppression of critical dynamics at quantum phase transitions of MnSi and $(\text{Sr}_{1-x}\text{Ca}_x)\text{RuO}_3$. *Nature Physics*, 3(1):29–35, 2006.
- [177] C. Pfleiderer. Non-Fermi liquid puzzle of MnSi at high pressure. *Physica B*, 328:100–104, 2003.
- [178] C. Pfleiderer, D. Reznik, L. Pintschovius, and J. Haug. Magnetic field and pressure dependence of small angle neutron scattering in MnSi. *Phys. Rev. Lett.*, 99(156406):156406, 2007.
- [179] U. K. Rößler, A. N. Bogdanov, and C. Pfleiderer. Spontaneous skyrmion ground states in magnetic metals. *Nature*, 442(05056):797–800, 2006.

- [180] N. Rivier and K. Adkins. Resistivity of spin glasses. *Journal of Physics F: Metal Physics*, 5(9):1745, 1975.
- [181] K. H. Fischer. On the electrical resistivity of spin glasses. *Zeitschrift für Physik B Condensed Matter*, 34:45–53, 1979.
- [182] S. Tewari, D. Belitz, and T. R. Kirkpatrick. Blue quantum fog: Chiral condensation in quantum helimagnets. *Phys. Rev. Lett.*, 96:047207, 2006.
- [183] I. Fischer, N. Shah, and A. Rosch. Crystalline phases in chiral ferromagnets: Destabilization of helical order. *Phys. Rev. B*, 77:024415, 2008.
- [184] C. Thessieu, J. Flouquet, G. Lapertot, A. N. Stepanov, and D. Jaccard. Magnetism and spin fluctuations in a weak itinerant ferromagnet: MnSi. *Solid State Commun.*, 95(10):707 – 712, 1995.
- [185] A. E. Petrova and S. M. Stishov. On the phase diagram of the itinerant helimagnet MnSi: Does MnSi become quantum critical? *arXiv preprint*, 1208.2174, 2012.
- [186] R. Gross. Spintronics. Lecture Notes, TU München, 2005.
- [187] A. Neubauer, C. Pfleiderer, R. Ritz, P. G. Niklowitz, and P. Böni. Hall effect and magnetoresistance in MnSi. *Physica B: Condensed Matter*, 404(19):3163 – 3166, 2009.
- [188] E. H. Hall. On a new action of the magnet on electric currents. *American Journal of Mathematics*, 2:287, 1879.
- [189] N. Nagaosa, J. Sinova, S. Onoda, A. H. MacDonald, and N. P. Ong. Anomalous Hall effect. *Rev. Mod. Phys.*, 82(2):1539, 2010.
- [190] Y. Taguchi, Y. Oohara, H. Yoshizawa, N. Nagaosa, and Y. Tokura. Spin chirality, Berry phase, and anomalous Hall effect in a frustrated ferromagnet. *Science*, 291(5513):2573–2576, 2001.
- [191] Y. Machida, S. Nakatsuji, Y. Maeno, T. Tayama, T. Sakakibara, and S. Onoda. Unconventional anomalous Hall effect enhanced by a noncoplanar spin texture in the frustrated Kondo lattice $\text{Pr}_2\text{Ir}_2\text{O}_7$. *Phys. Rev. Lett.*, 98:057203, 2007.
- [192] S. Hunklinger. *Festkörperphysik*. Oldenbourg Wissenschaftsverlag GmbH, München, 2009.
- [193] N. W. Ashcroft and D. N. Mermin. *Festkörperphysik*. Oldenbourg Wissenschaftsverlag, 2007.
- [194] E. M. Pugh. Hall effect and the magnetic properties of some ferromagnetic materials. *Phys. Rev.*, 36:1503–1511, 1930.
- [195] E. M. Pugh and T. W. Lippert. Hall e.m.f. and intensity of magnetization. *Phys. Rev.*, 42:709–713, 1932.

-
- [196] R. Karplus and J. M. Luttinger. Hall effect in ferromagnetics. *Phys. Rev.*, 95(5):1154–1160, 1954.
- [197] D. Xiao, M. C. Chang, and Q. Niu. Berry phase effects on electronic properties. *Rev. Mod. Phys.*, 82(3):1959, 2010.
- [198] N. P. Ong and W. L. Lee. Geometry and the anomalous Hall effect in ferromagnets. *arXiv preprint*, 0508236, 2005.
- [199] M. V. Berry. Quantal phase factors accompanying adiabatic changes. *Proceedings of the Royal Society of London. A. Mathematical and Physical Sciences*, 392(1802):45–57, 1984.
- [200] F. D. M. Haldane. Berry curvature on the Fermi surface: Anomalous Hall effect as a topological Fermi-liquid property. *Phys. Rev. Lett.*, 93:206602, 2004.
- [201] A. Rosch. To be published.
- [202] N. Kanazawa, Y. Onose, T. Arima, D. Okuyama, K. Ohoyama, S. Wakimoto, K. Kakurai, S. Ishiwata, and Y. Tokura. Large topological Hall effect in a short-period helimagnet MnGe. *Phys. Rev. Lett.*, 106(15):156603, 2011.
- [203] S. Ishiwata, M. Tokunaga, Y. Kaneko, D. Okuyama, Y. Tokunaga, S. Wakimoto, K. Kakurai, T. Arima, Y. Taguchi, and Y. Tokura. Versatile helimagnetic phases under magnetic fields in cubic perovskite SrFeO₃. *Phys. Rev. B*, 84:054427, 2011.
- [204] J. Ye, Y. B. Kim, A. J. Millis, B. I. Shraiman, P. Majumdar, and Z. Tešanović. Berry phase theory of the anomalous Hall effect: Application to colossal magnetoresistance manganites. *Phys. Rev. Lett.*, 83:3737–3740, 1999.
- [205] H. Yanagihara and M. B. Salamon. Skyrmion strings and the anomalous Hall effect in CrO₂. *Phys. Rev. Lett.*, 89:187201, 2002.
- [206] S. A. Baily and M. B. Salamon. Berry-phase contribution to the anomalous Hall effect in gadolinium. *Phys. Rev. B*, 71:104407, 2005.
- [207] T. Adams. Skyrmionengitter und partielle Ordnung in B20 Übergangsmetallverbindungen. Diploma Thesis, TU München, 2009.
- [208] C. Franz and C. Pfeleiderer. Unpublished.
- [209] J. Smit. The spontaneous Hall effect in ferromagnetics I. *Physica*, 21(6):877–887, 1955.
- [210] J. Smit. The spontaneous Hall effect in ferromagnetics II. *Physica*, 24(1-5):39–51, 1958.
- [211] L. Berger. Influence of spin-orbit interaction on the transport processes in ferromagnetic nickel alloys, in the presence of a degeneracy of the 3d band. *Physica*, 30(6):1141–1159, 1964.

- [212] L. Berger. Side-jump mechanism for the Hall effect of ferromagnets. *Phys. Rev. B*, 2(11):4559–4566, 1970.
- [213] M. Lee, Y. Onose, Y. Tokura, and N. P. Ong. Hidden constant in the anomalous Hall effect of high-purity magnet MnSi. *Phys. Rev. B*, 75(17):172403, 2007.
- [214] F. Freimuth. Private communication.
- [215] Y. Ishikawa, K. Tajima, D. Bloch, and M. Roth. Helical spin structure in manganese silicide MnSi. *Solid State Communications*, 19(6):525 – 528, 1976.
- [216] S. V. Grigoriev, S. V. Maleyev, A. I. Okorokov, Yu. O. Chetverikov, P. Böni, R. Georgii, D. Lamago, H. Eckerlebe, and K. Pranzas. Magnetic structure of MnSi under an applied field probed by polarized small-angle neutron scattering. *Phys. Rev. B*, 74:214414, 2006.
- [217] A. Neubauer, J. Bœuf, A. Bauer, B. Russ, H. Lohneysen, and C. Pfeleiderer. Ultra-high vacuum compatible image furnace. *Rev. Sci. Instrum.*, 82(1):013902–013902, 2011.
- [218] A. Bauer, A. Neubauer, C. Franz, W. Münzer, M. Garst, and C. Pfeleiderer. Quantum phase transitions in single-crystal $\text{Mn}_{1-x}\text{Fe}_x\text{Si}$ and $\text{Mn}_{1-x}\text{Co}_x\text{Si}$: Crystal growth, magnetization, ac susceptibility, and specific heat. *Phys. Rev. B*, 82(6):064404, 2010.
- [219] <http://www.ngkberylco.co.uk/charact.htm>.
- [220] I. R. Walker. Nonmagnetic piston–cylinder pressure cell for use at 35 kbar and above. *Review of scientific instruments*, 70:3402, 1999.
- [221] G. J. Piermarini, S. Block, and J. D. Barnett. Hydrostatic limits in liquids and solids to 100 kbar. *J. Appl. Phys.*, 44:5377, 1973.
- [222] J. A. Osborn. Demagnetizing factors of the general ellipsoid. *Phys. Rev.*, 67(11):351–357, 1945.
- [223] A. Aharoni. Demagnetizing factors for rectangular ferromagnetic prisms. *J. Appl. Phys.*, 83(6):3432–3434, 1998.
- [224] M. Halder. Präzisionsmessung der Magnetisierung an Systemen mit komplexer Ordnung. Diploma Thesis, TU München, 2012.
- [225] A. Bauer. Private communication.
- [226] T. F. Smith and C. W. Chu. Will pressure destroy superconductivity? *Physical Review*, 159(2):353–358, 1967.
- [227] T. Jeong and W. E. Pickett. Implications of the B20 crystal structure for the magnetoelectronic structure of MnSi. *Phys. Rev. B*, 70:075114, 2004.

-
- [228] S. A. Brown. PhD Thesis, University of Cambridge, 1990.
- [229] A. Chacon, T. Adams, G. Brandl, A. Bauer, R. Georgii, P. Böni, and C. Pfleiderer. Uniaxial stress studies of the skyrmion lattice in MnSi. Unpublished.
- [230] B. Fåk, R. A. Sadykov, J. Flouquet, and G. Lapertot. Pressure dependence of the magnetic structure of the itinerant electron magnet MnSi. *Journal of Physics: Condensed Matter*, 17(10):1635, 2005.
- [231] B. Binz, A. Vishwanath, and V. Aji. Theory of the helical spin crystal: A candidate for the partially ordered state of MnSi. *Phys. Rev. Lett.*, 96(207202), 2006.
- [232] P. G. Niklowitz, F. Beckers, G. G. Lonzarich, G. Knebel, B. Salce, J. Thomason, N. Bernhoeft, D. Braithwaite, and J. Flouquet. Spin-fluctuation-dominated electrical transport of Ni₃Al at high pressure. *Phys. Rev. B*, 72(024424), 2005.
- [233] X. Z. Yu, N. Kanazawa, W. Z. Zhang, T. Nagai, T. Hara, K. Kimoto, Y. Matsui, Y. Onose, and Y. Tokura. Skyrmion flow near room temperature in an ultralow current density. *Nature Commun.*, 3:988, 2012.
- [234] C. Schnarr. Spin Transfer Torque Effekte in chiralen Magneten. Diploma Thesis, TU München, 2012.
- [235] N. Romming, C. Hanneken, M. Menzel, J. E. Bickel, B. Wolter, K. von Bergmann, A. Kubetzka, and R. Wiesendanger. Writing and deleting single magnetic skyrmions. *Science*, 341(6146):636–639, 2013.